TESIS DE LA UNIVERSIDAD DE ZARAGOZA

2017

29

Julia Ramírez García

Prediction of Cardiac Death Risk by Analysis of Ventricular Repolarization Restitution from the Electrocardiogram Signal

Departamento

Instituto de Investigación en Ingeniería [I3A]

Director/es

Pueyo Paules, Esther
Laguna Lasaosa, Pablo

ISSN 2254-7606

Prensas de la Universidad Universidad Zaragoza

ISSN 2254-7606

Universidad Zaragoza
1542

Tesis Doctoral

PREDICTION OF CARDIAC DEATH RISK BY ANALYSIS OF VENTRICULAR REPOLARIZATION RESTITUTION FROM THE ELECTROCARDIOGRAM SIGNAL

Autor

Julia Ramírez García

Director/es

Pueyo Paules, Esther
Laguna Lasaosa, Pablo

UNIVERSIDAD DE ZARAGOZA

Instituto de Investigación en Ingeniería [I3A]

2017

Instituto Universitario de Investigación
en Ingeniería de Aragón
Universidad Zaragoza

Ph.D. Thesis

Prediction of Cardiac Death Risk by Analysis of Ventricular Repolarization Restitution from the Electrocardiogram Signal

Predicción del Riesgo de Muerte Cardiaca mediante el Análisis de la Restitución de la Repolarización Ventricular a partir de la Señal de Electrocardiograma

Julia Ramírez García

SUPERVISORS:
Esther Pueyo Paules
Pablo Laguna Lasaosa

Ph.D. in Biomedical Engineering

Zaragoza, March, 2017

Prediction of Cardiac Death Risk by Analysis of Ventricular Repolarization Restitution from the Electrocardiogram Signal

Prediction of Cardiac Death Risk by Analysis of Ventricular Repolarization Restitution from the Electrocardiogram Signal

Date of current version: Monday 13th February, 2017

This thesis was supported by a PIFUZ grant from the University of Zaragoza, REF: *PIFUZ-2011-B-TEC-001*, by a research contract from Centro de Investigación Biomédica en Red - Biomateriales, Bioingeniería y Nanomedicina (CIBER-BBN), and by two research projects from the University of Zaragoza, Refs: *TEC2013-42140-R*, and *TIN2014-53567-R*. The research stays were both supported by CIBER-BBN. The research presented in this thesis was also supported by the following national projects *INTERCARDIO* (CIBER-BBN), *INDI MUSICA* (CIBER-BBN), *TEC2010-19410* (Ministerio de Economía y Competitividad (MINECO), *TIN2013-41998-R* (MINECO) and *MULTITOOLS2HEART* (CIBER-BBN). In addition, it was supported by Aragón Government (Spain) and European Social Fund (Europe), through "Grupo Consolidado Biomedical Signal Interpretation and Computational Simulation" (BSICoS), Ref: *T96*, by "Grupo de Tecnologías de las Comunicaciones", Ref: *T30*, and by CIBER-BBN through Instituto de Salud Carlos III. The computations of some parts of the thesis were performed at the High Performance Computing platform of the NANBIOSIS ICTS, CIBER-BBN and Aragón Institute on Engineering Research, Zaragoza, Spain.

This thesis was printed thanks to the financial support of BSICoS Group at University of Zaragoza.

Abstract

Cardiovascular diseases remain the leading cause of deaths worldwide, and this number is expected to progressively grow with the ageing of the population. Non-invasive markers with strong mortality predictive value are needed to reduce the incidence of fatal endpoints.

Chronic heart failure (CHF) describes the condition where the heart is not able to pump enough blood to meet the demands of the body. It is commonly agreed that CHF patients may experience progressive symptomatic worsening, leading to pump failure death (PFD), or suffer from malignant arrhythmic events predisposing to sudden cardiac death (SCD). A major electrophysiological feature responsible for the generation of malignant arrhythmias is an increased dispersion of repolarization, representing augmented spatio-temporal heterogeneities of ventricular repolarization. The response of this dispersion to variations in heart rate, i.e. dispersion of repolarization restitution, has also been demonstrated to be linked with higher arrhythmic risk leading to SCD. On the other hand, worsening of CHF leading to PFD is reported to be manifested as a withdrawal of the response of the ventricles to autonomic stimulation, and as an abnormal sympathovagal balance. With the advent of implantable cardioverter defibrillators (ICDs), and cardiac resynchronization therapy (CRT), the most popular devices used in the clinical practice to prevent SCD and PFD, respectively, accurate risk stratification has become very relevant. Specifically, being able to predict the potential outcome (SCD, PFD or others) that a CHF patient may suffer is of great importance. The electrocardiogram (ECG) signal is a cheap, non-invasive tool, which contains important information regarding the electrical activity of the heart.

The main objective of this thesis is to develop ECG-derived risk markers characterizing ventricular repolarization restitution to improve the prediction of SCD and PFD in CHF patients. This objective has been addressed by using, on the one hand, time-interval indices like the QT interval and the Tpe interval, since the dynamics of these intervals (relationship between these intervals and the preceding RR interval values) are related to the repolarization restitution and its dispersion, respectively, and, on the other hand, morphological indices. To use the morphological information of the T-wave, an innovative methodology that allows for the comparison of two different shapes, and the quantification of their differences, has been developed.

In chapter 2 a fully automated algorithm was developed to estimate the slope and curvature of the QT/RR and Tpe/RR regression patterns from 24-h Holter ECG recordings of 651 CHF patients. Then, the modulation of the circadian pattern of the

slope and curvature of QT and Tpe dynamics was studied and their SCD and PFD predictive value was assessed. Finally, the classification performance of the analysed marker with the strongest predictive value, individually and in combination with two other previously proposed ECG risk markers reflecting electrophysiological and autonomic mechanisms, was investigated using two- and three-class "Support Vector Machine" classifiers. Results demonstrated that dispersion in repolarization restitution, quantified through the slope of the Tpe interval dynamics, is a strong and independent predictor of both SCD and PFD, with steeper slopes indicative of an arrhythmogenic substrate predisposing to SCD and flatter slopes indicating mechanical heart fatigue predisposing to PFD. However, the slope of the repolarization restitution, quantified via the slope of the QT/RR relationship, as well as the curvature parameters of the two relationships, were not associated with any mode of cardiac death. The circadian pattern modulated these markers, with significantly higher values during the day than at night. Finally, classification results proved that the combination of ECG-derived risk markers reflecting complementary information improves the discrimination between SCD, PFD and other outcomes. Results suggest that the slope of the Tpe dynamics could be included in the clinical practice as an adjunct tool to stratify patients according to their risk of suffering SCD or PFD and, thus, improve the benefit from ICD or CRT treatment.

Asymmetric, flat and notched T-waves have been shown to be associated with arrhythmic events and SCD. However, T-wave morphology abnormalities that may be relevant for SCD and PFD prediction are disregarded when assessing time-interval indices only. Therefore, in chapter 3 we developed a novel methodology to compare the morphology of two T-waves and we proposed and assessed the ability of new ECG-derived markers to quantify T-wave morphological variability. First, the performance of two algorithms, Dynamic Time Warping (DTW) and Square-Root Slope Function (SRSF) in removing (warping) time-domain variability was compared. Then, morphological indices were proposed and their robustness against noise was evaluated in a set up with synthetically generated signals. Next, an electrophysiological cardiac model (ECGSIM) was used to investigate the relation between the T-wave morphology variability indices and the morphological changes at cellular level. Finally, the T-wave morphological variations produced by a tilt test in ECG recordings were quantified by using the proposed markers and their correlation with heart rate and other traditional markers was studied. Our results showed that SRSF was able to separate temporal and amplitude variations of the T-wave. Also, the proposed T-wave morphological variability markers proved to be robust against additive Laplacian noise and demonstrated to reflect variations in the dispersion of repolarization at cellular level in simulation and actual ECG recordings. In conclusion, the proposed indices quantifying morphological variations in the T-wave have demonstrated a great potential to be used for arrhythmic risk prediction.

In chapter 4, dispersion of repolarization restitution was explored using the morphological variability indices presented in chapter 3. Under the assumption that the T-wave morphology reflects dispersion of repolarization, we hypothesized that restitution of the T-wave morphology would reflect dispersion of repolarization restitution. Thus, we calculated the slope of the T-wave morphology restitution and we assessed

its SCD and PFD predictive value. The circadian modulation and classification performance were also assessed, using the methods described in chapter 2. Results showed that dispersion of repolarization restitution quantified through the slope of the T-wave morphology restitution was specifically associated with SCD, with no relation to PFD risk. The SCD risk prediction was superior to that from the slope of the Tpe dynamics shown in chapter 2. The circadian pattern also modulated restitution of the T-wave morphology, with significantly higher values during the day than at night. Finally, classification results were also improved when using a combination of ECG-derived risk markers, with similar performance as those obtained in chapter 2. In conclusion, the slope of the T-wave morphology restitution could be used in the clinical practice as a tool to target a high SCD-risk population that could largely benefit from ICD implantation.

Although deriving an individual index with strong predictive value is still desirable, SCD and PFD events are a result of a combination of multiple mechanisms. Therefore, using a score that integrates several risk factors might improve prediction even further. Then, in chapter 5 clinical and ECG-based models to specifically predict SCD and PFD risk, respectively, were proposed and their predictive values were compared. Subsequently, combined risk models including clinical and ECG-derived markers were developed to optimally predict SCD and PFD risk. The clinical, ECG-based and combined risk models were shown to improve SCD and PFD risk prediction, as compared to individual markers. For SCD, the combination of clinical and ECG-derived variables substantially improved risk prediction as compared to the use of only one or the other type of characteristics. In contrast, PFD risk prediction was already optimal for the ECG-derived model and the combination with clinical variables did not add PFD prognostic information. Our results confirm the need for a multi-factorial index, including information from complementary mechanisms, to optimize SCD and PFD risk stratification.

In conclusion, two ECG-derived indices reflecting dispersion of repolarization restitution have been proposed in this thesis and their SCD and PFD predictive value has been proved. Each index exploits different information from the T-wave, one using the Tpe interval and the other using the overall T-wave morphology. For the quantification of differences in the morphology of the T-wave, a robust methodology, based on time-warping, has been developed.

Keywords: Chronic Heart Failure; Classification; Electrocardiogram; Risk Prediction; Pump Failure Death; Repolarization Restitution; Sudden Cardiac Death; Time-Warping; T-wave Processing

Resumen y Conclusiones

Las enfermedades cardiovasculares siguen siendo la mayor causa de muertes en todo el mundo, y se espera que el número de casos crezca progresivamente en los próximos años con el envejecimiento de la población. Por ello, se necesitan marcadores no invasivos con alta capacidad de predicción de muerte para reducir la incidencia de estos eventos fatales.

La insuficiencia cardiaca crónica (CHF, del inglés "Chronic Heart Failure") describe la condición por la cual el corazón no es capaz de bombear suficiente sangre para alcanzar las demandas del cuerpo. Se ha demostrado que los pacientes con CHF pueden experimentar un empeoramiento progresivo de los síntomas, pudiendo llegar a producirse la muerte por fallo de bomba (PFD, del inglés "Pump Failure Death"), o sufrir eventos arrítmicos malignos que lleven a la muerte súbita cardiaca (SCD, del inglés "Sudden Cardiac Death"). Uno de los factores electro-fisiológicos con mayor influencia en la generación de arritmias malignas es el aumento de la dispersión de la repolarización, o la variación espacio-temporal en los tiempos de repolarización. También se ha demostrado que la respuesta de esta dispersión a variaciones en el ritmo cardiaco, es decir, la dispersión de la restitución de la repolarización, está relacionada con mayor riesgo arrítmico y de SCD. Por otro lado, el empeoramiento de CHF se manifiesta con una reducción de la respuesta de los ventrículos a la estimulación autonómica, y con un balance simpato-vagal anormal. Con la llegada de los defibriladores cardioversores implantables (ICDs, del inglés "Implantable Cardioverter Defibrillators"), y de la terapia de resincronización cardiaca (CRT, del inglés "Cardiac Resynchronization Therapy"), los dos dispositivos más popularmente usados en la práctica clínica para prevenir SCD y PFD, respectivamente, la estratificación de riesgo se ha vuelto muy relevante. Específicamente, ser capaces de predecir el evento potencial que un paciente con CHF podría sufrir (SCD, PFD u otras causas) es de gran importancia. La señal de electrocardiograma (ECG) es un método barato y no invasivo que contiene información importante acerca de la actividad eléctrica del corazón.

El objetivo principal de esta tesis es desarrollar marcadores de riesgo derivados del ECG que caractericen la restitución de la repolarización ventricular para mejorar la predicción de SCD y PFD en pacientes con CHF. Para ello, se han utilizado, por un lado, índices basados en intervalos temporales, como los intervalos QT y Tpe, ya que las dinámicas de estos intervalos están asociadas con la restitución de la repolarización, y con su dispersión, respectivamente, y, por el otro lado, índices basados en la morfología de la onda T. Para utilizar la información de la morfología, se ha desarrollado una

metodología innovadora que permite la comparación de dos formas diferentes, y la cuantificación de sus diferencias.

En el capítulo 2 se desarrolló un algoritmo completamente automático para estimar la pendiente y la curvatura de las dinámicas de los intervalos QT y Tpe a partir de registros ECG Holter de 24 horas de 651 pacientes con CHF. A continuación, se estudió la modulación del patrón circadiano de las estimaciones propuestas, y se evaluó su valor predictivo de SCD y PFD. Finalmente, se estudió la capacidad de clasificación del marcador analizado con mayor valor predictivo, individualmente y en combinación con otros dos marcadores de riesgo de ECG previamente propuestos, que reflejan mecanismos electro-fisiológicos y autonómicos. Los resultados demostraron que la dispersión de la restitución de la repolarización, cuantificada a partir de la pendiente de la dinámica del intervalo Tpe, tiene valor predictivo de SCD y de PFD, con pendientes altas indicativas de sustrato arrímico predisponiendo a SCD y pendientes planas indicativas de fatiga mecánica del corazón predisponiendo a PFD. Sin embargo, la pendiente de la restitución de la repolarización, cuantificada como la pendiente de la relación QT/RR, así como los parámetros de curvatura de las dos relaciones, no mostraron asociación con ningún tipo de muerte cardiaca. El patrón circadiano moduló estos parámetros, con valores significativamente mayores durante el día que durante la noche. Finalmente, los resultados de clasificación probaron que la combinación de los marcadores de riesgo derivados del ECG que reflejan información complementaria mejora la discriminación entre SCD, PFD y otros pacientes. Nuestros resultados sugieren que la pendiente de la dinámica del intervalo Tpe podría incluirse en la práctica clínica como herramienta para estratificar pacientes de acuerdo a su riesgo de sufrir SCD o PFD y, por lo tanto, aumentar el beneficio del tratamiento con ICDs o CRT.

Considerando estos resultados, postulamos a continuación que la morfología de la onda T contiene información adicional, no tenida en cuenta al usar únicamente índices basados en intervalos temporales. Por lo tanto, en el capítulo 3 desarrollamos una metodología para comparar la morfología de dos ondas T, y propusimos y evaluamos la capacidad de nuevos marcadores derivados del ECG para cuantificar variaciones en la morfología de la onda T. Primero, comparamos la capacidad de eliminar la variabilidad en el dominio temporal de dos algoritmos, "Dynamic Time Warping" (DTW) y "Square-root Slope Function" (SRSF). Luego, se propusieron índices morfológicos y se evaluó su robustez ante la presencia de ruido aditivo con señales generadas sintéticamente. A continuación, se utilizó un modelo electrofisiológico cardiaco para investigar la relación entre los índices de variabilidad morfológica de onda T y los cambios morfológicos a nivel celular. Finalmente, se cuantificaron las variaciones en la morfología de la onda T producidas por una prueba de tabla basculante en registros de ECG con los marcadores propuestos y se estudió su correlación con el ritmo cardiaco y otros marcadores tradicionales. Nuestros resultados mostraron que SRSF fue capaz de separar las variaciones en el tiempo y en la amplitud de la onda T. Además, los marcadores propuestos de variabilidad morfológica probaron ser robustos frente a ruido aditivo Laplaciano y demostraron reflejar variaciones en la dispersión de la repolarización a nivel celular en simulación y en registros de ECG reales. En conclusión, los índices propuestos que cuantifican variaciones morfológicas de la onda T han demostrado un gran potential para ser usados como predictores de riesgo arrítmico.

En el capítulo 4, se exploró la restitución de la repolarización ventricular usando los índices de variabilidad morfológica presentados en el capítulo 3. Bajo la hipótesis de que la morfología de la onda T refleja la dispersión de la repolarización, hipotetizamos que la restitución de la morfología de la onda T reflejaría la dispersión de la restitución de la repolarización. Por lo tanto, calculamos la pendiente de la restitución de la morfología de la onda T y evaluamos su valor predictivo de SCD y PFD. También estudiamos, como en el capítulo 2, la modulación del patrón circadiano y la capacidad de clasificación. Los resultados mostraron que la dispersión de la restitución de la repolarización cuantificada a través de la pendiente de la restitución de la morfología de la onda T, estaba asociada específicamente con SCD, sin ninguna relación con PFD. El patrón circadiano también moduló la restitución de la morfología de la onda T, con valores significativamente mayores durante el día que durante la noche. Finalmente, los resultados de clasificación también mejoraron al utilizar una combinación de marcadores de riesgo derivados del ECG. En conclusión, la pendiente de la restitución de la morfología de la onda T podría usarse en la práctica clínica como herramienta para definir una población de alto riesgo de SCD que podría beneficiarse de implantación con ICDs.

Finalmente, aunque lo deseable es encontrar un índice individual con alto valor predictivo, los eventos de SCD y PFD son el resultado de una múltiple cadena de mecanismos. Por lo tanto, la predicción podría mejorarse todavía más si se usara un marcador que integrara varios factores de riesgo. En el capítulo 5 se propusieron modelos clínicos, basados en el ECG y otros combinando ambos tipos de variables, para predecir específicamente riesgo de SCD y de PFD. Además, se comparó tu valor predictivo. Los modelos clínicos, basados en ECG y combinado demostraron mejorar la predicción de SCD y de PFD, comparado con los marcadores individuales. Para SCD, la combinación de variables clínicas y derivadas del ECG mejoró sustancialmente la predicción de riesgo, comparado con el uso de uno de los dos tipos de variables. Sin embargo, la predicción de riesgo de PFD demostró ser óptima al utilizar el modelo derivado del ECG, ya que la combinación con variables clínicas no añadió ninguna información predictiva de PFD. Nuestros resultados confirman la necesidad de utilizar un índice multi-factorial, que incluya información de mecanismos complementarios, para optimizar la estratificación de riesgo de SCD y de PFD.

En conclusión, en esta tesis se han propuesto dos índices derivados del ECG, que reflejan dispersión de la restitución de la repolarización, y se ha demostrado su valor predictivo de SCD y PFD. Cada índice explota información diferente de la onda T, uno utiliza el intervalo Tpe y el otro utiliza la morfología completa de la onda T. Para la cuantificación de las diferencias en la morfología de la onda T, se ha desarrollado una metodología robusta que se basa en la re-parametrización en el tiempo.

Palabras clave: Clasificación; Electrocardiograma; Insuficiencia Cardiaca Crónica; Muerte por Fallo de Bomba; Muerte Súbita Cardiaca; Predicción de Riesgo; Procesado de Onda T; Re-parametrización Temporal; Restitución de la Repolarización;

Acknowledgements

I will always remember my first week at BSICoS group (former GTC group), meeting the crew, being nervous and also very excited with my first contact with research. Now, I am meeting new members of the group, and the excitement has grown exponentially. Above all, I feel specially proud of being a product of this group. Thank you for supporting me with every conference I have wanted to attend, and with every research stay. Thank you for giving me the opportunity to be a part of it, and to enjoy its multidisciplinarity. Thank you for the working atmosphere, and thank you for the after-work gatherings that make me feel as a member of a big family.

This thesis is the product of a strong physiological hypothesis, a detailed methodological work, thorough corrections and reconsiderations of the process, a long learning process, and an infinite joy. For that, I would like to thank my supervisors, Esther and Pablo. Thank you for your support, thank you for your encouragement, thank you for your knowledge, and thank you for creating the novel researcher I am now.

Michele, I would also like to thank you for your strong contribution in the last stage of this thesis. Having the opportunity to visit your lab in University College London, and doing a research stay with you was the genesis of a collaboration that has proven to be extremely efficient, with three papers and lots of laughters. Thank you for your warm welcome, your infinite ideas, your fast answers and your crackers. This has just started. I would also like to thank Laurence, for your hospitality during my first research stay and your contribution to the beginning of this thesis.

Also, I received a huge feedback from Derek, who provided me the data, papers, codes, and non-stop e-mail answers to help me understand the mathematical framework behind the warping concept. Thank you for being so enthusiastic, and for starting a collaboration with me, considering the distance.

Ana, this thesis started as the continuation of your thesis. Yours was the reference to-be-reached and I know it almost by heart. Thank you for your guidance, your help, your suggestions and your kind encouragement. Juan Pablo, your help has also been a significative marker for this thesis. Thank you for your fast answers any time I had panic dilemmas, for your support, and for your familiarity. Talk with you is always a pleasure. Violeta, thank you too for your support, and all your help with the statistical analyses and the MUSIC database. Also, thank you for your company in the conferences.

Of course, Arantxa, thank you for the administrative work, your immediate availability, your advice, the emergency coffees and your ability of making me laugh and

keeping the stress down. Bego and Marga, thank you too for your happiness, your charm and your optimism. I'm very lucky of working next to you!

Finally, I would also like to thank my lab friends for sharing with me this special stage of my life.

Contents

List of Figures

List of Tables

List of Acronyms

ACE angiotensin-converting-enzyme 17
ANS Autonomic Nervous System 8
AP action potential 2
APD AP duration 4
APDR APD restitution 6
ARB angiotensin receptor blocker 17
AUC area under the ROC curve 38
AV atrioventricular 4
BNP B-type Natriuretic Peptide 16
CD cardiac death 17
CHF chronic heart failure 15
CI confidence interval 37
CRT cardiac resynchronization therapy 17
dB decibel 69
DTW Dynamic Time Warping 60
ECG electrocardiogram
HAR Hazard ratio 37
HF Heart failure 15
HR heart rate 28
HRT Heart rate turbulence 22
HRV Heart rate variability 22
IAA index of average alternans 35
ICD implantable cardioverter defibrillator 17
IQR interquartile range 41
LVEF left ventricular ejection fraction 16
MUSIC MUerte Súbita en Insuficiencia Cardiaca 29

NSVT non-sustained ventricular tachycardia 49
NYHA New York Heart Association 16
PCA Principal Component Analysis 12
PFD pump failure death 17
ROC receiver operating characteristic 37
SA sinoatrial 4
SCD sudden cardiac death 17
Se sensitivity 29
SNR Signal to noise ratio 13
Sp specificity 29
SRSF Square-Root Slope Function 60
SVD singular value decomposition 12
SVM support vector machine 38
TA T-wave amplitude 60
TMR T-wave morphology restitution 106
TO turbulence onset 22
TS turbulence slope 22
TW T-wave width 60
TWA T-wave alternans 22
VAD ventricular assist device 17
VCG vectorcardiogram 11
VPB ventricular premature beat 22
WT wavelet transform 13

Chapter 1

Introduction

1.1 Motivation

Cardiovascular diseases remain the leading cause of deaths worldwide, with more than 17 million cases in 2015 and this number being expected to grow to >23.6 million by 2030 [1, 2]. More than 3 million of these deaths occurred before the age of 60 and could have largely been prevented [3]. The main causes underlying these deaths include high blood pressure, smoking, diabetes, lack of exercise, obesity, high blood cholesterol, poor diet, and excessive alcohol consumption, among others. These figures do justify any effort to reduce the incidence of cardiovascular diseases, including means to improve prediction, diagnosis and treatment.

1.2 The Heart

1.2.1 Electrophysiology

The heart is a muscular organ the size of a large fist whose primary function is to pump oxygen-rich blood throughout the body. Its anatomy is divided into two "mirrored" sides, left and right, which support different circulatory systems but which pump in a synchronized, rhythmic manner. Each side of the heart consists of two chambers, the *atrium* where the blood enters and the *ventricle* where the blood is forced into further circulation [4]. During each cardiac cycle (heart beat), the atria contract in diastole to fill the ventricles, which, then, contract during systole to supply blood to the lungs and the systemic circulation. The wall of the heart is called the *myocardium* and is primarily composed of muscle cells (*myocytes*) that produce mechanical force during contraction of the heart [5]. Contraction of the atria and ventricles is triggered by a wave of electrical excitation (*depolarization*) spreading through the myocardium of these chambers. The depolarization wave reflects movement of charge across the myocyte membranes, which results in an electrical current spreading through the heart. Following systole, cardiac muscle returns to a resting state and this is associated with reversal of the movement of charge across the myocyte membranes. This second wave of electrical activity is termed cardiac *repolarization* [6]. In this section, the electrical activity across the membrane of an isolated cardiac myocyte, and the electrical propagation throughout the heart are described.

Cellular Electrical Activity

At rest, the membrane potential, i.e. the voltage difference between the inside and the outside of the cell, is negative. A large enough stimulation of the myocardial cell is able to elicit an *action potential (AP)*, which is a representation of the electrical activity of a single cell. The myocardial AP has 5 phases (numbered 0-4), which are shown in Fig. 1.1 [7,8]:

- **Phase 4** corresponds to the resting membrane potential and describes the membrane potential when the cell is not being stimulated (-85 to -95 mV in ventricular myocardium).
- **Phase 0** corresponds to the depolarization phase where an initial fast upstroke results due to the opening of the fast inward sodium (Na^+) channels. This opening causes a rapid increase in the membrane conductance to Na^+ and thus a rapid influx of Na^+ ions into the cell, i.e. a Na^+ current. The ability of the cell to open the fast Na^+ channels during phase 0 is related to the membrane potential at the moment of excitation. If the membrane potential is at its baseline (about -85 mV), all the fast Na^+ channels are closed, and excitation will open them all, causing a large influx of Na^+ ions. If, however, the membrane potential is less negative, some of the fast Na^+ channels will be in an inactivated state insensitive to opening, thus causing a lesser response to excitation of the cell membrane and

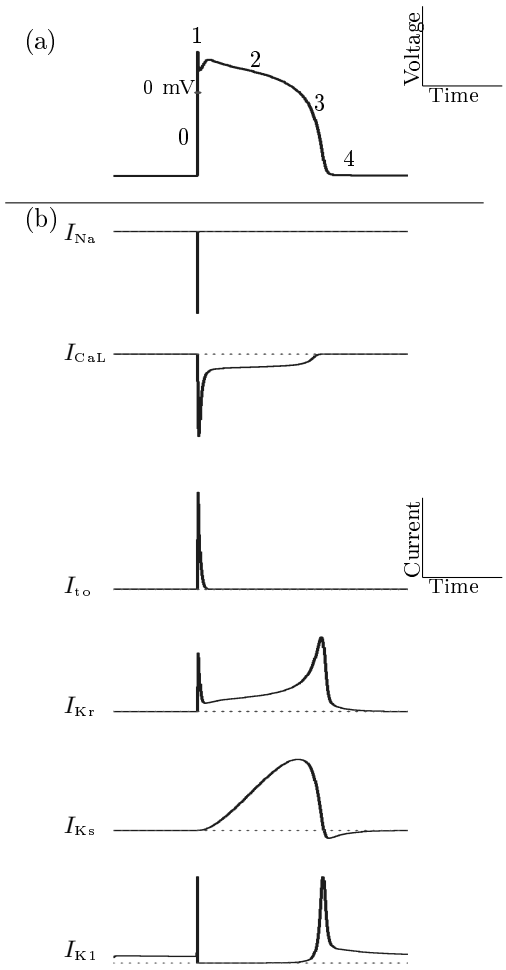

Figure 1.1: (a) Action potential of a ventricular myocyte, with indication of its phases. (b) Illustration of the ionic currents underlying the different AP phases. From [9].

a lower maximum potential. For this reason, if the resting membrane potential becomes too positive, the cell may not be excitable and conduction through the heart may be delayed.

- **Phase 1** represents an initial and brief repolarization and occurs with the inactivation of the fast Na^+ channels. The transient net outward current causing the small downward deflection of the AP is mainly due to the movement of potassium (K^+) ions, carried by the transient outward potassium current I_{to1}. Particularly the transient outward potassium current I_{to1} contributes to the "notch" of some ventricular myocyte APs.

- **Phase 2**, also called "plateau" phase of the cardiac AP, is sustained by a balance between inward movement of Ca^{2+} through L-type calcium channels and outward movement of K^+ through the slow delayed rectifier potassium channels, I_{Ks}. This plateau phase prolongs the *AP duration (APD)* and distinguishes cardiac APs from the much shorter APs found in nerves and skeletal muscle.

- **Phase 3**, the "rapid repolarization" phase, the L-type Ca^{2+} channels close, while the slow delayed rectifier (I_{Ks}) K^+ channels are still open. This ensures a net outward current, corresponding to a negative change in membrane potential, thus allowing more types of K^+ channels to open. These are primarily the rapid delayed rectifier K^+ channels (I_{Kr}) and the inwardly rectifying K^+ current, I_{K1}. This net outward, positive current (equal to loss of positive charge from the cell) causes the cell to repolarize. The delayed rectifier K^+ channels close when the membrane potential is restored to about -80 to -85 mV, while I_{K1} remains conducting throughout phase 4, contributing to set the resting membrane potential.

Electrical Activity of the Heart

Cardiac depolarization is triggered by an electrical pulse generated in the *sinoatrial (SA)* node, situated near the entry of the superior vena cava into the right atrium (Figure 1.2). This electrical pulse, then, spreads through the atria, triggering their contraction, late in diastole. The atria and ventricles, however, are separated by a non-conducting fibre septum, so the depolarization wave cannot penetrate this barrier. In order to activate ventricular contraction, the wave must be transmitted into the ventricles by the specialized cardiac conducting system. In a normal heart, the only route by which the depolarizing wave can enter the ventricular conducting system is through the *atrioventricular (AV)* node (Figure 1.2). In order to allow the ventricles to fill with blood following atrial contraction, the AV node initially delays the spread of the depolarization wave, and, after this short delay, the depolarizing signal is transmitted into the ventricles via the *bundle of His*. The bundle of His lies in the *interventricular septum*, and divides into right and left bundle branches. The right and left bundle branches transmit the depolarizing signal into the muscle mass of the right and left ventricles, respectively. The interventricular septum is the first part of the ventricular muscle mass to depolarize, and it does so by movement of current across the septum, from the left towards the right bundle branch. As septal depolarization is taking place, the depolarizing wave begins to spread rapidly to the book of the right and left ventricles. In the walls of the ventricles, depolarization spreads from the terminal fibers of the conducting system outwards from the inner layer (*endocardium*) towards the outer surface of the heart (*epicardium*), and also back along the ventricular wall to the atrioventricular groove [6].

Cardiac repolarization is not truly propagated between cells. However, cardiac myocytes repolarize at different rates, depending on their anatomical location within the heart. Research over the past two decades has suggested that significant differences exist in the time course of repolarization of endocardial, epicardial and mid-myocardial cells that comprise the ventricular myocardium [10–13]. These differences

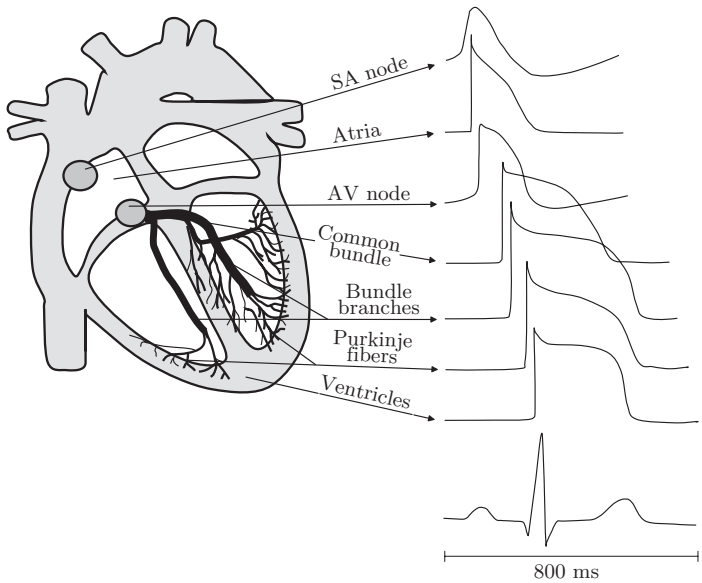

Figure 1.2: Electrical conducting system of the heart. The morphology and timing of action potentials from different regions of the heart and the related cardiac cycle of the electrocardiogram as measured on the body surface. From [5].

in repolarization time, i.e. dispersion of repolarization, are critical, when they become substantially augmented, for the genesis of a malignant arrhythmogenic substrate [14], and is the key concept of this thesis.

Dispersion of Repolarization

Different studies in the literature have provided evidence that myocytes near the epicardium have shorter APD at normal heart rates than myocytes near the endocardium [15, 16] and there is the notion that epicardial repolarization occurs earlier than endocardial repolarization. However, other studies have demonstrated that in some cases epicardial repolarization occurs later, not earlier, than endocardial repolarization [17]. Also, some studies show that mid-myocardial cells are the last cells to repolarize and, then, full repolarization of the mid-myocardium would mark the end of the repolarization of the heart [10, 18]. This contribution of mid-myocardial cells to regional dispersion of repolarization has been controversial [19–21]. Rather than contiguous layers of cells in the myocardium, different laboratories have shown that isolated islands of delayed repolarization exist across the ventricular wall [22, 23]. In any case, it is clear that repolarization time differences, or dispersion of repolarization, not only exist between cells of different chambers of the heart (i.e. atria, ventricles, nodal tissue) [24, 25], but also between myocytes of different regions within the ventricular wall, e.g. epicardium versus endocardium [16, 26–31], or apex versus base [30, 32–39].

Figure 1.3 (a) shows a schematic diagram of the ventricles. Figure 1.3 (b) presents the APs from three myocytes in the left ventricle, located near the base endocardium (1), epicardium (2) and apex endocardium (3). Vertical lines indicate the corresponding repolarization time and, thus, the time difference between them reflects their dispersion of repolarization. As it can be observed, the depolarization wave travels from 1 (endocardium) to 3 (epicardium) and the repolarization time increases as we move from 3 (epicardium) to 1 (endocardium).

The repolarization time of a cardiac myocyte is influenced by the time required for the impulse to propagate to and depolarize that myocyte, i.e. conduction velocity, and the myocyte's intrinsic APD. Therefore, spatial dispersion of repolarization in the ventricles is influenced by dispersion of conduction velocity and the spatial dispersion of APD, i.e. the difference between the APDs of different myocytes [14]. Such diversity in the electrophysiological characteristics of cellular ionic properties can strongly influence the arrhythmia vulnerability [14].

Repolarization Restitution

Repolarization restitution refers to mechanisms whereby the electrical recovery (repolarization) respond to a variation in the heart rate [41–44]. At fast heart rates, repolarization becomes faster while at slow heart rates repolarization is slower [45, 46].

The *APD restitution (APDR)* curve represents the APD as a function of the preceding RR interval (inverse of the heart rate) and is usually almost flat for RRs longer than 1 s and steeper for shorter RRs [46, 47]. Figure 1.3 (c) shows the APDR curves of the three myocytes selected in panel (a). The green curve corresponds to cell 3, with the minimum APD, the blue curve corresponds to cell 2, repolarizing when half the ventricle is repolarized and the other half is still depolarized, and the pink curve corresponds to cell 1, and, thus, the last cell to repolarize. The slope of the curves at a given RR interval value, denoted by α_1, α_2 and α_3, reflect the change in APDs 1, 2 and 3, respectively, as a response to the change in RR. As it will be discussed later, several studies have shown that the steepness of the APDR curves is relevant to arrhythmogenesis [48–51].

Dispersion of Repolarization Restitution

The above-mentioned phenomenon of dispersion produced by electrophysiological differences across the wall of the ventricle and between ventricles has also a dependence on heart rate, with the dispersion decreasing as heart rate increases [52].

This concept is illustrated in Figure 1.3 (c). Due to dispersion of repolarization and of restitution kinetics, the three curves exhibit differences in range and slope. The restitution kinetics of the repolarization times along the ventricle is also heterogeneous. As it will be discussed, several studies have proved that increased dispersion of repolarization restitution facilitates arrhythmia development [53, 54].

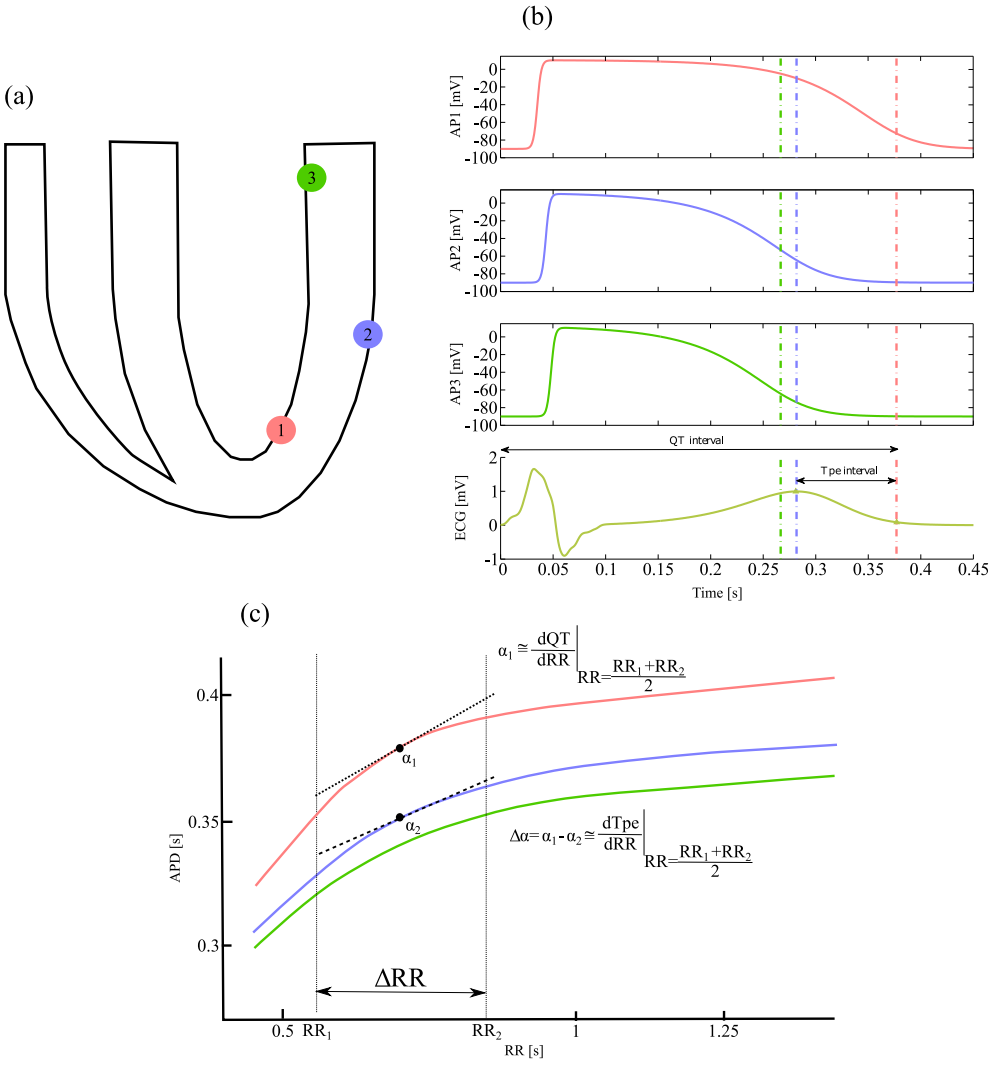

Figure 1.3: Schematic diagram showing the hypothesis of this thesis: estimation of dispersion of repolarization restitution, and the slope of total repolarization restitution, from the ECG. (a): Schematic diagram of the ventricles, with selected base-endocardial (1), epicardial (2), and apico-endocardial (3) ventricular myocytes. (b): Action potentials, generated with ECGSIM [40], from cells 1, 2 and 3, and the resulting ECG beat. Vertical lines indicate the corresponding repolarization times. The QT and Tpe intervals are also shown. (c): Action potential duration restitution curves from cells 1, 2 and 3. Black dots indicate the slopes of cells 1 and 2, α_1 and α_2, respectively, at a given RR interval value. Quantification of dispersion of repolarization restitution and the slope of total repolarization restitution, for a specific RR value, from the Tpe and QT intervals is defined in terms of α_1 and α_2.

1.2.2 Modulation by the Autonomic Nervous System

The *Autonomic Nervous System (ANS)* is a division of the peripheral nervous system that influences the function of internal organs, like the heart [55]. The ANS regulates cardiovascular functions such as the heart rate, the blood pressure or the respiratory rate, and it consists of two branches, the sympathetic and the parasympathetic systems, that work in a delicately tuned, yet opposing fashion in the heart [56, 57]. In other words, increasing the activity of one system while simultaneously decreasing the activity of the other results in very rapid and precise control of the function of the heart [58].

Each system is dominant under certain conditions. The sympathetic system predominates during emergency "fight-or-flight" reactions and during exercise. The overall effect of the sympathetic system under these conditions is to prepare the body for strenous physical activity. More specifically, sympathetic nervous activity increases the heart rate and the myocardial contractility to increase the *stroke volume*, which is the amount of blood pumped every beat [59]. Given the ability to modulate both cardiac rate and stroke volume, the sympathetic nervous system provides an important remote mechanism to rapidly meet short-term changes in the body needs. The parasympathetic system regulates "rest and digest" functions, predominating during quiet, resting conditions [60]. The overall effect of the parasympathetic system under these conditions is to conserve and store energy and to regulate basic body functions such as heart rate and respiration [58]. Under normal physiological conditions, parasympathetic stimulation inhibits sympathetic activation and its effects at rest and during exercise [60], by reducing heart rate and AV nodal conduction, and causing vasorelaxation [60].

1.3 Electrocardiogram

1.3.1 Definition and Waveforms

The *ECG* describes the electrical activity of the heart measured on the body surface by attaching a set of electrodes to the skin. The electrodes are positioned so that the spatio-temporal variations of the cardiac electrical field are sufficiently well-reflected. For an ECG recording, the difference in voltage between a pair of electrodes is referred to as a *lead*. The voltage variations measured by the leads are caused by the APs of the excitable cardiac cells as they contract. The resulting heartbeat in the ECG is manifested by a series of waves whose morphology and timing convey information that can be used for diagnosing diseases associated with disturbances of the heart's electrical activity [5].

To record a standard ECG, 10 electrodes are placed in standardized positions on the patient's body. The information obtained allows the analysis of the movement of electrical forces through the heart from 12 different perspectives around the organ. In this way, the ECG recording can provide information about disease processes affecting

different anatomical regions of the organ and can allow the detection of changes in the pattern of spread of electrical forces through the heart in disease. For now, we need to understand how an individual ECG lead reflects cardiac electrical events.

In any ECG lead, the flat line recorded when no net current is flowing in its direction is termed the *isoelectric line*. It is important to realize that all of the leads on the ECG recording system are set up in such a way that depolarizing current moving towards a lead produces a positive deflection on the ECG signal above the isoelectric line, while depolarizing current moving away from the lead produces a negative deflection below the isoelectric line. In contrast, repolarizing current has the opposite polarity to depolarizing current. Therefore, repolarizing current moving towards a lead produces a negative deflection on the signal, while repolarizing current moving away from the lead produces a positive deflection [5]. Figure 1.2 illustrates how the APs of different cardiac cells generate the ECG signal, in this example viewed by an exploring electrode which is positioned on the chest.

As described in section 1.2.1, the atrial depolarization wave not only spreads downwards and to the left but also outwards towards the front of the chest. As this depolarizing current is moving towards the chest leads, it produces a positive deflection on the ECG signal, which is the *P wave* of atrial depolarization. Then, the ventricular depolarizing current is first released from the left bundle branch of the conducting system into the interventricular septum, to the right bundle branch. This septal current is moving away from the chest and, therefore, produces an initial negative deflection in this lead (*Q wave*). To understand what happens next in the recording, it is important to appreciate that the magnitude of the electrical signal generated by the depolarizing muscle is directly proportional to the mass of muscle generating it. What this means is that the more muscle present, the more electrical signal generated and the more amplitude the ECG signal reflects. The left ventricle has a much greater muscle mass than the right one and, thus, dominates the electrical signal of ventricular depolarization in all leads. Therefore, after release of the depolarization wave from the conducting system into the main muscle mass of the ventricles, the endocardial to epicardial movement of current in the left ventricle overwhelms all other signals and, as it is moving towards the chest, it produces a strong positive deflection in this lead (*R wave*). Depolarization terminates with the dominant vector pointing away from the electrode, and thus a wave with negative polarity is produced in the ECG, the *S wave*. The group of these three waves is known as the *QRS complex*, with its morphology differing predictably in the ECG leads depending on their position relative to the heart [5].

When ventricular depolarization is complete, there is a brief period when no current is flowing and the recording returns to the isoelectric line. This period ends with the onset of ventricular repolarization. The deflection produced on the ECG by ventricular repolarization is again dominated by the signal from the left ventricle. As the repolarizing wave is moving away from the chest, it produces a positive deflection. This deflection is termed *T wave*. Note that the T-wave has a very different morphology to the QRS complex. Cardiac repolarization spreads relatively slowly through the myocardial muscle mass, outside the conducting system. Hence, the T-wave is

considerably longer in duration and, therefore, broader on the ECG signal than the QRS complex. In non-diseased hearts, the polarity of the QRS complex and the T-wave tend to be concordant. Also, atrial repolarization produces a relatively weak electrical signal which is buried in the QRS complex and is generally not detectable on a standard 12-lead ECG [5].

1.3.2 Leads

Standard Leads

Since the flow of depolarization and repolarization through the myocardium is a three dimensional process, it is important to realize that each of the leads of the ECG recording system examines the movement of the electrical waves through the heart in one plane only. In fact, based on the plane in which electrical events in the heart are analysed, the 12 leads of the ECG can be divided into two groups of six. The six *frontal* leads examine the flow of depolarization and repolarization through the heart in the vertical, or frontal, plane (Figure 1.4 (left)), while a second group of six leads, the *chest* leads, also referred to as the *precordial* leads, V1 to V6, examine these electrical events in the horizontal or transverse plane [5] (Figure 1.4 (right)).

The frontal leads can be further divided in two groups of three, the *standard limb* leads, leads I, II and III, and the *augmented vector* leads, aVR, aVL and aVF. By taking a representative frontal section through the chest, the perspective of each of these leads on cardiac electrical events can be understood. To remember the position of all 6 of the frontal leads relative to the heart, lead I is used as the reference point. Lead I looks directly at the heart from the patients left hand side and defines zero degrees. Lead II looks at the heart at an angle 60° further clockwise from lead I, while lead III is positioned a further 60° clockwise from lead II. aVL looks at the heart from the left (L is for left), but at 30° anticlockwise from lead I. aVR looks at the right side of the heart (R is for right), and, just like aVL, it is 30° above the horizontal relative to lead I. As aVL and aVR are set at 30° off the horizontal plane, they can be thought as the left and right Wings or "vings" of the ECG. aVF looks straight up at the inferior surface of the heart and is, therefore, at 90° clockwise from lead I. aVF can be thought of as looking straight up at the heart from the feet (F is for feet) [5].

The 6 chest leads, V1 to V6, are placed on the surface of the chest wall in an arc, from V1 in the 4th right intercostal space to the right of the sternum, to lead V2 in the fourth left intercostal space to the left of the sternum, and then at roughly equal intervals, to lead V6 in the fifth left intercostal space in the mid-axillary line. If we take a representative transverse section through the chest, it can be appreciated that, with the heart in anatomical position, the atria lie posterior to the ventricles and the right ventricle lies somewhat anterior to the left in this plane. Leads V1 and V2, therefore, face the surface of the right ventricle. However, note they also face the much larger muscle mass of the interventricular septum. Then, these leads are strongly influenced by electrical events in this structure and V1 and V2 are, therefore, often referred to as the septal leads. V3 and V4 face the anterior wall of the left ventricle, while V5 and

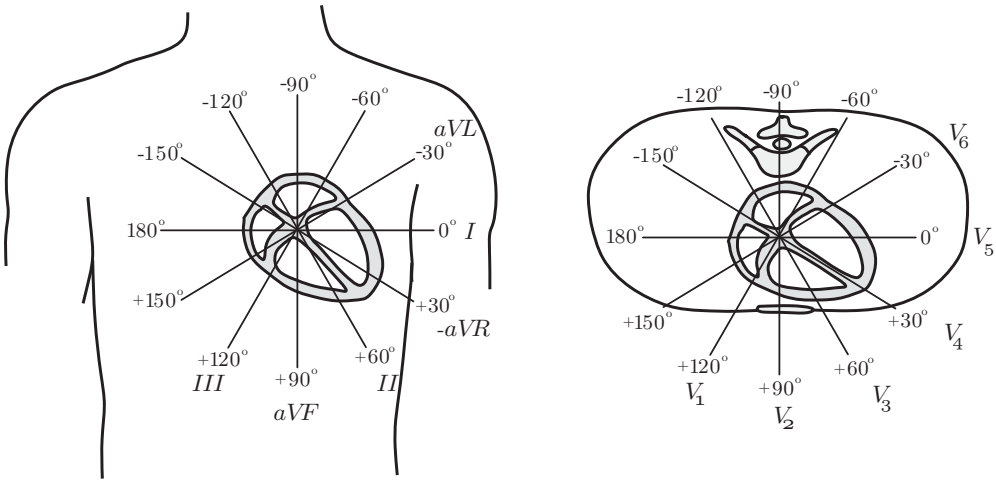

Figure 1.4: The six frontal (left) and horizontal (right) plane leads provide a three-dimensional representation of cardiac electrical activity. From [5].

V6 face the lateral wall of the left ventricle [5].

Only eight from these twelve acquired leads are independent. Then, it would be sufficient, as an example, to only consider the six precordial leads and two augmented vector leads to represent all the information from the twelve standard leads [5].

Orthogonal Leads

As mentioned above, the electrical flow through the heart is a three-dimensional process. Then, it is interesting to construct three *orthogonal leads* containing the electric information in the right-left axis (X), head-to-feet axis (Y), and front-back axis (Z). For such a lead system, the ECG interpretation is not confined to findings in individual leads, but additional information is acquired through the visualization of a three-dimensional loop together with its projection onto the XY-, XZ-, and YZ-planes, as seen in Figure 1.5. Since a loop is traced out by the tip of the vector that describes the dominant direction of the electrical wavefront during the cardiac cycle, this particular type of recording is referred to as a *vectorcardiogram (VCG)* [5].

Pairs of electrodes positioned along mutually perpendicular lines on the body surface may, at first glance, appear to produce leads that are orthogonal [61]. Based on mathematical modeling as well as on experimental results, however, it has been found that additional electrodes are required in order to account for the geometry of the human torso. The corrected orthogonal leads, known as the *Frank lead system* after its inventor [62], are obtained as linear combinations of seven electrodes positioned on the chest, back, neck, and left foot. The resulting leads X, Y, and Z view the heart from the left side, from below, and from the front [5].

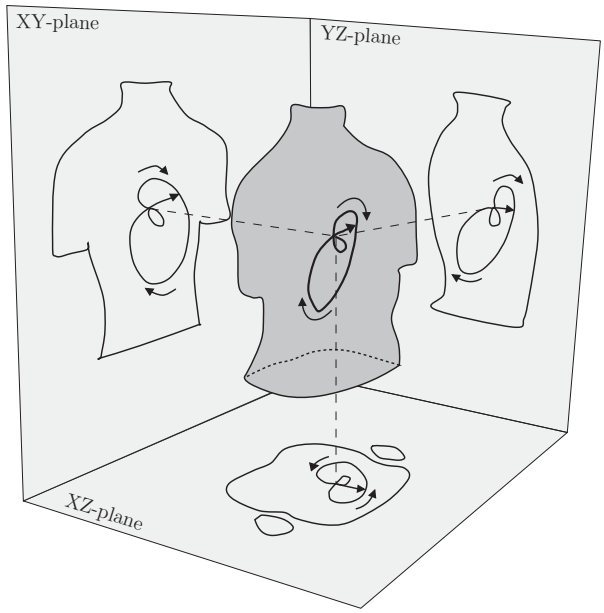

Figure 1.5: A vectorcardiographic loop and its projection onto the three orthogonal planes. From [5].

Synthesized Leads

It is possible to compute an orthogonal base composed of three leads from the standard 12-lead ECG, if the Frank lead system is not available [5]. Two main methodologies have been proposed, like the Dower's inverse transformation [63], and the Kors's inverse transformation [64], which has, so far, proven to be the best agreement with the original Frank leads, expressed in diagnostic terms [5]. An alternative option to derive an orthogonal base is to exploit the ECG signal statistics, rather than representing the spatial electric wavefront. For that purpose, in this thesis we have applied a statistical signal processing technique called *Principal Component Analysis (PCA)*.

The objective of PCA is to condense the information provided by a set of possibly correlated variables into uncorrelated variables. PCA is used in ECG signal processing to emphasize temporal and morphological properties, or to extract noisy interferences, from the characteristic waveforms [65].

One way of implementing PCA is by applying *singular value decomposition (SVD)* using the eight independent standard leads to obtain eight new transformed leads. Let the data matrix $\mathbf{X}$ be of nxp size, where n is the number of samples and p is the number of leads, 8 in this case. Now, let the training data matrix $\mathbf{L}$ be of mxp size, where m is the number of samples selected to calculate and learn the directions of maximal variance. If we now perform SVD of $\mathbf{L}$, we obtain a decomposition

$$\mathbf{L} = \mathbf{U}\mathbf{\Sigma}\mathbf{V}^T, \tag{1.1}$$

where $\mathbf{\Sigma}$ is the diagonal matrix of singular values, and $\mathbf{U}$ and $\mathbf{V}$ are matrices of left and right eigenvectors, respectively. The eigenvectors are called *principal axes* or *principal directions* of the data. Projections of the data onto the principal axes are called *principal components*. Then, the principal components are given by:

$$\mathbf{P}_c = \mathbf{XV} \tag{1.2}$$

The spatial meaning of PCA can be interpreted as the translation of the information to other coordinate system such that the principal coordinate (principal component) represents the direction of maximum variance, the second coordinate the direction of the second component of maximum variance, etc. Then, the obtained principal components reflect the level of morphological variability present in the ECG signal segment selected for the construction of matrix $\mathbf{L}$. When the eigenvalue associated with the first principal component is significantly higher than the others, the segment presents low morphological variability. In contrast, a large similarity among the eigenvalues indicates a great variability [65].

1.3.3 Detection and Delineation

The detection process consists of detecting the occurrence time of the heartbeats, while delineation consists of determining the boundaries of each wave within the heartbeat [5].

Single-lead Delineation

Single-lead delineation identifies the wave boundaries of a lead, independently from the others. In this thesis, an automatic method based on the *wavelet transform (WT)* has been used [66]. WT describes the signal in both time and frequency domains. Therefore, it allows the representation of wave features at different levels (scales) depending on their frequency content. This representation is proportional to the signal derivative when the proper wavelet mother function is used. Then, for example, a zero-crossing represents a peak in the original signal. QRS complex needs a different scale of that used to characterize P and T waves, because its frequency content is substantially different [66].

First, QRS complex *fiducial point* (QRS complex gravity center) is detected and, then, Q, R and S waves are separately delineated. Finally, P and T waves are delineated by sliding the analysis window [66]. *Signal to noise ratio (SNR)* constitutes a drawback in single-lead delineation because if the noise level is high it is difficult to correctly place the wave boundaries.

Multi-lead Delineation

The main problem with single-lead delineation is that it marks annotation points on a signal that is very dependent on the location where the electrode has been placed,

i.e. it provides a local information waveform onset and end. Then, the number of onset and end points is equal to the number of analysed leads. From these marks, it can be observed that in some leads a particular wave starts significantly earlier than in other leads. However, the onset and end of the electrical heartbeat is unique and, therefore, it is convenient to find a single mark that robustly indicates this phenomenon, which is achieved with multi-lead delineation.

- **Single-lead-and-rules delineation:** This method consists of selecting an annotation mark among the marks obtained using single-lead delineation in each heartbeat. If the mark is the onset of a wave, all the onset marks from all the leads are sorted and the first one (which marks the position of the first recorded electrical change) is chosen. A protection criteria which states that k leads must have their onset mark within a δ time interval needs to be accomplished. k and δ values are chosen depending on the delineated wave and the number of available leads. If the mark is the offset of a wave, the algorithm works similarly but the last annotation mark over leads is chosen. If the mark corresponds to the wave peak, the median criteria is used instead, i.e. all the marks are sorted and the one in the middle is selected. If the protection criteria is not accomplished, the mark is rejected [67].

- **3D Delineation:** This method considers three orthogonal leads [68]. Their canonical representation can be expressed as:

$$\mathbf{s}[n] = [x[n], y[n], z[n]]^T, \tag{1.3}$$

  where $x[n]$, $y[n]$ and $z[n]$ may be any of the three orthogonal or synthesized leads. If the canonical representation is plotted in the coordinate system, a spatial wave similar to a loop can be obtained. Then, WT is applied, obtaining [66]:

$$\mathbf{w}_s[n] = [w_{\mathrm{x,s}}[n], w_{\mathrm{y,s}}[n], w_{\mathrm{z,s}}[n]]^T, \tag{1.4}$$

  where $\mathbf{w}_s[n]$ defines a second spatial loop, which is the wavelet transformation of $\mathbf{s}[n]$. The parameter s is the scale (frequency band) at which the transformation is performed. The direction $\mathbf{u} = [u_x, u_y, u_z]^T$ defines the vector onto which the loop should be projected to obtain a 1-D signal with maximal SNR in the selected area and, then, optimal to delineate [68]. The lead resulting from the projection of $\mathbf{s}[n]$ onto such direction is calculated as:

$$d[n] = \frac{\mathbf{s}^T[n]\mathbf{u}}{\|\mathbf{u}\|}, \tag{1.5}$$

  while the projection of $\mathbf{w}_s[n]$ is obtained in an analogous way, by replacing $\mathbf{s}[n]$ with $\mathbf{w}_s[n]$ in the above equation. Next, the single-lead delineation technique explained in section 1.3.3 is performed, by considering that the projected lead

has been obtained to delineate a specific point (the delineation of the peak of a waveform would require a different projected lead than the delineation of the end of a waveform).

1.4 Chronic Heart Failure

1.4.1 Concept and Diagnosis

The amount of blood pumped to the body at any time is based on the demand that the cells in the body have for oxygen. As an example, if the body starts doing exercise, the demand increases. The heart is able to respond, pumping more blood to meet these new demands. *Heart failure (HF)* describes the condition where the heart is not able to pump enough blood to meet the demands of the body [69]. The two main types of HF are *acute heart failure* and *chronic heart failure (CHF)*. Acute heart failure develops suddenly and symptoms are initially severe, but may only last for a brief time and improve rapidly. CHF is more common and symptoms appear slowly over time and worsen gradually [69]. In this thesis, we used ECG recordings from healthy subjects and patients with CHF.

The total amount of blood pumped by the heart every minute is the *cardiac output*, and it is usually given in litres of blood per minute. The normal cardiac output is around 5 litres per minute. Cardiac output can be expressed as the product of the stroke volume and the heart rate (in beats per minute). In CHF, cardiac output is low because the heart is not able to pump as much blood per minute as the healthy heart. This is usually because there is a lowered stroke volume, or a lower amount of blood pumped out of the heart with each contraction. Usually CHF is considered a secondary disease, meaning that it is caused by a pre-existing or underlying disease that already affects cardiac output. Specifically, these diseases are those that cause the death of cardiac myocytes. When these muscle cells die, the heart gets weaker and pumps less blood. Then, the stroke volume decreases, and, hence, the cardiac output [70]. When the cardiac output goes down, the heart either contracts harder and increases stroke volume, or beats faster and increases heart rate. In the early stages of CHF, these methods can help in compensating for decreased supply, but, over time, those surviving muscle cells become overworked because they are constantly trying to either beat faster or contract harder. In addition, to do either of those things, those cells need more oxygen and, since the oxygen supply is low, more muscle cells tend to die. As a result, stroke volume decreases even more, leading to an increment in the contraction and heart rate, which worsens CHF. Also, maintained compensation of low cardiac output can produce irreversible structural changes in the heart, like enlargement of the cardiac muscle, and these structural changes may affect the electrophysiological properties of the heart [69].

The first group of methods to diagnose CHF is *imaging*, by taking an X-ray of the chest area. With imaging, the doctors are able to visualize the current state of the heart, to look for any sign of enlargement, where the heart is bigger than normal

due to the structural changes [71]. Another imaging technique normally applied is the *echocardiogram*, which uses sound waves, instead of electromagnetic radiation. The transducer sends sound waves towards the heart, and then receives the echo. This can be translated into an image, or a real-time video, which allows the evaluation of the *left ventricular ejection fraction (LVEF)*, which is the percentage of blood ejected from the left ventricle with each beat [72, 73].

The second group is based on *blood test*, to search for certain substances in the blood that are secreted or associated with CHF, like the *B-type Natriuretic Peptide (BNP)*. BNP is secreted by the ventricles in response to the excessive contraction of the muscle cells and changes in pressure in the ventricles. BNP levels below 100 pg/ml of blood indicates no CHF. BNP levels between 100 and 300 pg/ml might suggest the presence of CHF. Between 300 and 900, it might be considered mild-to-moderate CHF and, then, above 900 pg/ml would indicate a severe case of CHF [74, 75].

The last group is the *classification system*, which describes the severity of the symptoms. The first classification system is based on a *stress test*, which is also known as the *New York Heart Association (NYHA)* Functional Classification [76]. This test looks at how well the patient responds to physical exertion, because with more activity and exertion the body demands more blood. Therefore, depending on how well the heart can respond to increasing demands by increasing activity, the severity of CHF can be determined. Patients in class I have no limitation to physical activity. The stress test does not cost any out of the ordinary fatigue, palpitations or shortness of breath. Patients in class II experience some limitation to physical activity. The patient might be comfortable at rest, but any normal physical activity results in some symptoms of CHF. Patients in class III have a marked limitation of physical activity, but still no symptoms at rest. Finally, patients in class IV have a complete inability to undertake any physical activity without feeling no symptoms [76]. Furthermore, those symptoms even occur at rest. A second classification system is the "American Heart Association Stages of HF", which is more defined at the objective level by the amount of structural heart disease that is present in each patient [77].

1.4.2 Treatment

In the early stages of CHF, the patients might not even have symptoms and they might only have risk factors for CHF. This means that they probably have some kind of pre-existing condition that might, if left unchecked, lead to CHF in the future, or lead to worsening CHF if it is already present. At this stage, patients are still able to go about their daily lives. Some examples of risk factors might include hypertension, high blood pressure, coronary artery disease or diabetes. An early stage treatment that is recommended is exercise. With exercise, the cardiovascular fitness increases. This increases the efficiency of the heart and, then, the cardiac output increases. In addition to exercise, another lifestyle change that might be recommended is a change in diet, and reducing salt intake is a common and important change, since it reduces blood pressure, increasing the cardiac output. This decreases the chances of the heart to start compensating, and making structural changes to the ventricles. Medications

are also usually prescribed, like *angiotensin-converting-enzyme (ACE)* inhibitors and *angiotensin receptor blockers (ARBs)*, which are vasodilators that reduce blood pressure, and *beta-blockers*, which inhibit the activation of the sympathetic nervous system and prevent the heart rate to increase, and cause, again, structural changes [69].

In the late stages of CHF, when the symptoms associated with CHF have started to appear, a different set of medications is recommended for treatment. These medications are aimed at treating and controlling these symptoms, which have already started to affect the quality life of the patient [69].

Nevertheless, a CHF patient may get to the point where medications and lifestyle changes help but are not enough, and the patient is symptomatic almost all the time. Then, treatment is derived to implantation of *medical devices* or surgery. There are a few types of medical devices that can be used, the *ventricular assist device (VAD)*, the *cardiac resynchronization therapy (CRT)* and the *implantable cardioverter defibrillators (ICDs)*. The VAD takes control of the pumping for the ventricle of the patient. There is a small tube that attaches to the ventricle that needs help. Then, blood, instead of exiting to the artery, is rerouted to the VAD. The VAD, then, pumps it out through the next tube, which connects with the artery and, then, leaves the heart. Implantable VADs are usually reserved for people that are either waiting for a heart transplant, or as a long-term solution for those that cannot have heart transplants. CRT consists of a small pacemaker implanted in the chest, and, then, some electrical wires go from the pacemaker to both the left and the right ventricles. In CHF, the left and right ventricles may beat at different rates, making the heart less efficient to pump. The pacemaker sends signals via the electrical wires at the same time, to tell both ventricles to pump at the same time, leading to a normal and efficient pumping action. If the patient in CHF suffers from life-threatening arrhythmia, the ICD can deliver a shock that resets the heart to a normal rhythm. Surgery involves the implantation of stents, coronary artery bypass, or, eventually, a complete heart transplantation. This last option is limited to patients that are considered at end-stage CHF, or where other medical treatments in surgery have failed [69].

1.4.3 Principal Outcomes

The mode of death in patients with CHF is frequently difficult to determine. It is commonly agreed that CHF patients may experience progressive symptomatic worsening, leading to *pump failure death (PFD)*, or suffer from *sudden cardiac death (SCD)* [69]. SCD is the primary cause of death for the majority of patients with mild-to-moderate CHF, while PFD is more common among patients with advanced symptoms [78–81]. Then, diagnostic tools should be able to predict the potential outcome that a CHF patient may suffer, and, then, treatment should be oriented to specifically ease, or correct, the symptoms of each mode of *cardiac death (CD)*. Particularly relevant for the patient with CHF is the possibility that further myocardial necrosis, coupled with previous myocardial damage, may produce enough additional pump dysfunction that if sudden death does not occur, myocardial failure will rapidly develop. How do patients with CHF die from PFD or SCD?

Sudden Cardiac Death

SCD generally refers to an unexpected death from a cardiovascular cause in a person with or without preexisting heart disease. The specificity of this definition varies depending on whether the event was witnessed. However, most studies include cases that are associated with a witnessed collapse, death occurring within 1 hour of an acute change in clinical status, or an unexpected death that occurred within the last 24 hours [82]. Although it is still difficult to understand the underlying mechanisms leading to SCD, it is commonly presumed that many are related to arrhythmias [81]. A cardiac arrhythmia is a variation in the normal heart rate and/or rhythm that is not physiologically justified [83, 84]. The mechanisms responsible for cardiac arrhythmias are generally divided into three major categories, a vulnerable myocardium, a triggering factor and a modulator [84–86].

- **Vulnerable myocardium:** It is the substrate for arrhythmogenesis, meaning that when triggering factors appear, they can lead to malignant arrhythmias potentially ending in SCD [87]. A major, if not the major, electrophysiological feature responsible for the vulnerability of the myocardium in human CHF appears to be an increased dispersion of repolarization [88–90]. A heart that is totally homogeneous electrically, i.e. all cells are at the same stages of depolarization and repolarization and conduct normally without delay or block, very probably cannot develop ventricular arrhythmias. However, even in the normal state, these conditions do not exist, because, in the healthy heart, dispersion of repolarization allows efficient contraction and relaxation, as described in section 1.2.1 [91]. Under pathological conditions like CHF, dispersion can become extreme and promote the formation of a *unidirectional block* of a normal wave of electrical excitation [83, 88, 92–94]. A unidirectional block is a pathological failure of cardiac impulse conduction in one direction, while conduction is possible in the opposite direction [95]. Thus, pockets of cells that may be temporarily unable to conduct the normal flow of electrical activity in the heart, increase the spatial dispersion of repolarization and, eventually, create a substrate for arrhythmia [83, 96–100].
- **Triggering factor:** Although the unidirectional block can increase the risk of arrhythmia, it is not sufficient. Since a triggering mechanism is still required [83]. Automaticity is the property of cardiac cells to generate spontaneous APs. As explained in section 1.2.1, the SA node normally displays the highest intrinsic rate. All other pacemakers are referred to as subsidiary or latent pacemakers because they take over the function of initiating excitation of the heart only when the SA node is unable to generate impulses or when these impulses fail to propagate [84]. Ventricular myocardial cells do not display spontaneous diastolic depolarization or automaticity under normal conditions, but can develop these characteristics when depolarized, resulting in the development of repetitive impulse initiation [101]. Then, once an ectopic activation is triggered, it can be maintained by a regenerative circuit of electrical activity around the unidirectional block, a phenomenon known as *reentry* [84].

- **Modulator:** Among the modulating factors, the ANS is the most relevant one. In pathological states such as CHF [102], sympathetic stimulation predominates over parasympathetic stimulation [60]. Dispersion of repolarization can become enhanced and ventricular automaticity can be reinforced [103, 104]. Changes in autonomic nerve function can significantly affect reentry mechanisms, either by facilitating the appearance of a spontaneous ectopic activation, or by creating a vulnerable substrate along which the arrhythmia may be maintained.

Pump Failure Death

As mentioned in section 1.4.1, sympathetic activity increases during CHF to compensate for the low cardiac output. If the heart is capable of adapting to these rapid sympathetic strikes, and avoid ventricular arrhytmias, it is still burdened by other factors. On the one hand, the constant activation of the sympathetic nervous system may break the sympathovagal balance. As described in section 1.2.2, the sympathetic and parasympathetic branches work in an antagonistic manner. Thus, if the sympathetic system is systematically activated to compensate for the lowered cardiac output, the parasympathetic activity is systematically inactivated, breaking the homeostatic balance. On the other hand, in response to increased demands for cardiac output, the heart adapts through compensatory hypertrophy of myocytes [105, 106] and by increasing the myocite contractility. These short-term adaptive responses to maintain cardiac output eventually become maladaptive [105,107], leading to myocyte dropout, or apoptosis, and a progressive deterioration in myocardial function [108]. Therefore, patients in later stages of CHF are characterized by a withdrawal of vagal activity [57] and a reduction in the response of the ventricle to autonomic innervation [57].

1.4.4 Mortality Prediction Using Clinical Markers

With the advent of ICDs and CRT, accurate risk stratification has become very relevant. Several clinical markers have been proposed in the literature to risk-stratify patients according to their most probable outcome (SCD or PFD) and, then, facilitate the treatment decision-making process.

Based on the results of multiple clinical trials, LVEF is currently the only recommended tool to identify patients at higher risk of SCD that would benefit from a prophylactic ICD [109–112]. However, LVEF as standalone risk stratifier has major limitations: (i) the majority of SCD cases occur in patients with preserved or moderately reduced LVEF, (ii) only relatively few patients with reduced LVEF will benefit from an ICD (most will never experience a threatening arrhythmic event, others have a high risk for PFD), (iii) a reduced LVEF is a risk factor for both SCD and PFD [113]. Several other clinical markers have been proposed in the clinical practice, like age, gender (75% of SCD events occur in men with an annual incidence of 3 to 4 times higher than in women [94,114]), hypertension, dilated cardiomyopathy [94,115], intraventricular conduction block, elevated serum cholesterol, glucose intolerance, decreased vital capacity, smoking, diabetes mellitus [116,117], relative weight, ischaemic

heart disease [118], previous myocardial infarction [119] and heart rate [94]. PFD is also characterized by older age, lower heart rate and previous myocardial infarction [119, 120]. In addition, mortality rates increase the higher the NYHA class, but the proportion of patients dying from SCD is highest among those with less severe CHF (NYHA class II and III) [82]. However, none of these techniques has unequivocally demonstrated the efficacy when applied alone or in combination with LVEF. Apart from their limited sensitivity, most of them are risk factors for both SCD and PFD [113].

Considering the multiple mechanisms involved in cardiac mortality, it seems unlikely that a single test will prove adequate for all patients. Then, risk models based on a set of clinical variables have been proposed and evaluated in CHF patients for specific SCD and PFD prediction [121–124]. These risk scores are a critical first step to serve as a quick screen to identify subgroups that might benefit from further evaluation [125]. Then, additional risk models based on ECG-derived indices reflecting different mechanisms like ANS imbalance and electrophysiological dysfunctions could add complementary information and improve risk stratification by refining the clinical-based risk subgroups.

1.4.5 Mortality Prediction Using the ECG

The overall goal of the analysis of the ECG signal is to obtain information about the structure and function of the heart. Being able to extract and interpret the important information contained within the ECG waveforms and intervals can provide improved predictive tools to better stratify CHF patients according to their risk of suffering from SCD or PFD and, then, optimize the treatment. As already mentioned, the repolarization phase is critical in the inducibility of arrhythmogenic substrates, and an imbalanced ANS can be associated with electrical and/or mechanical malfunctioning of the heart. In the following, commonly used ECG-derived markers reflecting ventricular repolarization or autonomic conditions are described:

- **QT interval**: It is measured from the beginning of the QRS complex to the end of the T-wave (Figure 1.3 (b)). It is a measure of the total duration of ventricular depolarization and repolarization. Prolongation of the QT interval may be caused by an increase in the duration of depolarization (for example, in bundle branch block) or lengthening of the total time taken for repolarization, and is the most traditional ECG marker for arrhythmic risk prediction [126].

- **QT interval dynamics**: As described in section 1.2.1, cardiac repolarization adapts to heart rate. This critical feature ensures that with increasing heart rate, the myocardium remains constantly excitable, i.e. completely repolarized, before the next depolarization wave enters. This prevents incomplete repolarization and the subsequent possibility for re-entrant tachycardia. Experimental results have revealed that the APD restitution kinetics described in section 1.2.1 may provide relevant information for ventricular arrhythmic risk stratification [51, 127]. Specifically, individual APDR curves have been reported to play an important

role in the development of ventricular arrhythmias, with steeper slopes of APDR curves (higher values of α in Figure 1.3 (c)) being suggested to be linked to life-threatening arrhythmia [128, 129]. However, although shallow slopes (lower values of α in Figure 1.3 (c)), have been reported to reflect smaller APD disturbances that eventually return to a stable activation [47], they have also been related to a perpetuation of electrical instabilities [46]. At the ECG level, the slope of the relationship between the QT and RR intervals, which would quantify the velocity of adaptation of ventricular repolarization to changes in heart rate, has been suggested as an arrhythmic risk predictor, with increased slopes indicating higher arrhythmic risk [130–133]. Following the hypothesis illustrated in Figure 1.3, and assuming that depolarization duration is almost constant with heart rate (for RR interval values above 0.6 s), the QT/RR slope could to some extent be related to the slope of the APDR curve from the last cell to repolarize, i.e. α_1 in panel (c).

- **QRS-T angle**: It measures the difference in mean vectors of depolarization and repolarization in the vectorcardiogram. It characterizes a secondary dispersion of repolarization whereby repolarization abnormalities following changes in ventricular conduction are highlighted, in the absence of primary action potential morphology heterogeneity [134]. It has been found associated with SCD [135, 136].

- **Tpe interval**: It is measured from the T_{peak} to the T_{end} (Figure 1.3 (b)). It provides a measure of dispersion of repolarization during the last stages of ventricular repolarization [137], which have been shown to be more critical for developing malignant arrhythmias than the T-wave width [138] after acute myocardial infarction [139], in patients with left ventricular systolic dysfunction [140], in patients with hypertrophic cardiomyopathy [141] and in the general population [142].

- **Tpe interval dynamics**: Heterogeneities in the ventricle as a result of CHF lead to spatial differences in the restitution properties, which makes APDR curves present spatial variations [143]. Restitution dispersion is a measure of that spatial variation and can be quantified by taking the difference between the respective slopes, $\Delta\alpha = \alpha_1 - \alpha_2$ (Figure 1.3 (c)). Recent studies have suggested that increments in such dispersion (higher values of $\Delta\alpha$) are associated with greater propensity to suffer from malignant ventricular arrhythmias [54, 129]. Quantification of dispersion of repolarization restitution commonly uses invasive methods. As a non-invasive alternative, Mincholé at al. developed a methodology to estimate $\Delta\alpha$ from the surface ECG as the slope of the Tpe interval dynamics and proved that it was strongly correlated with the dispersion of repolarization restitution at tissue level [144].

- **Regional Restitution Instability Index (R2I2)**: It is another estimation of dispersion of repolarization restitution from the surface ECG. For each available lead, the standard deviation of the QT/TQ gradient slopes are taken as a measure of APD dispersion in each lead, where TQ is the interval between the T wave peak of a beat and the Q wave peak of the following beat. The

mean of this was then taken as the R2I2 (no units) [145]. This novel index was shown to predict ventricular arrhythmic risk, or death, in patients with ischemic cardiomyopathy [145].

- **T-wave alternans (TWA)**: It is a repeating ABABAB pattern in the morphology and amplitude of the ST-segment and/or T-wave and has long been recognized and linked to arrythmogenesis [146]. It has been postulated to reflect spatio-temporal dispersion of repolarization [147–149] and arises from beat-to-beat alternation of membrane voltage or intracellular calcium, underlying APD alternans at an ionic level [150–154]. Higher levels of TWA have been shown to indicate greater risk for arrhythmias under different conditions [148, 155, 156].

- **Heart rate variability (HRV)**: It is the beat-to-beat variation in either heart rate or the duration of the RR interval [157]. A reduced HRV is associated with poorer prognosis for a wide range of clinical conditions while, conversely, robust periodic changes in RR interval are often a hallmark of health [158]. A major portion of these temporal changes in heart rate occur synchronous with respiration and, therefore, are referred to as *respiratory sinus arrhythmia*. HRV has been shown to provide an indirect assessment of cardiac autonomic activity [157].

- **QT interval variability**: Common used variables of beat-to-beat QT interval variability (QTV) include the standard deviation (SDQT) or variance of QTV (QTvar) [159, 160], QT interval variance normalized to the square mean QT interval (QTVN) [161] and Poincaré plot-based, short-term variability [162, 163]. Additionally, the QT variability index (QTVi), quantifying the QT interval variability-to-HRV ratio is often calculated [161, 164, 165]. Frequency domain parameters quantifying QTV have also been explored [166–168]. The variability of the QT interval has been related to the activity of the sympathetic tone [164, 169]. Progressive rises in QT variability are associated with worsening functional status in patients with CHF [161] and enhanced arrhythmic risk [170, 171].

- **Heart rate turbulence (HRT)**: It describes the short-term fluctuation in the RR interval that follows a *ventricular premature beat (VPB)* [172]. In normal subjects, heart rate initially briefly accelerates and subsequently decelerates compared with the pre-VPB rate, before returning to baseline. This dynamics may be altered in pathophysiological conditions [173]. Two phases of HRT, the early heart rate acceleration and late deceleration, are quantified by 2 parameters termed *turbulence onset (TO)* and *turbulence slope (TS)* [174]. The initial heart rate acceleration is triggered by transient vagal inhibition in response to the missed baroreflex afferent input due to hemodynamically inefficient ventricular contraction. A simpathetically mediated overshoot of arterial pressure is responsible for the subsequent heart rate deceleration through vagal recruitment [175]. Its proven clinical significance lies in its ability to predict mortality, PFD and SCD following myocardial infarction and many other cardiac diseases [173, 176]. A model-based HRT detector, involving an index that characterizes HRT shape, was shown to outperform TO and TS in predicting cardiac death [177].

- **Deceleration Capacity**: It expresses the ability of the ANS to decelerate the heart rate [178, 179]. Beat-to-beat heart rate regulation is achieved through the rapid vagus nerve activity, which can change the heart rate substantially, even within one cardiac cycle [179]. Deceleration capacity was found to be linked to increased post-myocardial infarction mortality [179] and to increased HF diagnosis [180]. Then, a reduced deceleration capacity has been hypothesized to be linked to a diminished vagal modulation on the heart [179], based on previous clinical and experimental studies indicating a cardioprotective role of vagal activity [181]. Two additional methodologies to compute the deceleration capacity have been recently proposed [178].

- **Periodic Repolarization Dynamics**: It assesses the sympathetic effect on ventricular repolarization and was shown to predict mortality in survivors of acute myocardial infarction [182]. It integrates the spatio-temporal information of each T-wave into a single vector, T°. Then, the angle dT° between successive repolarization vectors is used as an estimate of the instantaneous repolarization instability. The index of periodic repolarization dynamics is then computed from the quantification of the low-frequency ($\leqslant$0.1Hz) periodic patterns in dT° [182].

1.5 Objectives and Structure of the Document

The main objective of this thesis is to develop ECG-derived risk markers related with ventricular repolarization restitution, and with its dispersion, to improve the prediction of SCD and PFD in CHF patients. The content of the thesis is organized as follows:

- **Chapter 1**: In the present chapter, we introduce the electrical activity of healthy hearts and of hearts from patients with chronic heart failure. Different causes underlying SCD and PFD in the context of CHF and the clinical need for non-invasive markers with high predictive value are described. Also, a variety of ECG-derived risk markers recently proposed in the literature for risk prediction in CHF are presented.

- **Chapter 2**: In this chapter, ventricular repolarization restitution and its dispersion are explored using traditional ECG-derived markers based on temporal intervals, namely the QT interval and the Tpe interval. As mentioned, the dynamics of these intervals are related to the repolarization restitution and its dispersion, respectively. Numerous studies have reported that steeper restitution slopes and increased dispersion of repolarization restitution indicate higher arrhythmic risk [54, 128, 129], but there are no previous studies assessing the SCD and PFD predictive value of ECG markers estimating those two concepts. Therefore, a fully automated method to estimate repolarization restitution and its dispersion from 24-h Holter ECG recordings from 651 CHF patients is presented and the SCD and PFD predictive value is evaluated. Three different estimations of the dispersion of repolarization restitution are compared and the

influence of the circadian modulation is evaluated. Finally, SCD and PFD risk stratification in combination with two other ECG-derived markers quantifying TWA and HRT is assessed. From the results of this chapter an ECG-derived index with strong capacity to predict both SCD and PFD is proposed. This could help deriving CHF patients to their most beneficial treatment, according to their risk of suffering from SCD or PFD. The research described in this chapter generated the following publications:

- J. Ramírez, A. Mincholé, J. Bolea, P. Laguna and E. Pueyo. Prediction of sudden cardiac death in chronic heart failure patients by analysis of restitution dispersion. *XL International Conference on Computing in Cardiology*, Zaragoza, Spain, 1-4, 2013.
- J. Ramírez, P. Laguna, A. B. De Luna, M. Malik and E. Pueyo. QT/RR and T-peak-to-end/RR curvatures and slopes in chronic heart failure: Relation to sudden cardiac death. *J Electrocardiol*, 2014;47:842-848.
- J. Ramírez, I. Cygankiewicz, P. Laguna, M. Malik and E. Pueyo. Circadian pattern and sex differences of QT/RR and T-peak-to-end/RR curvatures and slopes in chronic heart failure patients. *XLI International Conference on Computing in Cardiology*, Boston (MA), U.S.A., 173-176, 2014.
- J. Ramírez, V. Monasterio, A. Mincholé, M. Llamedo, G. Lenis, I. Cygankiewicz, A. B. De Luna, M. Malik, J. P. Martínez, P. Laguna and E. Pueyo. Automatic SVM classification of sudden cardiac death and pump failure death from autonomic and repolarization ECG markers. *J Electrocardiol*, 2015;48:551-557.

Also, this work was awarded with the following prizes:

- *Rosanna Degani Young Investigator Award for the best written and oral presentation.* Prediction of sudden cardiac death in chronic heart failure patients by analysis of restitution dispersion. *XL International Conference on Computing in Cardiology*, Zaragoza, Spain, 2013.
- *Jos Willems Young Investigator Finalist.* Prediction of sudden cardiac death by analysis of restitution dispersion. 30^{th} Annual conference of the international society for computerized electrocardiology. Jacksonville, Florida (USA), 2014.
- *Michael Ringborn Young Investigator Award for the best oral presentation.* DeltaAlpha repolarization dispersion. 12^{th} STAFF Studies Symposium. MIT Endicott House, Dedham, MA (USA), 2014.

- **Chapter 3**: Based on the results from chapter 2, the hypothesis that the morphology of the T-wave would contain additional information disregarded when using time-interval indices only was postulated. In this chapter, a novel methodology was developed to quantify indices capable of extracting morphological information independently from disturbances in temporal or amplitude domains,

or noise. Specifically, the ability of two new ECG-derived markers, d_w, and d_a, and their non-linearly restricted versions, d_w^{NL} and d_a^{NL}, to quantify single-lead T-wave morphological variability was assessed. The point-wise variability between the temporal domains of different T-waves, or the amount of warping needed to remove the time domain variability, is measured by d_w, while d_a quantifies the point-wise amplitude variability after time warping, or the amplitude variability after removing the temporal domain variability. The markers d_w^{NL} and d_a^{NL} quantify the strictly non-linear warping and amplitude levels within d_w and d_a, respectively. First, the performance of two warping algorithms was compared. Then, the robustness of d_w, d_a, d_w^{NL} and d_a^{NL} against noise was evaluated in a simulated set-up with synthetically generated signals. Next, an electrophysiological cardiac model was used to investigate the relation between d_w, d_a, d_w^{NL} and d_a^{NL} and the morphological changes of the AP at cell and tissue level. Finally, T-wave morphological variations produced by a tilt test in ECG recordings were quantified using d_w, d_a, d_w^{NL} and d_a^{NL}, and their correlation with heart rate, the QT and Tpe intervals and the T-wave width and amplitude were also studied. As a conclusion, the performance of the proposed methodology is discussed and the potential of the proposed markers as risk predictors is presented. The research described in this chapter generated the following publications:

- J. Ramírez, M. Orini, J. D. Tucker, E. Pueyo and P. Laguna. Variability of ventricular repolarization dispersion quantified by time-warping the morphology of the T-waves. *IEEE Transactions on Biomedical Engineering*, 2016; DOI: 10.1109/TBME.2016.2614899.
- J. Ramírez, M. Orini, J. D. Tucker, E. Pueyo and P. Laguna. An index for T-wave pointwise amplitude variability quantification. *XLIII International Conference on Computing in Cardiology*, Vancouver, Canada, 49-52, 2016.

Also, this work was awarded with the following prize:

- *Mortara mobility fellowship.* An index for T-wave pointwise amplitude variability quantification. Computing in Cardiology. *XLIII International Conference on Computing in Cardiology*, Vancouver, Canada, 2016.

- **Chapter 4**: In this chapter, dispersion of repolarization restitution was explored using the morphological indices presented in chapter 3. Under the assumption that the T-wave morphology reflects dispersion of repolarization, we hypothesized that the restitution of the T-wave morphology would reflect dispersion of repolarization restitution. The SCD and PFD predictive value of the quantified T-wave morphology variation after a change in heart rate was evaluated. Additionally, its circadian modulation, its robustness and its classification performance in combination with the same ECG-derived risk markers quantifying TWA and HRT used in chapter 2 were studied. From the results in this chapter, a second ECG-derived index specifically associated with SCD and with higher predictive value than the Tpe dynamics and other clinical and ECG-derived

indices was proposed. The following manuscript has been submitted with the results presented in this chapter:

  - J. Ramírez, M. Orini, A. Mincholé, V. Monasterio, I. Cygankiewicz, A. B. De Luna, J. P. Martínez, E. Pueyo and P. Laguna. T-wave Morphology Restitution Predicts Sudden Cardiac Death in Patients with Chronic Heart Failure. Submitted to *Journal of the American Heart Association*.

Also, this work was awarded with the following prize:

  - *Michael Ringborn Young Investigator Award for the best oral presentation.* T-wave morphological restitution evaluated by time-warping metrics and its value to predict sudden cardiac death and pump failure death. 14^{th} STAFF Studies Symposium. Bled, Slovenia, 2016.

- **Chapter 5**: Although deriving an individual index with strong predictive value is still desirable, SCD and PFD events are a result of a combination of failing mechanisms. Therefore, using a score that integrates several risk factors with individual predictive power might improve prediction even further. Then, in this chapter two ECG-based models that include markers assessing different arrhythmogenic and autonomic mechanisms to specifically predict either SCD or PFD were proposed. Their predictive value was compared to a model composed of commonly used clinical markers. Two optimal risk models combining ECG and clinical markers were finally proposed. As a conclusion, the performance of the ECG-based models, compared to that of the clinical models, and the improvement achieved by the combined model, are discussed. The following manuscript has been submitted with the results presented in this chapter:

  - J. Ramírez, M. Orini, A. Mincholé, V. Monasterio, I. Cygankiewicz, A. B. De Luna, J. P. Martínez, E. Pueyo and P. Laguna. Improvement of Sudden Cardiac Death and Pump Failure Death Prediction by Including ECG-derived Markers to a Clinical Model. Submitted to *Heart Rhythm*.

- **Chapter 6**: It presents the main conclusions of the thesis and discusses future methodological directions.

Chapter 2

Predictive Risk Value of Repolarization Restitution Estimated from Time-Interval ECG Markers

---

2.1 Introduction

As introduced in chapter 1, patients with mild-to-moderate CHF (NYHA classes II and III) represent a high-risk population for SCD and PFD [183]. ICDs have been shown to reduce SCD mortality [184], while CRT reduces PFD in CHF patients [185]. The cost effectiveness of these treatments is, however, limited, with a relatively small number of patients receiving appropriate ICD shocks or benefiting from an accurate CRT during follow-up [183, 185]. Then, finding effective techniques for risk stratification still remains a relevant clinical problem.

As described in section 1.2.1, APDR curves containing steep slopes are associated with malignant arrhythmias [128, 129], meaning that a big repolarization change as a response to a heart rate change can be arrhythmogenic. The QT interval is the most extensively used index of ventricular repolarization for arrhythmic risk prediction [126], and the slope of the QT interval dynamics, which we hypothesized it reflects the slope of the APDR curve from the last cell to repolarize, has been proposed as an arrhythmic risk predictor in numerous studies [130–133].

Additionally, increased dispersion of repolarization restitution, invasively quantified by $\Delta\alpha$, has been suggested to be a potent arrhythmogenic substrate, with increments in such dispersion being associated with greater propensity to suffer from malignant arrhythmias [54, 129]. The main limitation on the usability of $\Delta\alpha$ as a risk index is that its quantification usually requires invasive procedures. The Tpe interval reflects dispersion of repolarization and, thus, the slope of the Tpe interval dynamics would be a surrogate of the dispersion of repolarization restitution, estimated from the ECG, as hypothesized in the introduction, and as demonstrated in previous studies [144].

The relationship between the QT and Tpe intervals and the underlying heart rate (HR) has been previously quantified, after adjustment for hysteresis effects, selecting among ten biparametric fixed regression equations the one with the lowest residual fitting error, and evaluating the slope of the regression at the average heart rate change [130, 144]. In addition, the pattern of these relationships do not necessarily follow a linear regression [186], and, then, a recent study proposed a subject-dependent equation, with an additional parameter accounting for the curvatures of the regression patterns, after compensation for the hysteresis effects, and evaluated the slope of the regression in RR = 1s [187].

Also, the circadian pattern has shown to be a strong modulator of ventricular repolarization, with previous studies demonstrating that the slope of the QT interval dynamics is steeper during the day than at night in healthy subjects [188–190], and associated with higher risk of cardiac death [191] and total mortality [192].

Finally, although invasive and non-invasive markers have been proposed as SCD and/or PFD predictors, including LVEF [193], TWA [156], or autonomic indices such

as HRT [176], they do not provide a high enough *sensitivity (Se)*/specificity (Sp) ratio. Then, if such indices reflect different underlying physiological phenomena, they might add complementary information to each other and, consequently, a combined index might improve the capability for risk-stratification of patients.

In this chapter, we, first, developed a fully automated algorithm to calculate the slope of the QT and Tpe intervals dynamics in 24-h ECG recordings from 651 CHF patients, using a fixed biparametric regression, and evaluated at the average heart rate change as in [130, 144], and using a subject-dependent tri-parametric regression, evaluated at the average heart rate change and at RR = 1 s, as in [187]. The curvature of the QT/RR and Tpe/RR regressions were also calculated as in [187]. Then, we studied the modulation of the circadian pattern on the proposed parameters reflecting QT and Tpe dynamics, and we assessed their SCD and PFD predictive value. Finally, we studied the classification performance of the parameter with strongest predictive value, individually and in combination with two other ECG-derived risk markers quantifying TWA [156] and HRT [176].

2.2 Methods

2.2.1 The MUSIC Study

Study Population

The study population included 651 consecutive patients with symptomatic CHF corresponding to NYHA classes II and III enrolled in the *MUerte Súbita en Insuficiencia Cardiaca (MUSIC)* study, a prospective, multicenter study designed to assess risk predictors for cardiovascular mortality in ambulatory patients with CHF [122]. A two- or three-lead 24-hour Holter ECG sampled at 200 Hz was recorded in each patient at enrolment using ELA Medical equipment (Sorin Group, Paris, France). Baseline demographic and clinical data in sinus rhythm were available for the analysis. The MUSIC study included patients with both reduced and preserved LVEF, ranging from 10% to 70%. Patients with preserved LVEF were included if they had CHF symptoms, a prior hospitalization for CHF or objective CHF signs confirmed by chest X-ray and/or echocardiography. Patients were excluded if they had recent acute coronary syndrome or severe valvular disease amenable for surgical repair. Patients with other concomitant diseases expected to reduce life-expectancy were also excluded. The study protocol was approved by the institutional investigation committees and all patients signed informed consent. No medications were withdrawn during Holter monitoring. The clinical characteristics of the studied patients and medications are listed in Table 2.1.

Variables	Overall population ($n = 651$)	$\Delta\alpha^{\mathrm{Tpe}} \leqslant 0.022$ ($n = 285$)	$0.022 < \Delta\alpha^{\mathrm{Tpe}} < 0.028$ ($n = 59$)	$\Delta\alpha^{\mathrm{Tpe}} \geqslant 0.028$ ($n = 307$)	p-value
Clinical					
Age [years]	63±12	61±12	63±11	64±12	**0.006**
Gender [men]	464 (71.3%)	226 (79.3%)	41 (69.5%)	197 (64.2%)	**<0.001**
NYHA class III	115 (17.7%)	51 (17.9%)	8 (13.6%)	56 (18.2%)	0.682
LVEF $\leqslant$ 35%	356 (54.7%)	152 (53.3%)	34 (57.6%)	170 (55.4%)	0.789
Ischemic etiology	327 (50.2%)	152 (53.3%)	25 (42.4%)	150 (48.9%)	0.248
Diabetes	244 (37.5%)	95 (33.3%)	22 (37.3%)	127 (41.4%)	0.130
Beta-blockers	455 (69.9%)	210 (73.7%)	41 (69.5%)	204 (66.4%)	0.159
Amiodarone	61 (9.4%)	22 (7.7%)	3 (5.1%)	36 (11.7%)	0.123
ARB or ACE	576 (88.5%)	253 (88.8%)	53 (89.8%)	270 (87.9%)	0.898
ECG-derived					
Median RR [s]	0.85±0.12	0.85±0.12	0.86±0.13	0.84±0.12	0.669
RR range [s]	0.42±0.15	0.43±0.14	0.45±0.13	0.42±0.15	0.816
QRS > 120 ms	262 (40.2%)	112 (39.3%)	23 (39.0%)	127 (41.4%)	0.858
NSVT and > 240 VPBs in 24 h	168 (25.8%)	80 (28.1%)	15 (25.4%)	73 (23.8%)	0.490
IAA$\geqslant$3.7μV	153 (24.1%)	69 (28.8%)	18 (31.6%)	66 (22.0%)	0.280
TS$\leqslant$2.5ms/RR	281 (47.1%)	121 (45.3%)	20 (36.4%)	140 (50.9%)	0.106

Data are presented as absolute frequencies and percentages and as mean ± standard deviation. ACE = angiotensin-converting enzyme; ARB = angiotensin receptor blocker; IAA = Index of Average Alternans; LVEF = left ventricular ejection fraction; NYHA = New York Heart Association; NSVT = Non-sustained Ventricular Tachycardia; TS = Turbulence Slope; VPB = Ventricular Premature Beat; Significant differences are indicated in bold.

Table 2.1: Characteristics of patients in the overall population and in each of the three risk groups defined by $\Delta\alpha^{\mathrm{Tpe}}$.

Follow-up Period

Follow-up visits were conducted on an outpatient basis every 6 months, for a median of 44 months (range 28-51). Information about deceased patients was obtained from medical records, patients' physicians, and relatives. In each case, the attempt was made to determine the nature of death. Total mortality was divided into non-cardiac and CD, and the latter was further subdivided into PFD and SCD. SCD was defined as (i) a witnessed death occurring within 60 min from the onset of new symptoms, unless a cause other than cardiac was obvious; (ii) an unwitnessed death (<24 h) in the absence of pre-existing progressive circulatory failure or other causes of death; or (iii) a death during attempted resuscitation. Deaths occurring in hospitals as a result of refractory progressive end-stage CHF were defined as PFD. Patients lost to follow-up were censored in survival analysis. Patients who underwent cardiac transplantation were defined as PFD at the time of surgery, according to previously published CHF studies [121, 194]. Endpoints were reviewed and classified by the MUSIC Study Endpoint Committee.

2.2.2 ECG Pre-processing

Preprocessing of the ECG signals was performed using custom-written software and included low pass filtering at 40 Hz to remove electric and muscle noise, cubic splines interpolation for baseline wander removal, and ectopic beats detection.

PCA (section 1.3.2) was applied over the two-or-three available ECG leads to emphasize the energy of the T-wave and improve its delineation [195]. Then, in this thesis, the PCA training matrix, $\mathbf{L}_{\mathrm{T}}$, was built by only considering the samples from the T-waves on each lead. First, a single-lead-and-rules delineation technique (section 1.3.3) was applied to select the samples from the T-wave and compute the matrix $\mathbf{L}_{\mathrm{T}}$. Then, the first principal component was computed and delineated using a single-lead technique (section 1.3.3) [66]. From the delineation marks, the RR, QT and Tpe interval series were obtained and subsequently interpolated at a sampling frequency of $F_{\mathrm{S}} = 1$ Hz using a fully automated method.

2.2.3 Dispersion of Repolarization Restitution from the Tpe Interval Dynamics

Theoretical Hypothesis

The Tpe interval reflects differences in the time for completion of repolarization by different cells along the ventricle [137, 144]. Therefore, the Tpe interval may be expressed in terms of APDs as follows (Figure 1.3 (b)):

$$\mathrm{Tpe} \approx APD_1 - APD_2 - \Delta AT, \tag{2.1}$$

where APD_1 corresponds to the last cell to repolarize, and APD_2 is the cell with the minimum APD among those which are currently repolarizing at the T-wave peak instant [144]. ΔAT represents the activation time delay between the two cells associated with APD_1 and APD_2, and hardly changes with RR for RR intervals above 600 ms [50]. Therefore, changes in the Tpe interval under variations of the RR interval, measured at different steady-state heart rate levels, can be estimated as:

$$\frac{\partial \mathrm{Tpe}}{\partial RR} \approx \frac{\partial APD_1}{\partial RR} - \frac{\partial APD_2}{\partial RR}, \tag{2.2}$$

where $\partial\Delta\mathrm{AT}/\partial\mathrm{RR}$ has been neglected, under the premise that RR intervals above 600 ms are considered [144].

If we let α_1 and α_2 denote the slopes of APDR curves at the regions corresponding to APD_1 and APD_2, respectively (Figure 1.3 (c)):

$$\alpha_{\mathrm{i}} = \frac{\partial APD_{\mathrm{i}}}{\partial RR}, \quad i = \{1, 2\}, \tag{2.3}$$

the spatial difference $\Delta\alpha$ = (α_1 - α_2) (see Figure 1.3), which measures dispersion of repolarization restitution, can be estimated from the ECG by introducing (2.3) into (2.2), resulting in [144]:

$$\Delta\alpha^{\mathrm{Tpe}} = \frac{\partial \mathrm{Tpe}}{\partial RR} \tag{2.4}$$

Applicability of the Hypothesis to 24-h ECG Recordings

Each value of the APDR curve represents a stationary state corresponding to a specific RR value, and, therefore, the ECG measurement proposed to estimate dispersion of repolarization restitution should in principle be computed using ECG segments of stable heart rate [51]. However, these types of segments are difficult to get in clinical practice, provoking that the Tpe values not only depend on the preceding RR value, but on a history of RR values. Thus, ventricular repolarization presents a memory lag dependency on RR that should be compensated for to estimate $\Delta\alpha^{\mathrm{Tpe}}$ [196]. To overcome this limitation, an approach was recently proposed [130, 197] to model the dependence of the Tpe interval on a history of previous RR intervals, and, then, to compensate for the Tpe memory lag. The model shown in Fig. 2.1 was used to characterize the Tpe dependence on RR [130,197]. The input $\mathbf{x}_{\mathrm{RR}} = [x_{\mathrm{RR}}(1), \cdots, x_{\mathrm{RR}}(N)]$ and output $\mathbf{y}_{\mathrm{Tpe}} = [y_{\mathrm{Tpe}}(1), \cdots, y_{\mathrm{Tpe}}(N)]$ denote the RR and Tpe series of each recording, where N is the length of the series.

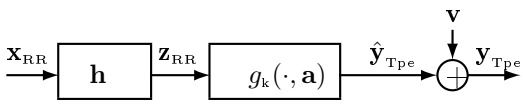

Figure 2.1: Block diagram describing the [RR,T_{pe}] relationship consisting of a time-invariant FIR filter (impulse response $\mathbf{h}$) and a nonlinear function $g_{\mathrm{k}}(\cdot, \mathbf{a})$. $\mathbf{v}$ accounts for the output estimation error. From [144].

The impulse response $\mathbf{h} = [h(1), \cdots, h(L)]^T$ includes information about the memory of the system, i.e. a characterization of the influence of a history of previous RR intervals on each Tpe measurement. Therefore, z_{RR}(n) represents a surrogate of x_{RR}(n) with the memory effect of Tpe compensated for. The length L of vector $\mathbf{h}$ was set to 300 samples, which widely exceeds the Tpe and QT memory lag for the data population used in this study [196]. In vector notation, $\mathbf{z}_{\mathrm{RR}}$ is the convolution between the input vector $\mathbf{x}_{\mathrm{RR}}$ and the impulse response $\mathbf{h}$. The function $g_{\mathrm{k}}(\cdot, \mathbf{a})$ represents the relationship between the RR interval and the Tpe interval at steady-state conditions. This function has been evaluated by using both bi- and tri-parametric equations:

- Regression fitting with biparametric equations: Ten different biparametric regression models were considered for $g_{\mathrm{k}}(\cdot, \mathbf{a})$, where $\mathbf{a} = [a_0, a_1]^T$ in this case, and the one that best fits the data of each subject was identified [130].

$$\text{Linear: } \hat{\mathbf{y}}_{\text{Tpe}} = a_0 + a_1\mathbf{z}_{\text{RR}}$$
$$\text{Hyperbolic: } \hat{\mathbf{y}}_{\text{Tpe}} = a_0 + \frac{a_1}{\mathbf{z}_{\text{RR}}}$$
$$\text{Parabolic: } \hat{\mathbf{y}}_{\text{Tpe}} = a_0(\mathbf{z}_{\text{RR}})^{a_1}$$
$$\text{Logarithmic: } \hat{\mathbf{y}}_{\text{Tpe}} = a_0 + a_1\ln(\mathbf{z}_{\text{RR}})$$
$$\text{Inverse logarithmic: } \hat{\mathbf{y}}_{\text{Tpe}} = \ln(a_0 + a_1\mathbf{z}_{\text{RR}})$$
$$\text{Exponential: } \hat{\mathbf{y}}_{\text{Tpe}} = a_0 + a_1.e^{-\mathbf{z}_{\text{RR}}}$$
$$\text{Arctangent: } \hat{\mathbf{y}}_{\text{Tpe}} = a_0 + a_1\text{arctag}(\mathbf{z}_{\text{RR}})$$
$$\text{Hyperbolic tangent: } \hat{\mathbf{y}}_{\text{Tpe}} = a_0 + a_1\text{tgh}(\mathbf{z}_{\text{RR}})$$
$$\text{Hyperbolic arcsine: } \hat{\mathbf{y}}_{\text{Tpe}} = a_0 + a_1\text{arcsinh}(\mathbf{z}_{\text{RR}})$$
$$\text{Hyperbolic arccosine: } \hat{\mathbf{y}}_{\text{Tpe}} = a_0 + a_1\text{arccosh}(\mathbf{z}_{\text{RR}}).$$

- Regression fitting with tri-parameter equation: we used a three-parameter equation, where, now, $\mathbf{a} = [a_0, a_1, \gamma^{\text{Tpe}}]^T$, and the third parameter accounts for the curvature of the Tpe/RR regression and acts as an extra level of fitting. Note that, in this case, k is, then, unique. Then, the data of each subjects were fitted with a non-linear regression function of the form [187]:

$$\hat{\mathbf{y}}_{\text{Tpe}} = a_0 + a_1(1 - \mathbf{z}_{\text{RR}}^{\gamma^{\text{Tpe}}}) \tag{2.5}$$

The estimated output $\widehat{y}_{T_{\text{pe}}}(\text{n})$ was defined as

$$\widehat{y}_{T_{\text{pe}}}(n) = g_{\text{k}}(z_{\text{RR}}(n), \mathbf{a}) \tag{2.6}$$

in which the optimum values of the FIR filter response $\mathbf{h}$, vector $\mathbf{a}$, and optimal function g_{k} (in the bi-parametric case) were searched for by minimizing the difference between the estimated output $\widehat{y}_{T_{\text{pe}}}(\text{n})$ and the system output $y_{T_{\text{pe}}}(\text{n})$, for each subject independently using the whole ECG recording [197]. In the three-parameter case, γ^{Tpe} was optimized such that the regression leaded to the lowest residual error by using the so-called "golden-cut" algorithm [187, 198]. The optimization algorithm seeks to minimize the following function:

$$J(\mathbf{h}, \mathbf{a}) = \|\mathbf{y}_{\text{Tpe}} - \widehat{\mathbf{y}}_{T_{\text{pe}}}\|^2 + \beta^2\|\mathbf{Dh}\|^2 \tag{2.7}$$

where $\mathbf{D}$ is a regularization matrix that penalizes the fact that $\mathbf{h}$ deviates from having an exponential decay [199] and β is the regularization parameter whose value was obtained by using the "L-curve" criterion [200]. With the computed value for β, the optimum values $\mathbf{h}$ and $\mathbf{a}$ in (2.7) were determined by using a "quasi-Newton" optimization technique described in [201], subject to two constraints: the sum of the $\mathbf{h}$ components is 1, to ensure normalized filter gain, and all the components of $\mathbf{h}$ are non-negative, to give a physiological plausible interpretation [197].

Finally, depending on the option chosen for the fitting equation (bi-parametric or tri-parametric), the estimate of dispersion of repolarization restitution derived in (2.4) can be replaced with the following equations:

$$\Delta\alpha = \alpha_1 - \alpha_2 = \frac{\partial APD_1}{\partial RR} - \frac{\partial APD_2}{\partial RR} \approx \Delta\alpha^{\mathrm{Tpe}} = \left.\frac{\partial g_{\mathrm{k}}(z_{\mathrm{RR}}, [a_0, a_1]^T)}{\partial z_{\mathrm{RR}}}\right|_{z_{\mathrm{RR}}=\overline{z_{\mathrm{RR}}}}, \tag{2.8}$$

$$\approx \Delta^{\mathrm{Tpe}}_{|z_{\mathrm{RR}}=\overline{z_{\mathrm{RR}}} \text{ or } 1\text{ s}} = \left. -a_1\gamma^{\mathrm{Tpe}} z_{\mathrm{RR}}^{\gamma^{\mathrm{Tpe}}-1}\right|_{z_{\mathrm{RR}}=\overline{z_{\mathrm{RR}}} \text{or } 1\text{s}} \tag{2.9}$$

when using the bi-parametric option [130] and evaluating the derivative at the mean z_{RR} value, $\overline{z_{\mathrm{RR}}}$, of the recording, or when using the tri-parametric option [187] and additionally evaluating the derivative at RR = 1 s. Then, $\Delta\alpha^{\mathrm{Tpe}}$, $\Delta^{\mathrm{Tpe}}_{|z_{\mathrm{RR}}=\overline{z_{\mathrm{RR}}}}$ and $\Delta^{\mathrm{Tpe}}_{|z_{\mathrm{RR}}=1}$ are three different estimations of the same concept, i.e. dispersion of repolarization restitution. The only difference lies on the regression equation used for their calculation and the point at which the slope is evaluated.

2.2.4 Repolarization Restitution from the QT Interval Dynamics

A similar analysis can be done to estimate the slope of the QT interval dynamics:

$$\alpha_1 = \frac{\partial APD_1}{\partial RR} \approx \Delta\alpha^{\mathrm{QT}} = \left.\frac{\partial g_{\mathrm{k}}(z_{\mathrm{RR}}, [a_0, a_1]^T)}{\partial z_{\mathrm{RR}}}\right|_{z_{\mathrm{RR}}=\overline{z_{\mathrm{RR}}}}, \tag{2.10}$$

$$\approx \Delta^{\mathrm{QT}}_{|z_{\mathrm{RR}}=\overline{z_{\mathrm{RR}}} \text{ or } 1\text{ s}} = \left. -a_1\gamma^{\mathrm{QT}} z_{\mathrm{RR}}^{\gamma^{\mathrm{QT}}-1}\right|_{z_{\mathrm{RR}}=\overline{z_{\mathrm{RR}}} \text{or } 1\text{s}}, \tag{2.11}$$

where now $\mathbf{h}$, $\mathbf{a}$, and the optimal function g_{k} in the bi-parametric case are calculated using the QT series. Again, $\Delta\alpha^{\mathrm{QT}}$, $\Delta^{\mathrm{QT}}_{|z_{\mathrm{RR}}=\overline{z_{\mathrm{RR}}}}$ and $\Delta^{\mathrm{QT}}_{|z_{\mathrm{RR}}=1}$ are three different estimations of the same concept, i.e. repolarization restitution slope, where their only difference is the regression equation used for their calculation and the point at which they are evaluated.

Figure 2.2 illustrates the regression of the QT/RR relationship, where the lineal and curved regression equations are plotted in green and red, respectively.

2.2.5 Circadian Modulation

Following previous results reporting day and night differences in repolarization dynamics in healthy subjects [188–190], and associated with increased arrhythmic risk [191, 192], we evaluated the circadian modulation of the eight parameters proposed in this chapter in 24-h hour Holter recordings from CHF patients. For the characterization of the circadian modulation of these parameters, we divided the 24-h ECG recordings into 6-hour segments ("00-06h";"06-12h";"12-18h";"18-24h"). Then, in each 6-hour segment, we derived $\Delta\alpha^{\mathrm{QT}}$, $\Delta^{\mathrm{QT}}_{|z_{\mathrm{RR}}=\overline{z_{\mathrm{RR}}}}$, $\Delta^{\mathrm{QT}}_{|z_{\mathrm{RR}}=1}$, γ^{QT}, $\Delta\alpha^{\mathrm{Tpe}}$, $\Delta^{\mathrm{Tpe}}_{|z_{\mathrm{RR}}=\overline{z_{\mathrm{RR}}}}$, $\Delta^{\mathrm{Tpe}}_{|z_{\mathrm{RR}}=1}$ and γ^{Tpe}, following the methodology described in the previous section.

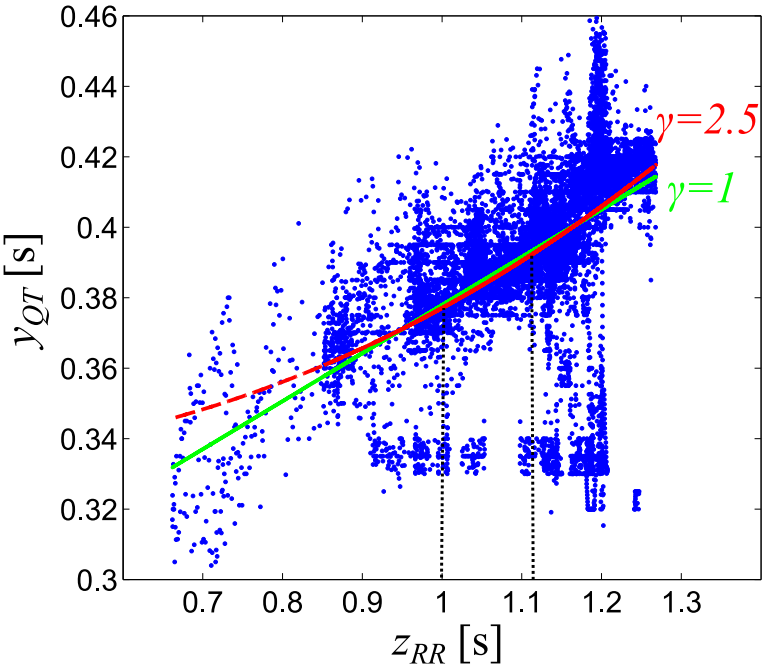

Figure 2.2: QT/RR regression pattern. Green line shows the linear regression equation ($\gamma = 1$), and red line shows equation (2.5), with $\gamma = 2.5$. Vertical lines indicate both points of evaluation of the slope, at $\mathbf{z}_{\mathrm{RR}} = \overline{\mathbf{z}}_{\mathrm{RR}}$, and at $\mathbf{z}_{\mathrm{RR}} = 1$.

2.2.6 T-wave Alternans and Heart Rate Turbulence Indices

As explained in section 1.4.5, TWA reflect dispersion of repolarization [147–149], and the HRT indicate the short- and long-term responses of the heart rate to a VPB [174, 175]. These indices reflect different electrophysiological and autonomic mechanisms and, thus, we hypothesized that their combination with the index with highest predictive value among those proposed in this chapter would improve SCD and PFD classification.

The *index of average alternans (IAA)*, an index reflecting the average TWA activity during a 24-h period, was computed by automatic ECG analysis [156]. The analysis was performed on every ECG recording in 3 steps: (a) selection of signal segments (of 128 beats with a 50% overlap between adjacent segments) that were suitable for automatic analysis, (b) estimation of TWA amplitude in those segments with a multi-lead scheme that combines periodic component analysis with the Laplacian likelihood ratio method, and (c) computation of the average of all segments' TWA amplitudes [156].

TS, a parameter measuring the turbulence slope of HRT, was calculated as in [176], considering patients having at least 1 VPB during the 24-h ECG recording. Details

on TS calculation can be found in [176].

2.2.7 Statistical Analysis

The Spearman's correlation coefficient was used to quantify the strength of the linear correlation. A p-value <0.05 was considered as statistically significant. Data were analysed by using version 22.0 of SPSS software. When plotting boxplots, the central mark is the median, the edges of the box are the 25th and 75th percentiles, and the whiskers extend to the most extreme data points not considered as outliers. The notches represent the 95% confidence interval of the median, calculated as $q2 \pm 1.57(q3-q1)/\sqrt{n}$, where $q2$ is the median, $q1$ and $q3$ are the 25th and 75th percentiles, respectively, and n is the number of subjects. Therefore, if the sample is small, the notches might extent beyond the end of the box in some cases. Computations were executed using Matlab 7.10.0 (2010a), Intel Core i7-2600 CPU, 3.40GHz, 8.00 GB RAM.

Quantitative Statistical Differences between Populations

Two-tailed *Mann-Whitney U test* and *Fisher exact tests* were used for univariate comparison of quantitative and categorical data, respectively. Although the *Student's t-test* is the standard test to determine if the means of two populations are equal, assuming equal variance, it should only be applied when the test statistic follows a normal distribution. When this condition does not hold, an alternative test is the Mann-Whitney U test. This test assesses, instead, if the medians of two populations are equal. Then, it is a non-parametric test used to determine if it is equally likely that a randomly selected value from one sample will be less than or greater than a randomly selected value from a second sample. Unlike the Student's t-test, it does not require the assumption of normal distributions. However, it is nearly as efficient as the t-test on normal distributions [202]. When using multiple comparisons (as when evaluating the effect of the circadian modulation in different segments of the ECG recording) Mann-Whitney U signed rank paired test with Bonferroni correction was applied. The Fisher's exact test was used for categorical data that result from classifying objects in two different ways. It is used to examine the significance of the association (contingency) between the two kinds of classification [203].

Survival Analysis

Survival analysis is a collection of statistical procedures for data analysis, for which the outcome variable of interest is time until an event occurs. It is the study of time between entry into observation and a subsequent event. Common events studied are death, disease, relapse, and recovery. Most survival analyses consider a key analytical problem called *censoring*. It occurs when some information about individual survival time is available, but the exact survival time is unknown. Three reasons of censoring are: When a person does not experience the event before the study ends, when a

person is lost to follow-up during the study period, and when a person withdraws from the study because of an event different from the one under study, i.e. dies from a different mode of death. The *survival function* gives the probability that a person survives longer than some specified time t. In contrast, the *hazard function* gives the instantaneous potential per unit time for the event to occur, given the individual has survived up to time t. The *Hazard ratio (HAR)* is akin to relative risk. It is an estimate of the ratio of the hazard function in the two risk groups [204].

Clinical trials commonly record the length of time from study entry to an endpoint for two different risk groups. These data are commonly depicted with a *Kaplan-Meier curve*. A plot of the Kaplan-Meier estimate of the survival function is a series of horizontal steps of declining magnitude which, when a large enough sample is taken, approaches the true survival function for that population. The opposite holds for the hazard function. The value of the survival function between successive distinct sampled observations is assumed to be constant. An important advantage of the Kaplan-Meier curve is that the method can take into account some types of censored data. On the plot, small vertical tick-marks indicate losses, where a patient's survival time has been censored [205].

The *Cox proportional hazards model* is a regression method for survival data. It provides an estimate of the HAR and its *confidence interval (CI)*. There are two assumptions about the Cox proportional hazard model: the HARs of two people are independent of time, and are valid only for time-independent covariates. This means that the hazard functions for any two individuals at any point in time are proportional. In other words, if an individual has a risk of death at some initial point in time that is twice as high as that of another individual, then at all later times the risk of death remains twice as high [206]. The *log-rank test* calculates a test statistic for testing a null hypothesis that the survival curves are the same for all groups, in other words, to test a null hypothesis where there is no difference between the populations in the probability of an event at any time point. For each time point the observed number of deaths in each group and the number expected if there has been no difference, are calculated. The number of expected is calculated as the proportion of subjects who are at risk at a given time point multiplied by the total number of events at that point. The log-rank test is based on the same assumptions as the HAR that the survival probabilities are the same for subjects early and late in the study, and the events happen at the time specified [204, 207].

Hazard probability was estimated in this thesis by using Kaplan-Meier methods with a comparison of cumulative events by using log-rank tests. The association of measurements with SCD or PFD endpoints was determined by univariate and multivariate Cox proportional hazard analyses. Patients who died from causes other than SCD or PFD, respectively, were censored at the time of death.

Classification

The *receiver operating characteristic (ROC)* curves were used to identify the optimal cut-off points. A ROC is a graphical plot which illustrates the performance of

a binary classifier system as its discrimination threshold is varied. It is created by plotting the fraction of true positives out of the positives (sensitivity) vs. the fraction of false positives out of the negatives (1-specificity), at various threshold settings [208]. If a classifier system is optimal at some threshold, its associated ROC curve would approach to the upper left corner (as a logarithmic function), pointing at the maximized sensitivity and specificity. If, on the contrary, there is no threshold optimizing the classification, its ROC curve would follow a diagonal line. Then, the *area under the ROC curve (AUC)* provides information about the separation of the ROC curve from the diagonal, indicating the potential classification ability of the system. Minimal Euclidean distance from the ROC curve to the upper-left corner was applied to select the threshold, with an AUC >0.55 required for setting the classification cut-off point.

A classifier was implemented based on a two- and three-class *support vector machine (SVM)* in the form of *C*-support vector classification [209]. The SVM classifier was optimized by quadratic programming [201] and the selected kernel for the proximity mapping was the inhomogeneous first order polynomial mapping [210]. Other more complex kernels were tested, but they increased complexity without improving the discriminative power of the SVM. We used the *prtools* toolbox [211] from Matlab to train and test the SVM models.

To train the SVM models, 5-fold cross validation was performed [212]. *C*-SVM classification adds a penalty parameter, C, in the optimization. Increasing C makes the optimization to attempt a stricter separation beteen modes of CD. Equivalently, reducing C towards 0 produces a smoother decision boundary at the expense of increasing the probability of misclassifying a patient (that would be treated as an outlier). The decision boundary of the SVM classifier was configures in two ways. The first configuration set a high value of C, defined as $C_1 = \left(1 - \left|\frac{(Lp-Lm)}{(Lp+Lm)}\right|\right)$, where C_1 represents the theoretical maximum of C that guarantees convergence of the optimization and Lp (Lm) is the number of positive (negative) samples [211]. The value of C used for the second configuration (C_2) (theoretical minimum value of C that guarantees convergence) was estimated by the "leave-one-out" error of the "1-Nearest Neighbour" rule [213]. In order to perform three-class classification, three two-class classifiers between each of the three classes (SCD, PFD, others) and the remaining two classes were computed. Each two-class classifier returned a score for each observation that could be interpreted as the probability of belonging to each class. Then, the final output class was chosen as the one associated with maximum score over the two-class classifiers [209].

The performance of the classifier was evaluated in terms of Se, Sp and the Cohen's Kappa coefficient (κ) from a confusion matrix. κ measures pairwise agreement between the expected and the true modes of CD, correcting for expected chance agreement. When there is no greater agreement than that which would be expected by chance, κ is zero. When there is total agreement, κ is one [214]. To calculate Se and Sp for each mode of death, that particular mode of death was defined as a positive event and all other modes of death as well as survival outcome were defined as a negative event. The final values of Se, Sp and κ were calculated as the mean of each individual

measurement of the cross-validation.

2.3 Results

2.3.1 Clinical Characteristics and Cardiac Events of the Study Population

The study population consisted of the total 651 CHF patients with sinus rhythm (462 men, 188 women) aged 18 to 89 years (mean 63 $\pm$ 12 years). The majority of patients (82%) were in heart failure NYHA class II, while the remaining 18% were in NYHA class III. LVEF ranged from 10% to 70% with a mean of 37% $\pm$ 14%. The detailed characteristics of the study population are shown in Table 2.1. No medications were withdrawn during Holter monitoring in any of the patients. Table 2.2 summarizes the number of cardiac deaths in the study population during the follow-up period.

Endpoint	Overall population (n = 651)	$\Delta\alpha^{\mathrm{Tpe}} \leqslant 0.022$ (n = 285)	$0.022 < \Delta\alpha^{\mathrm{Tpe}} < 0.028$ (n = 59)	$\Delta\alpha^{\mathrm{Tpe}} \geqslant 0.028$ (n = 307)	p-value
CD	122 (18.7%)	56 (19.6%)	4 (6.8%)	62 (20.2%)	**0.047**
SCD	55 (8.4%)	15 (5.3%)	2 (3.4%)	38 (12.4%)	**0.003**
PFD	67 (10.3%)	41 (14.4%)	2 (3.4%)	24 (7.8%)	**0.006**

Data are presented as absolute frequencies and percentages. CD = cardiac death; PFD = pump failure death; SCD = sudden cardiac death; Significant differences are indicated in bold.

Table 2.2: Cardiac events during follow-up in the overall population and in each of the three groups defined by $\Delta\alpha^{\mathrm{Tpe}}$.

2.3.2 Association of Repolarization Restitution Estimates with Clinical Data

The histograms of $\Delta\alpha$ (a), $\Delta_{|z_{\mathrm{RR}}=\overline{z_{\mathrm{RR}}}}$ (b), $\Delta_{|z_{\mathrm{RR}}=1}$ (c) and γ (d) for QT/RR (green) and Tpe/RR (blue) regression patterns, and their 25th, 50th and 75th percentiles are shown in Figure 2.3. The histograms were calculated using 50 equally spaced bins.

Table 2.3 shows the correlation coefficients between the parameters under study and the median RR and the range of RR. No correlation was found between γ^{QT} and $\Delta^{\mathrm{QT}}_{|z_{\mathrm{RR}}=1}$ and median RR. The markers $\Delta\alpha^{\mathrm{QT}}$ and $\Delta^{\mathrm{QT}}_{|z_{\mathrm{RR}}=\overline{z_{\mathrm{RR}}}}$, on the contrary, showed a weak significant correlation with median RR. Although no correlation was found between γ^{QT}, $\Delta^{\mathrm{QT}}_{|z_{\mathrm{RR}}=1}$ or $\Delta^{\mathrm{QT}}_{|z_{\mathrm{RR}}=\overline{z_{\mathrm{RR}}}}$ and RR range, $\Delta\alpha^{\mathrm{QT}}$ did show a significant correlation. Regarding the Tpe/RR relationship, no correlation was found between γ^{Tpe}, $\Delta\alpha^{\mathrm{Tpe}}$ and $\Delta^{\mathrm{Tpe}}_{|z_{\mathrm{RR}}=\overline{z_{\mathrm{RR}}}}$ and median RR. The index $\Delta^{\mathrm{Tpe}}_{|z_{\mathrm{RR}}=1}$, on the contrary, showed a weak significant correlation with median RR. No correlation was found between γ^{Tpe}, $\Delta^{\mathrm{Tpe}}_{|z_{\mathrm{RR}}=1}$, $\Delta\alpha^{\mathrm{Tpe}}$ or $\Delta^{\mathrm{Tpe}}_{|z_{\mathrm{RR}}=\overline{z_{\mathrm{RR}}}}$ with RR range (Table 2.3). A significant weak correlation was found between $\Delta\alpha^{\mathrm{Tpe}}$ and $\Delta\alpha^{\mathrm{QT}}$ (ρ=0.293, p<0.001).

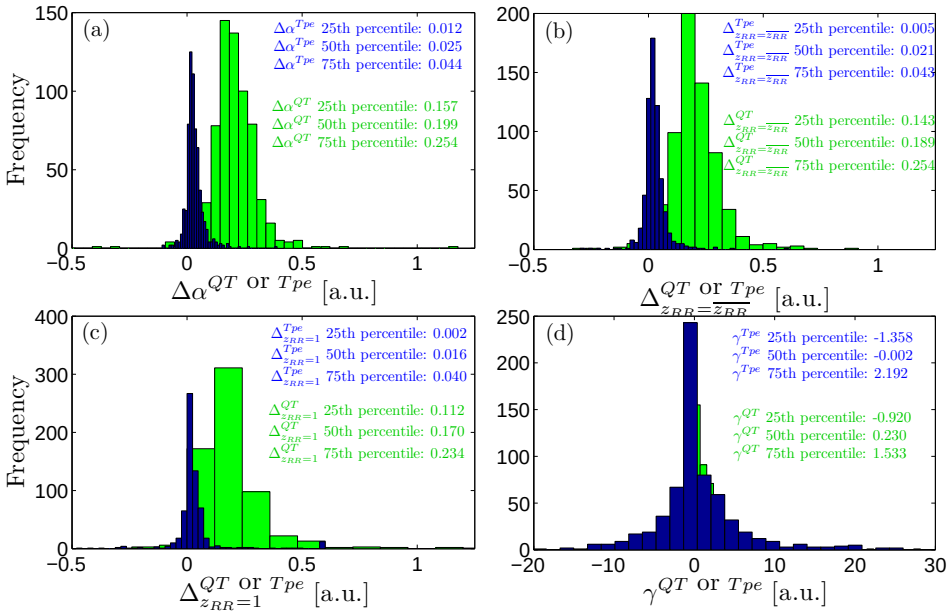

Figure 2.3: Histogram of $\Delta\alpha$ (a), $\Delta_{|z_{\mathrm{RR}}=\overline{z_{\mathrm{RR}}}}$ (b), $\Delta_{|z_{\mathrm{RR}}=1}$ (c) and γ (d) for QT/RR (green) and Tpe/RR (blue) regression patterns using 50 equally spaced bins.

Variable	Median RR		RR range	
	ρ	p	ρ	p
γ^{QT}	-0.042	0.290	0.039	0.327
$\Delta^{\mathrm{QT}}_{\lvert z_{\mathrm{RR}}=1}$	0.016	0.683	-0.025	0.526
$\Delta^{\mathrm{QT}}_{\lvert z_{\mathrm{RR}}=\overline{z_{\mathrm{RR}}}}$	0.325	**<0.001**	0.026	0.518
$\Delta\alpha^{\mathrm{QT}}$	-0.428	**<0.001**	-0.290	**<0.001**
γ^{Tpe}	-0.044	0.267	0.064	0.105
$\Delta^{\mathrm{Tpe}}_{\lvert z_{\mathrm{RR}}=1}$	-0.104	**0.008**	-0.021	0.595
$\Delta^{\mathrm{Tpe}}_{\lvert z_{\mathrm{RR}}=\overline{z_{\mathrm{RR}}}}$	0.015	0.713	-0.018	0.646
$\Delta\alpha^{\mathrm{Tpe}}$	-0.023	0.560	-0.029	0.467

Significant differences are indicated in bold.

Table 2.3: Correlation of γ^{QT}, $\Delta^{\mathrm{QT}}_{|z_{\mathrm{RR}}=1}$, $\Delta^{\mathrm{QT}}_{|z_{\mathrm{RR}}=\overline{z_{\mathrm{RR}}}}$, γ^{Tpe}, $\Delta^{\mathrm{Tpe}}_{|z_{\mathrm{RR}}=1}$, and $\Delta^{\mathrm{Tpe}}_{|z_{\mathrm{RR}}=\overline{z_{\mathrm{RR}}}}$ with median RR and RR range.

Mann-Whitney U-test showed that there were no significant differences in the median values of the QT/RR and Tpe/RR parameters between women and men. No significant differences in the median values of the slope of the Tpe dynamics were found between LVEF$\leqslant$35% and LVEF>35% groups or between NYHA classes II and III. However, significant differences in $\Delta\alpha^{\mathrm{QT}}$ were found between LVEF$\leqslant$35% and LVEF>35% groups ($p<0.001$), and between NYHA classes II and III ($p=0.028$).

2.3.3 Circadian Modulation

Figure 2.4 shows the circadian modulation of the eight parameters defining the dynamics of the QT (top) and Tpe (bottom) intervals. As shown, the slope of the QT/RR relationship was significantly higher during day than at night when quantified using $\Delta\alpha^{\mathrm{QT}}$ (a) and $\Delta^{\mathrm{QT}}_{|z_{\mathrm{RR}}=\overline{z_{\mathrm{RR}}}}$ (b). The curvature and $\Delta^{\mathrm{QT}}_{|z_{\mathrm{RR}}=1}$, however, were not significantly modulated by the circadian pattern (c) and (d). Regarding the Tpe dynamics, the slope, quantified as $\Delta\alpha^{\mathrm{Tpe}}$ and as $\Delta^{\mathrm{Tpe}}_{|z_{\mathrm{RR}}=\overline{z_{\mathrm{RR}}}}$, was significantly higher during evening, as compared to night (e) and (f). $\Delta\alpha^{\mathrm{Tpe}}_{|z_{\mathrm{RR}}=1}$ was not significantly modulated by the circadian pattern (g). The curvature of this regression showed to be significantly higher during early morning, as compared to night, and during evening, as compared to afternoon (h).

Table 2.4 shows the median (interquartile range (IQR)) values of the curvature and slope parameters of the QT/RR and Tpe/RR regression patterns in the "00-06" and "12-18" segments, but distinguishing between women and men. As shown, only $\Delta\alpha^{\mathrm{QT}}$ in the night segment was significantly higher in women than in men.

	Women	Men	p-value
$\Delta\alpha^{\mathrm{QT}}$			
"00-06"	0.185 (0.10)	0.187 (0.11)	0.807
"12-18"	0.178 (0.12)	0.165 (0.09)	**0.029**
$\Delta^{\mathrm{QT}}_{\lvert z_{\mathrm{RR}}=\overline{z_{\mathrm{RR}}}}$			
"00-06"	0.178 (0.12)	0.175 (0.12)	0.718
"12-18"	0.150 (0.14)	0.146 (0.12)	0.710
$\Delta^{\mathrm{QT}}_{\lvert z_{\mathrm{RR}}=1}$			
"00-06"	0.133 (0.17)	0.148 (0.17)	0.536
"12-18"	0.130 (0.17)	0.146 (0.17)	0.154
γ^{QT}			
"00-06"	-0.116 (3.66)	-0.045 (3.68)	0.359
"12-18"	-0.097 (5.93)	-0.028 (4.77)	0.586
$\Delta\alpha^{\mathrm{Tpe}}$			
"00-06"	0.024 (0.04)	0.019 (0.04)	0.093
"12-18"	0.017 (0.05)	0.014 (0.03)	0.378
$\Delta^{\mathrm{Tpe}}_{\lvert z_{\mathrm{RR}}=\overline{z_{\mathrm{RR}}}}$			
"00-06"	0.018 (0.05)	0.018 (0.04)	0.902
"12-18"	0.015 (0.05)	0.016 (0.04)	0.637
$\Delta^{\mathrm{Tpe}}_{\lvert z_{\mathrm{RR}}=1}$			
"00-06"	0.014 (0.04)	0.012 (0.03)	0.794
"12-18"	0.006 (0.05)	0.012 (0.04)	0.228
γ^{Tpe}			
"00-06"	-0.004 (3.15)	-0.005 (2.05)	0.627
"12-18"	-0.007 (4.13)	-0.008 (2.48)	0.926

Significant differences are indicated in bold

Data are represented as median (IQR).

Table 2.4: Gender differences for day and night values of QT/RR and Tpe/RR curvature and slope.

2.3.4 Survival Analysis

Figure 2.5 shows the boxplots of the QT/RR and Tpe/RR parameters, IAA and TS, in the group of SCD victims, PFD victims and in the rest of patients. No statistical differences (illustrated with *) were found in median between SCD victims and in others, or in PFD victims and in others for any of the QT/RR regression parameters, γ^{QT}, $\Delta^{\mathrm{QT}}_{|z_{\mathrm{RR}}=1}$, $\Delta\alpha^{\mathrm{QT}}$ and $\Delta^{\mathrm{QT}}_{|z_{\mathrm{RR}}=\overline{z_{\mathrm{RR}}}}$. In addition, no statistical differences were found between the median value of γ^{Tpe} in SCD victims and in others, and in PFD victims and in others. However, we found that $\Delta\alpha^{\mathrm{Tpe}}$, $\Delta^{\mathrm{Tpe}}_{|z_{\mathrm{RR}}=1}$ and $\Delta^{\mathrm{Tpe}}_{|z_{\mathrm{RR}}=\overline{z_{\mathrm{RR}}}}$, were significantly higher in SCD victims and significantly lower in PFD victims, as compared, in each case, with the rest of patients (Figure 2.5). No significant differences were found in IAA values for any of the comparisons (Figure 2.5, panel (e)). In contrast, TS values were significantly lower in SCD and PFD victims as compared, in each case, with the rest of patients (Figure 2.5, panel (i)). Figure 2.6 shows the Tpe/RR regression pattern of a SCD victim (a) and of a survivor (b), whose slopes approximately coincide with the median values of each subgroup.

According to the AUCs, the three Tpe/RR slope parameters, $\Delta\alpha^{\mathrm{Tpe}}$, $\Delta^{\mathrm{Tpe}}_{|z_{\mathrm{RR}}=1}$ and $\Delta^{\mathrm{Tpe}}_{|z_{\mathrm{RR}}=\overline{z_{\mathrm{RR}}}}$, separated SCD victims from the rest of patients, and also PFD victims from the rest of patients (Figure 2.7). The optimal thresholds for $\Delta\alpha^{\mathrm{Tpe}}$ based on ROC curve analysis (closest point to the upper-left corner) were $\Delta\alpha^{\mathrm{Tpe}}$=0.028 for SCD and $\Delta\alpha^{\mathrm{Tpe}}$=0.022 for PFD (marked with red dots in figure 2.7). The cut-off points 0.023 and 0.005 showed to be optimal for SCD and PFD, respectively, for $\Delta^{\mathrm{Tpe}}_{|z_{\mathrm{RR}}=1}$. Finally, regarding $\Delta^{\mathrm{Tpe}}_{|z_{\mathrm{RR}}=\overline{z_{\mathrm{RR}}}}$, these thresholds were 0.030 and 0.021, respectively (Figure 2.7). Although $\Delta\alpha^{\mathrm{QT}}$ was not strictly significantly different in the group of SCD victims, it was borderline significant (AUC=0.54; 95% CI 0.46-0.62). Then, we also calculated its optimal threshold for further analysis. We found that its optimal cut-off point was $\Delta\alpha^{\mathrm{QT}}$=0.228. IAA was previously reported to be associated with SCD when dichotomized at 3.73μV [156]. Similarly, TS was previously proved to predict both SCD and PFD victims when dichotomized at 2.5 ms/RR [176]. Then, we used these thresholds in our analysis.

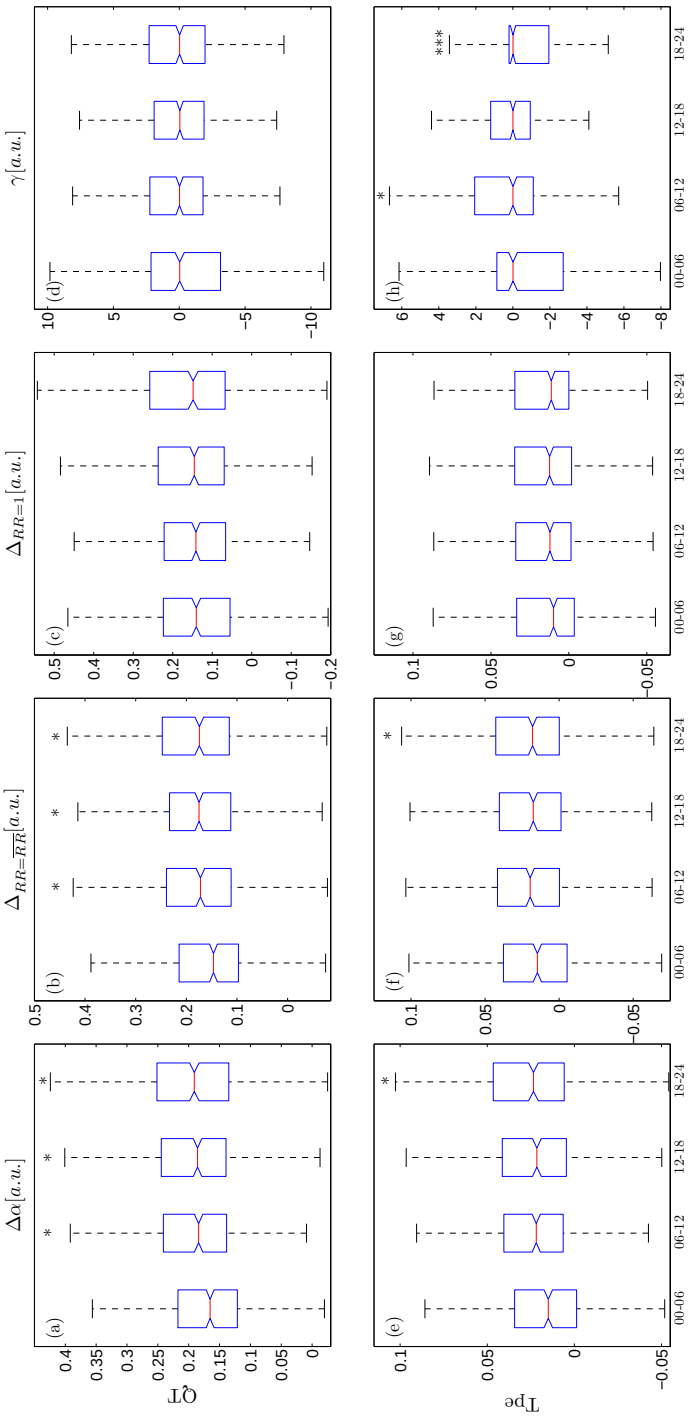

Figure 2.4: Circadian pattern of $\Delta\alpha^{\mathrm{QT}}$ (a), $\Delta^{\mathrm{QT}}_{|z_{\mathrm{RR}}=\overline{z_{\mathrm{RR}}}}$ (b), $\Delta^{\mathrm{QT}}_{|z_{\mathrm{RR}}=1}$ (c), γ^{QT} (d), $\Delta\alpha^{\mathrm{Tpe}}$ (e), $\Delta^{\mathrm{Tpe}}_{|z_{\mathrm{RR}}=\overline{z_{\mathrm{RR}}}}$ (f), $\Delta^{\mathrm{Tpe}}_{|z_{\mathrm{RR}}=1}$ (g), and γ^{Tpe} (h). * and *** indicate significant differences with respect to "00-06" and "06-12", respectively.

Figure 2.5: Boxplots of $\Delta\alpha^{\mathrm{QT}}$ (a), $\Delta^{\mathrm{QT}}_{|z_{\mathrm{RR}}=\overline{z_{\mathrm{RR}}}}$ (b), $\Delta^{\mathrm{QT}}_{|z_{\mathrm{RR}}=1}$ (c), γ^{QT} (d), IAA (e), $\Delta\alpha^{\mathrm{Tpe}}$ (f), $\Delta^{\mathrm{Tpe}}_{|z_{\mathrm{RR}}=\overline{z_{\mathrm{RR}}}}$ (g), $\Delta^{\mathrm{Tpe}}_{|z_{\mathrm{RR}}=1}$ (h), γ^{Tpe} (i) and TS (j) for SCD, PFD victims and survivors of CD. * Indicates statistical significance between each outcome and the group formed by the other two. The horizontal lines illustrate the optimal threshold for CD (dashed), SCD (dotted) and PFD (dot-dashed).

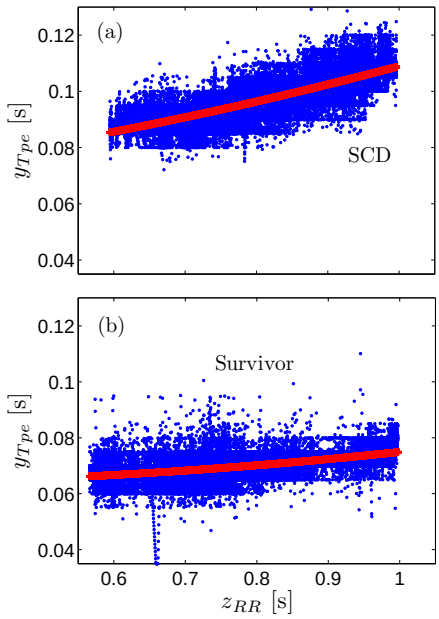

Figure 2.6: Tpe/RR regression pattern (blue) and the linear fitted regression (red) of a SCD victim (a) and of a survivor (b).

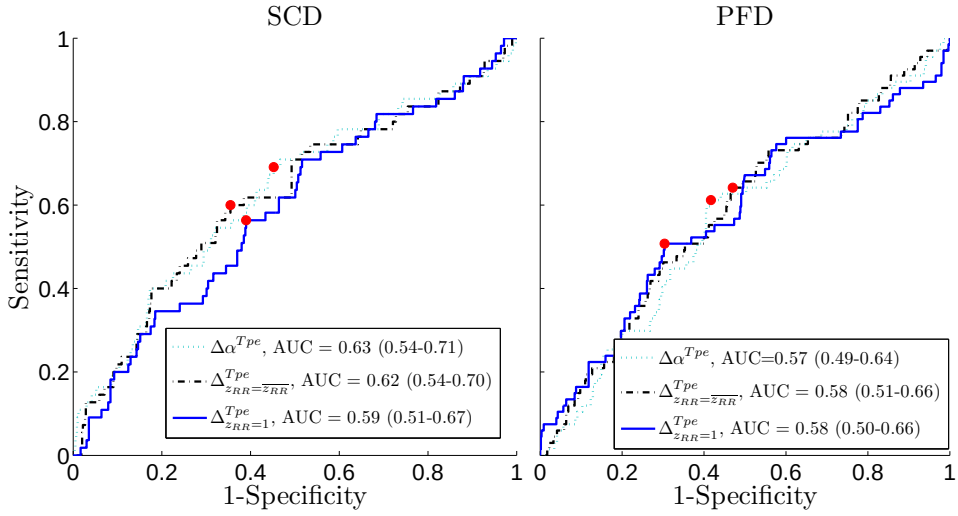

Figure 2.7: ROC curve for $\Delta^{\mathrm{Tpe}}_{|z_{\mathrm{RR}}=1}$ (solid blue), $\Delta^{\mathrm{Tpe}}_{|z_{\mathrm{RR}}=\overline{z_{\mathrm{RR}}}}$ (dashed-dotted black), and $\Delta\alpha^{\mathrm{Tpe}}$ (dotted cyan), in the classification of SCD and PFD victims. Red dots indicate the selected thresholds.

Table 2.1 shows the percentage of patients in the three groups defined by $\Delta\alpha^{\mathrm{Tpe}}$

with the categorical variables described in the first column. For continuous variables, data represents mean±standard deviation. Upon comparison of clinical variables, significant differences were found for age and gender between the three groups, showing that patients with $\Delta\alpha^{\mathrm{Tpe}} \leqslant 0.022$ were more frequently men, and younger than the rest of patients. No significant differences were found in any case for LVEF, NYHA class or any of the other covariates listed in Table 2.1.

Table 2.2 shows the percentage of patients in the three groups defined by $\Delta\alpha^{\mathrm{Tpe}}$ with the modes of death defined in the first column. As it can be observed, SCD was significantly higher in the $\Delta\alpha^{\mathrm{Tpe}} \geqslant 0.028$ group as compared to the two other groups, while PFD was significantly higher in the $\Delta\alpha^{\mathrm{Tpe}} \leqslant 0.022$ group as compared to the rest of patients. In the evaluation of gender differences, the population was divided into women and men groups. $\Delta\alpha^{\mathrm{Tpe}} \geqslant 0.028$, $\Delta^{\mathrm{Tpe}}_{|z_{\mathrm{RR}}=\overline{z_{\mathrm{RR}}}} \geqslant 0.030$ and $\Delta^{\mathrm{Tpe}}_{|z_{\mathrm{RR}}=1} \geqslant 0.023$ did not predict SCD in women. Regarding PFD, $\Delta\alpha^{\mathrm{Tpe}} \leqslant 0.022$, $\Delta^{\mathrm{Tpe}}_{|z_{\mathrm{RR}}=\overline{z_{\mathrm{RR}}}} \leqslant 0.021$ was also not predictive in women, but $\Delta^{\mathrm{Tpe}}_{|z_{\mathrm{RR}}=1} \leqslant 0.005$ remained predictive.

Table 2.5, first column, shows the univariate HAR and 95 % CI of the markers significantly associated with SCD (upper sub-table), and PFD (bottom sub-table). As it can be seen, the three Tpe/RR slope parameters were significantly associated with increased SCD risk, and with increased PFD risk when dichotomized with their respective thresholds, specific for each outcome (Table 2.5). The dichotomized parameter $\Delta\alpha^{\mathrm{QT}} \geqslant 0.228$ was also associated with significantly increased SCD risk in univariate Cox analysis.

Figure 2.8 shows Kaplan-Meier probabilities of SCD (top panels) and PFD (bottom panels) for the three risk groups defined by $\Delta\alpha^{\mathrm{Tpe}}$ (left panels), $\Delta^{\mathrm{Tpe}}_{|z_{\mathrm{RR}}=1}$ (middle panels) and $\Delta^{\mathrm{Tpe}}_{|z_{\mathrm{RR}}=\overline{z_{\mathrm{RR}}}}$ (right panels). The high SCD risk group is illustrated in dashed red, the high PFD risk group is plotted in dotted green, and group formed by the remaining patients, corresponding to the low CD risk group, is shown in solid blue. The p-value was calculated using the log-rank test. Patients with $\Delta\alpha^{\mathrm{Tpe}} \geqslant 0.028$ had an estimated 4-year SCD rate of 14% vs 6% in patients with $0.022 < \Delta\alpha^{\mathrm{Tpe}} < 0.028$ and vs 4% in patients with $\Delta\alpha^{\mathrm{Tpe}} \leqslant 0.022$. Patients with $\Delta\alpha^{\mathrm{Tpe}} \leqslant 0.022$ had an estimated 4-year survival rate from PFD of 15% vs 4% in patients with $0.022 < \Delta\alpha^{\mathrm{Tpe}} < 0.028$ and vs 10% in patients with $\Delta\alpha^{\mathrm{Tpe}} \geqslant 0.028$. Figure 2.9 shows the SCD probability curves for the high- (dashed red), and low-SCD (solid blue) risk groups defined by $\Delta\alpha^{\mathrm{QT}}$.

	Univariable		Multivariable	
	HAR (95% CI)	p-value	HAR (95% CI)	p-value
SCD				
Gender [men]	**2.14** (1.05-4.38)	**0.037**	**2.27** (1.06-4.85)	**0.035**
NYHA class III	**2.21** (1.23-3.95)	**0.008**	**1.95** (1.03-3.68)	**0.039**
LVEF$\leqslant$35%	**2.35** (1.30-4.25)	**0.005**	1.87 (0.98-3.55)	0.057
RR range [per 1 SD inc]	**0.75** (0.57-0.98)	**0.035**	0.97 (0.71-1.31)	0.826
NSVT and $>$ 240 VPBs in 24h	**2.08** (1.22-3.57)	**0.008**	1.25 (0.68-2.29)	0.468
IAA$\geqslant$3.7μV	**2.34** (1.32-4.13)	**0.004**	**2.14** (1.21-3.79)	**0.009**
TS$\leqslant$2.5 ms/RR	**2.64** (1.45-4.80)	**0.001**	**2.26** (1.23-4.17)	**0.009**
			Below variables added one at a time to the multivariate model	
$\Delta\alpha^{\mathrm{Tpe}} \geqslant 0.028$	**2.61** (1.47-4.62)	**0.001**	**2.92** (1.59-5.33)	**0.001**
$\Delta^{\mathrm{Tpe}}_{\lvert z_{\mathrm{RR}}=1} \geqslant 0.023$	**1.90** (1.12-3.24)	**0.018**	**2.26** (1.30-3.93)	**0.004**
$\Delta^{\mathrm{Tpe}}_{\lvert z_{\mathrm{RR}}=\overline{z_{\mathrm{RR}}}} \geqslant 0.030$	**2.60** (1.52-4.46)	**0.001**	**2.98** (1.71-5.20)	**$<$0.001**
$\Delta\alpha^{\mathrm{QT}} \geqslant 0.228$	**1.79** (1.06-3.04)	**0.031**	1.57 (0.88-2.80)	0.126
PFD				
Age [per 1 SD inc]	**1.46** (1.12-1.90)	**0.006**	1.18 (0.90-1.54)	0.231
NYHA class III	**2.55** (1.52-4.28)	**$<$0.001**	**2.47** (1.42-4.30)	**0.001**
LVEF$\leqslant$35%	**1.83** (1.10-3.04)	**0.021**	1.50 (0.85-2.67)	0.165
Diabetes	**1.85** (1.15-2.99)	**0.012**	1.66 (0.99-2.76)	0.053
Beta-blockers	**2.08** (1.28-3.36)	**0.003**	0.74 (0.43-1.25)	0.258
Amiodarone	**2.09** (1.09-3.98)	**0.026**	1.35 (0.63-2.90)	0.440
ARB or ACE inhibitors	**2.05** (1.12-3.76)	**0.020**	**0.36** (0.18-0.71)	**0.003**
RR range [per 1 SD inc]	**0.61** (0.47-0.78)	**$<$0.001**	0.81 (0.61-1.08)	0.145
NSVT and $>$ 240 VPBs in 24h	**2.15** (1.32-3.50)	**0.002**	1.54 (0.92-2.58)	0.103
TS$\leqslant$2.5 ms/RR	**4.98** (2.70-9.17)	**$<$0.001**	**4.51** (2.42-8.39)	**$<$0.001**
			Below variables added one at a time to the multivariate model	
$\Delta\alpha^{\mathrm{Tpe}} \leqslant 0.022$	**1.97** (1.21-3.22)	**0.007**	**2.11** (1.26-3.54)	**0.005**
$\Delta^{\mathrm{Tpe}}_{\lvert z_{\mathrm{RR}}=1} \leqslant 0.005$	**2.19** (1.36-3.54)	**0.001**	**2.03** (1.24-3.33)	**0.005**
$\Delta^{\mathrm{Tpe}}_{\lvert z_{\mathrm{RR}}=\overline{z_{\mathrm{RR}}}} \leqslant 0.021$	**1.83** (1.11-3.02)	**0.018**	**1.86** (1.10-3.15)	**0.020**

ACE=angiotensin-converting enzyme; ARB=angiotensin receptor blocker; CI= confidence interval; HAR=hazard ratio; IAA=index of average alternans; LVEF= left ventricular ejection fraction; NSVT=Non-sustained ventricular tachycardia; NYHA=New York Heart Association; SCD=sudden cardiac death; SD=standard deviation; TS=turbulence slope; VPB=Ventricular premature beat; Statistically significant values are marked in bold.

Table 2.5: Association of $\Delta\alpha^{\mathrm{Tpe}}$, $\Delta^{\mathrm{Tpe}}_{\lvert z_{\mathrm{RR}}=1}$, $\Delta^{\mathrm{Tpe}}_{\lvert z_{\mathrm{RR}}=\overline{z_{\mathrm{RR}}}}$, and $\Delta\alpha^{\mathrm{QT}}$ with SCD and PFD in univariate and multivariate Cox analysis.

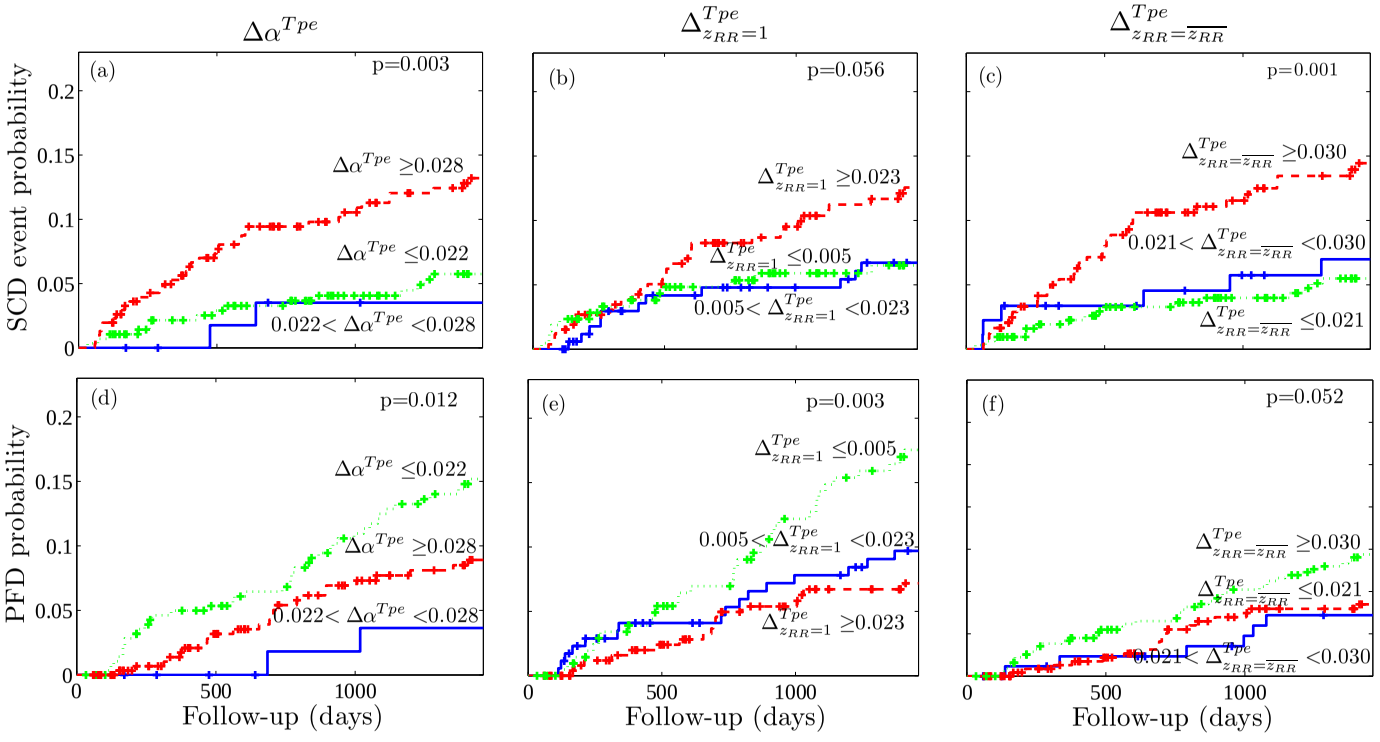

Figure 2.8: Probability curves of SCD (top) and PFD (bottom) for $\Delta\alpha^{\mathrm{Tpe}}$ (left), $\Delta^{\mathrm{Tpe}}_{|z_{\mathrm{RR}}=1}$ (middle) and $\Delta^{\mathrm{Tpe}}_{|z_{\mathrm{RR}}=\overline{z_{\mathrm{RR}}}}$ (right).

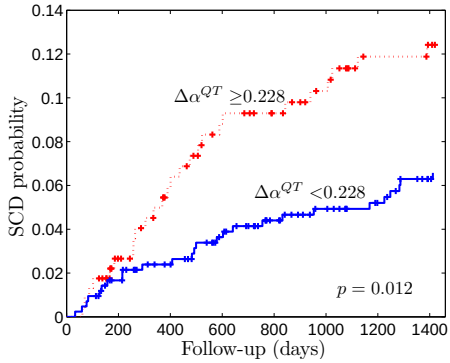

Figure 2.9: Probability curves of SCD for $\Delta\alpha^{\mathrm{QT}}$.

Multivariable Cox analysis was constructed by adjusting for the variables that were significantly associated with SCD or PFD in univariate analysis. Then, for SCD, multivariable Cox analysis was adjusted for gender, NYHA class, LVEF, range of RR and non-sustained ventricular tachycardia (NSVT) and more than 240 VPBs in 24 h. For PFD, the adjusted variables were age, NYHA class, LVEF, diabetes, beta-blockers, amiodarone, ARB or ACE inhibitors, range of RR, NSVT and more than 240 VPBs in 24 h (Table 2.5). The QT/RR and Tpe/RR dichotomized indices that were significantly associated with SCD or PFD in univariate analysis were included one at a time in the SCD multivariable model. Results showed that $\Delta\alpha^{\mathrm{Tpe}} \geqslant 0.028$, $\Delta^{\mathrm{Tpe}}_{|z_{\mathrm{RR}}=1} \geqslant 0.023$, and $\Delta^{\mathrm{Tpe}}_{|z_{\mathrm{RR}}=\overline{z_{\mathrm{RR}}}} \geqslant 0.030$, and $\Delta\alpha^{\mathrm{Tpe}} \leqslant 0.022$, $\Delta^{\mathrm{Tpe}}_{|z_{\mathrm{RR}}=1} \leqslant 0.005$, and $\Delta^{\mathrm{Tpe}}_{|z_{\mathrm{RR}}=\overline{z_{\mathrm{RR}}}} \leqslant 0.021$ remained significantly associated with increased SCD and PFD risk, respectively, after adjustment for significant clinical and other ECG-derived covariables (Table 2.5). In fact, $\Delta\alpha^{\mathrm{Tpe}} \geqslant 0.028$ and $\Delta^{\mathrm{Tpe}}_{|z_{\mathrm{RR}}=\overline{z_{\mathrm{RR}}}} \geqslant 0.030$ were the variables most strongly associated with SCD, while $\Delta\alpha^{\mathrm{Tpe}} \leqslant 0.022$ was the variable most significantly associated with PFD among the Tpe/RR slope parameters (Table 2.5). The dichotomized marker $\Delta\alpha^{\mathrm{QT}} \geqslant 0.228$, however, lost its significant association with increased SCD risk. Then, the time to SCD event was approximately doubled among patients with $\Delta^{\mathrm{Tpe}}_{|z_{\mathrm{RR}}=1} < 0.023$ in comparison to those with $\Delta^{\mathrm{Tpe}}_{|z_{\mathrm{RR}}=1} \geqslant 0.023$ and tripled among patients with $\Delta\alpha^{\mathrm{Tpe}} < 0.028$ or $\Delta^{\mathrm{Tpe}}_{|z_{\mathrm{RR}}=\overline{z_{\mathrm{RR}}}} < 0.030$ in comparison to those with $\Delta\alpha^{\mathrm{Tpe}} \geqslant 0.028$ or $\Delta^{\mathrm{Tpe}}_{|z_{\mathrm{RR}}=\overline{z_{\mathrm{RR}}}} \geqslant 0.030$ (Table 2.5). Similarly, the time to PFD event was approximately doubled in the low risk groups defined by the three indices of slope, as compared to the high risk groups (Table 2.5).

2.3.5 Classification

Based on the results showing that $\Delta\alpha^{\mathrm{Tpe}}$ was the index with highest joint SCD and PFD predictive value among those proposed in this chapter, we chose it for the classification study, in combination with IAA and TS.

Two-class Classification of Cardiac Death Mode Using one ECG Index

Using the individual dichotomized variables for classification of SCD vs. the rest of patients, IAA$\geqslant$3.73μV was the risk marker with maximum value of κ. For classification of PFD vs. the rest of patients, TS$\leqslant$2.5 ms/RR was the ECG index with maximum κ (Table 2.6).

	SCD			PFD		
	Se (%)	Sp (%)	κ	Se (%)	Sp (%)	κ
$\Delta\alpha^{\mathrm{Tpe}}$+	65.1	56.0	0.07	63.0	57.4	0.08
IAA+	40.7	77.4	0.10	75.6	24.1	0
TS+	67.1	54.7	0.07	79.0	56.6	0.14

$\Delta\alpha^{\mathrm{Tpe}}$+ represents $\Delta\alpha^{\mathrm{Tpe}} \geqslant$0.028 for SCD and $\Delta\alpha^{\mathrm{Tpe}} \leqslant$0.022 for PFD. IAA+ represents IAA$\geqslant$3.73 μV for SCD. TS+ represents TS$\leqslant$2.5 ms/RR for both SCD and PFD.

Table 2.6: Two-class classification performance for SCD vs the rest of patients and PFD vs. the rest of patients individually using $\Delta\alpha^{\mathrm{Tpe}}$, IAA and TS. The optimal risk marker for each mode of cardiac death is indicated in bold.

Two-class Classification of Cardiac Death Mode Using a Combination of ECG Indices

The study sub-population consisted of those 597 patients with computable values of IAA and TS (the other patients did not have any VPB, or segment suitable for TWA analysis). In this sub-population, during the 4-year follow up, 134 (22%) patients died. Of these, 111 (19% of the total sample) were CD victims and 23 (4%) non-CD victims. Among CD victims, 49 (8% of the total sample) were categorized as SCD and 62 (10%) as PFD.

Table 2.7 shows the Se, Sp and κ values for SCD and PFD classification using two-class SVMs. As indicated, the combination of $\Delta\alpha^{\mathrm{Tpe}}$ and IAA showed the maximum value of κ for both configurations (C_1 and C_2, respectively) of the SVM two-class classifier for separating SCD from the rest of patients.

Regarding the separation of PFD from the rest of patients, $\Delta\alpha^{\mathrm{Tpe}}$ and TS was the combination of risk markers with the maximum κ for the first configuration (C_1), while $\Delta\alpha^{\mathrm{Tpe}}$, TS and IAA was the preferred combination for the second configuration (Table 2.7). Then, since a classifier with higher Sp value is preferred, we selected $\Delta\alpha^{\mathrm{Tpe}}$ and TS as the optimal combination for separating PFD from the rest of patients.

Three-class Classification of Cardiac Death Mode Using a Combination of ECG Indices

Table 2.8 summarizes the performance of the two configurations of the SVM three-class classifier for separating SCD from PFD and from the rest of patients in the

Combination	Configuration	SCD			PFD		
		Se (%)	Sp (%)	κ	Se (%)	Sp (%)	κ
$\Delta\alpha^{Tpe}$ and TS	C_1	12.2	98.4	0.14	48.3	82.8	0.22
	C_2	28.0	81.0	0.03	42.6	73.5	0.07
$\Delta\alpha^{Tpe}$ and IAA	C_1	12.2	98.5	0.15	11.7	89.3	0
	C_2	52.7	71.3	0.10	57.8	48.2	0.02
TS and IAA	C_1	38.0	81.4	0.10	55.9	78.6	0.19
	C_2	73.1	45.0	0.05	50.5	71.1	0.08
$\Delta\alpha^{Tpe}$, IAA and TS	C_1	12.2	98.0	0.13	46.7	83.2	0.21
	C_2	52.9	69.5	0.09	74.2	53.6	0.11

Table 2.7: Two-class classification performance for SCD, PFD and others (non-cardiac death and survivors) using SVM. The optimal combination for each mode of cardiac death is indicated in bold.

overall population, in patients with LVEF$\leqslant$35% and in patients with LVEF>35%. The combination of risk markers with the highest κ when evaluating the overall population, the group formed by patients with LVEF$\leqslant$35%, and patients with LVEF>35% was TS and IAA, using the first configuration of the classifier. However, the combination of $\Delta\alpha^{Tpe}$, IAA and TS was the one with the highest κ using the second configuration of the classifier.

The performance of the three-class classifier using the optimal combination of risk markers for each configuration in the sub-populations defined by the NYHA class is shown in (Table 2.9).

2.4 Discussion

In this chapter, a fully automated method was presented to estimate repolarization restitution slope and its dispersion from the QT and Tpe intervals dynamics, respectively, in 24-hour ambulatory ECG recordings from 651 CHF patients. The main result is that the slope of the Tpe/RR regression pattern is able to identify three subpopulations of CHF patients, with steeper slopes indicating higher SCD risk, flatter slopes being associated with PFD risk and middle slopes suggesting low CD risk. For the best of our knowledge, no other single ECG-derived marker has shown independent capacity for such risk stratification. The restitution of total ventricular repolarization, however, estimated as the relationship between the QT interval and the underlying HR, was not associated with any mode of cardiac death. Additional results showed that the circadian pattern modulated the curvatures and slopes, with significantly higher values during the day than at night. Finally, the combination with other ECG risk markers, IAA and TS, to classify a population of CHF patients into SCD victims, PFD victims and others improved risk stratification.

Combination	Configuration	Sample population	SCD		PFD		κ
			Se (%)	Sp (%)	Se (%)	Sp (%)	
$\Delta\alpha^{\mathrm{Tpe}}$ and TS		Overall population	12.2	98.4	6.7	97.8	0.09
	C_1	LVEF>35%	6.7	98.8	20.0	95.9	0.16
		LVEF⩽35%	11.4	98.3	24.4	91.0	0.12
		Overall population	10.0	91.9	58.1	65.6	0.09
	C_2	LVEF>35%	0.0	92.9	45.0	69.3	0.05
		LVEF⩽35%	44.2	73.0	70.0	71.5	0.17
$\Delta\alpha^{\mathrm{Tpe}}$ and IAA		Overall population	6.2	98.5	3.3	98.1	0.04
	C_1	LVEF>35%	13.3	99.2	5.0	97.1	0.11
		LVEF⩽35%	11.4	98.0	4.7	99.3	0.10
		Overall population	50.7	72.2	6.7	86.9	0.02
	C_2	LVEF>35%	6.7	93.6	30.0	64.5	0.01
		LVEF⩽35%	45.0	74.7	22.8	77.6	0.04
TS and IAA		**Overall population**	20.0	89.4	24.9	88.8	0.15
	C_1	**LVEF>35%**	30.0	94.0	35.0	81.3	0.17
		LVEF⩽35%	18.6	84.6	16.9	91.0	0.13
		Overall population	46.7	66.7	38.1	76.6	0.10
	C_2	LVEF>35%	6.7	92.0	55.0	49.7	0.03
		LVEF⩽35%	69.3	49.2	15.0	92.1	0.12
$\Delta\alpha^{\mathrm{Tpe}}$, IAA and TS		Overall population	12.2	98.0	6.7	97.6	0.09
	C_1	LVEF>35%	0.0	99.6	20.0	94.3	0.11
		LVEF⩽35%	11.4	98.0	21.9	92.8	0.11
		Overall population	50.9	73.1	48.3	75.5	0.13
	C_2	**LVEF>35%**	10.0	95.6	50.0	64.9	0.08
		LVEF⩽35%	45.4	73.7	67.5	72.2	0.17

Table 2.8: Three-class classification performance for SCD, PFD and others (non-cardiac death and survivors) in the overall population, in patients with LVEF⩽35% and in patients with LVEF>35%. The optimal combination for each configuration (C_1 and C_2, see text) and mode of cardiac death is indicated in bold.

Combination	Sample population	SCD		PFD		κ
		Se (%)	Sp (%)	Se (%)	Sp (%)	
TS and IAA (C_1)	Overall population	20.0	89.4	24.9	88.8	0.15
	NYHA II	2.9	96.8	14.4	91.0	0.03
	NYHA III	36.7	96.8	32.0	89.1	0.30
$\Delta\alpha^{\mathrm{Tpe}}$, IAA and TS ($C_2$)	Overall population	50.9	73.1	48.3	75.5	0.13
	NYHA II	20.0	84.8	31.4	81.4	0.05
	NYHA III	36.7	85.7	24.0	71.3	0.09

Table 2.9: Three-class classification performance for SCD, PFD and others (non-cardiac death and survivors) in the overall population, in patients in NYHA class II and in patients in NYHA class III for the optimal combination for each configuration (C_1 and C_2, see text).

2.4.1 Dispersion of Repolarization Restitution Distinguishes Three Groups of Risk

Cox regression analysis and Kaplan-Meier cumulative survival analysis confirmed the ability of the slope of the Tpe/RR relationship to separate CHF patients in three risk sub-populations, with patients presenting steeper slopes being more prone to suffer from SCD, patients with flatter slopes being more likely to suffer from PFD, and patients with intermediate slope values being at low CD risk during follow-up. Upon confirmation by further investigations, such a differentiation could be of great clinical significance in the diagnosis and treatment of CHF patients.

Upon the comparison among the three Tpe/RR slope parameters, $\Delta\alpha^{\mathrm{Tpe}}$ was the Tpe/RR slope parameter most strongly associated with SCD and PFD risk, possibly because its calculation is less sensitive to outliers (see Figures 2.6 and 2.10). The fact that the index $\Delta\alpha^{\mathrm{Tpe}}$ remained significant after clinical and other ECG-derived variables, like IAA ot TS, indicates that this marker contains complementary information and, thus, its inclusion in a combined predictive model is recommended to help refining two SCD and PFD high-risk populations. The SCD and PFD predictive capacity of $\Delta\alpha^{\mathrm{Tpe}}$ cannot be attributed to HR-related differences, since the correlation analysis between $\Delta\alpha^{\mathrm{Tpe}}$ and median RR and RR range was not significant (Table 2.3).

If our initial hypothesis of $\Delta\alpha^{\mathrm{Tpe}}$ being related to increased dispersion of repolarization restitution is proven, our results associating elevated $\Delta\alpha^{\mathrm{Tpe}}$ with SCD would be in agreement with [54] and [53], where an increase in dispersion of repolarization restitution was associated with greater propensity to suffer from ventricular tachycardia/fibrillation. On the other hand, previous studies have reported a reduction in dispersion of repolarization restitution in end-stage failing hearts as compared to non-failing hearts for cycle lengths greater than 0.5 s [22] and greater than 1 s [215]. Again, under the hypothesis of $\Delta\alpha^{\mathrm{Tpe}}$ being to some extent related to dispersion of repolarization restitution, those reported differences could serve to support our observations linking lower values of $\Delta\alpha^{\mathrm{Tpe}}$ with PFD. Therefore, flatter Tpe/RR slopes may indicate a failure of the ventricle myocites response to changes in HR. However, further studies are needed to confirm the value of the Tpe/RR slope variable as SCD and PFD risk stratifier and to elucidate its underlying mechanisms.

2.4.2 Repolarization Restitution is not Associated with Mortality

Regarding the QT/RR relationship, we did not find any significant association between QT/RR curvatures or slopes and SCD or PFD, as opposed to previous results in other patient populations reporting association between QT/RR slopes and arrhythmic risk [130–133]. However, other study using the same population of this chapter reported that increased slopes of QT dynamics were associated with increased risk of total mortality but with no significant relation to SCD [216]. The correlation results indicated that the slope of the QT/RR regression pattern was highly correlated with the RR median, range of RR, NYHA class, LVEF and even $\Delta\alpha^{\mathrm{Tpe}}$, suggesting that

this index does not carry significant additional information to that already provided by these markers. It is not surprising, then, that this marker did not remain significant when adjusting for a multivariable model (Table 2.5).

Considering the initial hypothesis of this chapter where $\Delta\alpha^{QT}$ would reflect the slope of the APDR curve corresponding to the last cell to repolarize, our results confirm that is the spatial heterogeneity, i.e. dispersion, rather than the restitution of the total repolarization phase, which sets the vulnerability for malignant cardiac arrhythmia.

2.4.3 Risk-stratification Improves by Combining ECG Risk Markers

The combination of $\Delta\alpha^{Tpe}$ and IAA showed to be the one with the best performance in two-class SVM classification of SCD vs. the rest of patients, with a value of κ higher than that obtained when using the markers individually. This result confirmed the hypothesis that $\Delta\alpha^{Tpe}$ and IAA add complementary information and, consequently, their combination would improve the stratification of CHF patients at risk of SCD, with higher values of $\Delta\alpha^{Tpe}$ and IAA indicating higher propensity to suffer from a SCD event.

Regarding two-class classification of PFD vs. the rest of patients, TS$\leqslant$2.5 ms/RR was the dichotomized individual risk marker with the highest association with this mode of CD, presenting a value of κ higher than that of $\Delta\alpha^{Tpe}$ $\leqslant$0.022. When combining ECG indices, the combination of $\Delta\alpha^{Tpe}$, TS and IAA was the one with the highest κ coefficient for the second configuration of the classifier, but not improving the performance of TS individually, indicating that the classifying performance of the combined index was merely due to the power of TS. For the first configuration of the classifier, $\Delta\alpha^{Tpe}$ and TS showed a notably higher κ value than the individual TS marker. This is concordant with the fact that $\Delta\alpha^{Tpe}$ was also associated with PFD, although to a lesser extent than with SCD. This combination would, then, be recommended for PFD classification, with lower values of TS and $\Delta\alpha^{Tpe}$ indicating higher propensity to suffer from PFD outcome.

In the three-class classification of SCD, PFD and others (i.e. survivors and non-cardiac death victims), the combination of TS and IAA showed to be the one with the best performance for the first configuration of the classifier, while $\Delta\alpha^{Tpe}$, IAA and TS was the best one for the second configuration. Considering the higher Sp values in the identification of SCD and PFD for the first configuration of the classifier, the combination of TS and IAA would more robustly distinguish CHF patients at no risk of SCD or PFD. $\Delta\alpha^{Tpe}$, IAA and TS achieved higher Se (at the expense of lower Sp) in the second configuration of the classifier, indicating that $\Delta\alpha^{Tpe}$, IAA and TS would be capable of more powerfully identifying CHF patients at SCD or PFD risk.

To assess to which extent our results would vary when applied to populations of CHF patients with depressed or preserved LVEF or with different NYHA classes, we evaluated our SVM classifiers in these sub-populations. Normally, predicting CD risk

in patients with preserved LVEF (LVEF>35%) is a tricky task since LVEF⩽35% is a traditional indicator of cardiac risk [113]. Our classification results indicate that the combination of $\Delta\alpha^{\mathrm{Tpe}}$, IAA and TS in a three-class classifier is able to stratify CHF patients with preserved LVEF in SCD risk, PFD risk and low CD risk (Table 2.8). On the contrary, our results indicate that the classification of mode of CD in a population of patients in NYHA class III is easier than in patients in NYHA class II, which is not surprising considering that the CHF pathology is more advanced and, then, the symptoms indicating SCD or PFD risk may be enhanced (Table 2.9).

Our combination results indicate that improved risk stratification of CHF patients can be achieved based on the combination of ECG risk markers. The three markers investigated in the present study provide complementary information for identification of SCD and PFD. The index $\Delta\alpha^{\mathrm{Tpe}}$ and the index IAA are both indicative of processes related to ventricular repolarization and the two of them have shown strong association with SCD. Regarding IAA, autonomic neurotransmitters decompensation and changes in myocardial substrate can lead to elevated levels of TWA, serving as arrhythmogenic factors. Clinical studies have shown the value of high TWA magnitudes as a marker of increased risk for ventricular taquarrhythmias in CHF patients [150, 156]. Regarding TS, HRT is a recently recognized electrocardiographic phenomenon reflecting minute hemodynamic disturbance caused by a VPB. Lower TS (HRT slope) values would reflect a reduced baroreflex mediated response of the sinus node to this disturbance and thus poor regulation properties of the ANS. Several clinical studies have established that HRT is a strong and independent risk predictor of PFD and, to a lesser extent, SCD [217]. The results in this chapter are in line with the fact that abnormal repolarization patterns are more strongly related with arrhythmic risk while indices reflecting cardiac autonomic modulation are more likely to predict PFD and, thus, the combination of all of them would allow for improved separation of the two modes of cardiac death.

2.4.4 The Circadian Pattern Modulates Repolarization Restitution

We found that the QT/RR and Tpe/RR slopes were significantly higher during the day than at night (Figure 2.4). In the case of the dynamics of the Tpe interval, this modulation was only significant when quantifying with $\Delta\alpha^{\mathrm{Tpe}}$ and $\Delta^{\mathrm{Tpe}}_{|z_{\mathrm{RR}}=\overline{z_{\mathrm{RR}}}}$. These results may suggest that the evaluation of the slope at the average heart rate range [130,144] may be more capable of capturing the dynamics of ventricular repolarization restitution than when evaluating at $z_{\mathrm{RR}} = 1$s [187]. Our results are in agreement with previous studies suggesting that there is a higher incidence of cardiac arrhythmias and SCD in the morning hours [218].

2.4.5 Technical Considerations

The values of slopes showed higher inter-individual variability, with larger variability of $\Delta^{\mathrm{Tpe}}_{|z_{\mathrm{RR}}=1}$ as compared to $\Delta^{\mathrm{Tpe}}_{|z_{\mathrm{RR}}=\overline{z_{\mathrm{RR}}}}$ and $\Delta\alpha^{\mathrm{Tpe}}$. A possible reason for this

variability is presented in Figure 2.10, which shows an example of a Tpe/RR regression pattern with a very negative slope (PFD victim) (when evaluated at $z_{\mathrm{RR}} = 1$ s) (a) and with a very positive slope (survivor) (also when evaluated at $z_{\mathrm{RR}} = 1$ s) (b). Parameters from Eq. (2.5) have been optimized in order to minimize the residual error by fitting the Tpe and RR data. If there are no Tpe data in $z_{\mathrm{RR}} = 1$ s, Tpe values must be extrapolated for the analysis, thus, due to the curvature, producing higher absolute values of the slope when evaluated at $z_{\mathrm{RR}} = 1$ s than when evaluated at the averaged RR interval. Although evaluation of the slope at $z_{\mathrm{RR}} = 1$ s allows assessing this characteristic of the Tpe/RR patterns at the same heart rate for all patients, the recordings of many patients of this study did not contain RR values around 1 s, which led to substantial extrapolation of the $\Delta^{\mathrm{Tpe}}_{|z_{\mathrm{RR}}=1}$ measurements. This fact may also explain the differences in the circadian modulation between the evaluation of the Tpe dynamics at $z_{\mathrm{RR}} = \overline{z_{\mathrm{RR}}}$ or $z_{\mathrm{RR}} = 1$, as discussed before.

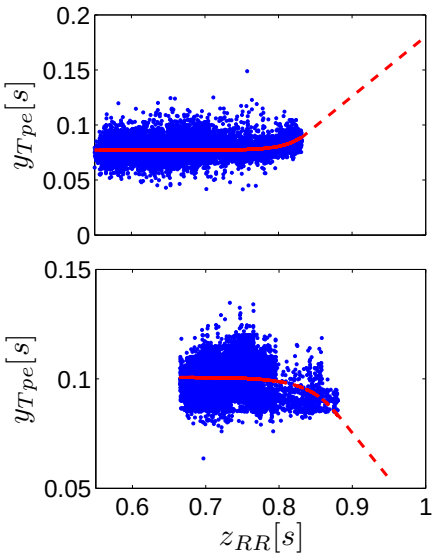

Figure 2.10: Tpe/RR regression pattern (blue) and the fitted regression curvature (red) with negative (a) and positive (b) slope.

2.4.6 Limitations

This study used fully automated ECG measurements that are likely to suffer imprecision, especially when applied to abnormal ECGs in CHF patients. A retrospective study of this kind may only be hypothesis generating. Prospective studies are needed to verify that the observations presented here have a role in SCD and PFD prediction in CHF patients. Both tachycardia and bradycardia cases were likely included. The definition of SCD and PFD used in this study was the same as in other similar studies

but might not be uniform in respect of the underlying pathophysiology. The number of SCD and PFD victims was relatively low not only in comparison with survivors but also with victims of other modes of death. This might have imposed some limitations on the statistical comparisons. Further investigations on the applicability of the defined cut-off point and on the extension of the analysis to other CHF and non-CHF populations are needed to confirm the prognostic value of the proposed index. Future studies may include the splitting of the data into training and test sets so that the thresholds developed in the training set could be evaluated in the test set. Also, further studies may aim at separately analysing patients with and without ventricular conduction defects to assess potential differences in their QT/RR and Tpe/RR regression patterns. Finally, the classification regularization parameters C_1 and C_2 were selected as two extreme cases, but intermediate values should have also been investigated.

2.5 Conclusions

In this chapter, we estimate ventricular repolarization restitution, and its dispersion, from the slope of the QT and Tpe interval dynamics. We demonstrate that steeper Tpe/RR slopes are indicative of an arrhythmogenic substrate predisposing to SCD and flatter slopes reflect mechanical heart fatigue leading to PFD. The information contained in these slopes was complementary to that from two indices quantifying TWA and HRT since their combination improved SCD and PFD risk stratification. Nevertheless, the slopes of the QT interval dynamics were not associated with higher risk of SCD or PFD. The curvature parameter helped fitting the QT/RR and Tpe/RR regressions but did not show predictive value. We also conclude that these parameters are modulated by the circadian pattern and, thus, the time of the day should be considered when using ECG recordings shorter than 24 hours. Our results suggest that the slope of the Tpe dynamics could be included in the clinical practice as an adjunct tool to stratify patients according to their risk of suffering SCD or PFD and, thus, improve the benefit from ICD or CRT treatment.

Chapter 3

A Novel Methodology to Quantify Morphological Differences between T-waves

3.1 Introduction

The T-wave reflects the spatio-temporal dispersion of repolarization of the ventricular myocytes [219]. The morphology of this wave depends on the repolarization sequence of the ventricle, as well as on the characteristics (morphology, APD, etc) of the APs of the ventricular myocytes. Thus, if any of the ionic exchanges during ventricular repolarization is not produced normally, it will be reflected on the morphology of the T-wave [220–222]. As demonstrated in the previous chapter, steeper slopes of the Tpe dynamics, reflecting enhanced spatio-temporal dispersion of repolarization restitution, are related to the generation of ventricular arrhythmias that could lead to SCD [223], while flatter slopes indicate mechanical heart fatigue predisposing to PFD. Then, the hypothesis of this chapter is that the information contained in the morphology of the T-wave may provide a stronger prediction than that obtained when using the Tpe interval only. Although there are T-wave morphology indices recently proposed in the literature, like the total cosine R-to-T descriptor, the morphology dispersion index or the T-wave residuum [224], they still lack sufficient superiority and they require the information provided by the VCG, which could also become a restriction in the clinical practice.

In addition, variations in the temporal domain, or misalignments between T-waves, might complicate the comparison and corrupt the measurement of variability. Linear and non-linear temporal re-parameterization (warping) techniques have been used to overcome this limitation, align ECG waves and measure amplitude differences with improved accuracy [225–227]. However, the warping information has never been used as a marker to assess the variability in the temporal domain.

The main objective of the study presented in this chapter is to propose and assess the ability of two ECG-derived markers, d_w, and d_a, and their non-linearly restricted versions, d_w^{NL} and d_a^{NL}, to quantify single-lead T-wave morphological variability. The variability between the temporal domains of different T-waves, or the amount of warping needed to remove the time domain variability, is measured by d_w, while d_a quantifies the amplitude variability after time warping, or the amplitude variability after removing the temporal domain variability. The markers d_w^{NL} and d_a^{NL} quantify the strictly non-linear warping and amplitude levels within d_w and d_a, respectively. First, we compared the performances of two warping algorithms, *Dynamic Time Warping (DTW)* and *Square-Root Slope Function (SRSF)* in removing time domain variability. Next, the robustness of d_w, d_a, d_w^{NL} and d_a^{NL} against noise in a simulated set up was evaluated and compared to that of d_x and d_y, two morphological variability markers already present in the literature [228, 229]. Then, an electrophysiological cardiac model was used to investigate the relation between d_w, d_a, d_w^{NL} and d_a^{NL} and the morphological changes of the APs at cellular level. Finally, the T-wave morphological variations produced by a tilt test in real ECG are quantified using d_w, d_a, d_w^{NL} and d_a^{NL}, and their correlation with the RR, the QT and Tpe intervals, and the T-wave width (TW) and T-wave amplitude (TA) is also studied.

3.2 Methods

3.2.1 Mathematical Framework

Time-warping Algorithms

To exemplify the process of T-wave morphology comparison, consider two T-waves, $\boldsymbol{f}^r(\boldsymbol{t}^r) = [f^r(t^r(1)), ..., f^r(t^r(N_r))]^\top$ and $\boldsymbol{f}^s(\boldsymbol{t}^s) = [f^s(t^s(1)), ..., f^s(t^s(N_s))]^\top$, where $\boldsymbol{t}^r = [t^r(1), ..., t^r(N_r)]^\top$, and $\boldsymbol{t}^s = [t^s(1), ..., t^s(N_s)]^\top$, and N_r and N_s are the total duration of $\boldsymbol{t}^r$ and $\boldsymbol{t}^s$, respectively, as illustrated in Figure 3.1(a). We take $\boldsymbol{f}^r(\boldsymbol{t}^r)$ as the reference T-wave and $\boldsymbol{f}^s(\boldsymbol{t}^s)$ as the T-wave to be compared with respect to $\boldsymbol{f}^r(\boldsymbol{t}^r)$.

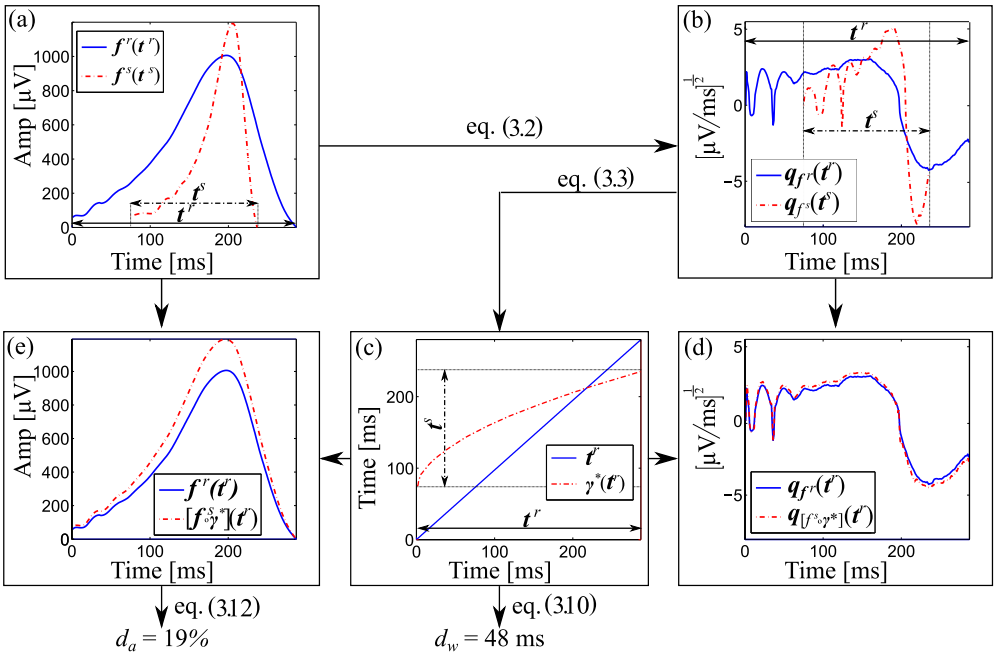

Figure 3.1: Diagram illustrating the computation of d_w and d_a. (a): Reference T-wave (solid blue) and a T-wave presenting both time and amplitude variability (shorter duration and larger amplitude) (dashed red). (b): Applying eq. (3.2) we obtain their respective square-root slope functions. (c): Optimizing eq. (3.3) with the DP algorithm, we get $\boldsymbol{\gamma}^*(\boldsymbol{t}^r)$, the warping function that optimally relates $\boldsymbol{t}^r$ and $\boldsymbol{t}^s$. (e): The re-parameterization of $\boldsymbol{f}^s(\boldsymbol{t}^s)$ using $\boldsymbol{\gamma}^*(\boldsymbol{t}^r)$ leads to $[\boldsymbol{f}^s \circ \boldsymbol{\gamma}^*](\boldsymbol{t}^r)$, the warped T-wave with no remaining time domain variability, and only presenting amplitude variability. (d): Square-root slope functions of the reference (solid blue) and warped (dashed red) T-waves.

Let $\boldsymbol{\gamma}(\boldsymbol{t}^r)$ be the warping function that relates $\boldsymbol{t}^r$ and $\boldsymbol{t}^s$, such that the composition $[\boldsymbol{f}^s \circ \boldsymbol{\gamma}](\boldsymbol{t}^r) = \boldsymbol{f}^s(\boldsymbol{\gamma}(\boldsymbol{t}^r))$ denotes the re-parameterization or time domain warping of $\boldsymbol{f}^s(\boldsymbol{t}^s)$ using $\boldsymbol{\gamma}(\boldsymbol{t}^r)$, i.e. $\boldsymbol{f}^s(\boldsymbol{\gamma}(\boldsymbol{t}^r))$ represents the amplitude values of $\boldsymbol{f}^s(\boldsymbol{t}^s)$ if its temporal vector was $\boldsymbol{t}^r$.

The most traditional algorithm for time domain warping is DTW [230], which

performs a sample-to-sample projection of two T-waves that aims at minimizing the Euclidean distance between them. In particular, the DTW algorithm finds the optimal warping function, $\boldsymbol{\gamma}^*_{\mathrm{w}}(\boldsymbol{t}^r)$, as:

$$\boldsymbol{\gamma}^*_{\mathrm{w}}\left(\boldsymbol{t}^r\right) = \underset{\boldsymbol{\gamma}(\boldsymbol{t}^r)}{\arg\min}\left(\left\|\boldsymbol{f}^r\left(\boldsymbol{t}^r\right) - \boldsymbol{f}^s\left(\boldsymbol{\gamma}\left(\boldsymbol{t}^r\right)\right)\right\|\right). \tag{3.1}$$

DTW leads to a warping function that can be used to remove the time domain variability present in the original T-waves. However, this metric has some limitations. Since it is not symmetric ($\|\boldsymbol{f}^r(\boldsymbol{t}^r) - \boldsymbol{f}^s(\boldsymbol{\gamma}(\boldsymbol{t}^r))\| \neq \|\boldsymbol{f}^s(\boldsymbol{t}^s) - \boldsymbol{f}^r(\boldsymbol{\gamma}^{-1}(\boldsymbol{t}^s))\|$), it is not a proper distance and can lead to degenerate results if $\boldsymbol{f}^r(\boldsymbol{t}^r)$ and $\boldsymbol{f}^s(\boldsymbol{t}^s)$ present variations in the amplitude domain ("pinching effect") [231], as it will be shown in this chapter. To address this, the SRSF was proposed [228, 229] to solve the warping in a geometrical space by warping, instead, the SRSF transformation of the original functions. This transformation is defined as the square-root of the derivative of $\boldsymbol{f}(\boldsymbol{t})$,

$$\boldsymbol{q}_{\mathrm{f}}\left(\boldsymbol{t}\right) = \mathrm{sign}\left(\dot{\boldsymbol{f}}\left(\boldsymbol{t}\right)\right)\sqrt{\left|\dot{\boldsymbol{f}}\left(\boldsymbol{t}\right)\right|}. \tag{3.2}$$

The SRSF of $\boldsymbol{f}^r(\boldsymbol{t}^r)$ and $\boldsymbol{f}^s(\boldsymbol{t}^s)$, $\boldsymbol{q}_{f^r}(\boldsymbol{t}^r)$ and $\boldsymbol{q}_{f^s}(\boldsymbol{t}^s)$, respectively, are shown in Figure 3.1 (b). Now, the SRSF optimal warping function is the one that minimizes the Euclidean distance between the SRSF of $\boldsymbol{f}^r(\boldsymbol{t}^r)$ and $\boldsymbol{f}^s(\boldsymbol{\gamma}(\boldsymbol{t}^r))$, $\boldsymbol{q}_{f^r}(\boldsymbol{t}^r)$ and $\boldsymbol{q}_{[f^s\circ\gamma]}(\boldsymbol{t}^r) = \boldsymbol{q}_{f^s}(\boldsymbol{\gamma}(\boldsymbol{t}^r))\sqrt{\dot{\boldsymbol{\gamma}}(\boldsymbol{t}^r)}$, respectively [228, 229]:

$$\begin{aligned}\boldsymbol{\gamma}^*_{\mathrm{TW}}\left(\boldsymbol{t}^r\right) &= \underset{\boldsymbol{\gamma}(\boldsymbol{t}^r)}{\arg\min}\left(\left\|\boldsymbol{q}_{f^r}\left(\boldsymbol{t}^r\right) - \boldsymbol{q}_{[f^s\circ\gamma]}\left(\boldsymbol{t}^r\right)\right\|\right) \\ &= \underset{\boldsymbol{\gamma}(\boldsymbol{t}^r)}{\arg\min}\left(\left\|\boldsymbol{q}_{f^r}\left(\boldsymbol{t}^r\right) - \boldsymbol{q}_{f^s}\left(\boldsymbol{\gamma}\left(\boldsymbol{t}^r\right)\right)\sqrt{\dot{\boldsymbol{\gamma}}\left(\boldsymbol{t}^r\right)}\right\|\right).\end{aligned} \tag{3.3}$$

The dynamic programming algorithm was used to obtain the solution of both the DTW and the SRSF optimizations [232]. The optimal warping function, $\boldsymbol{\gamma}^*_{\mathrm{TW}}(\boldsymbol{t}^r)$, that optimally warps $\boldsymbol{f}^r(\boldsymbol{t}^r)$ and $\boldsymbol{f}^s(\boldsymbol{t}^s)$ using SRSF is shown in Figure 3.1 (c). The warped T-wave, $\boldsymbol{f}^s(\boldsymbol{\gamma}^*(\boldsymbol{t}^r))$ is shown in Figure 3.1 (e), together with the reference T-wave, $\boldsymbol{f}^r(\boldsymbol{t}^r)$, while their corresponding SRSFs are shown in Figure 3.1 (d).

Dynamic Programming Algorithm

Let $\boldsymbol{f}^r(\boldsymbol{t}^r) = [f^r(t^r(1)), ..., f^r(t^r(N_r))]^T$ and $\boldsymbol{f}^s(\boldsymbol{t}^s) = [f^s(t^s(1)), ..., f^s(t^s(N_s))]^T$, be two given functions and we want to solve for:

$$\boldsymbol{\gamma}^*\left(\boldsymbol{t}^r\right) = \underset{\boldsymbol{\gamma}(\boldsymbol{t}^r)}{\arg\min}\left(\left\|\boldsymbol{f}^r\left(\boldsymbol{t}^r\right) - \boldsymbol{f}^s\left(\gamma\left(\boldsymbol{t}^r\right)\right)\right\|\right), \tag{3.4}$$

where $\boldsymbol{\gamma}(\boldsymbol{t}^r)$ is a function that matches each point in $\boldsymbol{f}^s(\gamma(\boldsymbol{t}^r))$ with each point in $\boldsymbol{f}^r(\boldsymbol{t}^r)$, and $\boldsymbol{\gamma}^*(\boldsymbol{t}^r)$ is the optimal warping function. We can solve a discrete approximation of this problem using dynamic programming. To decompose the large problem into several sub-problems, we define a local cost function:

$$E\left(\tau_1, \tau_2; \boldsymbol{\gamma}\right) = \left\| \boldsymbol{f}^r\left(\boldsymbol{\tau}\right) - \boldsymbol{f}^s\left(\boldsymbol{\gamma}\left(\boldsymbol{\tau}\right)\right)\right\| \quad \tau_1 \leqslant \boldsymbol{\tau} \leqslant \tau_2, \tag{3.5}$$

so that the original cost function is simply $E(t^r(1), t^r(N_r); \boldsymbol{\gamma})$. A necessary condition for applying dynamic programming to such problems is that the cost function is additive in time. Consider the 2D time coordinates grid formed by $[\boldsymbol{t}^r, \boldsymbol{t}^s]$, with size $N_r \times N_s$. We will conveniently view γ as a graph in this grid from $[t^r(1), t^s(1)]$ to $[t^r(N_r), t^s(N_s)]$, such that the slope of this graph is always strictly positive. Let $[t^r(a), t^s(b)]$ be a point on the grid. Since we have a constraint on the slope of the graph, there are only certain nodes, N_{ab}, that are allowed to go to $[t^r(a), t^s(b)]$:

$$N_{ab} = \{\left[t^r(a'), t^s(b')\right] | t^r(1) \leqslant t^r(a') < t^r(a), t^s(1) \leqslant t^s(b') < t^s(b)\} \tag{3.6}$$

Define $L(a', b'; a, b)$ as a straight line with strictly positive slope joining the nodes $[t^r(a'), t^s(b')]$ and $[t^r(a), t^s(b)]$. This sets up the local optimization problem:

$$\left[t^{r*}(a'), t^{s*}(b')\right] = \underset{\{t^r(a'), t^s(b')) \in N_{ab}}{\arg\min} \left(E\left(t^r(a'), t^r(a); L\left(a', b'; a, b\right)\right)\right), \tag{3.7}$$

Let $H(t^r(a), t^r(b))$ be the minimum cumulative cost needed to reach the point $[t^r(a), t^s(b)]$, defined as:

$$\begin{aligned} H\left(t^r(a), t^s(b)\right) = & E\left(t^{r*}(a'), t^r(a); L\left(a', b'; a, b\right)\right) \\ + & \quad H\left(t^{r*}(a'), t^{s*}(b')\right). \end{aligned} \tag{3.8}$$

This minimization problem is solved sequentially for each node $[t^r(a), t^s(b)]$, starting from $[t^r(1), t^s(1)]$, and with $H(t^r(1), t^s(1)) = 0$, and increasing a and b until the node $[t^r(N_r), t^s(N_s)]$ is reached. Tracing the path created by the set of pairs $\{[t^{r*}(1), t^{s*}(1)], ..., [t^{r*}(N_r), t^{s*}(N_s)]\}$ provides a discrete version of the optimal continuous γ. It is important to highlight that the dynamic programming algorithm provides the exact optimal warping function for each node, i.e. the warping function found can never be a local optimum of the objective function, and, therefore, the validity of d_w and d_a will not be compromised.

Markers of Morphological Variability

The level of warping may be different under various situations and it reflects important information regarding time domain variability. If $\boldsymbol{\gamma}^*(\boldsymbol{t}^r) = \boldsymbol{t}^r$, then the functions are perfectly aligned, so it makes sense to use the difference between $\boldsymbol{\gamma}^*(\boldsymbol{t}^r)$ and $\boldsymbol{t}^r$

to quantify the variability between each T-wave time domain. We define two metrics, d_x and d_w, that quantify the level of warping needed to optimally align any two T-waves. The index d_x was initially proposed in [229] and quantifies the projection of the SRSF transformation of the optimal warping function, $\boldsymbol{q}_{\gamma *}\left(\boldsymbol{t}^r\right)$, onto the SRSF transformation of $\boldsymbol{t}^r$:

$$d_x = \arccos\left(\frac{1}{N_r}\sum_{n=1}^{N_r} q_{\gamma *}\left(t^r\left(n\right)\right)\right) = \arccos\left(\frac{1}{N_r}\sum_{n=1}^{N_r}\sqrt{\dot{\gamma}^*\left(t^r\left(n\right)\right)}\right), \tag{3.9}$$

where the SRSF transformation of $\boldsymbol{t}^r$ is a vector of ones and, thus, has been omitted. Also, since the optimal warping function has always a positive slope, the sign of its derivative is always one (see equation 3.2).

The second metric, d_w, is defined in the original domain and measures the average of the absolute difference value between $\boldsymbol{\gamma}^*(\boldsymbol{t}^r)$ and $\boldsymbol{t}^r$:

$$d_w = \frac{1}{N_r}\sum_{n=1}^{N_r}\left|\gamma^*\left(t^r\left(n\right)\right) - t^r\left(n\right)\right|. \tag{3.10}$$

Figure 3.1 shows the value of d_w quantifying the time domain variability between $\boldsymbol{f}^r(\boldsymbol{t}^r)$ and $\boldsymbol{f}^s(\boldsymbol{t}^s)$.

Once the time domain variability has been compensated for by optimally warping $\boldsymbol{f}^s(\boldsymbol{t}^s)$, the remaining variability is merely amplitude variability, as shown in Figure 3.1 (e). Therefore, we can define two markers of amplitude variability, that are independent from the underlying time domain variability, one calculated in the SRSF domain, d_y, and another calculated in the original domain, d_a:

$$\begin{aligned} d_y &= \text{sign}\left(e_y\right)\cdot\frac{\overbrace{\left\|\boldsymbol{q}_{f^r}\left(\boldsymbol{t}^r\right) - \boldsymbol{q}_{f^s}\left(\boldsymbol{\gamma}^*_{\text{TW}}\left(\boldsymbol{t}^r\right)\right)\cdot\sqrt{\dot{\boldsymbol{\gamma}}^*_{\text{TW}}(\boldsymbol{t}^r)}\right\|}^{\boldsymbol{v}_y}}{\left\|\boldsymbol{q}_{f^r}\left(\boldsymbol{t}^r\right)\right\|}\times 100, \\ e_y &= \sum_{n=1}^{N_r} v_y(n). \end{aligned} \tag{3.11}$$

$$\begin{aligned} d_a &= \text{sign}\left(e_a\right)\cdot\frac{\left\|\overbrace{\boldsymbol{f}^r\left(\boldsymbol{t}^r\right) - \boldsymbol{f}^s\left(\boldsymbol{\gamma}^*_{\text{TW}}\left(\boldsymbol{t}^r\right)\right)}^{\boldsymbol{v}_a}\right\|}{\left\|\boldsymbol{f}^r\left(\boldsymbol{t}^r\right)\right\|}\times 100, \\ e_a &= \sum_{n=1}^{N_r} v_a(n). \end{aligned} \tag{3.12}$$

Figure 3.1 shows the value of d_a, measuring the amplitude variability between $\boldsymbol{f}^r(\boldsymbol{t}^r)$ and $\boldsymbol{f}^s(\boldsymbol{t}^s)$.

Extracting Non-linear T-wave Morphological Variability

The proposed markers contain information about linear and non-linear differences in both time and amplitude, respectively. Isolating the strictly non-linear variability information might provide additional understanding on the different sources generating the morphology of the T-wave.

Figure 3.2 (a), shows the optimal warping function from Figure 3.1 (c). As explained in equation (2.4), the marker d_w is calculated as the mean deviation of $\boldsymbol{\gamma}^*(\boldsymbol{t}^r)$ from $\boldsymbol{t}^r$, marked in yellow in Figure 3.2 (a). By fitting $\boldsymbol{\gamma}^*(\boldsymbol{t}^r)$ with a linear regression, $\boldsymbol{\gamma}_l^*(\boldsymbol{t}^r)$, (black dashed line), and measuring the mean deviation of $\boldsymbol{\gamma}^*(\boldsymbol{t}^r)$ with respect to this regression, we can have a quantification of the level of non-linear warping (dashed cyan region). This can be expressed as:

$$d_w^{\text{NL}} = \frac{1}{N_r} \sum_{n=1}^{N_r} |\gamma^*(t^r(n)) - \gamma_l^*(t^r(n))|, \tag{3.13}$$

where $\boldsymbol{\gamma}_l^*(\boldsymbol{t}^r)$ is the linear fitting of $\boldsymbol{\gamma}^*(\boldsymbol{t}^r)$ using the least absolute residual method [233] (Figure 3.2 (a)). The linear warping can be quantified by measuring the mean deviation of $\boldsymbol{\gamma}_l^*(\boldsymbol{t}^r)$ from $\boldsymbol{t}^r$ (non-dashed region in Figure 3.2 (a).

Regarding d_a, normalizing the warped T-waves, we can quantify non-linear amplitude differences not due to homogeneous scaling, and possibly caused by heterogeneous dispersion of repolarization times:

$$d_a^{\text{NL}} = \left\| \frac{\boldsymbol{f}^r(\boldsymbol{t}^r)}{\|\boldsymbol{f}^r(\boldsymbol{t}^r)\|} - \frac{\boldsymbol{f}^s(\boldsymbol{\gamma}^*(\boldsymbol{t}^r))}{\|\boldsymbol{f}^s(\boldsymbol{\gamma}^*(\boldsymbol{t}^r))\|} \right\| \times 100. \tag{3.14}$$

This is depicted in Figure 3.2 (b). Panel (b.1) shows the reference, $\boldsymbol{f}^r(\boldsymbol{t}^r)$ (solid blue), and studied, $\boldsymbol{f}^s(\boldsymbol{t}^s)$ (dashed red), T-waves with only amplitude variability (we assumed $\boldsymbol{\gamma}^*(\boldsymbol{t}^r) = \boldsymbol{t}^r$ in this example for clarity). Panel (b.2) shows the remaining non-linear amplitude variability after normalization.

3.2.2 Mean Warped T-wave

From a set of I T-waves, $\{\boldsymbol{f}_1^s(\boldsymbol{t}_1^s), \boldsymbol{f}_2^s(\boldsymbol{t}_2^s), ..., \boldsymbol{f}_I^s(\boldsymbol{t}_I^s)\}$ with temporal and amplitude variability it is possible to calculate a mean warped T-wave that is an optimal representative average both in temporal and amplitude domains. Consequently, we will iteratively search for the optimal mean warped T-wave in the SRSF domain, $\overline{\boldsymbol{q}}^k(\boldsymbol{t}^r)$, where k is the iteration, that minimizes the average of the difference between $\overline{\boldsymbol{q}}^k(\boldsymbol{t}^r)$ and each of the SRSF transformations of the set of T-waves, $\{\boldsymbol{q}_{f_1^s}(\boldsymbol{t}_1^s), \boldsymbol{q}_{f_2^s}(\boldsymbol{t}_2^s), ..., \boldsymbol{q}_{f_I^s}(\boldsymbol{t}_I^s)\}$. Therefore, we initialize $\overline{\boldsymbol{q}}^{k=1}(\boldsymbol{t}^r)$ as the average of $\{\boldsymbol{q}_{f_1^s}(\boldsymbol{t}_1^s), \boldsymbol{q}_{f_2^s}(\boldsymbol{t}_2^s), ..., \boldsymbol{q}_{f_I^s}(\boldsymbol{t}_I^s)\}$ and, then, for iteration k, we look for the optimal set of $\{\boldsymbol{\gamma}_1^{*^k}(\boldsymbol{t}^r), \boldsymbol{\gamma}_2^{*^k}(\boldsymbol{t}^r), ..., \boldsymbol{\gamma}_I^{*^k}(\boldsymbol{t}^r)\}$ that minimizes:

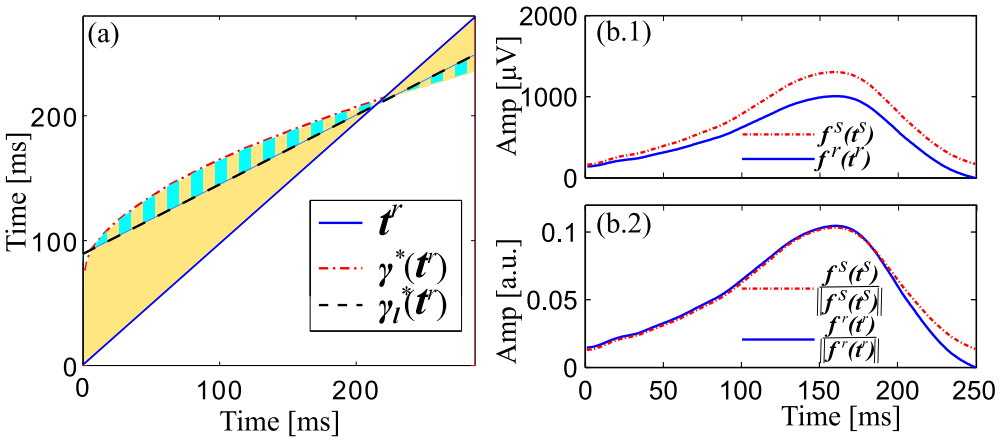

Figure 3.2: Calculation of the non-linear warping and amplitude information. (a): The area between $\boldsymbol{\gamma}^*(\boldsymbol{t}^r)$ and $\boldsymbol{t}^r$ (yellow region) represents the total warping information, quantified by d_w, while the area between $\boldsymbol{\gamma}^*(\boldsymbol{t}^r)$ and $\boldsymbol{\gamma}_l^*(\boldsymbol{t}^r)$ represents the non-linear warping information (dashed cyan region), quantified by d_w^{NL}. (b.1): Reference, $\boldsymbol{f}^r(\boldsymbol{t}^r)$ (solid blue), and studied, $\boldsymbol{f}^s(\boldsymbol{t}^s)$ (dashed red), T-waves with only amplitude variability ($\boldsymbol{\gamma}^*(\boldsymbol{t}^r) = \boldsymbol{t}^r$). (b.2): Normalized reference, $\frac{\boldsymbol{f}^r(\boldsymbol{t}^r)}{\|\boldsymbol{f}^r(\boldsymbol{t}^r)\|}$, and studied, $\frac{\boldsymbol{f}^s(\boldsymbol{\gamma}^*(\boldsymbol{t}^r))}{\|\boldsymbol{f}^s(\boldsymbol{\gamma}^*(\boldsymbol{t}^r))\|}$, T-waves.

$$\boldsymbol{\gamma}_i^{*^k}(\boldsymbol{t}^r) = \underset{\boldsymbol{\gamma}_i(\boldsymbol{t}^r)}{\arg\min} \left(\left\| \overline{\boldsymbol{q}}^k(\boldsymbol{t}^r) - \boldsymbol{q}_{f_i^s(\boldsymbol{\gamma}_i)}(\boldsymbol{t}^r) \right\| \right), \quad i = 1, ..., I. \tag{3.15}$$

The updated SRSF transformation of the mean warped T-wave can be calculated as:

$$\overline{\boldsymbol{q}}^{k+1}(\boldsymbol{t}^r) = \frac{1}{I} \sum_{i=1}^{I} \boldsymbol{q}_{[f_i^s \circ \boldsymbol{\gamma}_i^{*^k}]}(\boldsymbol{t}^r) \tag{3.16}$$

We repeated eq. (3.15) and (3.16) until the difference between the energies of $\overline{\boldsymbol{q}}^{k+1}(\boldsymbol{t}^r)$ and $\overline{\boldsymbol{q}}^k(\boldsymbol{t}^r)$ was lower than 0.1%.

The final mean warped T-wave can be obtained by transforming $\overline{\boldsymbol{q}}^k(\boldsymbol{t}^r)$ back to the original domain [228, 229]. Considering equation 3.2, the following holds:

$$\mathrm{sign}(\overline{\boldsymbol{q}}^k(\boldsymbol{t}^r)) = \mathrm{sign}\left(\dot{\overline{\boldsymbol{f}}}(\boldsymbol{t}^r)\right) \tag{3.17}$$

Also, by squaring equation 3.2:

$$\overline{\boldsymbol{q}}^k(\boldsymbol{t}^r)^2 = \left|\dot{\overline{\boldsymbol{f}}}(\boldsymbol{t}^r)\right| = \dot{\overline{\boldsymbol{f}}}(\boldsymbol{t}^r)\,\mathrm{sign}\left(\dot{\overline{\boldsymbol{f}}}(\boldsymbol{t}^r)\right) \tag{3.18}$$

Then, solving for $\dot{\overline{\boldsymbol{f}}}(\boldsymbol{t}^r)$, and using the relation from equation 3.17:

$$\dot{\overline{\boldsymbol{f}}}(\boldsymbol{t}^r) = \overline{\boldsymbol{q}}^k(\boldsymbol{t}^r)^2 \text{sign}(\overline{\boldsymbol{q}}^k(\boldsymbol{t}^r)) = \overline{\boldsymbol{q}}^k(\boldsymbol{t}^r)\left|\overline{\boldsymbol{q}}^k(\boldsymbol{t}^r)\right| \tag{3.19}$$

Finally, integrating equation 3.19:

$$\overline{f}(t^r(n)) = \frac{1}{I}\sum_{i=1}^{I} f_i^s(t_i^s(1)) + \sum_{l=1}^{n} \overline{q}^k(t^r(l))\left|\overline{q}^k(t^r(l))\right| \tag{3.20}$$

When the morphology of the set of T-waves is very homogeneous, the morphology of the mean warped T-wave will be very similar and representative of the set. However, if the morphologies in the set are heterogeneous, like when a large portion of T-waves are biphasic or S-shaped while another portion is monophasic, the mean warped T-wave morphology will resemble the dominant T-wave shape, in case there exists one, or the arithmetic T-wave mean (after warping), if the different populations have the same weight. Therefore, it would be advisable to include a pre-processing step to remove any undesired T-wave morphology prior the computation of the mean warped T-wave.

3.2.3 Separating Time and Amplitude Components

In this section, we performed two simulations, one to compare the performances of DTW and SRSF in removing time domain variability, and another to evaluate the accuracy of the morphology markers to capture the simulated time and amplitude variability under the presence of additive Laplacian noise.

Let the T-wave from a reference noise-free cardiac beat, sampled at 1 kHz, be the reference T-wave, $\boldsymbol{f}^r(\boldsymbol{t}^r)$. This reference cardiac beat was obtained from the first principal component, calculated as described in section 1.3.2, over the 8-standard leads recorded at supine position from a healthy subject.

Comparison of Dynamic Time Warping and Square-Root Slope Function Warping Algorithms

T-wave amplitude variability was modelled by multiplying the deviations from the iso-electric line of each i-th T-wave by a sinusoidally evolving factor in the following way:

$$\begin{aligned} \boldsymbol{f}_i^s(\boldsymbol{t}^r) &= \boldsymbol{f}^r(\boldsymbol{t}^r) \cdot \left(1 + 0.25 \cdot \sin\left(\frac{\pi(i-1)}{I-1}\right)\right), \\ i &= 1, ..., I, \end{aligned} \tag{3.21}$$

T-wave time domain modulation was introduced by modifying the temporal domain of $\boldsymbol{f}^r(\boldsymbol{t}^r)$ to induce T-wave asymmetry, but without altering the width of the T-wave, according to the following equation:

$$\begin{aligned} \boldsymbol{t}_i^s &= t^r(1) + \left(t^r(N_r) - t^r(1)\right) \cdot \left(\frac{\boldsymbol{t}^r - t^r(1)}{t^r(N_r) - t^r(1)}\right)^{\alpha(i)} \\ \alpha(i) &= \left(\frac{0.45(i-1)}{I-1} + 0.8\right), \quad i = 1, ..., I \end{aligned} \tag{3.22}$$

where i is the heart beat index.

Evaluation of the Performance of the Morphology Markers

The accuracy of d_x, d_w, d_y, d_a, d_w^{NL} and d_a^{NL} in capturing linear and non-linear T-wave time and amplitude variations was assessed by simulating controlled variations in the T-wave duration and amplitude under the presence of different levels of additive noise.

The non-linear T-wave amplitude variability was modelled by adding a sinusoidal wave, of period 0.25 times N_r and amplitude function of each beat, to $\boldsymbol{f}^r(\boldsymbol{t}^r)$ in the following way:

$$\begin{aligned} \boldsymbol{f}_i^{\mathrm{NL}}\left(\boldsymbol{t}^r\right) &= \boldsymbol{f}^r\left(\boldsymbol{t}^r\right) + c\left(i\right) \cdot \sin\left(2\pi \frac{1}{4N_r} \boldsymbol{t}^r\right), \\ c\left(i\right) &= 150. \sin\left(\frac{\pi\left(\frac{I}{2} + i - 1\right)}{I}\right), \quad i = 1, ..., I, \end{aligned} \tag{3.23}$$

Then, the T-wave linear amplitude variability was modelled by multiplying the deviations from the iso-electric line of $\boldsymbol{f}_i^{\mathrm{NL}}\left(\boldsymbol{t}^r\right)$ by a factor sinusoidally modulated across beats:

$$\boldsymbol{f}_i^s\left(\boldsymbol{t}^r\right) = \boldsymbol{f}_i^{\mathrm{NL}}\left(\boldsymbol{t}^r\right) \cdot \left(1 + 0.15 \cdot \sin\left(\frac{\pi\left(\frac{I}{2} + i - 1\right)}{I}\right)\right). \tag{3.24}$$

Next, linear variations in the duration of the T-wave were simulated according to:

$$\boldsymbol{t}_i^l = \boldsymbol{\gamma}_i\left(\boldsymbol{t}^r\right), \quad i = 1, ..., I \tag{3.25}$$

where now $\boldsymbol{\gamma}_i(\boldsymbol{t}^r)$ is the operator that up- and downsamples $\boldsymbol{t}^r$ according to the sampling factor, $\alpha(i)$:

$$\alpha\left(i\right) = \frac{0.6 \cdot (i-1)}{(I-1)} + 0.7, \quad i = 1, ..., I \tag{3.26}$$

when simulating large time variations (like those found under appreciably different RR values, which for a reference $RR = 1$ s, would produce an RR spanning from

$RR = 0.7$ s (85 bpm) to $RR = 1.3$ s (46 bpm), representing a heart rhythm change after moving from activity to relax, as an example, [158]) and:

$$\alpha(i) = \frac{0.2 \cdot (i-1)}{(I-1)} + 0.9, \quad i = 1, ..., I \tag{3.27}$$

when simulating small time variations (like those found when analizing short-term variability, which for a reference $RR = 1$ s, would produce an RR spanning from $RR = 0.9$ s (66 bpm) to $RR = 1.1$ s (54 bpm), representing the beat-to-beat heart rate variability under stationary conditions [158]).

Non-linear variations in the temporal domain of the T-wave were introduced by adding a sinusoidal modulation of period N_r and linearly varying amplitude, guaranteeing a monotonic increasing function:

$$\begin{aligned} \boldsymbol{t}_i^s &= \boldsymbol{t}_i^l + d(i) \frac{N_r}{N_{s_i}} \cdot \sin\left(2\pi \frac{1}{N_r} \boldsymbol{t}_i^l\right), \\ d(i) &= \frac{30(i-1)}{I-1} - 15, \quad i = 1, ..., I \end{aligned} \tag{3.28}$$

where N_{s_i} is, now, the duration of $\boldsymbol{t}_i^l$.

The re-parameterized i-th T-wave was, then, obtained using:

$$\boldsymbol{f}_i^s(\boldsymbol{t}_i^s) = \boldsymbol{f}_i^s\left(\boldsymbol{\gamma}_i(\boldsymbol{t}^r) + d(i) \frac{N_r}{N_{s_i}} \cdot \sin\left(2\pi \frac{1}{N_r} \boldsymbol{\gamma}_i(\boldsymbol{t}^r)\right)\right). \tag{3.29}$$

The i-th modulated cardiac beat was obtained by transforming $\boldsymbol{f}^r(\boldsymbol{t}^r)$ to $\boldsymbol{f}_i^s(\boldsymbol{t}_i^s)$. A simulated ECG signal was obtained by concatenating the $I = 300$ modulated cardiac beats. This led to a 300-beat ECG signal which was filtered as explained in section 1.3.2, and the T-waves were selected using the known delimitation marks. The morphological average of the 300 T-waves, $\overline{\boldsymbol{f}}(\boldsymbol{t}^r)$, was obtained with the algorithm explained in section 3.2.2, and this mean warped T-wave was chosen as the reference for comparison.

The reference $\boldsymbol{d}_x^r = [d_x^r(1), ..., d_x^r(I)]$, $\boldsymbol{d}_w^r = [d_w^r(1), ..., d_w^r(I)]$, $\boldsymbol{d}_y^r = [d_y^r(1), ..., d_y^r(I)]$, $\boldsymbol{d}_a^r = [d_a^r(1), ..., d_a^r(I)]$, $\boldsymbol{d}_w^{\mathrm{NL}^r} = [d_w^{\mathrm{NL}^r}(1), ..., d_w^{\mathrm{NL}^r}(I)]$ and $\boldsymbol{d}_a^{\mathrm{NL}^r} = [d_a^{\mathrm{NL}^r}(1), ..., d_a^{\mathrm{NL}^r}(I)]$ series were obtained by comparing each $\boldsymbol{f}_i^s(\boldsymbol{t}_i^s)$ with $\overline{\boldsymbol{f}}(\boldsymbol{t}^r)$, following the procedure explained in section 3.2.1. Before applying the warping algorithm, the reference and the studied T-waves were aligned according to their gravity centres, so that $\boldsymbol{\gamma}^*(\boldsymbol{t}^r)$ is only dependent on changes in the T-wave morphology, and not on global shifts. The center of gravity was calculated as the shift in $\boldsymbol{t}_i^s$ that offered the maximum cross-correlation between $\boldsymbol{f}^r$ and $\boldsymbol{f}_i^s$. In case $\boldsymbol{f}^r$ and $\boldsymbol{f}_i^s$ had different polarities, $\boldsymbol{f}^s$ was inverted to match the polarity of $\boldsymbol{f}^r$.

Then, zero mean Laplacian noise was iteratively added to the simulated ECG signal, such that the SNR was, in decibels (dBs): $SNR = \{5, 10, ..., 35\}$. The estimated $\boldsymbol{d}_x^{\mathrm{SNR}} = [d_x^{\mathrm{SNR}}(1), ..., d_x^{\mathrm{SNR}}(I)]$, $\boldsymbol{d}_w^{\mathrm{SNR}} = [d_w^{\mathrm{SNR}}(1), ..., d_w^{\mathrm{SNR}}(I)]$, $\boldsymbol{d}_y^{\mathrm{SNR}} = [d_y^{\mathrm{SNR}}(1), ..., d_y^{\mathrm{SNR}}(I)]$,

$\boldsymbol{d}_a^{\text{SNR}} = [d_a^{\text{SNR}}(1), ..., d_a^{\text{SNR}}(I)]$, $\boldsymbol{d}_w^{\text{NL}^{\text{SNR}}} = [d_w^{\text{NL}^{\text{SNR}}}(1), ..., d_w^{\text{NL}^{\text{SNR}}}(I)]$ and $\boldsymbol{d}_a^{\text{NL}^{\text{SNR}}} = [d_a^{\text{NL}^{\text{SNR}}}(1), ..., d_a^{\text{NL}^{\text{SNR}}}(I)$ series were obtained by comparing the T-waves from the noisy modulated ECG signal with their mean warped T-wave. The normalized relative errors were, then, calculated as:

$$e_d\left(SNR\right) = \sqrt{\frac{\sum_{i=1}^{I}\left(d^{\text{SNR}}\left(i\right) - d^r\left(i\right)\right)^2}{\sum_{i=1}^{I}\left(d^r\left(i\right)\right)^2}} \times 100, \tag{3.30}$$

where $d \in \{d_x, d_w, d_y, d_a, d_w^{\text{NL}}, d_a^{\text{NL}}\}$. The noise generation and relative error measurement steps were repeated 50 times to have robust relative error values.

3.2.4 Electrophysiological Model

The relation between changes in myocardial repolarization dynamics and the morphological variability markers was explored using an electrophysiological model [234]. This model presents a formalization of the forward problem in which action potentials at M ventricular sites are projected onto the body surface.

The transmembrane potentials, $\boldsymbol{v}(t) = [v_1(t), ..., v_M(t)]$, of $M = 257$ sources (*nodes*), each one located at a given point on the epi- and endocardium, were generated for each node m by using the analytical expression proposed in [235], and already used for similar purposes in [236, 237]:

$$\begin{aligned} v_m\left(t\right) &= a_m \cdot d_m\left(t\right) \cdot r_m\left(t\right) + v_0, \quad m = 1..M, \\ d_m\left(t\right) &= \frac{1}{1 + e^{-\alpha_m\left(t - \delta_m\right)}}. \\ r_m\left(t\right) &= \left(1 - \frac{1}{1 + e^{-\beta_m\left(t - \rho_m\right)}}\right) \cdot \left(1 - \frac{1}{1 + e^{-\mu_m\left(t - \rho_m\right)}}\right). \end{aligned} \tag{3.31}$$

In these expressions, δ_m and ρ_m are the depolarization and repolarization times, and α_m, β_m and μ_m describe the upslope during repolarization, and the leading and trailing downslope during repolarization, respectively, at node m. a_m is the amplitude of the transmembrane potential and v_0 is the resting potential. The values of the parameters were obtained by fitting $v_m(t)$ with the transmembrane potential of each node provided by ECGSIM [40] for a normal male. Figure 3.3 shows the analytical expressions $d_m\left(t\right)$ (a), $r_m\left(t\right)$ (b) and the transmembrane potential $v_m\left(t\right)$ (c), for m =100.

A L-lead ECG beat, with $L = 8$, was generated by using the model proposed and validated in [234]. This model is derived from the equivalent surface source model [238], assuming that the sources are of the double layer type. The ECG potential (one for each of the L leads considered) on the body surface can be expressed as:

$$\boldsymbol{\phi}\left(t\right) = \mathbf{A}\boldsymbol{v}\left(t\right), \tag{3.32}$$

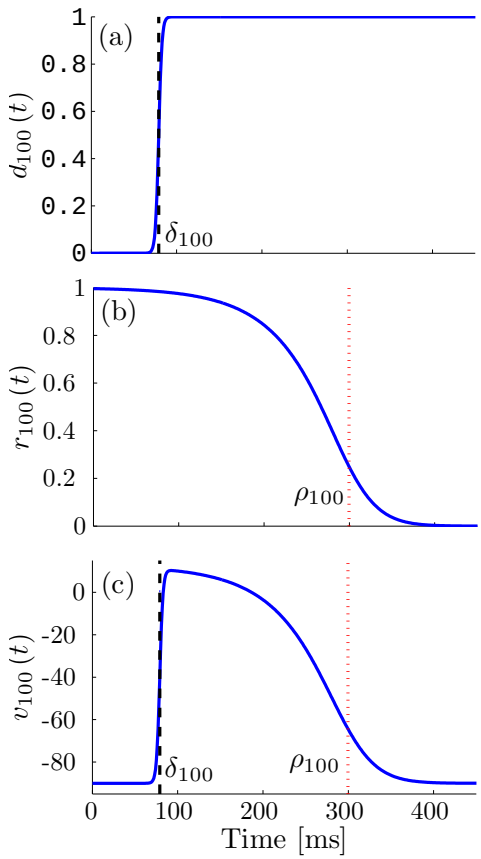

Figure 3.3: Analytical expressions $\mathfrak{d}_m(t)$ (a), $\mathfrak{r}_m(t)$ (b) and the transmembrane potential $v_m(t)$ (c), for m =100. Vertical lines indicate the depolarization time, δ_m, (dashed black) and repolarization time, ρ_m, (dotted red).

where matrix $\mathbf{A}$ has size $(8 \times M)$ and reflects the complexity of the torso (geometry and conductivity). Each row of $\mathbf{A}$ expresses the linear weighting of all action potentials, $\boldsymbol{v}(t)$, for each standard lead [234].

In [234], the author pointed out that it was possible to link the shape of the T-wave in each lead to the transmembrane potential using equation (3.32). In fact, making the further approximation that the only difference across different $v_m(t)$ functions is the repolarization time ρ_m, i.e., $v_m(t) = v(t - \rho_m)$, then the repolarization time of each node may be expressed as $\rho_m = \overline{\rho} + \Delta\rho_m$, where $\overline{\rho} = \sum_{m=1}^{M} \rho_m / M$ is the average repolarization time, and $\Delta\rho_m \ll \overline{\rho}$ is the deviation (difference) of repolarization times at cardiac site m, with standard deviation σ, from the mean repolarization time, with

$\sum_{m=1}^{M} \Delta\rho_m = 0$.

Next, principal component analysis was performed over the ECG leads and the first principal component was preprocessed and delineated using a single-lead technique [66]. The extracted T-wave was considered as the reference T-wave in this simulation study.

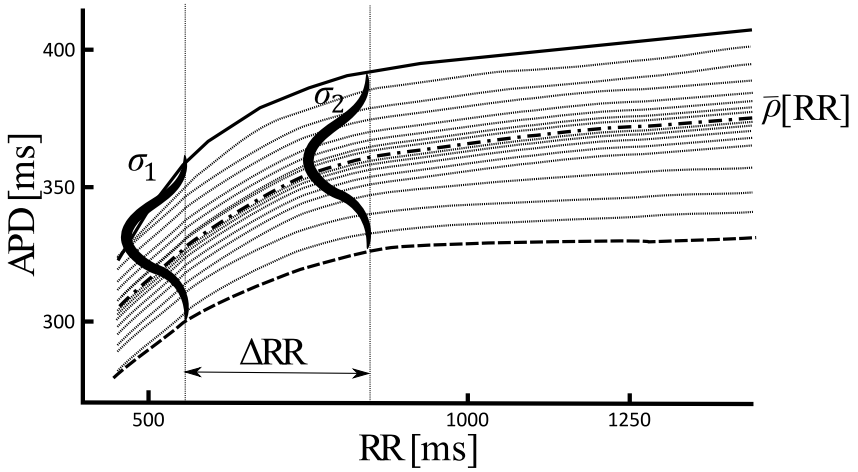

Figure 3.4: Diagram illustrating the hypothesis of this thesis: the dispersion of repolarization changes with RR. Different action potential duration restitution curves from different ventricular cells are plotted. σ indicates the standard deviation of the dispersion of repolarization at each value of RR interval.

We assessed the morphological variability reflected on the j-th T-wave using d_w, d_a, d_w^{NL} and d_a^{NL}, where $j = 1, ..., 5$ is the level of variation in ρ_m at each situation, under four scenarios:

1. Lengthening of the mean repolarization time, $\overline{\rho}$, according to the following equation:

$$\overline{\rho}\,(j) = \overline{\rho} + 25 \cdot (j-1)\,, \quad j = 1, ..., 5 \tag{3.33}$$

where $\overline{\rho}(j)$ is in ms. This is equivalent to move from a beat with σ_1 to other beat with $\sigma_2 = \sigma_1$ and different $\overline{\rho}$, if $\overline{\rho}$ is varying with the RR interval (see Figure 3.4).

2. Increasing the dispersion of repolarization by modifying σ, using the following equation:

$$\begin{aligned} \Delta\rho_m\,(j) &= \Delta\rho_m\,(1 + 0.2\,(j-1))\,, \quad j = 1, ..., 5 \\ \sigma\,(j) &= \sqrt{\frac{1}{M-1}\sum_{m=1}^{M}\left(\Delta\rho_m\,(j) - \overline{\rho}\right)^2}, \end{aligned} \tag{3.34}$$

where $\Delta\rho_m(j)$ and $\sigma(j)$ are in ms. This is equivalent to move from a beat with σ_1 to a beat with $\sigma_2 \neq \sigma_1$ and same $\overline{\rho}$ (see Figure 3.4).

3. In the third scenario we combined simulations 1 and 2.

4. Progressive variations of the epicardial APDs, defined as the difference between the maximum repolarization and depolarization slopes, (by only modifying the repolarization times, ρ_m, of epicardial nodes) towards the mean endocardial APD. This emulates the reduction in the dispersion of repolarization after reducing the spatial dispersion of I_{ks} current as reported in [222].

PCA was performed on the resulting ECG leads, and the first principal component was preprocessed and delineated using a single-lead technique [66]. The subsequent $d_w(j)$, $d_a(j)$, $d_w^{\text{NL}}(j)$, and $d_a^{\text{NL}}(j)$ series were obtained for each scenario by comparing the resulting j-th T-wave with the reference T-wave. Their gravity centres were also aligned to make $\boldsymbol{\gamma}^*(\boldsymbol{t}^r)$ only dependent on changes in the T-wave morphology, and not on global shifts.

3.2.5 ECG recordings

The Tilt Table Test

ECG signals recorded during a tilt table test were studied since it is a standard procedure that induces variations in the modulation of the autonomic nervous system, i.e. heart rate, and in the repolarization features, i.e. T-wave morphology [144]. Therefore, our objective was to evaluate the ability of d_w, d_a, d_w^{NL} and d_a^{NL} to capture the T-wave morphological changes induced by the orthostatic stress, and their interaction with changes in the heart rate. ECG recordings from 17 healthy subjects (age 28.5±2.8 years, 11 males) with no previous medical history related to cardiovascular diseases, acquired at the University of Zaragoza (ANS-UZ database) were analysed [144]. Each recording consisted of 8 ECG leads, sampled at 1 KHz, acquired during a 13-min head-up tilt test (4-min supine, 5-min at 70°, 4-min supine).

Preprocessing of the ECG signals included low-pass filtering at 40 Hz with a butterworth filter of order 6 to remove electric and muscle noise but still allow QRS detection, cubic splines interpolation for baseline wander removal and ectopic beats detection. A single-lead-plus-rules delineation technique [67] (section 1.3.3) was applied over all leads in the ECG record to delimitate the T-waves. Then, PCA was calculated lead-wise over the selected T-waves to emphasize the T-wave components, improve its delineation and enhance morphological differences [65]. Finally, the first principal component was further delineated using a single-lead technique [66], and the T-waves were confined from the T-wave onset and T-wave end delineation marks. Then, each T-wave was further low-pass filtered at 20 Hz, using a butterworth filter of order 6, to remove remaining out-of-band high frequency components that could potentially corrupt the T-wave shape. The filtered T-waves were visually checked for

artefacts related to onset/end filtering discontinuities, observing no issues in this respect. The reference and the studied T-waves were also aligned according to their gravity centres before applying the warping algorithm.

We assumed stationarity in three windows, *early supine (ES)*, *Tilt (TL)*, and *late supine (LS)*, as done in [239]. These windows had a length of 20 beats and finished 30 s before any transition during the tilt test. Then, for each subject and window, we calculated the RR, QT, TW, and Tpe interval values as the differences between subsequent QRS fiducial points, T-wave end and QRS complex onset, T-wave end and T-wave onset, and T-wave end and T-wave peak, respectively, from the annotation marks calculated in delineation step [66]. Similarly, the TA values were obtained from the T-wave amplitude values. Finally, for each subject and window, we calculated the median RR, QT, TW, Tpe and TA values. In addition, the mean warped T-wave of the 20 T-waves in each window and subject was calculated following the algorithm explained in section 3.2.2.

Analysis of Long-term T-wave Morphological Variability

To evaluate the variations of the T-wave produced by the orthostatic stress, we compared each mean warped T-wave with the other two ((*LS* - *ES*), (*TL* - *ES*) and (*LS* - *TL*)), and we calculated the difference between each median RR, Tpe, TW, QT and TA values and the other two, obtaining three values of d_w, d_a, d_w^{NL}, d_a^{NL}, ΔRR, ΔTpe, ΔTW, ΔQT and ΔTA per subject.

We also calculated for each subject the mean warped T-wave among 20 T-waves from the beginning of the recording, and we compared it with every T-wave along the recording, creating two series, $x_{d_w}(i)$ and $x_{d_a}(i)$, where i is the beat index. The RR series, $x_{RR}(i)$ was also calculated.

Analysis of Short-term T-wave Morphological Variability

To evaluate the variability of the T-wave at steady-state conditions, we calculated the median absolute deviation of QT, TW, Tpe and TA with respect to their median value, for each subject and window [240]. Regarding the proposed morphological markers, we calculated the median of the 20 absolute values of d_w, d_a, d_w^{NL} and d_a^{NL}, obtained when comparing each T-wave in the window with its mean warped T-wave. Finally, we measured the SNR value of the T-waves in the window, defined as the ratio between the root mean squared values of their arithmetic mean T-wave and the difference between each T-wave and this arithmetic mean T-wave, in decibels. Therefore, we assumed that noise level was higher than the variability itself. This definition can be argued at situations where the T-wave variability is high, as compared to noise. However, for Holter ECG records at stationary conditions, it is expected to have low T-wave variability and high noise levels. Then, for general cases, this will be an appropriate assumption when estimating correlation for the whole range of SNR.

3.3 Results

3.3.1 Separating Time and Amplitude Components

Comparison of Dynamic Time Warping and Square-Root Slope Function Warping Algorithms

Figure 3.5 shows an example of DTW (eq. (3.1)) and SRSF (eq. (3.3)) warping algorithms for $i = 200$ in the first simulation study. Panel (a) shows $\boldsymbol{f}^r(\boldsymbol{t}^r)$ (solid blue) and $\boldsymbol{f}^s_{200}(\boldsymbol{t}^s_{200})$ (dashed red), where the simulated amplitude scaling (by a factor of 1.2) and temporal asymmetry ($\alpha_{(200)} = 1.1$) can be appreciated. The black dotted lines illustrate the pointwise warping reflected by $\boldsymbol{\gamma}^*_{\mathrm{W}}(\boldsymbol{t}^r)$ (depicted on panel (e)). The resulting warped $\boldsymbol{f}^s_{200}(\boldsymbol{\gamma}^*_{\mathrm{W}}(\boldsymbol{t}^r))$ is shown in panel (b). Panels (c) and (d) show the same process, but using the SRSF warping algorithm. It can be observed how DTW produces a singularity, or unintuitive warping, leading to a degenerate warped T-wave. This occurs because DTW compares amplitude values, rather than match the features of both T-waves (up-/downslopes, peaks, etc). For instance, in panel (a), $\boldsymbol{\gamma}^*_{\mathrm{W}}(\boldsymbol{t}^r)$ has matched the peak of $\boldsymbol{f}^r(\boldsymbol{t}^r)$ to the first point found in $\boldsymbol{f}^s_{200}(\boldsymbol{t}^s_{200})$ with the same amplitude value, without considering if this point is also the peak. SRSF is based on the comparison of two transformed functions that are proportional to the derivative of the original signals so that, together with its built-in regularization term, $\sqrt{\dot{\boldsymbol{\gamma}}^*_{\mathrm{TW}}(\boldsymbol{t}^r)}$, SRSF achieves a feature-to-feature warping (green dotted lines, panels (c) and (e)), leading to a warped $\boldsymbol{f}^s_{200}(\boldsymbol{\gamma}^*_{\mathrm{TW}}(\boldsymbol{t}^r))$ that is just a scaled version of $\boldsymbol{f}^r(\boldsymbol{t}^r)$, as expected. Therefore, $\boldsymbol{\gamma}^*_{\mathrm{TW}}(\boldsymbol{t}^r)$ has proved to perform better than $\boldsymbol{\gamma}^*_{\mathrm{W}}(\boldsymbol{t}^r)$, and, then, was the chosen methodology in the rest of the work.

Performance of the Morphology Markers

Figure 3.6 shows six examples of the linear and non-linear time and amplitude simulations of the T-wave. The reference T-wave, $\boldsymbol{f}^r(\boldsymbol{t}^r)$ is displayed in solid blue in every panel, and the simulated T-wave, $\boldsymbol{f}^s_i(\boldsymbol{t}^s_i)$ is plotted in dashed red, for $i = \{1, 60, 120, 180, 240, 300\}$.

The comparison of the noise robustness of the T-wave amplitude and time variability markers, d_y and d_a, and d_x and d_w, is shown in figure 3.7, panels (a) and (b), respectively. As observed, the markers d_w and d_a are more robust against noise than d_x and d_y, respectively. Then, the preferred morphological variability markers and, thus, chosen for the rest of the study, were d_w and d_a. The mean$\pm$standard deviation of the relative error between d^{SNR}_a and d^r_a, d^{SNR}_y and d^r_y, d^{SNR}_x and d^r_x, and d^{SNR}_w and d^r_w is displayed for different values of SNR.

Figure 3.8 shows the evolution of d^r_w (a), d^r_a (b), $d^{\mathrm{NL}^r}_w$ (c), and $d^{\mathrm{NL}^r}_a$ (d) series as the linear and non-linear time and amplitude modulations induced in the T-wave change. The evolution of d^{20}_w, d^{20}_a, $d^{\mathrm{NL}^{20}}_w$, and $d^{\mathrm{NL}^{20}}_a$ is illustrated in red.

Figure 3.9 shows the relative error between $\boldsymbol{d}^{\mathrm{SNR}}_w$ and $\boldsymbol{d}^r_w$ (a), $\boldsymbol{d}^{\mathrm{SNR}}_a$ and $\boldsymbol{d}^r_a$ (b),

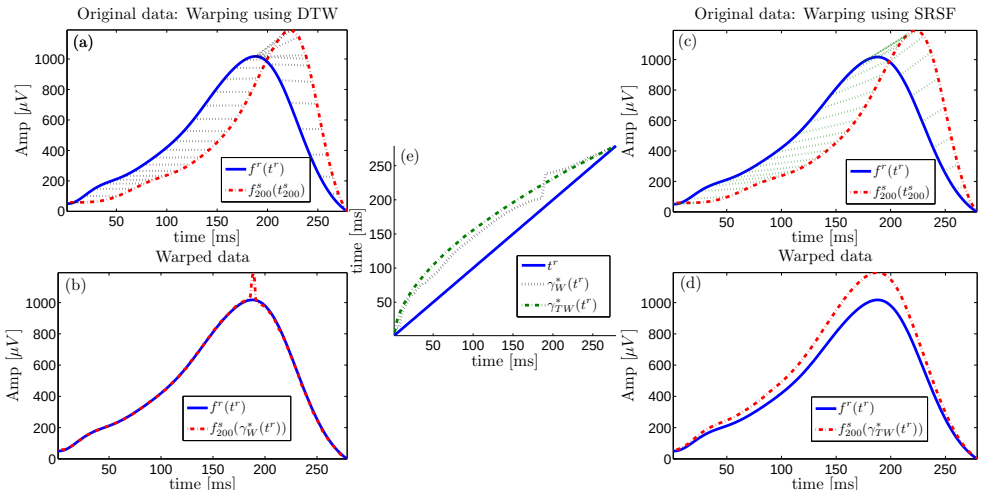

Figure 3.5: Comparison of DTW and SRSF warping algorithms. Panels (a) and (c) show $\boldsymbol{f}^r(\boldsymbol{t}^r)$ (solid blue) and $\boldsymbol{f}^s_{200}(\boldsymbol{t}^s_{200})$ (dashed red). The dotted lines illustrate the relation between $\boldsymbol{t}^r$ and $\boldsymbol{t}^s$ using $\boldsymbol{\gamma}^*_{\mathrm{W}}(\boldsymbol{t}^r)$ and $\boldsymbol{\gamma}^*_{\mathrm{TW}}(\boldsymbol{t}^r)$, respectively (plotted in panel (e)). Panels (b) and (d) show $\boldsymbol{f}^s_{200}(\boldsymbol{\gamma}^*_{\mathrm{W}}(\boldsymbol{t}^r))$ and $\boldsymbol{f}^s_{200}(\boldsymbol{\gamma}^*_{\mathrm{TW}}(\boldsymbol{t}^r))$, respectively.

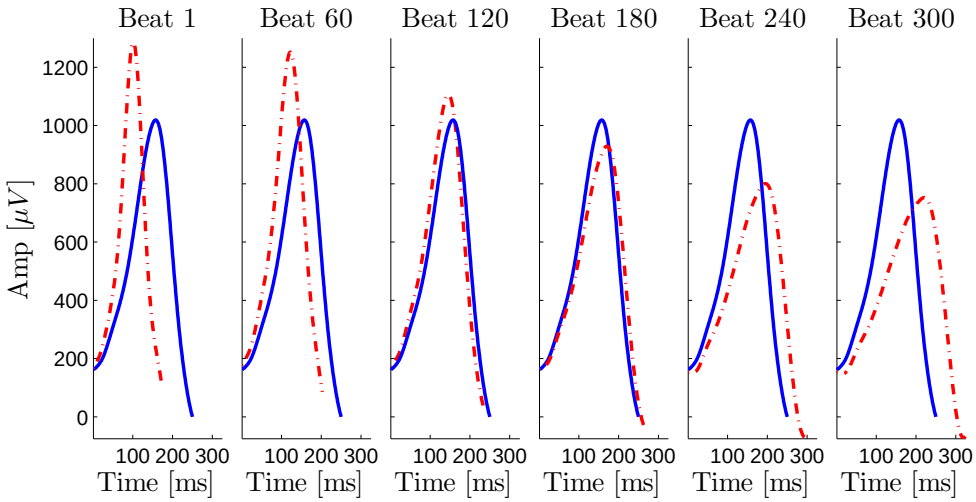

Figure 3.6: Evolution of linear and non-linear time and amplitude simulated variations. The reference T-wave, $\boldsymbol{f}^r(\boldsymbol{t}^r)$, is displayed in solid blue, and the simulated T-wave, $\boldsymbol{f}^s_i(\boldsymbol{t}^s_i)$, is plotted in dashed red, for $i = \{1, 60, 120, 180, 240, 300\}$.

$\boldsymbol{d}_w^{\mathrm{NL}^{\mathrm{SNR}}}$ and $\boldsymbol{d}_w^r$ (c), and $\boldsymbol{d}_a^{\mathrm{NL}^{\mathrm{SNR}}}$ and $\boldsymbol{d}_a^r$ (d), for different SNR when simulating large (red) and small (black) linear time variations.

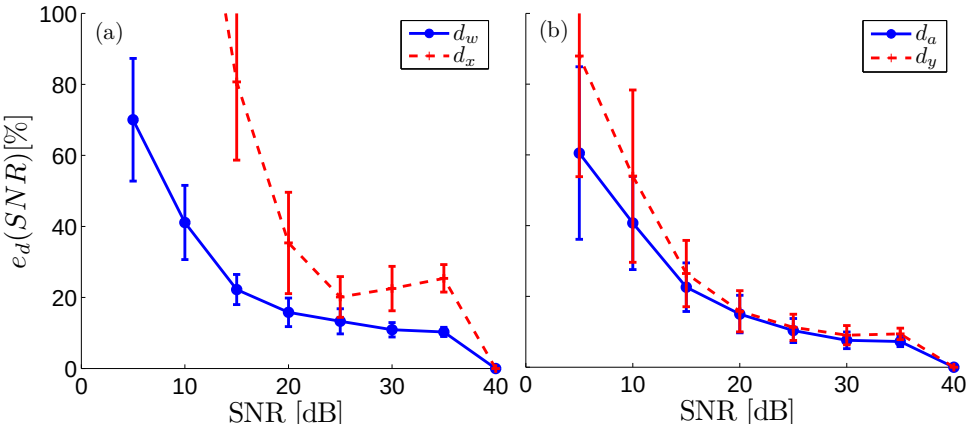

Figure 3.7: Relative error between (a) reference and estimated d_w (solid blue) and d_x (dashed red), and (b) reference and estimated d_a (solid blue) and d_y (dashed red), under the presence of additive Laplacian noise.

3.3.2 Electrophysiological Model

Figure 3.10, panels (a), show the simulation of the first scenario described in section 3.2.4, i.e. lengthening of the mean repolarization time, $\overline{\rho}$. Panels (b) illustrate the simulation of the second scenario, i.e. an increment of the dispersion of action potential repolarization times, σ. Panels (c) show the combined simulation of $\overline{\rho}$ and σ variation. Panels (d) show the simulation results of the fourth scenario described in section 3.2.4. Panels (a.1), (a.2) and (a.3) illustrate the range between the minimum and the maximum APD, with respect to $\overline{\rho}$ (a.1), σ (b.1) and $\overline{\rho}$ (c.1). Panel (d.1) shows an endocardial action potential, which does not change. Panels (a.2), (b.2) and (c.2) illustrate the mean action potential. The horizontal bars represent the corresponding range between the minimum and the maximum repolarization time. It should be noted that they are located slightly away from the mean repolarization time to avoid overlapping with the neighbouring horizontal bars, but it is only a matter of display. Panel (d.2) shows an epicardial action potential and the result of progressively increasing its duration (each color represents a different duration). Panels (a.3-d.3) show the principal component as a result of the projection of the modified action potentials. Panels (a.4-d.5) show the values of d_w (circle) and d_w^{NL} (triangle), and of d_a (circle) and d_a^{NL} (triangle), respectively in the four simulations.

3.3.3 ECG recordings

Analysis of Long-term T-wave Morphological Variability

Figure 3.11, left column, shows the boxplots of ΔRR (a.1), ΔQT, ΔTW and ΔTpe (a.2), ΔTA (a.3), d_w and d_w^{NL} (a.4) and d_a and d_a^{NL} (a.5) values, measured for (*LS-ES*),

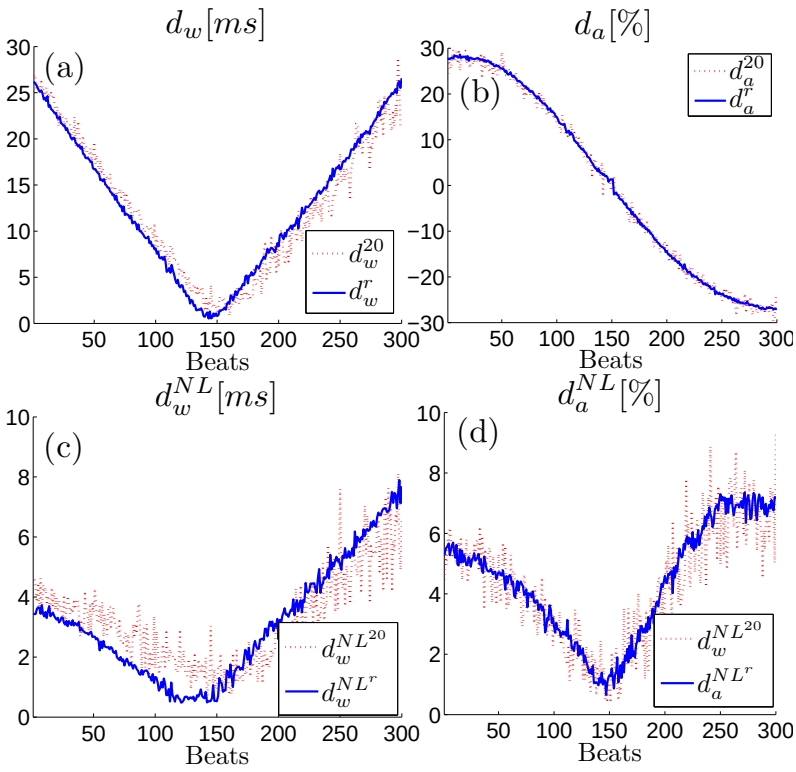

Figure 3.8: Evolution of d_w, d_a, d_w^{NL} and d_a^{NL} with respect to the level of linear and non-linear time and amplitude modulations in a noise-free scenario (solid blue) and under the presence of additive Laplacian noise with $SNR = 20$ dB (dashed red), when simulating large temporal variations, as in eq.(3.26).

(*TL-ES*) and (*LS-TL*).

Table 3.1 shows the correlation coefficient, when comparing *LS-ES*, *TL-ES*, and *LS-TL*, between (i) d_w and d_a, and between d_w^{NL} and d_a^{NL}; (ii) d_w and d_w^{NL} and each of the repolarization markers measuring time intervals, ΔQT, ΔTW and ΔTpe; (iii) d_a and d_a^{NL} and the repolarization marker measuring amplitude differences, ΔTA; and (iv) d_w, d_w^{NL}, d_a and d_a^{NL} and ΔRR.

The median (solid blue) and median + median absolute deviation (dotted red) of the resulting $x_{RR}(i)$, $x_{d_w}(i)$ and $x_{d_a}(i)$ series, calculated across subjects, are reported in Figure 3.12. Table 3.2 shows the median (IQR) values of $x_{RR}(i)$, $x_{d_w}(i)$ and $x_{d_a}(i)$ in the three windows.

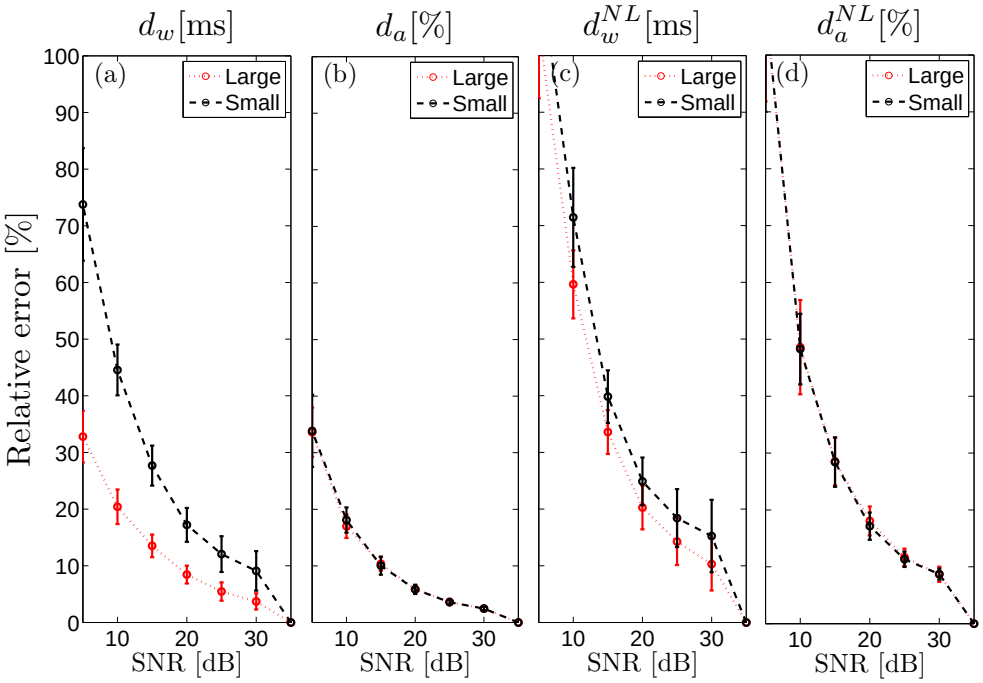

Figure 3.9: Relative error between reference and estimated d_w, d_a, d_w^{NL} and d_a^{NL} under the presence of additive Laplacian noise, when simulating large (solid) and small (dotted) time variations, as in eq.(3.26) and (3.27), respectively. Non-linear time variations and linear and non-linear amplitude changes are the same in all situations.

r	*LS-ES*	*TL-ES*	*LS-TL*
d_w vs. d_a	**-0.53**	-0.07	0.23
d_w^{NL} vs. d_a^{NL}	**0.72**	**0.77**	**0.69**
d_w vs. ΔQT	**0.55**	-0.38	**0.69**
d_w^{NL} vs. ΔQT	0.36	-0.36	0.18
d_w vs. ΔTW	**0.81**	**-0.60**	**0.71**
d_w^{NL} vs. ΔTW	**0.70**	-0.34	0.44
d_w vs. ΔTpe	**0.65**	0.10	-0.16
d_w^{NL} vs. ΔTpe	0.45	**0.75**	**-0.60**
d_a vs. ΔTA	**0.95**	**0.87**	**0.88**
d_a^{NL} vs. ΔTA	-0.41	-0.43	0.28
d_w vs. ΔRR	**0.55**	-0.41	**0.63**
d_w^{NL} vs. ΔRR	0.54	-0.45	0.26
d_a vs. ΔRR	-0.07	**0.55**	0.28
d_a^{NL} vs. ΔRR	0.36	-0.40	0.44

Table 3.1: Spearman's correlation coefficient, r, in the long-term analysis. Significant correlations are indicated in bold.

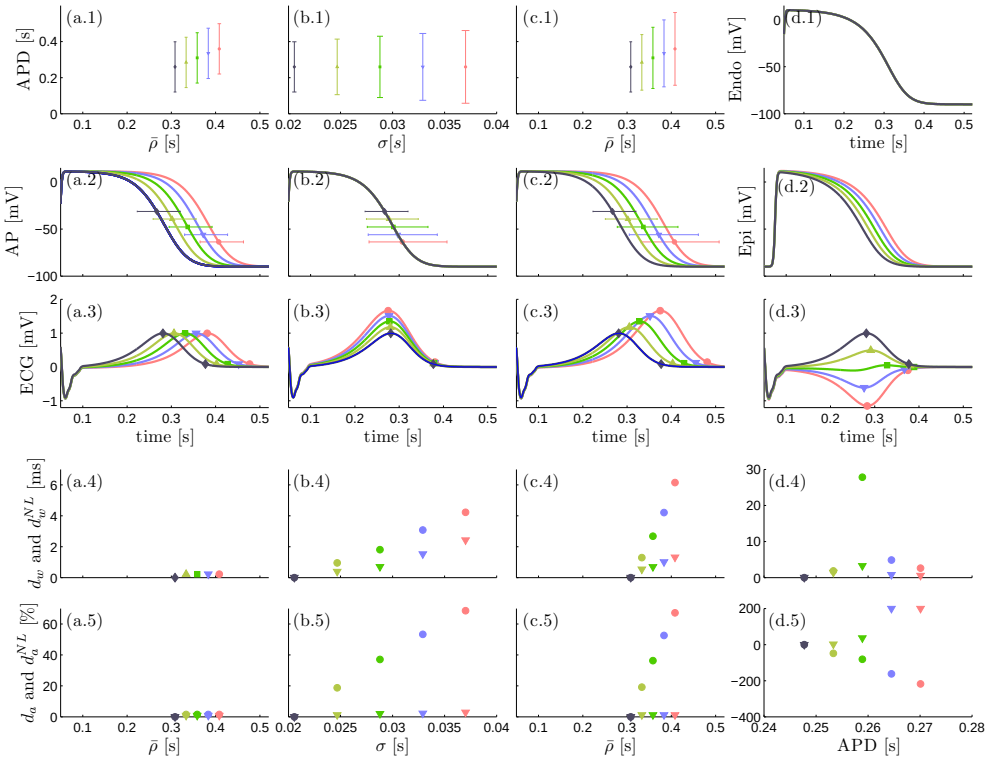

Figure 3.10: Performance evaluation using an electrophysiological cardiac model. (a.1-5): Increments of the mean repolarization time, $\overline{\rho}$. (b.1-5): Increments of the standard deviation of the dispersion of repolarization, σ. (c.1-5): Combined variation of $\overline{\rho}$ and σ. (d.1-5): Progressive variations of the epicardial APDs. (a.1-c.1): Range between the minimum and the maximum APD with respect to the variation. (a.2-c.2): Mean action potentials with respect to the variation. (d.1-2): Simulated action potential of endocardial and epicardial cells, respectively. (a.3-d.3): ECG beats corresponding to the modified action potentials. (d.4-d.5): d_w and d_a values (circles) and d_w^{NL} and d_a^{NL} values (triangles). Each color indicates a level of variation. Horizontal bars represent the range between the minimum and the maximum repolarization time.

	Early Supine	*Tilt*	*Late Supine*
$\mathbf{x_{RR}}$ [s]	1.01 (0.1)	0.77(0.2)*	1.06(0.2)†
$\mathbf{x_{d_w}}$ [ms]	1.30 (1.1)	6.64(3.3)*	1.97(2.3)*†
$\mathbf{x_{d_a}}$ [%]	-2.99 (7.9)	-9.36 (31.6)	-4.03 (17.8)

* Indicates significantly different ($p< 0.01$) with respect to *Early Supine*. † Indicates significantly different with respect to *Tilt*.

Table 3.2: Temporal evolution of the median (interquartile range), calculated across subjects, of RR, d_w and d_a during a Tilt test.

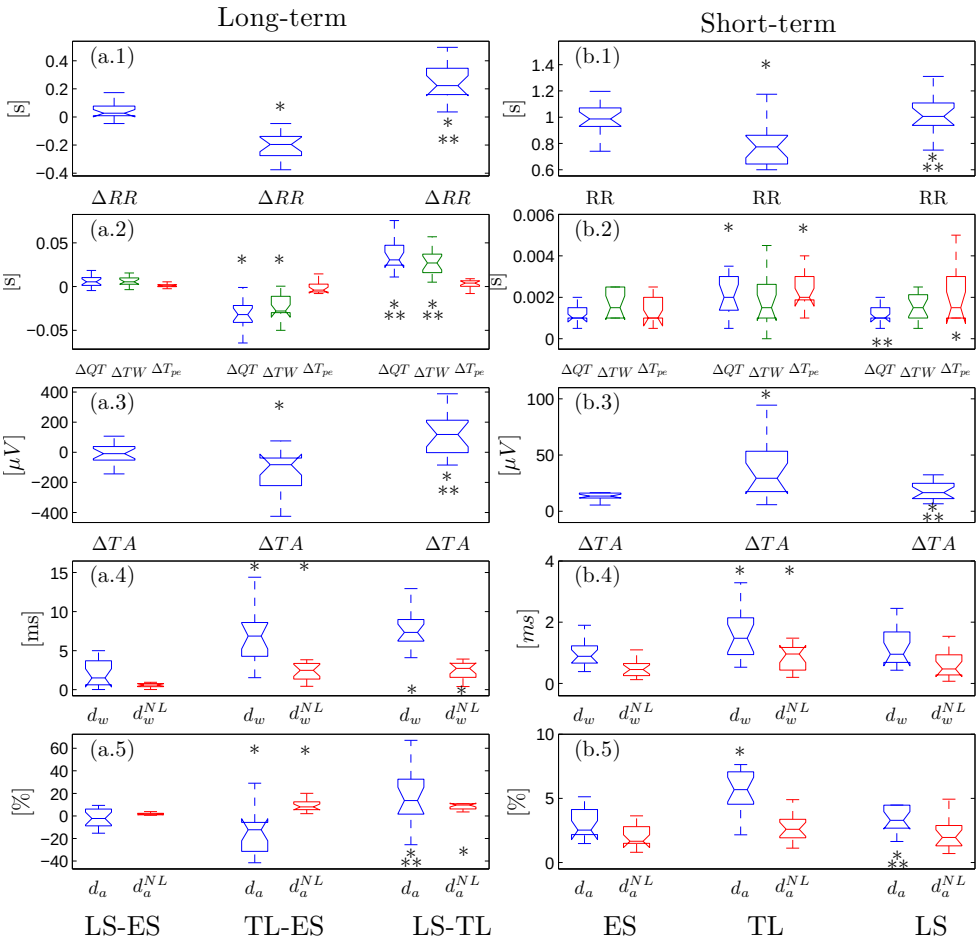

Figure 3.11: Left column, boxplots of ΔRR (a.1), ΔQT, ΔTW and ΔTpe (a.2), ΔTA (a.3), d_w and d_w^{NL} (a.4) and d_a and d_a^{NL} (a.5) values, across subjects, between the three windows along the recording. Right column, boxplots of the mean values of RR (b.1), median absolute deviation of QT, TW and Tpe (b.2) and TA (b.3), and mean d_w and d_w^{NL} (b.4) and d_a and d_a^{NL} (b.5) values at the three windows. $*$ indicates statistically significant differences with respect to the leftmost boxplot. $**$ indicates statistically significant differences between the central and rightmost boxplots. It should be noted that left and right panels have different scale.

Analysis of Short-term T-wave Morphological Variability

Figure 3.11, right column, shows the boxplots of the mean values of RR (b.1), median absolute deviation values of QT, TW and Tpe (b.2) and TA (b.3) with respect to their median value, d_w and d_w^{NL} (b.4) and d_a and d_a^{NL} (b.5) at the three windows.

Table 3.3 shows the correlation coefficient between d_w, d_w^{NL}, d_a and d_a^{NL}, and the median RR and SNR values for each window separately and when pooling them into

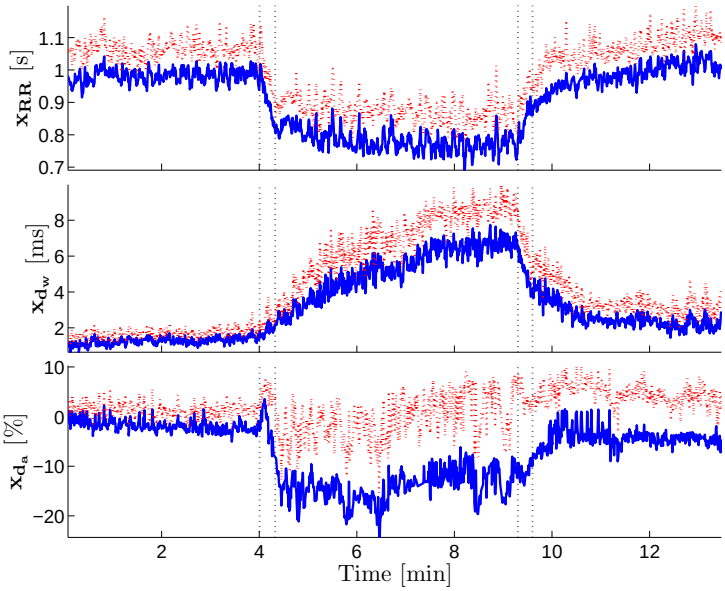

Figure 3.12: Median (blue) and median + median absolute deviation (red) of the RR (top panel), d_w (middle panel) and d_a (bottom panel) series during a Tilt test, calculated across subjects. The mean warped T-wave of 20 T-waves from the beginning of the recording is selected as the reference T-wave for the computation of the d_w and d_a series. Vertical lines indicate the start and end of the change in the table tilt.

a single group *ES+TL+LS*.

r	*ES*	*TL*	*LS*	*ES+TL+LS*
d_w vs. SNR	**-0.68**	**-0.60**	**-0.61**	**-0.70**
d_w^{NL} vs. SNR	**-0.61**	**-0.55**	**-0.81**	**-0.74**
d_w vs. RR	-0.16	**-0.54**	-0.14	**-0.37**
d_w^{NL} vs. RR	0.01	-0.40	-0.01	**-0.30**
d_a vs. SNR	**-0.93**	**-0.71**	**-0.83**	**-0.85**
d_a^{NL} vs. SNR	**-0.90**	**-0.69**	**-0.86**	**-0.84**
d_a vs. RR	-0.17	-0.17	-0.09	**-0.39**
d_a^{NL} vs. RR	-0.19	-0.41	-0.28	**-0.41**

Table 3.3: Spearman's correlation coefficient, r, in the short-term analysis. Significant correlations are indicated in bold.

3.3.4 Computational Time

As a reference for computational time estimation, the calculation of d_w and d_a when comparing two T-waves took 1.31 seconds with the personal computer and software

described in section 2.2.7. The computation of the mean warped T-wave was slower, needing 47 seconds to calculate the mean warped T-wave of a set of 20 T-waves. It should be advised that the algorithm has not been optimized in terms of computational time, since the current time is not considered a bottle neck for the technology to be used in clinical practice.

3.4 Discussion

In this chapter, we introduced four novel ECG-derived indices, d_w and d_a, that independently quantify T-wave morphological variability in the temporal and amplitude domains, respectively, and d_w^{NL} and d_a^{NL}, that isolate the non-linear information present within d_w and d_a, respectively. We evaluated the accuracy of d_w, d_a, d_w^{NL} and d_a^{NL} under the presence of additive Laplacian noise. We investigated the relationship between d_w, d_a, d_w^{NL} and d_a^{NL} and the induced morphological variations at cardiac cellular level and we evaluated the extent of T-wave time and amplitude changes produced by a tilt test in real ECG, and the correlation of d_w, d_a, d_w^{NL} and d_a^{NL} with the heart rate and with well-known time and amplitude-based repolarization markers.

3.4.1 Square-root Slope Function Outperforms Dynamic Time Warping in Removing Temporal Variability

The warping algorithm is expected to selectively compensate for the time domain variability, so in our first simulation (section 3.2.3), the resulting warped T-wave should be a scaled version of the original $\boldsymbol{f}^r(\boldsymbol{t}^r)$. However, this is only obtained using SRSF (Figure 3.5, right panels), because DTW (left panels) provides a warped T-wave different from the expected one. We, thus, have supported previous studies reporting the limitations of DTW [228, 229, 241]. Since it is not symmetric ($\|\boldsymbol{f}^r(\boldsymbol{t}^r) - \boldsymbol{f}^s(\boldsymbol{\gamma}(\boldsymbol{t}^r))\| \neq \|\boldsymbol{f}^s(\boldsymbol{t}^s) - \boldsymbol{f}^r(\boldsymbol{\gamma}^{-1}(\boldsymbol{t}^s))\|$), it is not a proper distance and leads to degenerate results if $\boldsymbol{f}^r(\boldsymbol{t}^r)$ and $\boldsymbol{f}^s(\boldsymbol{t}^s)$ present variations in the amplitude domain ("pinching effect") [231]. The SRSF metric, however, is a proper distance, and overcomes the limitations of DTW [228, 229, 241].

3.4.2 The Markers d_w and d_a Are More Robust than d_x and d_y

The relative error values of d_x and d_y are higher than those from d_w and d_a for every value of SNR (Figure 3.7). This is because the SRSF transformation used for the calculation of d_x and d_y (equations 3.9 and 3.11) highlights the high-frequency components of the signal, resulting in less robust estimates against additive broadband noise (derivative transformation in equation 3.2). Therefore, d_w and d_a were chosen as the preferred markers of time and amplitude variability, given their superior robustness against noise and their physiological interpretation (they are both calculated in the original domain).

3.4.3 The Markers d_w and d_w^{NL}, and d_a and d_a^{NL} Independently Capture Time and Amplitude Variability

The evaluation of the accuracy of d_w, d_a, d_w^{NL} and d_a^{NL} in detecting linear and non-linear modulations of the T-wave time domain and amplitude, respectively, in a simulated ECG signal under the presence of additive Laplacian noise confirmed that the four markers were able to robustly and independently capture both modes of variation, with no coupling between the different sources of variability, i.e. the evolution of d_w and d_w^{NL} was independent from that of d_a and d_a^{NL} (Figure 3.8). The values of relative error remained lower than 20% for $SNR = 20$ dB, indicating that these markers can be robustly used in ambulatory Holter ECG (Figure 3.9). When the simulated time domain variations were small, the relative error increased for low SNR because noise dominates over time domain variations of the T-wave.

3.4.4 The Markers d_w, d_w^{NL}, d_a and d_a^{NL} Reflect Variations in Dispersion of Repolarization

The assessment of the relationship between T-wave time and amplitude variations and morphological changes at cardiac cellular level using an electrophysiological cardiac model [234] showed that a variation in the mean repolarization time, $\overline{\rho}$, provoked a shift in the T-wave but with no significant T-wave temporal or amplitude variation (Figure 3.10, (a.3)). Therefore, d_w, d_w^{NL}, d_a and d_a^{NL} were equal to zero for every $\overline{\rho}(j)$ ((a.4)-(a.5)). On the contrary, increments of the dispersion of action potential repolarization times, σ, produced an increment in the range of the APD (b.1) and in the range between the minimum and the maximum repolarization time (b.2). This led to an homogeneous increment in the amplitude and to a linear and non-linear increment of the width of the T-wave, which was reflected in higher values of d_w, d_w^{NL} and d_a, while d_a^{NL} remained zero (panels (b.3)-(b.5)). The combined variation of $\overline{\rho}$ and σ produced values of d_w, d_w^{NL}, d_a and d_a^{NL} very similar to those of scenario 2. Progressive increments in the epicardial repolarization time provoked heterogeneous changes in the morphology of the T-wave (d.3) and eventually, when the mean epicardial repolarization time was longer than the mean endocardial repolarization time, its inversion. Panels (d.4)-(d.5) illustrate that d_a followed the increment in amplitude variability (due to the T-wave inversion), while d_w measured the asymmetry present in the T-wave when its amplitude was close to zero. In this case, both d_w^{NL} and d_a^{NL} captured the non-linear time and amplitude, respectively, variations induced by the simulation. These results suggest that d_w, d_w^{NL}, d_a and d_a^{NL} mainly represent changes in spatio-temporal dispersion of repolarization rather than in its mean, with d_w^{NL} and d_a^{NL} being only sensitive to the variations of spatio-temporal dispersion of repolarization times reflected as non-linear morphological changes of the T-wave.

The purpose of the long-term analysis was to evaluate the ability of the proposed markers to capture the T-wave morphological changes induced by the orthostatic stress, and their interaction with changes in the heart rate. We, then, assumed a similar situation to that from scenario 3) in section 3.2.4, i.e. variations in repolariza-

tion dispersion as a result of variations in heart rate, but in actual ECG records. The orthostatic stress produced significant decrements of the RR, QT, TW and TA values (Figure 3.11). Regarding Tpe, 13 subjects reflected a shorter Tpe during *TL*, while this interval increased for the other 4 subjects. The proposed markers supported these results, showing significant increments in linear and non-linear temporal and amplitude variations after an orthostatic stress. The correlation analysis (Table 3.1) showed that d_w was correlated with ΔRR, ΔQT and ΔTW, whereas d_w^{NL} was only correlated with ΔTpe. These results may indicate that the orthostatic stress produces a change in heart rate, inducing linear variations in the QT and TW intervals, which dominate in d_w. The strong correlation between d_w^{NL} and ΔTpe suggests that d_w^{NL} is mainly related to variations in the dispersion of repolarization, independently from changes in heart rate. Regarding the amplitude markers, d_a was highly correlated with ΔTA, whereas d_a^{NL} was completely uncorrelated to it, therefore reflecting information not contained in ΔTA. It can be observed in Figure 3.12 how the d_w series follows opposite dynamic to the RR series, with significantly higher values during the Tilt, confirming that an orthostatic challenge provokes an increment in the time domain differences of the T-waves. The adaptation of the values of d_w to those of RR is slow, indicating that this series is also affected by the memory present in ventricular repolarization. The d_a series, however, shows that, in median, the T-wave amplitude decreases during Tilt, but the variability is very large, so the differences between stages are not significative (Table 3.1).

The purpose of the short-term analysis was similar to that from scenario 2) in section 3.2.4, i.e. evaluation of the variations in repolarization dispersion at stable heart rate. Results showed that the variability of QT and Tpe intervals, and TA was significantly higher during *TL* than *ES* or *LS*. This was supported by the values of d_w, d_a and d_w^{NL}, which reflected significantly increased variability in *TL* as compared to supine (Figure 3.11). There was a weak negative correlation between d_w, d_a, d_w^{NL} and d_a^{NL}, and the median RR (Table 3.3), indicating that the short-term changes in dispersion of repolarization, reflected on the ECG through linear and non-linear T-wave morphological variations, increase at shorter RR interval values. This may be in corcondance with studies reporting steeper slopes of repolarization restitution at shorter RR values (Figure 3.4) [53]. The correlation values with respect to the SNR indicate that beat-to-beat analysis should be done on clean recordings.

Considering the results of this work, the proposed methodology and morphological variability markers might provide additional information to that offered by time-interval markers, which may eventually lead to an improved prediction.

3.4.5 Technical Considerations

Warping of time domain has often been used in the ECG signal to compensate for the missalignments before measuring amplitude differences, or to quantify time interval variabilities, like those from the QT interval, using linear [161, 171, 242] and non-linear [243] time warping. The most common algorithm for non-linear time warping is DTW [243], but it fails when the two observed functions also present amplitude

variabilities [231]. To prevent this problem, the derivative DTW was proposed [244]. This modification aligns the derivative of the observed functions, rather than their amplitude values. The SRSF used in this work makes the norm to be minimized in equation (3.3) to become a proper distance and overcome the "pinching effect", as explained in [228,229,231]. Also, a novel technique to allow for warping in both temporal and amplitude domains has been recently proposed to enable complex adaptations to the morphology of the waveform [227]. The novelty of this work is based on the extraction of indices from the warping information and from the warped signals to quantify the amount of morphological variability.

We applied principal component analysis to obtain a lead projected onto the direction of maximal energy of the T-wave. However, the selection of the lead does not affect the technicalities of the proposed algorithm, since this methodology can be applied to any single lead, which is its main advantage with respect to other methodologies that require the vectorcardiogram, or the information of more than one lead [224].

3.4.6 Limitations

There are several aspects that could influence the estimation reliability of the proposed indices. First, due to the high sensitivity of the warping function, erroneous extraction of the morphology of the T-wave, due to excessive noise or delineation errors, will lead to incorrect values of d_w and d_w^{NL}, and an incorrect warping. Therefore, the markers d_a and d_a^{NL} could also be affected, coupling, in some way, the robustness and sensitivity of the indices. Second, although the proposed markers capture many T-wave morphologies, there can appear extreme morphological variations which will lead to meaningless interpretations of d_w, d_a, d_w^{NL} and d_a^{NL}. However, we have not found any such extreme variation in the analysed T-waves, since even for biphasic or S-shaped T-waves we still obtained interpretable results. Next, we selected the first principal component as the lead capturing the direction of maximal variation of the repolarization gradient. Although we assumed that a projection of the maximal energy onto this component also implied a maximal projection of the repolarization variability, given the physiological additive generation of the ECG signals, this may not always be guaranteed. Finally, this first principal component may be dominated by precordial lead T-waves, which have the highest amplitude and, therefore, in this study, the algorithm did not capture the morphological variation reflected in other leads.

3.5 Conclusion

In this chapter, we introduced two ECG-derived markers, d_w and d_a, and their nonlinearly restricted versions, d_w^{NL} and d_a^{NL}, to quantify single-lead T-wave morphological variability by time-warping metrics. Our findings demonstrate that variations in the dispersion of repolarization, reflected in the ECG through changes in the temporal and amplitude organization of the T-wave, can be robustly captured by d_w and d_a,

respectively, with d_w^{NL} and d_a^{NL} measuring the heterogeneous T-wave variations. In the next chapter we will evaluate the potential of the proposed markers of T-wave time and amplitude variability to be used as arrhythmic risk predictors.

Chapter 4

Predictive Risk Value of Repolarization Restitution Estimated from Morphological ECG Markers

4.1 Introduction

Figure 4.1 (a), shows a diagram of the hypothesis presented in this chapter. The different curves represent the relationship between different ventricular APDs computed at steady-state and the corresponding RR values at which those APDs were measured, i.e. the dynamic APDR curves. The morphology of the T-wave reflects the distribution of the repolarization sequence along the ventricle [220–222]. Then, the dispersion of the restitution curves at a certain RR value (RR_1) is reflected in the ECG as a certain T-wave morphology (solid blue T-wave). Dispersion of the restitution curves at a different RR (RR_2) may have a different distribution (in the figure, this concept is illustrated as an increased separation of the restitution curves), corresponding in the ECG with a different T-wave morphology (dashed red T-wave). Then, based on previous evidences [53, 54], our hypothesis is that higher variations in the dispersion of repolarization restitution will be manifested as higher variations in the T-wave morphology per increment in the RR interval, i.e. steeper slopes of T-wave morphology restitution, and this will be related with an increased arrhythmic risk.

Therefore, in this chapter we developed a fully automated algorithm to calculate the slope of the T-wave morphology restitution using the methodology that quantifies the morphological differences between T-waves [245], described in the previous chapter. Then, we studied the modulation of the circadian pattern on this slope and we assessed its SCD and PFD predictive value. Finally, we studied the classification performance, individually and in combination with the two ECG-derived indices quantifying TWA and HRT used for the same objective in chapter 2.

4.2 Methods

4.2.1 Study Population

We used the 24-h ECG recordings from the MUSIC study (section 2.2.1) for the assessment of the predictive value and classification performance, of the T-wave morphology restitution in 651 CHF patients.

4.2.2 ECG Pre-processing

Preprocessing of the ECG signals was performed using custom-written software and included low pass filtering at 40 Hz to remove electric and muscle noise, cubic splines interpolation for baseline wander removal, and ectopic beats detection.

PCA (section 1.3.2) was applied over the two-or-three available ECG leads to emphasize the energy of the T-wave and improve its delineation [195]. As previously described, the PCA training matrix, $\mathbf{L}_{\mathrm{T}}$, was built by only considering the samples

from the T-waves on each lead. First, a single-lead-and-rules delineation technique (section 1.3.3) was applied to select the samples from the T-wave and compute the matrix $\mathbf{L}_{\mathrm{T}}$. Then, the first principal component was computed and delineated using a single-lead technique (section 1.3.3) [66]. From the delineation marks, the RR interval series was obtained and the T-waves were selected using the known delimitation marks.

4.2.3 Dispersion of Repolarization Restitution from the T-wave Morphology

Automatic quantification of the T-wave morphology restitution was performed on every ECG recording in 4 steps:

1. **Selection of T-waves:** First, the histogram of the RR series was calculated during the entire 24-h recording, and it was divided into bins of 10 ms wide. Then, only the bins having at least 50 values were selected (bins above the horizontal dotted line in Figure 4.1 (b)). Next, two RR bins, distributed symmetrically around the median RR (Figure 4.1 (b), green arrow), were chosen as those defining the maximum intra-subject RR range, ΔRR, for the study (Figure 4.1 (b), blue and red bins, respectively). These two bins would correspond to RR_1 and RR_2 in panel (a). Then, the T-waves corresponding to the beats associated with the RR intervals within these two bins were considered for the analysis.

2. **Mean warped T-waves:** The methodology described in the previous chapter (section 3.2.2) was applied to calculate the mean warped T-waves of those T-waves selected from each RR bin (Figure 4.1 (c)). These mean warped T-waves are representatives of the average T-wave morphology at each RR. Based on our assumption, they would, then, reflect the dispersion of repolarization at each RR (panel a).

3. **Quantification of the T-wave morphological differences:** The morphological differences between both mean warped T-waves were quantified using the morphological variability indices proposed in the previous chapter [245]. Before applying the methodology, the gravity centres of both signal-averaged T-waves were also aligned to make the optimal warping function, $\boldsymbol{\gamma}^*_{\mathrm{TW}}(\boldsymbol{t}^r)$, only dependent on changes in the T-wave morphology, and not on global shifts. Figure 4.1 (d.1), shows both mean warped T-waves, where their morphological difference can be appreciated, and panel (d.2) shows $\boldsymbol{\gamma}^*_{\mathrm{TW}}$. As a reminder, the separation of this function from the diagonal, quantified by d_w and d_w^{NL} [245], measures the morphological differences in the time domain between the two mean warped T-waves. Note that, as explained in chapter 3, if this line corresponded to the diagonal, no temporal transformation would be needed meaning that the morphological differences would be non-existent. Panel (d.3) shows the warped mean T-waves. The amplitude difference between these warped T-waves would be quantified by d_a and d_a^{NL}.

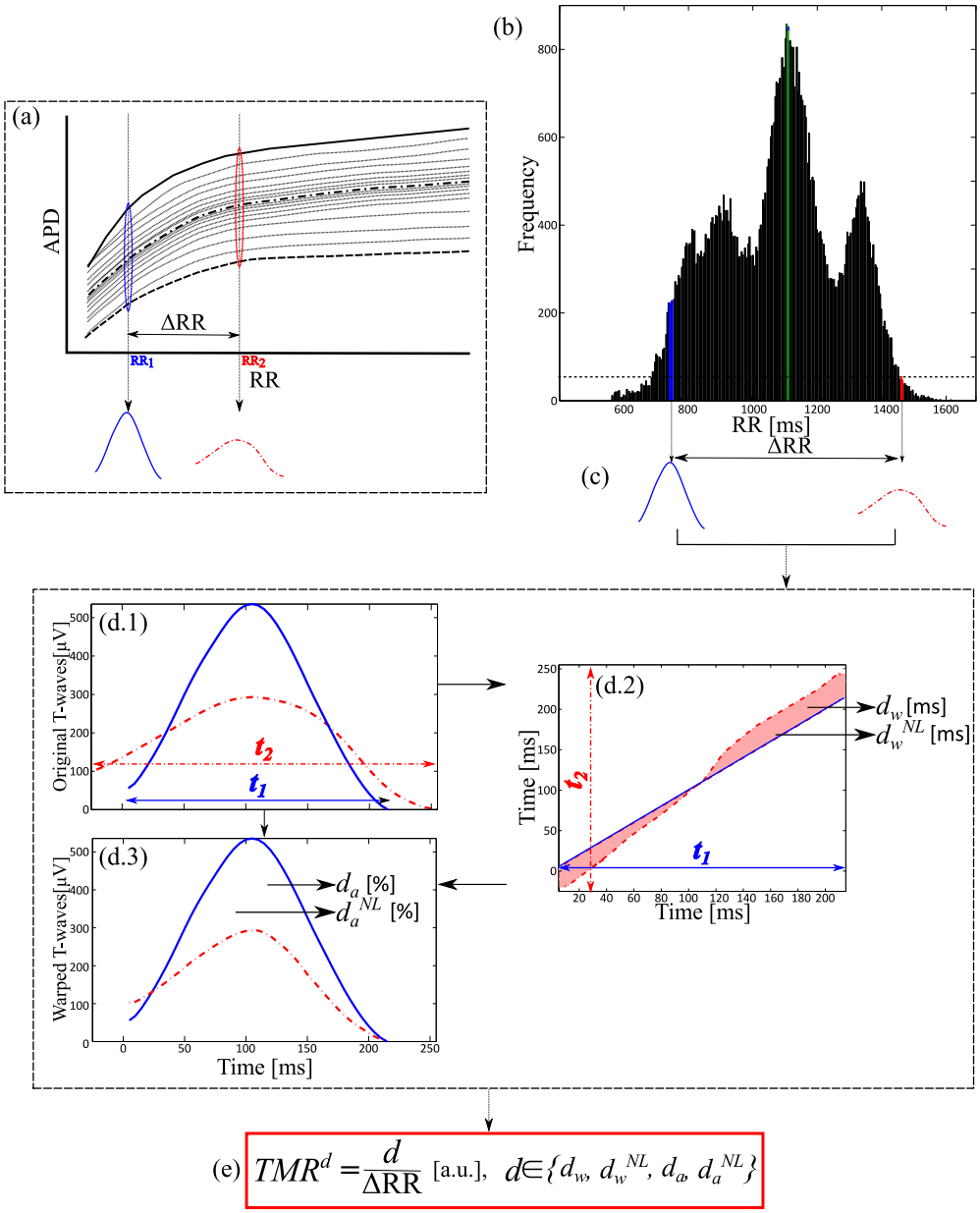

Figure 4.1: Quantification of the T-wave morphology restitution. (a) Diagram illustrating the hypothesis underlying the proposed methodology: changes in the dispersion of repolarization with RR are reflected as a variation in the morphology of the T-wave with RR. (b): RR histogram with bins of RR=10 ms. Green bin shows the median RR interval value. Blue and red bins indicate the RR values defining the maximum intra-subject range. (c): Mean warped T-waves of those T-waves associated with the RR values selected in (b). (d) Quantification of the morphological difference between both mean warped T-waves using the methodology from chapter 3. (e) The indices of T-wave morphology restitution are calculated as the quantification of the T-wave morphological difference using the morphological variability markers from chapter 3, normalized by the difference between the RR values of both bins, ΔRR.

4. **Computation of the indices of T-wave morphology restitution:** The indices TMR^d, where $d \in \{d_w, d_w^{\text{NL}}, d_a, d_a^{\text{NL}}\}$, were calculated by dividing any of the morphological markers presented in the previous chapter by ΔRR (Figure 4.1 (e)). The markers TMR^d, then, are a measure of the T-wave morphological change per RR increment and were estimated in analogy to a restitution slope.

4.2.4 Circadian Modulation

As described in chapter 2, we evaluated the circadian modulation of TMR^d in 24-h hour Holter recordings from CHF patients. For the characterization of the circadian modulation of these parameters, we divided the 24-h ECG recordings into 6-hour segments. Then, in each 6-hour segment, we derived TMR^d, following the methodology described in the previous section.

4.2.5 Comparison with other ECG Risk Markers

We used the markers $\Delta\alpha^{\text{QT}}$, $\Delta\alpha^{\text{Tpe}}$, IAA and TS, computed in chapter 2, for the comparison with the morphological restitution indices proposed in this chapter.

4.2.6 Statistical Analysis

Two-tailed Mann-Whitney and Fisher exact test were used for univariate comparison of quantitative and categorical data, respectively. Correlation was evaluated with Spearman's correlation coefficient. ROC curves were used to test the ability to predict the endpoint and to set cut-off points for risk-stratification. Survival probability was estimated by Kaplan-Meier methods with a comparison of cumulative events performed by using log-rank tests. Patients who died from causes not included in the endpoints were censored at the time of death. Univariate and multivariate Cox regression analyses were performed to determine the predictive value of the risk markers. For multivariate analysis, only the clinical and ECG-derived variables with significant association with SCD in univariate analysis were included in the model. Then, the morphological restitution indices proposed in this chapter were added one at a time into the model. A classifier was also implemented based on a two- and three-class SVM, as done in chapter 2.

4.2.7 Robustness Evaluation

To evaluate the robustness of TMR^d, we repeated the calculation in the even and odd hours, and in the first and last 12 h of the ECG recordings, separately, and we computed the Spearman correlation coefficient and the Kendall's W coefficient of concordance. Bland-Altman was also used to visualize the possible bias that the calculation of TMR^d in different ECG segments may introduce.

4.3 Results

4.3.1 Association with Clinical Data

The histogram of TMR^{d_w}, $TMR^{d_w^{\mathrm{NL}}}$, TMR^{d_a}, and $TMR^{d_a^{\mathrm{NL}}}$ is shown in Figure 4.2 and their 25th, 50th, and 75th percentiles are specified in each panel.

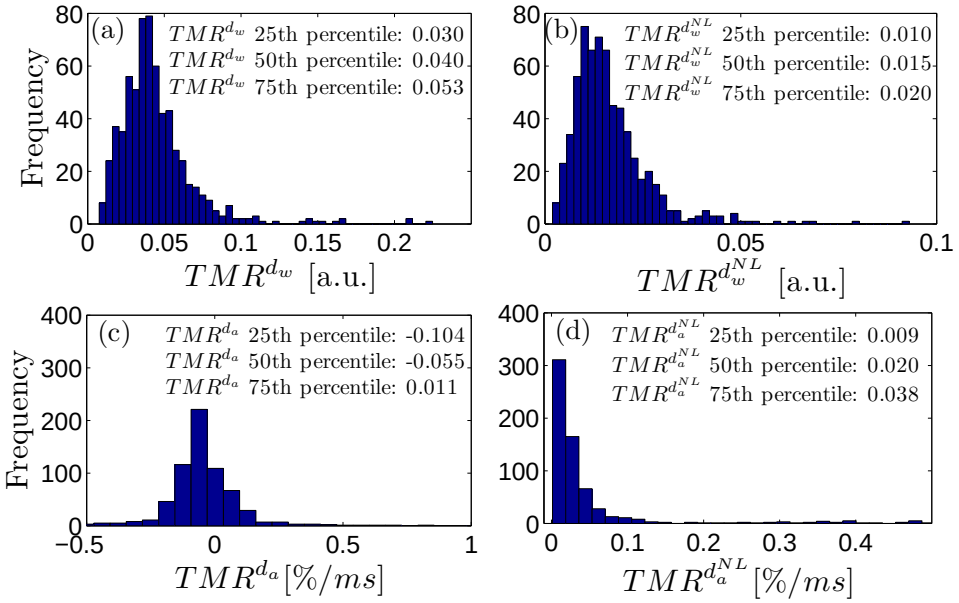

Figure 4.2: Histogram of TMR^{d_w} (a), $TMR^{d_w^{\mathrm{NL}}}$ (b), TMR^{d_a} (c) and $TMR^{d_a^{\mathrm{NL}}}$ (d) using 50 equally spaced bins.

Table 4.1 shows the correlation coefficients between the parameters under study and the median RR and the range of RR. As observed, the markers of restitution of the time domain morphological variability, TMR^{d_w} and $TMR^{d_w^{\mathrm{NL}}}$, presented a significantly weak correlation with the range of RR. The correlation between these two markers was $\rho = 0.557$ ($p<0.001$), the correlation between the markers of restitution of the amplitude domain morphological variability, TMR^{d_a} and $TMR^{d_a^{\mathrm{NL}}}$, was $\rho = -0.094$ ($p=0.017$). The correlation between TMR^{d_w} and TMR^{d_a} was $\rho = 0.091$ ($p=0.021$), and between $TMR^{d_w^{\mathrm{NL}}}$ and $TMR^{d_a^{\mathrm{NL}}}$ was $\rho = 0.280$ ($p<0.001$).

Mann-Whitney U-test showed that TMR^{d_w} and TMR^{d_a} (in absolute value) were significantly higher in women ($p<0.001$) and ($p=0.004$), respectively. The index TMR^{d_a} was the only marker of restitution of morphological variability being significantly different in patients with depressed LVEF, as compared to patients with preserved LVEF ($p<0.001$), showing lower absolute values in the latter. Similarly, this index was the only marker with significant differences between NYHA classes

Variable	Median RR		RR range	
	ρ	p	ρ	p
TMR^{d_w}	-0.008	0.847	**-0.287**	**<0.001**
$TMR^{d_w^{\mathrm{NL}}}$	**-0.107**	**0.006**	**-0.365**	**<0.001**
TMR^{d_a}	**0.095**	**0.016**	**0.094**	**0.017**
$TMR^{d_a^{\mathrm{NL}}}$	-0.004	0.916	**-0.088**	**0.024**

Significant differences are indicated in bold.

Table 4.1: Correlation of TMR^{d_w}, $TMR^{d_w^{\mathrm{NL}}}$, TMR^{d_a} and $TMR^{d_a^{\mathrm{NL}}}$ with median RR and RR range.

(p=0.020), presenting higher absolute values in patients in NYHA class III.

4.3.2 Circadian Modulation

Figure 4.3 shows the circadian modulation of the four parameters defining the T-wave morphology restitution. As shown, the restitution of the amplitude variations of the T-wave, quantified by TMR^{d_a}, was significantly higher, in absolute values, during all day segments (early morning, afternoon and evening), as compared to night (c). The restitution of the parameters quantifying time and non-linear amplitude variations was not significantly modulated by the circadian pattern.

Table 4.2 shows the median (IQR) values of the parameters defining the T-wave morphology restitution in the "12-18" and "00-06" segments, but distinguishing between women and men. As shown, the four markers reflecting restitution of the T-wave morphology were significantly higher in women than in men during day and during night.

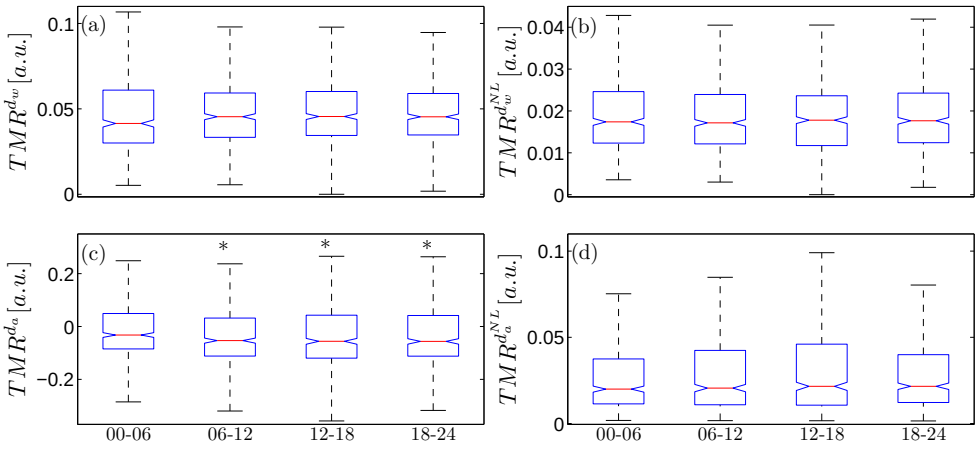

Figure 4.3: Circadian pattern of TMR^{d_w} (a), $TMR^{d_w^{\mathrm{NL}}}$ (b), TMR^{d_a} (c), and $TMR^{d_a^{\mathrm{NL}}}$ (d). * indicates significant differences with respect to "00-06".

	Women	Men	p-value
TMR^{d_w}			
"12-18"	0.058 (0.04)	0.044 (0.03)	**<0.001**
"00-06"	0.048 (0.04)	0.038 (0.03)	**<0.001**
$TMR^{d_w^{\mathrm{NL}}}$			
"12-18"	0.021 (0.02)	0.018 (0.01)	**0.012**
"00-06"	0.018 (0.01)	0.016 (0.01)	**0.004**
TMR^{d_a}			
"12-18"	-0.093 (0.16)	-0.042 (0.16)	**<0.001**
"00-06"	-0.067 (0.15)	-0.017 (0.12)	**<0.001**
$TMR^{d_a^{\mathrm{NL}}}$			
"12-18"	0.025 (0.04)	0.022 (0.04)	0.071
"00-06"	0.023 (0.04)	0.018 (0.03)	**0.005**

Significant differences are indicated in bold
Data are represented as median (IQR).

Table 4.2: Gender differences for day and night values of the parameters definind the T-wave morphology restitution

4.3.3 Survival Analysis

Figure 4.4 shows the boxplots of TMR^{d_w} (a), $TMR^{d_w^{\mathrm{NL}}}$ (b), TMR^{d_a} (c) and $TMR^{d_a^{\mathrm{NL}}}$ (d) in the group of SCD victims, PFD victims and in the rest of patients. As shown, TMR^{d_w} was the only marker with significantly higher values in SCD ($p<0.001$) and CD ($p=0.029$) victims, as compared to non-SCD and non-CD victims, respectively. The values of TMR^{d_w} were not significantly different in the group of PFD victims. The three other indices, $TMR^{d_w^{\mathrm{NL}}}$, TMR^{d_a} and $TMR^{d_a^{\mathrm{NL}}}$, were not significantly different in any of the three groups (SCD victims, PFD victims or non-CD patients).

According to the AUC, TMR^{d_w} separated SCD victims from the rest of patients ($p<0.001$) (Figure 4.5). The optimal threshold, based on ROC curve analysis, was $TMR^{d_w} = 0.040$. Therefore, patients were dichotomized into $TMR^{d_w}<0.040$ and $TMR^{d_w} \geqslant 0.040$ groups. Of the 651 patients studied, 340 (52%) were included in the $TMR^{d_w}<0.040$ group and 311 (48%) in the $TMR^{d_w} \geqslant 0.040$ group.

Table 4.3 shows the percentage of patients in the two risk groups defined by TMR^{d_w}, with the categorical variables described in the first column. For continuous variables, data are represented as mean $\pm$ standard deviation. Upon comparison of clinical variables, patients in the $TMR^{d_w} \geqslant 0.040$ group, as compared to patients in the $TMR^{d_w}<0.040$ group, were more frequently women, more frequently had ischaemic etiology, showed lower values of median RR, RR range, QRS width and TS, and higher values of $\Delta\alpha^{\mathrm{QT}}$ and $\Delta\alpha^{\mathrm{Tpe}}$.

Table 4.4 shows the percentage of patients in the two groups defined by TMR^{d_w}, with the modes of death defined in the first column. As it can be observed, SCD was significantly higher in the $TMR^{d_w} \geqslant 0.040$ group as compared to the other group. There was no significant association between $TMR^{d_w} \geqslant 0.040$ and CD or PFD.

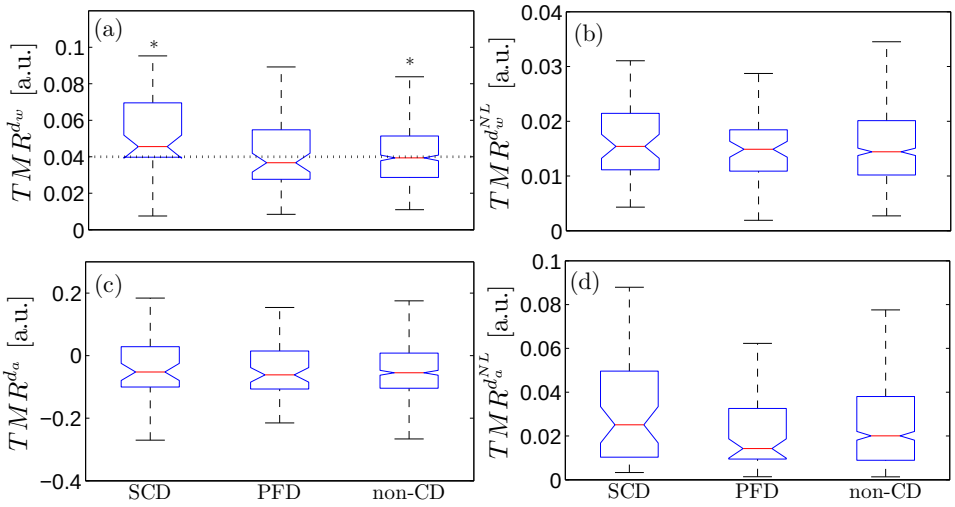

Figure 4.4: Boxplot of TMR^{d_w} (a), $TMR^{d_w^{\mathrm{NL}}}$ (b), TMR^{d_a} (c) and $TMR^{d_a^{\mathrm{NL}}}$ (d) for SCD, PFD victims and survivors of CD. * Indicates statistical significance between each outcome and the group formed by the other two. The dotted horizontal line illustrates the optimal threshold for SCD.

Univariate Cox analysis revealed that $TMR^{d_w} \geqslant 0.040$ was the variable with the highest hazard ratio among those associated with SCD (Table 4.5). Univariate Cox analysis confirmed that no significant association was found between $TMR^{d_w} \geqslant 0.040$ and CD or PFD. The only clinical and ECG-derived indices with significant association with SCD were gender, NYHA class, LVEF, TS$\leqslant$ 2.5 ms/RR, IAA$\geqslant$3.7μV, NSVT and more than 240 VPBs in 24 h, and the range of RR. The duration of the QRS complex was not associated with increased SCD risk. Figure 4.6 shows Kaplan-Meier probabilities of SCD for the two groups defined by TMR^{d_w}. The high SCD risk group is illustrated in dashed red, and the low SCD risk group is shown in solid blue. Patients with $TMR^{d_w} \geqslant 0.040$ had an estimated 4-year SCD rate of 13% vs 4% in patients with $TMR^{d_w} < 0.040$. Table 4.6 shows the univariate hazard ratios of TMR^{d_w} for SCD risk prediction in the overall population and when dividing according to different clinical variables. As observed, $TMR^{d_w} \geqslant 0.040$ was not significantly associated with SCD in women, in NYHA class III, in patients with preserved LVEF or in patients under treatment with amiodarone. The association with SCD was significant in both ischemic and non-ischemic patients.

Multivariate Cox proportional hazard models were constructed by adjusting for the variables that were significantly associated with SCD in univariate analysis. The variables that remained significant were gender, NYHA class, TS, IAA and $\Delta\alpha^{\mathrm{Tpe}}$. When adding $TMR^{d_w} \geqslant 0.040$ to the multivariate model, it was the variable most significantly associated with SCD risk, followed by gender (Table 4.5). As observed, the time to SCD event was approximately tripled among patients with $TMR^{d_w} < 0.040$ in comparison to those with $TMR^{d_w} \geqslant 0.040$.

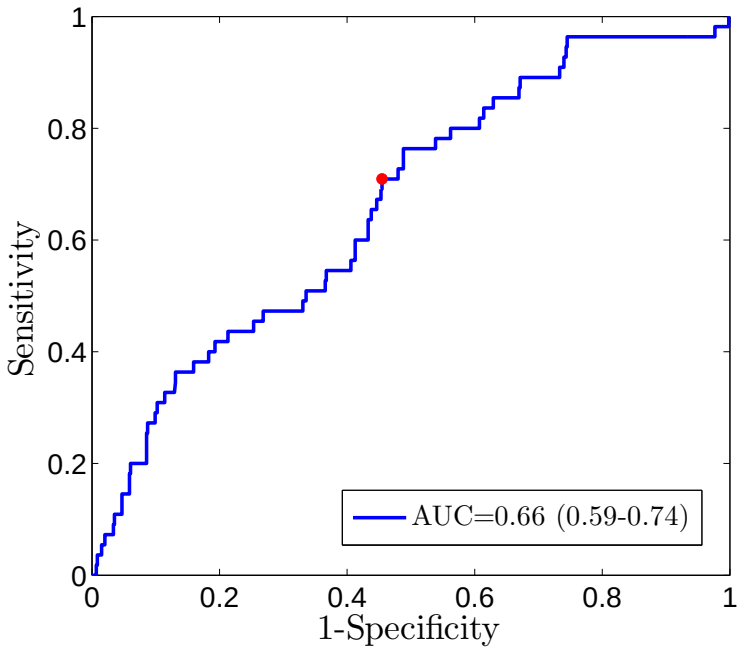

Figure 4.5: ROC curve for TMR^{dw} in the classification of SCD victims. Red dot indicates the selected threshold.

4.3.4 Classification

Two-class Classification of Cardiac Death Mode Using one ECG Index

Using the individual dichotomized variable for classification of SCD vs. the rest of patients, $TMR^{dw} \geqslant 0.040$ showed a value of κ of 0.08, with a Se of 75.1% and a Sp of 52.4%. For classification of PFD vs. the rest of patients, $TMR^{dw} < 0.040$ showed a Se of 59.6% and a Sp of 59.0% (κ=0.04).

Two-class Classification of Cardiac Death Mode Using a Combination of ECG Indices

The combination of TMR^{dw} and TS showed the maximum value of κ for both configurations (C_1 and C_2, respectively) of the SVM two-class classifier for separating SCD from the rest of patients. Regarding the separation of PFD from the rest of patients, IAA and TS was the combination of risk markers with the maximum κ for the first configuration (C_1), while TMR^{dw}, TS and IAA was the preferred combination for the second configuration (Table 4.7). Then, since a classifier with higher Sp value is preferred, we selected IAA and TS as the optimal combination for separating PFD from the rest of patients.

Variable	Overall population (n = 651)	TMR^{dw} <0.040 (n = 340)	TMR^{dw} ⩾0.040 (n = 311)	p-value
Clinical variables				
Age [years]	64(17)	63(18)	66(17)	0.155
Gender [men]	464 (71%)	263 (77%)	201 (65%)	**<0.001**
NYHA class III	115 (18%)	62 (18%)	53 (17%)	0.758
LVEF ⩽ 35%	356 (55%)	190 (56%)	166 (53%)	0.529
Ischemic etiology	327 (50%)	153 (45%)	174 (56%)	**0.006**
Diabetes	244 (38%)	119 (35%)	125 (40%)	0.195
Beta-blockers	455 (70%)	237 (70%)	218 (70%)	0.932
Amiodarone	61 (9%)	27 (8%)	34 (11%)	0.226
ARB or ACE inhibitors	576 (89%)	303 (89%)	273 (88%)	0.624
ECG variables				
Median RR [s]	0.86 (0.18)	0.86 (0.17)	0.84 (0.21)	**0.027**
RR range [s]	0.42 (0.22)	0.45 (0.20)	0.37 (0.21)	**<0.001**
QRS > 120 ms	262 (40%)	152 (45%)	110 (35%)	**0.016**
NSVT and > 240 VPBs in 24 h	168 (26%)	87 (26%)	81 (26%)	0.929
IAA ⩾ 3.7μV	153 (24.1%)	74 (22.3%)	79 (26.1%)	0.267
TS⩽2.5ms/RR	281 (47.1%)	125 (39.8%)	156 (55.1%)	**<0.001**
T-wave restitution parameters				
$\Delta\alpha^{\mathrm{Tpe}}$	0.025 (0.03)	0.020 (0.03)	0.032 (0.04)	**<0.001**
$\Delta\alpha^{\mathrm{QT}}$	0.199 (0.10)	0.188 (0.08)	0.215 (0.10)	**<0.001**

ACE = angiotensin-converting enzyme; ARB = angiotensin receptor blocker; IAA = Index of maximum alternans; LVEF = left ventricular ejection fraction; NSVT = Non-sustained ventricular tachycardia; NYHA = New York Heart Association; TMR^{dw}=T-wave Morphological Restitution; TS=turbulence slope; VPB=ventricular premature beat; Significant differences are indicated in bold.

Table 4.3: Characteristics of patients in the overall population and in each of the two risk groups defined by TMR^{dw}.

Endpoint	Overall population (n = 651)	TMR^{dw} < 0.040 (n = 340)	TMR^{dw} ⩾ 0.040 (n = 311)	p-value
CD	122 (18.7%)	55 (16.2%)	67 (21.5%)	0.088
SCD	55 (8.4%)	16 (4.7%)	39 (12.5%)	**<0.001**
PFD	67 (10.3%)	39 (11.5%)	28 (9.0%)	0.366

Data are presented as absolute frequencies and percentages. CD = cardiac death; PFD = pump failure death; SCD = sudden cardiac death; Significant differences are indicated in bold.

Table 4.4: Cardiac events during follow-up in the overall population and in each of the three groups defined by TMR^{dw}.

Three-class Classification of Cardiac Death Mode Using a Combination of ECG Indices

Table 4.8 summarizes the performance of the two configurations of the SVM three-class classifier for separating SCD from PFD and from the rest of patients in the overall population, in patients with LVEF⩽35% and in patients with LVEF>35%. The

	Univariable		Multivariable	
	HAR (95% CI)	p-value	HAR (95% CI)	p-value
Clinical variables				
Gender [men]	**2.14** (1.05-4.38)	**0.037**	**2.85** (1.32-6.14)	**0.008**
NYHA class III	**2.21** (1.23-3.95)	**0.008**	**2.63** (1.40-4.95)	**0.003**
LVEF$\leqslant$35%	**2.35** (1.30-4.25)	**0.005**	**1.95** (1.03-3.70)	**0.041**
ECG variables				
RR range [per 1 SD inc]	**0.75** (0.57-0.98)	**0.035**	1.13 (0.83-1.55)	0.429
NSVT and $>$ 240 VPBs in 24h	**2.08** (1.22-3.57)	**0.008**	1.37 (0.75-2.50)	0.314
IAA$\geqslant$3.7μV	**2.34** (1.32-4.13)	**0.004**	**2.36** (1.33-4.20)	**0.003**
TS$\leqslant$2.5 ms/RR	**2.64** (1.45-4.80)	**0.001**	1.70 (0.91-3.17)	0.095
$\Delta\alpha^{\mathrm{Tpe}} \geqslant 0.028$	**2.61** (1.47-4.62)	**0.001**	**2.42** (1.32-4.44)	**0.004**
$TMR^{dw} \geqslant 0.040$	**2.81** (1.57-5.02)	**0.001**	**2.94** (1.57-5.53)	**0.001**

CI=confidence interval; HAR=hazard ratio; IAA=index of average alternans; LVEF= left ventricular ejection fraction; NSVT=Non-sustained ventricular tachycardia; NYHA=New York Heart Association; SCD=sudden cardiac death; SD=standard deviation; TS=turbulence slope; VPB=Ventricular premature beat; Statistically significant values are marked in bold.

Table 4.5: Association of TMR^{dw} with SCD in univariate and multivariate Cox analysis.

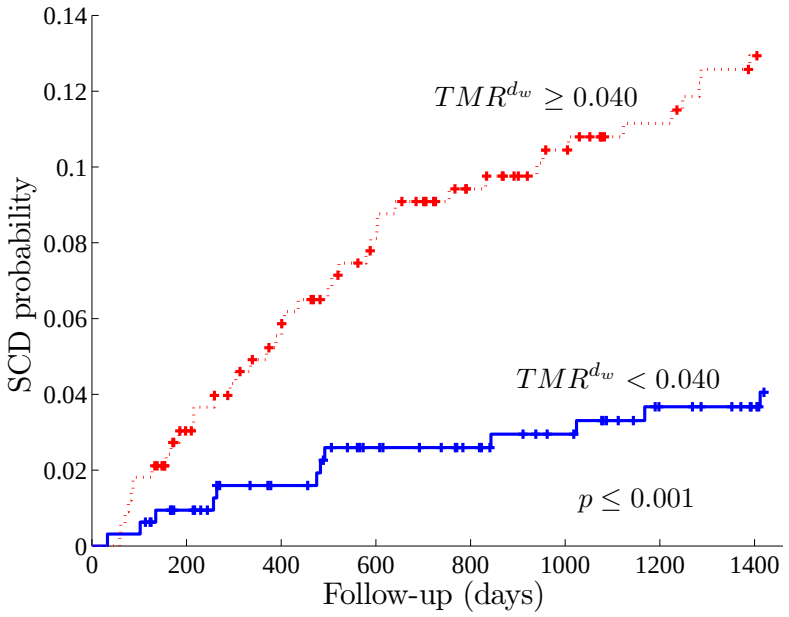

Figure 4.6: Probability curves of SCD for TMR^{dw}.

combination of risk markers with the highest κ when evaluating the overall population, patients with LVEF>35% and patients with LVEF$\leqslant$35% was TS and IAA using the

	Hazard ratio (95% CI)	p-value
Overall population (n=651)	2.81 (1.57-5.02)	**0.001**
Female population (n=187)	2.56 (0.53-12.31)	0.252
Male population (n=464)	3.19 (1.70-5.97)	**<0.001**
NYHA class II (n=536)	3.22 (1.57-6.60)	**0.001**
NYHA class III (n=115)	2.32 (0.84-6.39)	0.104
LVEF⩽35% (n=356)	3.27 (1.64-6.56)	**0.001**
LVEF>35% (n=295)	2.10 (0.72-6.15)	0.175
amiodarone (n=61)	1.73 (0.32-9.44)	0.528
No amiodarone (n=590)	2.97 (1.60-5.52)	**0.001**
Ischemic (n=327)	2.52 (1.17-5.43)	**0.018**
Non ischemic (n=324)	2.97 (1.21-7.29)	**0.017**

CI = confidence interval; SCD = sudden cardiac death; NYHA = New York Heart Association;LVEF = left ventricular ejection fraction; NSVT = Non-sustained ventricular tachycardia; VPB = Ventricular premature beat; SD = standard deviation; Statistically significant values are marked in bold.

Table 4.6: Association of TMR^{d_w} with SCD in univariate Cox analysis in different populations.

Combination	Configuration	SCD			PFD		
		Se (%)	Sp (%)	κ	Se (%)	Sp (%)	κ
TMR^{d_w} and TS	C_1	10.2	97.8	0.11	31.4	85.8	0.12
	C_2	48.9	70.6	0.07	74.2	53.4	0.10
TMR^{d_w} and IAA	C_1	8.2	97.6	0.08	17.6	83.9	0.01
	C_2	42.9	72.8	0.07	56.3	46.5	0.01
TS and IAA	C_1	38.0	81.4	0.10	55.9	78.6	0.19
	C_2	73.1	45.0	0.05	50.5	71.1	0.08
TMR^{d_w}, IAA and TS	C_1	10.2	97.6	0.11	30.1	87.7	0.11
	C_2	22.9	82.7	0.02	74.2	53.8	0.10

Table 4.7: Two-class classification performance for SCD, PFD and others (non-CD and survivors) using SVM. The optimal combination for mode of cardiac death is indicated in bold.

first configuration of the classifier. However, the combination of TMR^{d_w} and TS was the preferred for the second configuration.

TS and IAA, in the first configuration (C_1), also showed the highest values of κ in patients in NYHA class II and in NYHA class III. For the second configuration (C_2), TMR^{d_w}, and TS was the combination with the highest κ values in NYHA class II and in NYHA class III (Table 4.9).

4.3.5 Robustness Evaluation

Figure 4.7 shows the Bland-Altman plot of TMR^{d_w} calculated in the even and odd hours (a) and in the first and second 12 h (b). Spearman's correlation coefficient between TMR^{d_w} calculated in the even and the odd hours was 0.7333 ($p<0.001$), while Kendall's W coefficient of concordance was 0.8666. These values were 0.5284 ($p<0.001$) and 1 for the calculation in the first and second 12 h.

Combination	Configuration	Sample population	SCD		PFD		κ
			Se (%)	Sp (%)	Se (%)	Sp (%)	
TMR^{dw} and TS		Overall population	8.2	98.5	6.3	97.0	0.07
	C_1	LVEF>35%	20.0	95.3	5.0	91.9	0.06
		LVEF⩽35%	5.7	98.0	2.2	98.6	0.06
		Overall population	40.2	79.8	27.8	86.2	0.11
	C_2	**LVEF>35%**	43.3	72.2	35.0	77.6	0.06
		LVEF⩽35%	42.1	74.1	38.1	74.9	0.12
TMR^{dw} and IAA		Overall population	8.2	97.8	1.7	99.8	0.06
	C_1	LVEF>35%	20.0	95.7	0	99.2	0.06
		LVEF⩽35%	2.9	97.6	0	99.3	0.02
		Overall population	38.9	72.6	8.2	90.5	0.05
	C_2	LVEF>35%	36.7	70.6	20.0	79.9	0.04
		LVEF⩽35%	44.6	72.4	6.9	93.8	0.07
TS and IAA		**Overall population**	20.0	89.4	24.9	88.8	0.15
	C_1	**LVEF>35%**	30.0	94.0	35.0	81.3	0.17
		LVEF⩽35%	18.6	84.6	16.9	91.0	0.13
		Overall population	46.7	66.7	38.1	76.6	0.10
	C_2	LVEF>35%	6.7	92.0	55.0	49.7	0.03
		LVEF⩽35%	69.3	49.2	15.0	92.1	0.12
TMR^{dw}, IAA and TS		Overall population	10.2	97.8	6.3	97.4	0.08
	C_1	LVEF>35%	20.0	96.1	0	92.7	0.02
		LVEF⩽35%	5.7	97.0	2.2	98.6	0.04
		Overall population	22.9	83.1	50.9	67.3	0.11
	C_2	LVEF>35%	43.3	77.8	45.0	68.5	0.08
		LVEF⩽35%	42.1	74.8	33.1	76.6	0.11

Table 4.8: Three-class classification performance for SCD, PFD and others (non-CD and survivors) in the overall population, in patients with LVEF⩽35% and in patients with LVEF>35%. The optimal combination for each configuration (C_1 and C_2, see text) and mode of cardiac death is indicated in bold.

Combination	Sample population	SCD		PFD		κ
		Se (%)	Sp (%)	Se (%)	Sp (%)	
TS and IAA (C_1)	Overall population	20.0	89.4	24.9	88.8	0.15
	NYHA II	2.9	96.8	14.4	91.0	0.03
	NYHA III	36.7	96.8	32	89.1	0.30
TMR^{dw} and TS (C_2)	Overall population	40.2	79.8	27.8	86.2	0.11
	NYHA II	45.7	70.5	39.4	80.3	0.10
	NYHA III	53.3	65.8	28.0	79.8	0.18

Table 4.9: Three-class classification performance for SCD, PFD and others (non-CD and survivors) in the overall population, in patients in NYHA class II and in patients in NYHA class III for the optimal combination for each configuration (C_1 and C_2, see text).

4.4 Discussion

In this chapter, a fully automated method was presented to estimate dispersion of repolarization restitution from the slope of the restitution of the T-wave morphology

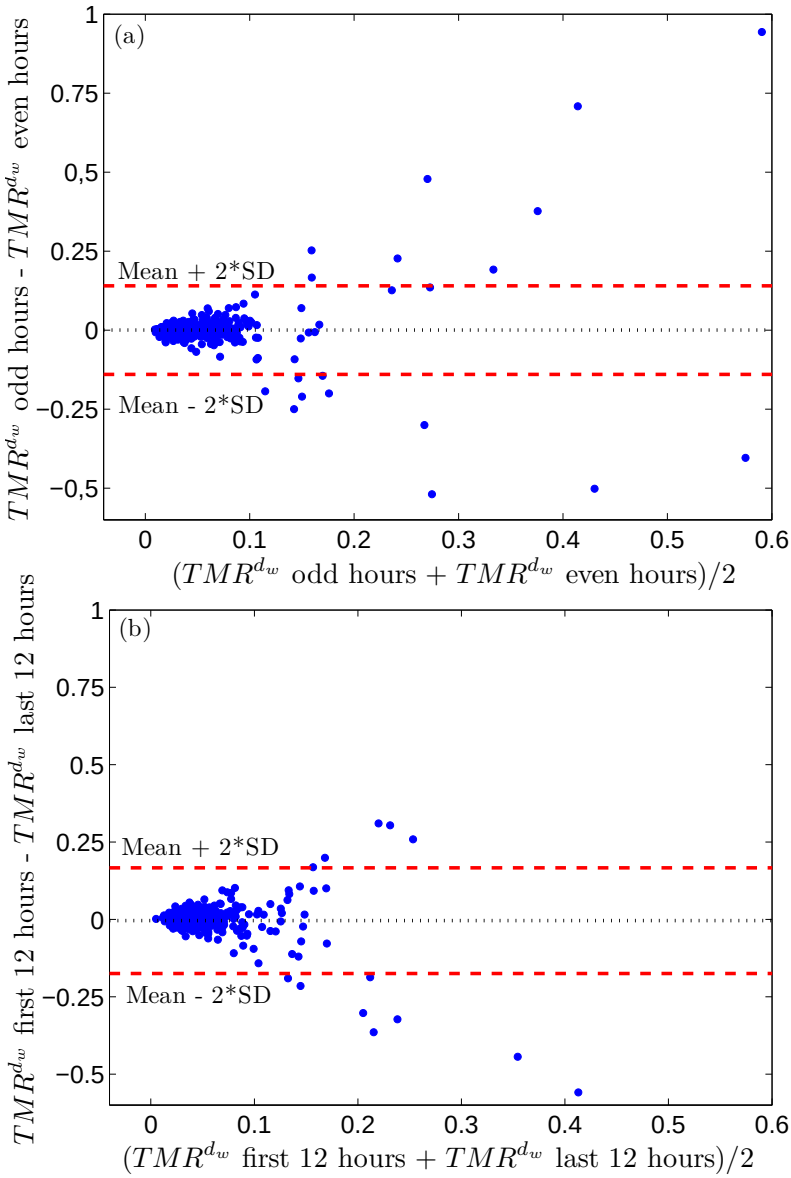

Figure 4.7: Bland-Altman plot of TMR^{d_w} calculated in the even and odd hours (a) and in the first and last 12 hours (b). The red horizontal dashed lines indicate the mean $\pm$ 2 SD of the difference between TMR^{d_w} in the even and the odd hours, and in the first and last 12 hours, respectively.

in 24-hour ambulatory ECG recordings of 651 CHF patients. The main result is that

the slope of the restitution of the T-wave morphological variations in the temporal domain, quantified by TMR^{d_w}, specifically predicts SCD, with no association with PFD. TMR^{d_w} was the strongest predictor of SCD, independently to clinical variables like the LVEF or the NYHA class, other ECG-derived risk indices, such as the T-wave alternans, the QRS duration or the HRT, and other restitution indices like $\Delta\alpha^{\mathrm{QT}}$ and $\Delta\alpha^{\mathrm{Tpe}}$. The restitution of other markers of T-wave morphology variability, however, was not associated with any mode of cardiac death. Finally, the combination of TMR^{d_w}, TS and IAA improved SCD, PFD and non-CD risk stratification.

4.4.1 Dispersion of Repolarization Restitution from the T-wave Morphology Predicts SCD with no Association with PFD

Cox regression analysis and Kaplan-Meier cumulative event analysis confirmed the ability of the slope of the T-wave morphology restitution to separate CHF patients in two risk subpopulations, with patients presenting steeper slopes being more prone to suffer from SCD, and patients with flatter slopes being at low SCD risk during follow-up. Upon confirmation by further investigations, such a specific prediction of SCD risk could be of great importance to define a high SCD risk population that could be highly benefited from an ICD implantation.

Although in the previous chapter we demonstrated that the four morphological variability markers, d_w, d_a, d_w^{NL} and d_a^{NL}, reflected variations in the dispersion of ventricular repolarization, the index d_w was the only marker with significant SCD predictive value when normalizing by ΔRR. One possible explanation to the amplitude variability indices can be that the variation in the T-wave amplitude with changes in heart rate is highly heterogeneous across subjects (see, for example, the histogram in Figure 4.2), and, therefore, not related to a particular endpoint. In fact, there were subjects whose T-wave amplitude decreased at higher RR interval values, whereas there were others whose amplitude increased. Regarding d_w^{NL}, although there was a trend showing that increased ranges of RR produced increased non-linearities in the T-wave morphology, these increments were not, themselves, significantly higher in SCD victims than in the rest of patients (Figure 4.4). Our results suggest that variations in the distribution of the repolarization times along the ventricle, predisposing to SCD, are merely manifested as alterations in the temporal domain of the T-wave, rather than in the amplitude.

Also, the value of d_w itself showed to be significantly higher in SCD victims as compared to the rest of patients, but also significantly lower in PFD victims than in the rest of patients (Figure 4.8 (a)). However, when normalizing by ΔRR and, then, obtaining TMR^{d_w}, the significant PFD prediction was lost. This could be explained by evaluating the significant predictive value of ΔRR itself. We, in fact, found that ΔRR was significantly lower in CD victims, i.e. both SCD and PFD victims (Figure 4.8 (b)). Therefore, the T-wave morphological variation per RR increment was increased in SCD victims, but also in PFD victims, losing its statistical significance.

Regarding the comparison with clinical and other ECG-derived indices, TMR^{d_w} showed the highest hazard ratio in both univariate and multivariate Cox analyses

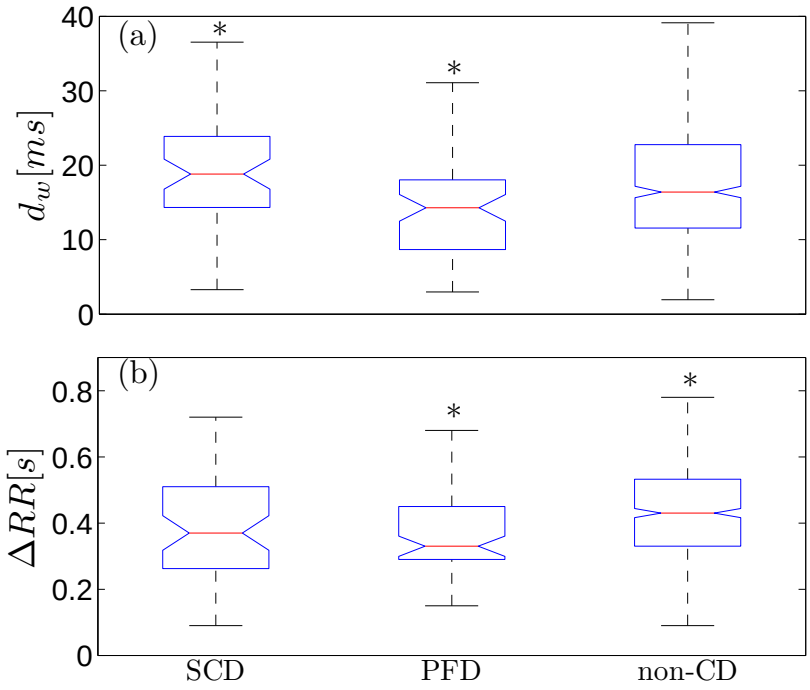

Figure 4.8: Boxplot of d_w (a) and ΔRR (b) for SCD, PFD victims and survivors of CD. * Indicates statistical significance between each outcome and the group formed by the other two.

(Table 4.5). This suggests that TMR^{d_w} contains specific information on arrhythmia not included in other variables like the LVEF, the NYHA class, the TWA, the QRS duration of the HRT. However, sub-population analysis (Table 4.6) showed that the prognostic value of $TMR^{d_w} \geqslant 0.040$ was mostly due to its association with SCD in patients with depressed LVEF. Importantly, the combination of LVEF$\leqslant$35% and $TMR^{d_w} \geqslant 0.040$ in a single score resulted in a 60% increase in the hazard ratio, suggesting that TMR^{d_w} captures information related to the electrophysiological substrate that complements systolic function markers and improves prediction. Also, it must be noted that the lack of association of TMR^{d_w} with SCD in some of the sub-populations in Table 4.6 may be due to their small size.

The performance of our proposed TMR^{d_w} index can be compared with that from $\Delta\alpha^{\mathrm{Tpe}}$, characterizing the Tpe interval dynamics. Although the index $\Delta\alpha^{\mathrm{Tpe}}$ showed to be related to increased SCD risk (chapter 2) [246], TMR^{d_w} demonstrated a stronger association with SCD risk than $\Delta\alpha^{\mathrm{Tpe}}$ in a multivariate analysis. This strengthens the hypothesis that the quantification of the overall T-wave morphological variations is a better estimate of the total spatio-temporal dispersion of repolarization restitution than interval-based markers, and, thus, provides improved arrhythmic risk prediction. Future studies will be needed to assess the relation between TMR^{d_w} and other

restitution indices, such as the recently proposed R212 index [145, 247].

4.4.2 Risk Stratification Improves by Combining ECG Risk Markers

The combination of TMR^{d_w} and TS showed to be the one with the best performance in two-class SVM classification of SCD vs. the rest of patients, with a value of κ higher than that obtained when using the markers individually. This indicates that TMR^{d_w} and TS add complementary information and, consequently, their combination would improve the stratification of patients at risk of SCD, with higher values of TMR^{d_w} and lower values of TS indicating higher propensity to suffer from a SCD event. It is surprising that is TS, and not IAA, the index with optimal SCD classification performance when combined with T-wave morphology restitution (TMR), considering that $\Delta\alpha^{\mathrm{Tpe}}$ and IAA was the optimal combination in chapter 2. This could mean that the information contained in TMR^{d_w} and in IAA is not completely complementary.

Regarding two-class classification of PFD vs. the rest of patients, the combination of TMR^{d_w}, TS and IAA was the one with the highest κ coefficient for the second configuration of the classifier, but, as with $\Delta\alpha^{\mathrm{Tpe}}$, not improving the performance of TS individually. For the first configuration of the classifier, TS and IAA improved the κ value from the individual TS marker. This combination is concordant with the fact that TMR^{d_w} was not associated with PFD, and its κ value for classifying PFD vs. the rest of patients was very low.

In the three-class classification of SCD, PFD and the rest of patients, the combination of TS and IAA showed, as in chapter 2, to be the one with the best performance for the first configuration of the classifier, while TMR^{d_w} and TS was the best one for the second configuration. According to the preference of maximizing the Sp, we would, then, recommend the combination of TS and IAA using the first configuration for an optimal classification.

When dividing the population into preserved and depressed LVEF and into NYHA classes II and III, our results confirmed that the classification is easier in patients with depressed LVEF and NYHA class III.

The combination results in this chapter indicate that SCD risk is produced by abnormal repolarization patterns and by imbalanced autonomic modulation, while the latter would be the main indicator of PFD.

4.4.3 The Circadian Pattern Modulates T-wave Amplitude Restitution

We found that the restitution of the T-wave amplitude variations was significantly higher during the day than at night (Figure 4.3). These results suggest that the variations in the temporal domain of the T-wave, which are those with predictive

value, are independent from the time of the day, while the circadian modulation of repolarization is mainly reflected as variations in the amplitude of the T-waves.

4.4.4 Technical Considerations

It is well-known that the repolarization response to changes in heart rate is not immediate and a time lag exists in the adaptation of repolarization (section 2.2.3) [130]. This hysteresis was compensated for the calculation of $\Delta\alpha^{\mathrm{QT}}$ and $\Delta\alpha^{\mathrm{Tpe}}$ as described in chapter 2, but using the same methodology to compensate for the memory of the T-wave morphology is not straightforward. To overcome this difficulty, we calculated an average of, at least, 50 T-waves recorded at the same RR, but at different time instants, i.e. different history of RR. Thus, we expected a significant reduction of the hysteresis effect.

The computation of TMR^{d_w} does not require a minimum recording duration. However, a wide RR range is recommended to ensure an appreciable variation in the morphology of the T-wave. In addition, the methodology requires sinus rhythm. TMR^{d_w} was computable in all patients available for the study, and there were no artifacts or unusable portions of the Holter ECGs limiting its measurement. Also, in contrast with beat-to-beat repolarization metrics, TMR^{d_w} is not affected by VPBs and it only requires waveforms from few beats at different RR intervals to be computed.

Regarding the robustness of TMR^{d_w}, we showed that there was a strong correlation and concordance between the TMR^{d_w} indices, computed at even and odd hours and at the first and last 12 hours, indicating that the index is repeatable and independent from the ECG segments considered for its evaluation. These results also reflect that TMR^{d_w} is not influenced by the circadian pattern, as discussed before.

4.4.5 Limitations

Prospective studies are needed to verify that the observations presented here have a role in SCD prediction in CHF patients. This study only considered consecutive patients, so the number of SCD victims was low and this has limited the possibility of performing further statistical analyses. Since this is a retrospective study, further investigations on the applicability of the defined cut-off point and on the extension of the analysis to other CHF and non-CHF populations are needed to confirm the prognostic value of the proposed index. Next, although the T-wave morphology is related to the lead configuration, spatial dependency of TMR^{d_w} is limited because TMR^{d_w} measured changes within a mathematically constructed lead that represents global repolarization.

4.5 Conclusion

Dispersion of repolarization restitution, quantified from Holter ECG recordings through the slope of the T-wave morphology restitution, is a strong and indepen-

dent predictor of SCD, with steeper slopes indicative of an arrhythmogenic substrate predisposing to SCD. No association was found between the slope of the T-wave morphology restitution and PFD. Regarding the source of T-wave morphological variability, only those variations in the temporal domain of the T-wave, quantified by TMR^{d_w}, reflected higher arrhythmic risk. T-wave amplitude and strictly non-linear temporal variations were independent from the mode of death. TMR^{d_w} showed higher predictive value than other clinical variables like the LVEF, or the NYHA class, and other ECG-derived indices like the TWA, the QRS duration or the HRT. Again, the combination of TMR^{d_w} with other ECG-derived risk markers improved SCD risk prediction. The variations in the temporal domain of the T-wave are not influenced by the circadian pattern, but this modulation should be taken into account when measuring the restitution of the T-wave amplitude. Our results suggest that the slope of the T-wave morphology restitution could be used in the clinical practice as a tool to target a high SCD-risk population that could largely benefit from ICD implantation.

Chapter 5

Predictive Value Improvement by Adding ECG-derived Markers to a Clinical Model

5.1 Introduction

As explained in chapter 1, CHF is a complex clinical syndrome that can result from a number of functional or structural cardiac disorders, impairing the ventricle's ability to fill with or eject blood [248]. A common finding in CHF patients is a chronic sympathetic over-activity [249], a risk factor for both SCD and PFD [250,251]. Initial sustained sympathetic activation increases the vulnerability to ventricular arrhythmias by enhancing the spatio-temporal dispersion of repolarization [252], and the ventricular response to heart rate changes [253]. As demonstrated by the results in this thesis, this phenomena is manifested in the ECG-derived markers presented in this document as increased values of IAA, $\Delta\alpha^{\mathrm{Tpe}}$ and TMR^{d_w}. Enduring sympathetic activation,

however, ends up provoking withdrawal of vagal activity [57] and a weakened ventricular response [254], which are manifested as lower values of $\Delta\alpha^{\mathrm{Tpe}}$ and TS. Considering the interaction of multiple factors in both SCD and PFD, and the classification results of the combination of $\Delta\alpha^{\mathrm{Tpe}}$ and TMR^{d_w} with IAA and TS (chapters 2 and 4), the combination of indices reflecting complementary cardiac mechanisms rather than the use of individual markers could improve SCD and PFD risk stratification.

Risk models based on a set of clinical variables have been proposed and evaluated in CHF patients for specific SCD and PFD prediction [121–123]. These risk models are an important first step to serve as a quick screen to identify subgroups that might benefit from further evaluation for specific risk stratification [125]. In this chapter, we hypothesized that additional risk models based on ECG-derived indices reflecting different mechanisms like ANS imbalance and repolarization instability could add complementary information for improving the specificity of SCD and PFD risk stratification.

Then, in this chapter we developed new risk models that integrate clinical indices with ECG-derived markers to specifically predict SCD and PFD and eventually improve the prognostic value of current stratification tools in CHF.

5.2 Methods

5.2.1 Study Population

We used the 651 ECG recordings from the MUSIC study for the evaluation of the optimal SCD and PFD risk models in CHF patients.

5.2.2 Clinical and ECG-derived Parameters

The clinical variables used in this study are listed in Table 5.1. For the derivation of the risk models from the Holter recordings, we used the ECG-derived markers studied in this thesis. This includes $\Delta\alpha^{\mathrm{QT}}$ and $\Delta\alpha^{Tpe}$, reflecting repolarization restitution, and being associated with SCD when dichotomized at 0.228 and 0.028, respectively [246], as described in chapter 2. Also, in that chapter, $\Delta\alpha^{\mathrm{Tpe}}$ was shown to be related to PFD when dichotomized at 0.022 [246]. Then, IAA, the index reflecting spatio-temporal dispersion of repolarization, and associated with SCD when categorized at 3.7μV [156]. In addition, TS, measuring the sympathovagal balance [173,174], and predicting SCD and PFD when dichotomized at 2.5 ms/RR [174, 176]. Finally, TMR^{d_w}, reflecting dispersion of repolarization restitution, and associated with SCD when dichotomized at 0.040.

5.2.3 Statistical Analysis

In order to create the prediction models, the univariate association between each variable and SCD and PFD risk was first evaluated. Those variables associated with

each endpoint at p<0.05 were included as candidate variables into three multivariable models: a clinical model (including clinical variables only), an ECG model (including ECG-derived variables only), and a combined model (combining clinical and ECG-derived risk markers). Backwards stepwise regression was then performed and a retention criteria of p<0.05 was used to identify the variables for our prediction models. Based on the 4-year follow-up, the β-coefficients for each variable retained in the final multivariable model were used when constructing the prediction models [121].

Finally, prediction models for SCD and PFD were calculated. The SCD and PFD prediction models were defined according to the following equation:

$$S_{\mathrm{M}}^{\mathrm{E}} = \sum_{i=1}^{I} \beta_i x_i, \tag{5.1}$$

where S denotes the score, M denotes the model, either the clinical ("Cli"), the ECG-based ("ECG"), or the combined ("Com"); E denotes the endpoint, SCD or PFD; I is the number of dichotomized variables retained in the multivariable model, β_i is the coefficient of the i-th dichotomized variable; and x_i is the i-th dichotomized variable (i.e. x_i takes the value 0 when the variable is below the defined cut-off point and 1 when it is above, see Table 5.2).

The AUC was calculated and the ability of each prediction model to separate patients who experience a specific outcome from those who do not was quantified. SCD and PFD probabilities were estimated by Kaplan-Meier methods with a comparison of cumulative events performed by using log-rank tests. Based on the risk scores, the population was divided in three groups: Low-risk (first and second quintiles (Q1-Q2)), middle-risk (third and fourth quintiles (Q3-Q4)) and high-risk (fifth quintile (Q5)). HARs were calculated using the low risk group as a reference. Patients who died from causes not included in the endpoints were censored at the time of death. A p-value <0.05 was considered statistically significant. Statistical analysis was performed using SPSS version 22.0 (SPSS, Inc. Chicago IL).

5.3 Results

5.3.1 Association of Variables with SCD and PFD

As shown in Table 5.1, SCD victims were more frequently men (p=0.048), were in NYHA class III (p=0.047) and had low LVEF (p=0.010), while PFD victims were more frequently older than the rest of patients (p=0.013), were more frequently diabetic (p=0.009), in NYHA class III (p=0.001), were not under treatment with beta-blockers (p=0.012) and also had low LVEF (p=0.044). Ischaemic aetiology was not associated with SCD or PFD.

Regarding the ECG-derived risk markers, SCD victims more frequently had higher $\Delta\alpha^{\mathrm{Tpe}}$ (p=0.002), $\Delta\alpha^{\mathrm{QT}}$ (p=0.041), IAA (p=0.008) and TMR^{d_w} (p=0.001), while lower TS (p=0.004). PFD victims more frequently showed lower RR range (p<0.001),

Variable	Survivors (n = 503)	SCD (n = 55)	PFD (n = 67)	non-cardiac death (n = 26)
Clinical variables				
Age [years]	63(18)*	67 (12)	69(17)*	71 (15)
Gender [men]	351 (70%)	46(84%)*	49 (73%)	18 (69%)
Diabetes	175(35%)*	24 (44%)	34(51%)*	11 (42%)
NYHA class III	68(14%)*	16(29%)*	21(31%)*	10(39%)*
Ischemic etiology	239(48%)*	33 (60%)	39 (58%)	16 (62%)
ARB or ACE inhibitors	451 (90%)	45 (82%)	54(81%)*	26 (100%)
Beta-blockers	366(73%)*	39 (71%)	37(55%)*	13(50%)*
Amiodarone	38(8%)*	6 (11%)	11(16%)*	6(23%)*
LVEF $\leqslant$ 35%	252(50%)*	40(73%)*	45(67%)*	19 (73%)
ECG variables				
Median RR [s]	0.86 (0.18)	0.85 (0.21)	0.85 (0.21)	0.83 (0.17)
RR range [s]	0.43(0.21)*	0.37 (0.25)	0.33(0.16)*	0.35 (0.25)
QRS $>$ 120 ms	195 (39%)	25 (46%)	32 (48%)	10 (39%)
NSVT and $>$ 240 VPBs in 24 h	113(23%)*	22(40%)*	27(40%)*	6 (23%)
$\Delta\alpha^{\mathrm{Tpe}} \geqslant 0.028$	230 (46%)	38(69%)*	24 (36%)	15 (58%)
$\Delta\alpha^{\mathrm{Tpe}} \leqslant 0.022$	220 (44%)	15(27%)*	41(61%)*	9 (35%)
$\Delta\alpha^{\mathrm{QT}} \geqslant 0.228$	165 (33%)	26 (47%)	24 (36%)	12 (46%)
IAA$\geqslant$3.7μV	107(22%)*	22(42%)*	15 (23%)	9 (35%)
TS$\leqslant$2.5ms/RR	186(40%)*	33(67%)*	49(79%)*	13 (57%)
$TMR^{dw} \geqslant$0.040	229(46%)*	39(71%)*	28 (42%)	15 (58%)

ACE = angiotensin-converting enzyme; ARB = angiotensin receptor blocker; HR = Heart Rate; IAA = Index of Average Alternans; LVEF = left ventricular ejection fraction; NSVT = Non-Sustained Ventricular Tachycardia; NYHA = New York; Heart Association; PFD = Pump Failure Death; SCD = Sudden Cardiac Death; TMR^{dw} = T-wave Morphology Restitution; TS = Turbulence Slope; VPB = Ventricular Premature Beat; *p$<$0.05 for comparison against the group formed by the other modes of death.

Table 5.1: Characteristics of patients according to their outcome.

$\Delta\alpha^{\mathrm{Tpe}}$ (p=0.003) and TS values (p$<$0.001), while a higher rate of NSVT and more than 240 VPBs in 24 h (p=0.014). The QRS duration was not associated with SCD or PFD.

5.3.2 Predictors of SCD and PFD

The definition of the dichotomized variables, x_i, introduced in the Cox analysis is presented in Table 5.2. Tables 5.3 and 5.4 show the risk markers that significantly contributed to SCD and PFD prediction, respectively, in univariate and multivariate analyses. In the univariate analysis, SCD was related to male gender, NYHA class III, LVEF$\leqslant$35%, $\Delta\alpha^{\mathrm{Tpe}} \geqslant$0.028, $\Delta\alpha^{\mathrm{QT}} \geqslant$0.228, IAA$\geqslant$3.7$\mu$V, TS$\leqslant$2.5 ms/RR and $TMR^{dw} \geqslant$0.04 (Table 5.3). Similarly, PFD was associated with age, diabetes, NYHA class III, absence of treatment with beta-blockers, LVEF$\leqslant$35%, reduced RR range, NSVT and more than 240 VPBs in 24 h, $\Delta\alpha^{\mathrm{Tpe}} \leqslant$0.022 and TS$\leqslant$2.5 ms/RR (Table 5.4).

Dichotomized variable	Definition
x_g	1, if male gender; 0, otherwise
x_{NYHA}	1, if NYHA class III; 0, otherwise
x_{Diab}	1, if diabetic; 0, otherwise
x_β	1, if treatment with beta-blockers; 0, otherwise
x_{LVEF}	1, if LVEF$\leqslant$35%; 0, otherwise
x_{NSVT}	1, if NSVT and >240 VPBs/24-h; 0, otherwise
$x_{\Delta\alpha_{Tpe}^{SCD}}$	1, if $\Delta\alpha^{\mathrm{Tpe}} \geqslant$0.028; 0, otherwise
$x_{\Delta\alpha_{\mathrm{PFD}}^{\mathrm{Tpe}}}$	1, if $\Delta\alpha^{\mathrm{Tpe}} \leqslant$0.022; 0, otherwise
$x_{\Delta\alpha\mathrm{QT}}$	1, if $\Delta\alpha^{\mathrm{QT}} \geqslant$0.228; 0, otherwise
x_{IAA}	1, if IAA$\geqslant$3.7μV; 0, otherwise
x_{TS}	1, if TS$\leqslant$2.5ms/RR; 0, otherwise
$x_{TMR^{dw}}$	1, if $TMR^{dw} \geqslant$0.040; 0, otherwise

IAA = Index of Average Alternans; LVEF = left ventricular ejection fraction; NSVT = Non-Sustained Ventricular Tachycardia; NYHA = New York Heart Association; PFD = Pump Failure Death; SCD = Sudden Cardiac Death; TMR^{dw} = T-wave Morphology Restitution; TS = Turbulence Slope; VPB = Ventricular Premature Beat.

Table 5.2: Definition of the dichotomized variables used to build the SCD and PFD risk models.

Risk markers	Univariate		Clinical Multivariate			ECG Multivariate			Combined Multivariate		
	HAR (95% CI)	p	HAR (95% CI)	β	p	HAR (95% CI)	β	p	HAR (95% CI)	β	p
Clinical variables											
Gender [men]	2.159 (1.012-4.606)	0.046	2.248 (1.050-4.814)	0.810	0.037	-	-	-	2.750 (1.276-5.927)	1.012	0.010
NYHA class III	2.189 (1.177-4.071)	0.013	2.221 (1.189-4.150)	0.798	0.012	-	-	-	2.499 (1.328-4.702)	0.916	0.005
LVEF $\leqslant 35\%$	2.335 (1.238-4.403)	0.009	2.165 (1.146-4.092)	0.772	0.017	-	-	-	1.997 (1.052-3.792)	0.692	0.035
ECG variables											
$\Delta\alpha^{\mathrm{Tpe}} \geqslant 0.028$	2.676 (1.524-4.700)	0.001	-	-	-	2.365 (1.329-4.210)	0.861	0.003	2.550 (1.440-4.515)	0.936	0.001
$\Delta\alpha^{\mathrm{QT}} \geqslant 0.228$	1.921 (1.097-3.364)	0.022	-	-	-	N.S.	N.S.	N.S.	N.S.	N.S.	N.S.
IAA$\geqslant$3.7μV	2.335 (1.321-4.128)	0.004	-	-	-	2.377 (1.339-4.221)	0.866	0.003	2.271 (1.278-4.035)	0.820	0.005
TS$\leqslant$2.5ms/RR	2.641 (1.453-4.802)	0.001	-	-	-	2.180 (1.193-3.986)	0.780	0.011	N.S.	N.S.	N.S.
$TMR^{dw} \geqslant 0.040$	2.929 (1.576-5.445)	0.001	-	-	-	2.193 (1.162-4.140)	0.785	0.015	2.883 (1.531-5.429)	1.059	0.001

ACE = angiotensin-converting enzyme; ARB = angiotensin receptor blocker; HAR = Hazard Ratio; HR = Heart Rate; IAA = Index of Average Alternans; LVEF = left ventricular ejection fraction; NSVT = Non-Sustained Ventricular Tachycardia; NYHA = New York Heart Association; PFD = Pump Failure Death; SCD = Sudden Cardiac Death; TMR^{dw} = T-wave Morphology Restitution; TS = Turbulence Slope; VPB = Ventricular Premature Beat; *p$<$0.05 for comparison against the group formed by the other modes of death.

Table 5.3: Univariable and multivariable predictors of SCD.

Risk markers	Univariate		Clinical Multivariate			ECG Multivariate			Combined Multivariate		
	HAR (95% CI)	p	HAR (95% CI)	β	p	HAR (95% CI)	β	p	HAR (95% CI)	β	p
Clinical variables											
Age [per 1 SD inc.]	1.378 (1.047-1.813)	0.022	N.S.	N.S.	N.S.	-	-	-	N.S.	N.S.	N.S.
Diabetes	2.011 (1.221-3.312)	0.006	1.842 (1.112-3.049)	0.611	0.018	-	-	-	1.697 (1.022-2.818)	0.529	0.041
NYHA class III	2.892 (1.709-4.896)	<0.001	2.305 (1.342-3.959)	0.835	0.002	-	-	-	1.972 (1.154-3.370)	0.679	0.013
Beta-blockers	0.498 (0.302-0.823)	0.007	1.859 (1.118-3.091)	0.620	0.017	-	-	-	N.S.	N.S.	N.S.
LVEF $\leqslant 35\%$	1.792 (1.052-3.053)	0.032	1.768 (1.034-3.026)	0.570	0.037	-	-	-	N.S.	N.S.	N.S.
ECG variables											
ΔRR [per 1 SD inc.]	0.587 (0.451-0.764)	<0.001	-	-	-	0.753 (0.566-1.000)	-0.284	0.050	N.S.	N.S.	N.S.
NVST and more than 240 VPBs in 24-h	2.034 (1.220-3.391)	0.006	-	-	-	N.S.	N.S.	N.S.	N.S.	N.S.	N.S.
$\Delta\alpha^{\mathrm{Tpe}} \leqslant 0.022$	2.068 (1.235-3.462)	0.006	-	-	-	2.174 (1.298-3.642)	0.777	0.003	2.219 (1.320-3.730)	0.797	0.003
TS$\leqslant$2.5ms/RR	4.975 (2.698-9.172)	<0.001	-	-	-	4.132 (2.165-7.884)	1.419	<0.001	4.160 (2.225-7.779)	1.425	<0.001

ACE = angiotensin-converting enzyme; ARB = angiotensin receptor blocker; HAR = Hazard Ratio; HR = Heart Rate; IAA = Index of Average Alternans; LVEF = left ventricular ejection fraction; NSVT = Non-Sustained Ventricular Tachycardia; NYHA = New York Heart Association; PFD = Pump Failure Death; SCD = Sudden Cardiac Death; TMR^{dw} = T-wave Morphology Restitution; TS = Turbulence Slope; VPB = Ventricular Premature Beat; *p<0.05 for comparison against the group formed by the other modes of death.

Table 5.4: Univariable and multivariable predictors of PFD.

5.3.3 Prediction models

When only adjusting for the clinical variables, all factors remained significant after backward stepwise selection for SCD prediction in multivariate Cox analysis (Table 5.3. When adjusting for the ECG-derived markers, $\Delta\alpha^{\mathrm{QT}} \geqslant 0.228$ lost its significance to the model. When adjusting for both clinical and ECG-derived markers, $\Delta\alpha^{\mathrm{Tpe}} \geqslant 0.028$, IAA$\geqslant 3.7\mu$V, $TMR^{d_w} \geqslant 0.04$ and the three clinical variables remained significantly associated with SCD (Table 5.3). Therefore, the final SCD clinical, $S^{\mathrm{SCD}}_{\mathrm{Cli}}$, ECG, $S^{\mathrm{SCD}}_{\mathrm{ECG}}$, and combined, $S^{\mathrm{SCD}}_{\mathrm{Com}}$, prediction models were:

$$
\begin{aligned}
S^{\mathrm{SCD}}_{\mathrm{Cli}} &= 0.810x_g + 0.798x_{\mathrm{NYHA}} + 0.772x_{\mathrm{LVEF}} \\
S^{\mathrm{SCD}}_{\mathrm{ECG}} &= 0.861x_{\Delta\alpha^{\mathrm{Tpe}}_{\mathrm{SCD}}} + 0.866x_{\mathrm{IAA}} + 0.780x_{\mathrm{TS}} + 0.785x_{TMR^{d_w}} \\
S^{\mathrm{SCD}}_{\mathrm{Com}} &= 1.012x_g + 0.916x_{\mathrm{NYHA}} + 0.692x_{\mathrm{LVEF}} + 0.936x_{\Delta\alpha^{\mathrm{Tpe}}_{\mathrm{SCD}}} + 0.810x_{\mathrm{IAA}} + 1.059x_{TMR^{d_w}}.
\end{aligned}
\tag{5.2}
$$

Regarding PFD risk prediction, all clinical variables excepting age remained significant when adjusting for clinical factors (Table 5.4). When adjusting for ECG-derived markers, NSVT and more than 240 VPBs in 24-h lost its significance to the model. The clinical and ECG-derived risk markers that remained significant when computing the combined PFD prediction model were diabetes, NYHA class III, $\Delta\alpha^{\mathrm{Tpe}} \leqslant 0.022$ and TS$\leqslant$2.5ms/RR. Clinical, ECG, and combined models specific for PFD were:

$$
\begin{aligned}
S^{\mathrm{PFD}}_{\mathrm{Cli}} &= 0.611x_{\mathrm{Diab}} + 0.835x_{\mathrm{NYHA}} + 0.620x_{\beta} + 0.570x_{\mathrm{LVEF}} \\
S^{\mathrm{PFD}}_{\mathrm{ECG}} &= -0.284\Delta RR + 0.777x_{\Delta\alpha^{\mathrm{Tpe}}_{\mathrm{PFD}}} + 1.419x_{\mathrm{TS}} \\
S^{\mathrm{PFD}}_{\mathrm{Com}} &= 0.529x_{\mathrm{Diab}} + 0.679x_{\mathrm{NYHA}} + 0.797x_{\Delta\alpha^{\mathrm{Tpe}}_{\mathrm{PFD}}} + 1.425x_{\mathrm{TS}},
\end{aligned}
\tag{5.3}
$$

where each increment unit in ΔRR corresponds to one standard deviation.

5.3.4 SCD and PFD prediction

Figure 5.1 shows the ROCs and AUCs for the clinical (solid blue), ECG (dashed red), and combined (dotted-dashed black) prediction models for SCD (a) and PFD (b). According to ROC analysis, ECG-derived markers provided a more accurate prediction of both SCD and PFD with respect to clinical markers. Accuracy further increased for SCD prediction when combining clinical and ECG-derived markers.

Figure 5.2 shows the results of Kaplan-Meier analyses. SCD probability for the high-risk group was higher in the ECG- than in the clinical model and it further increased in the combined model (Figure 5.2 (a)-(c)). Moreover, in the combined model, SCD probability for the low-risk group was lower than in the ECG and clinical models, therefore further increasing the distance between the curves for low and high risk group. Regarding PFD, the distance between low- and high-risk groups was significant for all three models, but larger for the combined one (Figure 5.2 (d)-(f)).

Figure 5.3 shows the univariate HARs of the low- (blue square), middle- (green circle) and high-risk (red diamond) groups when compared to the low-risk group for SCD (a) and (b), and PFD (c) and (d) risk, using the models specific for each endpoint. * Indicates $p<0.005$ with respect to the low risk group. ** indicates $p<0.05$ with respect to the low risk group. Both SCD and PFD prediction improved when clinical and ECG markers were integrated into the combined model, with median HARs for the high SCD risk group equal to 4, 9 and 14 (panel (a)) for clinical, ECG and combined models, respectively, and median HARs for the high PFD risk group equal to 4, 11 and 13 (panel (d)) for clinical, ECG and combined models, respectively. Importantly, panels (b)-(c) show that models designed to predict SCD did not predict PFD and models designed to predict PFD did not predict SCD, therefore demonstrating specificity, on top of sensitivity, in the prediction of the designated mode of death.

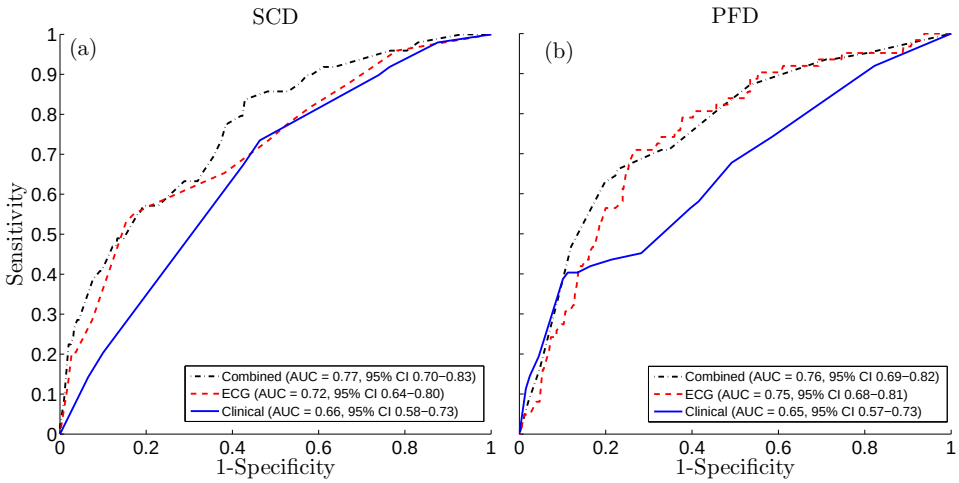

Figure 5.1: ROC curves for the clinical (solid blue), ECG (dashed red) and combined (dotted black) specific risk models in the classification of SCD (a) and PFD (b) victims.

5.4 Discussion

In this chapter, risk models combining clinical and ECG-derived markers were proposed to specifically predict SCD and PFD in CHF patients. The ECG-derived markers were those studied in this thesis, reflecting different repolarization and autonomic mechanisms. In mild-to-moderate CHF patients the inclusion of ECG-derived indices quantifying dispersion of repolarization, dispersion of repolarization restitution and autonomic condition into a clinical model significantly improves SCD predictive value. In contrast, the combination of these ECG-derived indices already reaches the maximum PFD predictive value, with no improvement when also including clinical variables. This indicates a possible new strategy to identify CHF patients specifically

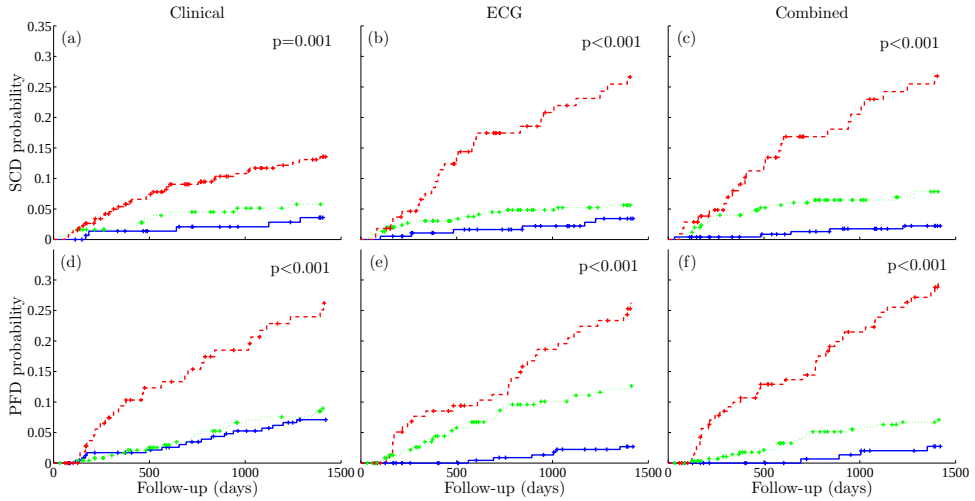

Figure 5.2: Probability curves of the three risk groups, low (solid blue), middle (dotted green) and high (dashed red) defined in the clinical (left), ECG (middle) and combined (right) specific risk models for SCD (top) and PFD (bottom).

at risk of arrhythmias or mechanical fatigue, that would or would not benefit from therapy with ICD or CRT.

In a multivariate analysis, the clinical variables that predicted SCD were male gender, NYHA class III and LVEF$\leqslant$35%. Previous studies have also shown that men have higher SCD risk than women [114, 255], while the contribution of the NYHA class to SCD risk is still unclear [94, 118]. Impaired LVEF is at present the only risk factor considered for ICD implantation in high SCD risk patients, but its specificity is insufficient [256].

Diabetes, NYHA class III, absence of treatment with beta-blockers and LVEF$\leqslant$35% predicted PFD in a multivariate analysis. These results agree with previous findings reporting the relation between end-stage CHF and low cardiac output and LVEF, diabetes due to increased congestion as well as advanced stages of NYHA class [257]. Also, treatment with beta-blockers, or limiting neuro-hormonal activation has been shown to be especially important in retarding CHF progression [258, 259].

The ECG variables that independently predicted SCD were $\Delta\alpha^{\mathrm{Tpe}}$, IAA, TS and TMR^{d_w}. SCD is a multifactorial event and our results confirm that SCD risk is reflected by increased dispersion of repolarization restitution [53,54], increased variability of temporal dispersion of repolarization [260] and baroreceptor-heart rate reflex sensitivity [174,261]. More importantly, this confirms our hypothesis that a combination of ECG markers that capture complementary information about arrhythmic substrates would improve SCD prediction. The performance of the ECG-derived model in predicting SCD can be compared to that using the markers individually. In chapter 2 we demonstrated that patients in the high-SCD risk group ($\Delta\alpha^{\mathrm{Tpe}} \geqslant 0.028$) showed a 14% SCD probability after the follow-up period, and a HAR of 3, while in chapter 4 these

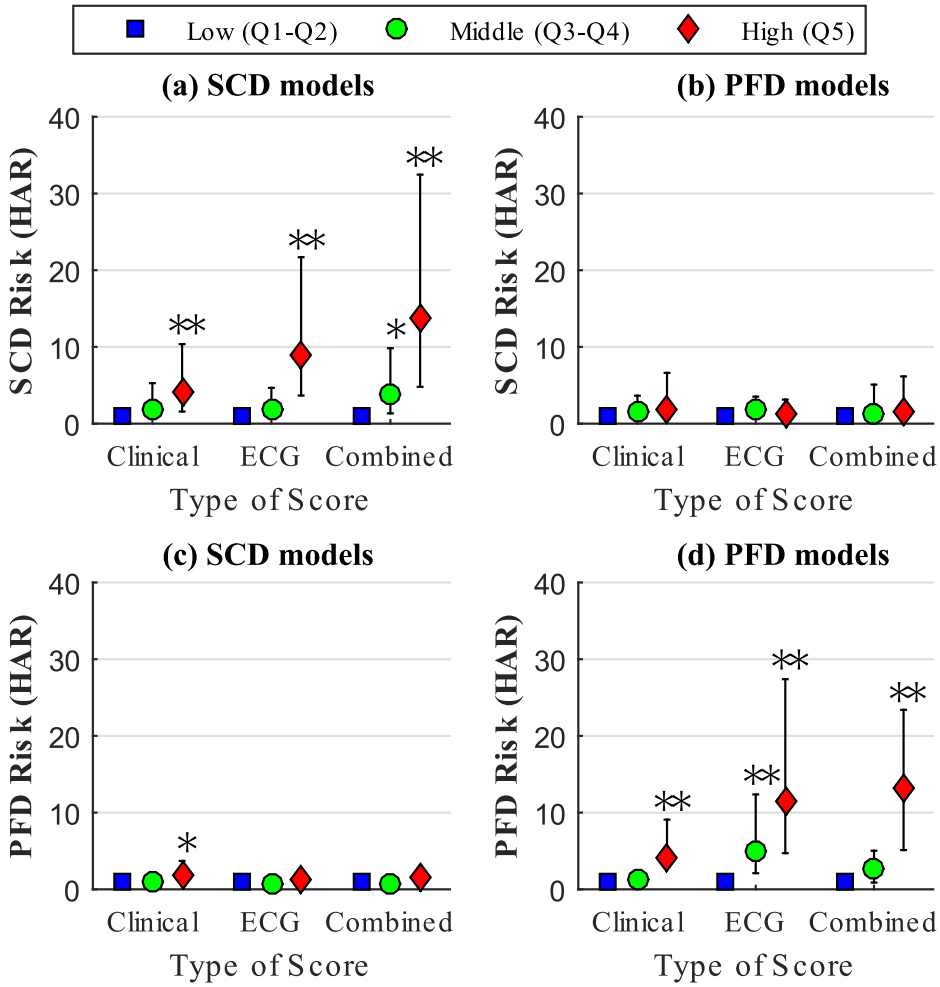

Figure 5.3: Hazard ratios of SCD (A and B) and PFD (C and D) for the three risk groups, low (blue square), middle (green circle) and high (red diamond) risk groups defined in the clinical, ECG and combined specific models. * and ** indicate $p<0.05$ and $p<0.005$ with respect to the low risk group, respectively.

values were 13% and 3 for patients with $TMR^{d_w} \geqslant 0.040$. The high-risk group of the ECG-derived model reaches a 26% SCD probability, with a HAR of 9, confirming the benefit of combining risk markers. Future studies could include promising indices assessing dispersion of repolarization from the ECG [262] into the proposed models.

The ECG variables that independently predicted PFD were $\Delta\alpha^{\mathrm{Tpe}}$, TS and the range of RR. This indicates that PFD is also characterized by baroreceptor-heart rate reflex sensitivity [174, 261]. However, lower values of $\Delta\alpha^{\mathrm{Tpe}}$ indicative of higher PFD risk suggest that PFD victims experience a reduction in the ability of the ventricles

to adapt to changes in heart rate, as opposed to SCD victims [22]. Again, when comparing with the performance of individual markers, patients with $\Delta\alpha^{\mathrm{Tpe}} \leqslant 0.022$ had 15% PFD probability and a HAR of 2. The high-PFD risk group of the PFD ECG-derived model achieves a 26% PFD probability, and a HAR of 12, also confirming the need for using a combined score in mortality prediction, rather than individual markers only.

The ECG models for SCD and PFD showed better prognostic value than the clinical models. The combination of clinical and ECG-derived markers synergistically improved the prognostic values for both SCD and PFD. However, in the case of PFD prediction, the improvement achieved by the integration of clinical and ECG-derived markers was only marginal with respect to the results of the ECG model. This suggests that clinical variables do not contain complementary information for PFD risk prediction to that within the ECG markers. More importantly, both ECG and combined risk models demonstrated high sensitivity (association with the designated mode of death) and specificity (no association with the alternative mode of death) for SCD and PFD prediction. In contrast, the clinical risk model for SCD prediction lacked specificity and predicted PFD in addition to SCD (Figure 5.3).

5.4.1 Technical Considerations

We applied an iterative algorithm to validate the thresholds of the ECG-derived variables when building the risk scores and the optimal thresholds were the same as those proposed in the literature.

5.4.2 Limitations

Prospective studies are needed to verify that the observations presented here have a role in SCD and PFD prediction in CHF patients. This study only considered consecutive patients, so the number of SCD and PFD victims was relatively low and this has limited the possibility of performing further statistical analyses. In addition, the risk scores proposed in this work were elaborated in sinus rhythm. Therefore, they may not be applicable in CHF patients with other rhythms. Only standard clinical variables were available for this study. The assessment of clinical and combined models integrating further variables needs further investigation.

5.5 Conclusion

In this chapter, we demonstrate that two risk prediction models that combine indices describing clinical as well as novel ECG-based measures of electrophysiological and autonomic abnormalities improve SCD and PFD risk prediction, as compared to individual markers. For SCD, the combination of clinical and ECG-derived variables substantially improved risk prediction as compared to the use of only one or the other type of variables. In contrast, PFD risk prediction for the ECG-derived model was

already satisfactory and only marginally improved with the integration of clinical information.

Chapter 6

Final Discussion, Conclusions and Future Work

6.1 Summary and Discussion

The main objective of this thesis was to find ECG-derived markers of ventricular repolarization restitution to improve the prediction of SCD and PFD. This objective has been faced using, on the one hand, time-interval indices and, on the other hand, morphological indices. To use the morphological information of the T-wave, we have developed an innovative methodology that allows the comparison of two different shapes, and the quantification of their differences.

6.1.1 The Quantification of Dispersion of Repolarization Restitution from the ECG Predicts Mortality

This thesis started by evaluating whether the dispersion of repolarization restitution, estimated from the slope of the Tpe/RR relationship, was associated with increased arrhythmic risk, leading to SCD in CHF patients. Not only we found that the Tpe/RR slope was related to SCD, but we proved that this index also indicated increased PFD risk. For the best of our knowledge, no previous ECG-derived index has been able to risk-stratify CHF patients into three risk bands: steeper slopes indicating high SCD risk, flatter slopes indicating high PFD risk and middle slope values indicating low CD risk.

We also quantified the dispersion of the repolarization restitution using the overall morphology of the T-wave, rather than just considering the Tpe interval. Then, we calculated two mean warped T-waves, one representative of the T-wave morphology at short RRs, and another representative of the T-wave morphology at long RRs. Then, we compared them using our proposed warping methodology, normalizing by the variation in RR. We found that TMR^{d_w}, the normalized d_w, was the only morphological marker significantly associated with SCD. This suggests that the variations in the dispersion of repolarization restitution are mainly reflected on the ECG as variations in the temporal domain of the T-wave. When comparing the predictive value of TMR^{d_w} and the slope of the Tpe dynamics, we found that TMR^{d_w} outperformed the interval-based index. This confirms our hypothesis suggesting that the quantification of the overall T-wave morphology, rather than just the Tpe interval, provides additional information reflecting the distribution of dispersion of repolarization, critical for the prediction of SCD. Surprisingly, TMR^{d_w} did not show PFD predictive value. We are still uncertain about the significance of these results. One possible explanation may be that the lack of ventricle response to autonomic innervation, manifested in victims of PFD, is mainly reflected on the last phase of repolarization. Then, the Tpe interval captures this information, but it is hidden in TMR^{d_w} because of considering the overall T-wave morphology. A logical future work is to repeat the calculus of TMR^{d_w} but by only considering the morphology of the T-wave from the peak to the end.

6.1.2 The Quantification of Repolarization Restitution from the ECG does not Predict Mortality

Considering that the QT interval is the most traditional index of ventricular repolarization for arrhythmic risk prediction [126], and its dynamics extensively used associated with arrhythmogenicity [130–133], we evaluated the predictive value of the slope of the QT dynamics. However, we did not find any association between this index and any mode of CD. These results may suggest that, as previously stated [17, 263], the last stages of repolarization, quantified by the Tpe interval, are those with higher arrhythmic vulnerability. Then, our results demonstrate that the intrinsic heterogeneity of repolarization along the ventricle is more critical for SCD risk than the response

of the total repolarization wave to variations in heart rate.

6.1.3 The Combination of Indices Quantifying Different electrophysiological and Autonomic Mechanisms Improves Prediction

After demonstrating that the slope of the Tpe dynamics and TMR^{d_w} strongly predicted SCD and PFD, we used classification analysis to separate CHF patients according to their risk of suffering from these cardiac events, using baseline information. This means that, in contrast with survival analysis, we did not use the time-to-death information for classification. Using two- and three-class SVM classifiers, we confirmed the risk-stratification potential of both indices. When introducing two other ECG-derived predictors of SCD and PFD, like the IAA or TS, the risk-stratification was significantly improved. This indicates that the three indices are reflecting different and complementary underlying mechanisms. IAA measures spatio-temporal dispersion of repolarization, TS reflects sympathovagal balance, and the slope of the Tpe dynamics and TMR^{d_w} quantify dispersion of repolarization restitution.

The results from the last chapter also demonstrate the importance of joining the individual predictive power of ECG-derived markers reflecting complementary mechanisms into a single combined score with optimal capacity of predicting SCD and PFD. As explained in the introduction, SCD is the result of a series of failing mechanisms that might be harmless when occurring isolated, but fatal when occurring together. These mechanisms have different sources, being mainly electrophysiological, autonomic, anatomic, or even genetic. This means that if a person has a genetic predisposition for SCD, and suffers a cardiac disease that leads to CHF, the subject might experience some physical damage affecting the correct electrical conduction by, for example, increasing the dispersion of repolarization. Then, if by any reason the heart rate increases, it could trigger a malignant arrhythmia, that will be maintained due to the already vulnerable myocardium. Therefore, using an index that contains information about the dispersion of repolarization, its adaptation to changes in heart rate, and other clinical, genetic and demographic variables, may be very effective for preventing the arrhythmic event and the SCD.

6.1.4 Methodological Contribution

The quantification of the T-wave morphological variation was not straightforward and, therefore, we had to conceive a methodology and propose morphology variability markers to face this task. For that, we had to, first, demonstrate that our proposed methodology was robust against any noise level possibly found in actual ECG recordings, and, second, to prove that the variations in the proposed indices quantifying T-wave morphology variability were meaningful, i.e. related to variations in the dispersion of ventricular repolarization. Therefore, we adapted a mathematical framework proposed for statistical data [228,229] to solve our problem. The basic idea

of this methodology is to separate both temporal and amplitude sources of variability when working in a transformed domain, the SRSF. Then, the first step is to warp the T-wave with a warping algorithm capable of removing the strictly temporal variability, so that the remaining variability is amplitude.

In this thesis we have compared SRSF and DTW algorithms and we have demonstrated that SRSF is independent from the amplitude values of the T-waves and, thus, this warping algorithm does not experience the "pinching effect", as DTW does. This is specially important when analysing actual ECG recordings, where there is high variability in both temporal and amplitude domains. In order to cope with the "pinching effect", DTW adds some penalties into its minimization equation, but, then, the warping function might be highly dependent on these constraints. SRSF includes a regularization term in its optimization equation which avoids this limitation. After separating both sources of variability, we quantified them, with d_w and d_w^{NL}, and d_a and d_a^{NL} measuring the temporal and amplitude variability levels, respectively, which were proved to be associated with variations in the dispersion of repolarization, using an electrophysiological cardiac model, and using actual ECG recordings. Therefore, the methodological contribution of this thesis is a robust and strong framework to compare the morphology of different T-waves, where the quantification of morphological variability using our proposed indices reflects changes in the dispersion of repolarization.

6.1.5 Clinical Significance

The ECG recording is a very fast, easy, non-invasive and cheap method of evaluating the autonomic and electric condition of the heart. We have used the last wave of the ECG signal, the T-wave, to extract information reflecting the repolarization phase of the ventricles. Using that information, we have shown in this thesis that it is possible to specifically improve prediction of SCD and PFD risk in a 4-years follow-up period. With the contribution of this thesis, we have shed more light into the phenomena of malignant ventricular arrhythmias, and the relation between ventricular repolarization and the ANS innervation. Then, using an every-day ambulatory recording, a clinician could diagnose the current state of the heart of a patient using the values of our proposed indices, $\Delta\alpha^{\text{Tpe}}$ and TMR^{d_w}. Based on the result of the diagnostic, and considering that $\Delta\alpha^{\text{Tpe}}$ separates SCD potential victims from PFD potential victims, and from survivors of CD, while TMR^{d_w} refines the SCD risk population, the clinician may derive the potential SCD victim for an ICD implantation, or the potential PFD victim for CRT.

6.1.6 Main Limitations

First, this thesis used fully automated ECG measurements that are likely to suffer imprecision, especially when applied to abnormal ECGs in CHF patients. Prospective studies are needed to verify that the observations presented here have a role in SCD and PFD prediction in CHF patients. Second, the definition of SCD and PFD used in this study was the same as in other similar studies but might not be uniform in

respect of the underlying patho-physiology. Both tachycardia and bradycardia cases were likely included. The number of SCD and PFD victims was relatively low not only in comparison with survivors but also with victims of other modes of death. This might have imposed some limitations on the statistical comparisons. Next, future studies may include the splitting of the data into training and test sets so that the thresholds developed in the training set could be evaluated in the test set. Further investigations on the applicability of the defined cut-off point and on the extension of the analysis to other CHF and non-CHF populations are needed to confirm the prognostic value of the proposed index.

Regarding the warping methodology, due to the high sensitivity of the warping function, erroneous extraction of the morphology of the T-wave, due to excessive noise or delineation errors, will lead to incorrect values of d_w and d_w^{NL}, and an incorrect warping. Therefore, the markers d_a and d_a^{NL} could also be affected, coupling, in some way, the robustness and sensitivity of the indices. Also, although the proposed markers capture many T-wave morphologies, there can appear extreme morphological variations which will lead to meaningless interpretations of d_w, d_a, d_w^{NL} and d_a^{NL}. However, we have not found any such extreme variation in the analysed T-waves, since even for biphasic or S-shaped T-waves we still obtained interpretable results. Next, we selected the first principal component as the lead capturing the direction of maximal variation of the repolarization gradient. Although we assumed that a projection of the maximal energy onto this component also implied a maximal projection of the repolarization variability, given the physiological additive generation of the ECG signals, this may not always be guaranteed. Finally, this first principal component may be dominated by precordial lead T-waves, which have the highest amplitude and, therefore, in this study, the algorithm did not capture the morphological variation reflected in other leads.

6.2 Conclusion

This thesis proposes and proves that two ECG-derived markers of dispersion of repolarization restitution, $\Delta\alpha^{\mathrm{Tpe}}$ and TMR^{d_w}, predict SCD or PFD in a population of CHF patients. The index $\Delta\alpha^{\mathrm{Tpe}}$ is calculated using the Tpe interval, while TMR^{d_w} uses the overall morphology of the T-wave. For the quantification of the T-wave morphological variability, a novel signal processing technique based on time-warping has also been proposed in this thesis. The predictive value of the proposed markers may help clinicians to better diagnose the CD risk of a patient and, then, to better decide the specific treatment the patient would require.

6.3 Future Work

Some of the possible straightforward future research lines derived from the development presented in this thesis are:

- The cellular and sub-cellular mechanisms that could explain the origin of the different observed patterns in the analysed ventricular repolarization indices remain to be elucidated. An electrophysiological modelling investigation is proposed to be carried out to better understand APDR dynamics and their eventual relationship with arrhythmic risk and SCD, and with ventricular response to autonomic innervation and PFD risk.

- The morphological index d_w was basically computed as the average separation of the optimal warping function from the reference temporal domain. However, this optimal warping function carries much more information, i.e. non-linearities, specific manifestations of the first and last phases of repolarization, etc, that we suggest to explore in future studies.

- The indices $\Delta\alpha^{\mathrm{Tpe}}$ and TMR^{d_w} have been measured on the first principal component when applying PCA to the available leads. Then, we assumed that the T-waves in this first principal component carried the principal morphological variation reflecting the variations in ventricular repolarization. However, the two other principal components may still carry important physiological information. Then, we propose to extend the morphological analysis to the application on the VCG. For that, the warping method must be extended to a 3-D coordinate system, and the morphological indices would account for the morphological variation in the three coordinates. Then, we would have a clearer information of the spatial variation of ventricular repolarization dispersion.

- As suggested in the previous section, to only account for the last phase of repolarization, we suggest to repeat the calculus of TMR^{d_w}, but only considering the T-wave morphology contained from its peak to its end. Then, based on the SCD and PFD predictive value of $\Delta\alpha^{\mathrm{Tpe}}$, the risk stratifying ability of the new-defined TMR^{d_w} might improve.

- The methodological framework proposed in this thesis is not restricted to the T-wave and may be applied to quantify morphological variability in other waveforms. For example, it could be used to quantify the variations in the overall depolarization and repolarization waves in the ventricles, through the comparison of the morphology of the QRS-T complex. Another option could be to apply this framework to the QRS complex, as an alternative measure of ischemia, which is manifested in the ECG as a widening of this complex.

- T-wave alternans are defined as an alternant pattern in the amplitude and morphology of the T-wave. Then, we suggest to explore if the morphology variability markers d_w and d_a are capable of following this alternant variation, and test if they capture additional information not contained in the current methods of quantifying this phenomenon.

- Along the thesis we have evaluated the MUSIC database, which consists of a complete study population of CHF patients. A reasonable future work is to validate the predictive value of the indices proposed in this thesis, $\Delta\alpha^{\mathrm{Tpe}}$ and TMR^{d_w} in different study populations to assess their reproducibility.

Bibliography

[1] World Health Organization, *Cardiovascular disease: Global atlas on cardiovascular disease prevention and control.* Geneva, Switzerland, 2012.

[2] L. J. Laslett et. al., "The worldwide environment of cardiovascular disease: prevalence, diagnosis, therapy, and policy issues. A report from the American College of Cardiology," *J Am Coll Cardiol*, vol. 60, no. 25, pp. S1–S49, 2012.

[3] S. C. Jr. Smith et. al., "Our time: a call to save preventable death from cardiovascular disease (heart disease and stroke).," *J Am Coll Cardiol*, vol. 60, pp. 2343–2348, 2012.

[4] J. S. Robb and R. C. Robb, "The normal heart: anatomy and physiology of the structural units," *Am Heart J*, vol. 23, no. 4, pp. 455–467, 1942.

[5] L. Sörnmo and P. Laguna, *Bioelectrical Signal Processing in Cardiac and Neurological Applications.* 2005.

[6] D. Durrer., "Electrical aspects of human cardiac activity: a clinical-physiological approach to excitation and stimulation," *Cardiovasc Res*, vol. 2, no. 1, pp. 1–18, 1968.

[7] R. E. Klabunde, *Electrical activity of the heart.* Lippincott Williams and Wilkins, cardiovascular physiology concepts ed., 2005.

[8] R. Berne et. al., *Physiology.* Elsevier Mosby, 2004.

[9] E. Pueyo et. al., "Cardiac repolarization analysis using the surface electrocardiogram," *Philos Trans A Math Phys Eng Sci*, vol. 367, no. 1887, pp. 213–233, 2009.

[10] S. B. Prenner et. al., "Repolarization heterogeneity: Beyond the QT interval," *J Am Heart Assoc*, vol. 5, p. e003607, 2016.

[11] G. X. Yan and W. Shimizu and C. Antzelevitch, "The characteristics and distribution of M cells in arterially-perfused canine left ventricular wedge preparations," *Circulation*, vol. 98, pp. 1921–1927, 1998.

[12] T. Stankovicova et. al., "M cells and transmural heterogeneity of action potential configuration in myocytes from the left ventricular wall of the pig heart," *Cardiovasc Res*, vol. 45, pp. 952–960, 2000.

[13] E. Drouin et. al., "Electrophysiologic characteristics of cells spanning the left ventricular wall of human heart: evidence for presence of M cells," *J Am Coll Cardiol*, vol. 26, pp. 185–192, 1995.

[14] F. G. Akar and K. R. Laurita and D. S. Rosenbaum., "Cellular basis for dispersion of repolarization underlying reentrant arrhythmias," *J Electrocardiol*, vol. 33, no. Supp, pp. 23–31, 2000.

[15] S. H. Litovsky and C. Antzelevitch, "Transient outward current prominent in canince ventricular epicardium but not endocardium," *Circ Res*, vol. 62, no. 1, pp. 116–126, 1988.

[16] T. Furukawa et. al., "Differences in transient outward currents of feline endocardial and epicardial myocytes," *Circ Res*, vol. 67, no. 5, pp. 1287–1291, 1990.

[17] T. Opthof et. al., "Dispersion of repolarization in canine ventricle and the electrocardiographic T-wave: Tp-e interval does not reflect transmural dispersion," *Heart Rhythm*, vol. 4, no. 3, pp. 341–348, 2007.

[18] G. X. Yan and C. Antzelevitch, "Cellular basis for the normal T-wave and the electrocardiographic manifestations of the long QT syndrome.," *Circulation*, vol. 98, pp. 1928–1936, 1998.

[19] Y. Xia et. al., "In vivo validation of the coincidence of the peak and end of the t wave with full repolarization of the epicardium and endocardium in swine," *Heart Rhythm*, vol. 2, pp. 162–169, 2005.

[20] E. P. Anyukhovsky et. al., "The controversial M cell," *J Cardiovasc Electrophysiol*, vol. 10, pp. 244–260, 1999.

[21] P. Taggart et. al., "Electrotonic cancellation of transmural electrical gradients in the left ventricle in man," *Prog Biophys Mol Biol*, vol. 82, pp. 243–254, 2003.

[22] A. V. Glukhov et. al., "Transmural dispersion of repolarization in failing and nonfailing human ventricle," *Circ Res*, vol. 106, no. 5, pp. 981–991, 2010.

[23] F. G. Akar et. al., "Unique topographical distribution of M cells underlies reentrant mechanism of torsade de pointes in the long-QT syndrome," *Circulation*, vol. 105, pp. 1247–1253, 2002.

[24] J. M. Di Diego and Z. Q. Sun and C. Antzelevitch, "Ito and action potential notch are smaller in left vs. right canine ventricular epicardium.," *Am J Physiol*, vol. 271, pp. H548–H561, 1996.

[25] P. G. Volders et. al., "Repolarizing K+ currents Ito1 and Iks are larger in right than left canine ventricular midmyocardium," *Circulation*, vol. 99, pp. 206–210, 1999.

[26] D. W. Liu and C. Antzelevitch, "Characteristics of the delayed rectifier current (Ikr and Iks) in canine ventricular epicardial, midmyocardial, and endocardial myocytes: A weaker Iks contributes to the longer action potential of the M cell," *Circ Res*, vol. 76, pp. 351–365, 1995.

[27] D. Fedida and W. R. Giles, "Regional variations in action potentials and transient outward curent in myocytes isolated from rabbit left ventricle.," *J Physiol*, vol. 442, pp. 191–209, 1991.

[28] R. B. Clark et. al., "Heterogeneity of action potential waveforms and potassium currents in rat ventricle," *Cardiovasc Res*, vol. 27, pp. 1795–1799, 1993.

[29] D. L. Campbell et. al., "The calcium-independent transient outward potassium current in isolated ferret right ventricular myocytes," *J Gen Physiol*, vol. 101, pp. 571–601, 1993.

[30] M. Nabauer et. al., "Regional differences in current density and rate-dependent properties of the transient outward current in subepicardial and subendocardial myocytes of human left ventricle.," *Circulation*, vol. 93, pp. 168–177, 1996.

[31] E. Wettwer et. al., "Transient outward current in human ventricular myocytes of subepicardial and subendocardial origin.," *Circ Res*, vol. 75, pp. 473–482, 1994.

[32] T. Watanabe et. al., "Heterogeneity of the action potential in isolated rat ventricular myocytes and tissue," *Circ Res*, vol. 52, pp. 280–290, 1983.

[33] C. Antzelevitch et. al., "Heterogeneity within the ventricular wall: electrophysiology and pharmacology of epicardial, endocardial, and M cells," *Circ Res*, vol. 69, pp. 1427–1449, 1991.

[34] S. M. Bryant and et. al, "Regional differences in the delayed rectifier current (IKr and IKs) contribute to the differences in action potential duration in basal left ventricular myocytes in guinea-pig," *Cardiovasc Res*, vol. 40, pp. 322–331, 1998.

[35] J. Cheng et. al., "Heterogeneous distribution of the two components of delayed rectifier K+ current: a potential mechanisms of the proarrhythmia effects of methanesulfonanilideclass III agents," *Cardiovasc Res*, vol. 43, pp. 135–147, 1999.

[36] G. R. Li et. al., "Transmural heterogeneity of action potentials and Ito1 in myocytes isolated from the human right ventricle," *Am J Physiol*, vol. 275, pp. H369–H377, 1998.

[37] N. Ueda and D. P. Zipes and J. Wu, "Functional and transmural modulation of M cell behaviour in canine ventricular wall," *Am J Physiol Heart Circ Physiol*, vol. 287, pp. H2569–H2575, 2004.

[38] T. Volk et. al., "Relationship between transient outward K+ current and Ca2 influx in rat cardiac myocytes of endo- and epicardial origin," *J Physiol*, vol. 519, no. 3, pp. 841–850, 1999.

[39] T. Volk et. al., "Regional alterations of repolarizing K+ currents among the left ventricular free wall of rats with ascending aortic stenosis," *J Physiol*, vol. 530, pp. 443–455, 2001.

[40] A. van Oosterom and T. F. Oosterndorp, "ECGSIM: an interactive tool for studying the genesis of qrst waveforms," *Heart*, vol. 90, no. 2, pp. 165–168, 2004.

[41] M. Hiraoka and S. Kawano., "Mechanism of increased amplitude and duration of the plateau with sudden shortening of diastolic intervals in rabbit ventricular cells.," *Circulation*, vol. 60, no. 1, pp. 14–26, 1987.

[42] Y. Kobayashi et. al., "Cellular mechanisms of differential action potential duration restitution in canine ventricular muscle cells during single versus double premature stimuli," *Circulation*, vol. 86, no. 3, pp. 955–967, 1992.

[43] M. Watanabe and N. F. Otani and R. F. Gilmour., "Biphasic restitution of action potential duration and complex dynamics in ventricular myocardium," *Circ Res*, vol. 76, no. 5, pp. 915–921, 1995.

[44] M. Orini et. al., "Interactions between activation and repolarization restitution properties in the intact human heart: In vivo whole-heart data and mathematical description," *Plos One*, vol. 11, no. 9, p. e0161765, 2016.

[45] M. R. Franz et. al., "Cycle length dependence of human action potential duration in vivo. Effects of single extrastimuli, sudden sustained rate acceleration and deceleration, and different steady-state frequencies," *J Clin Invest*, vol. 82, pp. 972–979, Sep 1988.

[46] M. R. Franz., "The electrical restitution curve revisted: steep or flat slope- which is better?," *J Cardiovasc Electrophysiol*, vol. 14, pp. S140–S147, 2003.

[47] M. L. Riccio and M. L. Koller and R. F. G. Jr, "Electrical restitution and spatiotemporal organization during ventricular fibrillation," *Circ Res*, vol. 84, pp. 955–963, 1999.

[48] A. Garfinkel et. al., "Preventing ventricular fibrillation by flattening cardiac restitution," *Proc Natl Acad Sci U S A*, vol. 97, pp. 6061–6066, May 2000.

[49] J. N. Weiss et. al., "From pulsus to pulseless: The saga of cardiac alternans.," *Circ Res*, vol. 98, no. 10, pp. 1244–1253, 2006.

[50] K. T. Tusscher and A. Panfilov, "Alternans and spiral breakup in a human ventricular tissue model," *Am J Physiol*, vol. 291, pp. H1088–H1100, 2006.

[51] M. L. Koller and M. L. Riccio and R. F. Gilmour, "Dynamic restitution of action potential duration during electrical alternans and ventricular fibrillation," *Am J Physiol*, vol. 275, pp. 1635–1642, 1998.

[52] F. L. Burton and S. M. Cobbe., "Dispersion of ventricular repolarization and refractory period," *Cardiovasc Res*, vol. 50, no. 1, pp. 10–23, 2001.

[53] M. P. Nash et. al., "Whole heart action potential duration restitution properties in cardiac patients: a combined clinical and modelling study," *Exp Physiol*, vol. 91, no. 2, pp. 339–354, 2006.

[54] H. N. Pak et. al., "Spatial dispersion of action potential duration restitution kinetics is associated with induction of ventricular tachycardia/fibrillation in humans.," *J Cardiovasc Electrophysiol*, vol. 15, no. 12, pp. 1357–1363, 2004.

[55] W. A. N. Dorland, *Dorland's medical dictionary.* Saunders, 1968.

[56] G. Pocock and C. D. Richards and D. Richards, *Human physiology.* Oxford university press, 2013.

[57] V. G. Florea and J. N. Cohn., "The autonomic nervous system and heart failure.," *Circ Res*, vol. 114, pp. 1815–1826, 2014.

[58] L. K. McCorry, "Physiology of the autonomic nervous system," *Am J Pharmaceut Educat*, vol. 71, no. 4, pp. 1–11, 2007.

[59] N. Charkoudian and J. A. Rabbitts, "Sympathetic neural mechanisms in human cardiovascular health and disease," *Mayo Clinic Proceedings*, vol. 84, no. 9, pp. 822–830, 2009.

[60] B.N Olshansky et. al., "Parasympathetic nervous system and heart failure," *Circulation*, vol. 118, no. 8, pp. 863–871, 2008.

[61] R. L. Lux, *Mapping techniques*, vol. 2 of *Comprehensive Electrocardiology. Theory and Practice in Health and Disease*, ch. 26, pp. 1001–1014. New York: Pergamon Press, 1989.

[62] E. Frank, "An accurate, clinically practical system for spatial vectorcardiography," *Circulation*, 1956.

[63] G. E. Dower, "The ECGD: A derivation of the ECG from VCG leads," *J Electrocardiol*, vol. 17, pp. 189–191, 1984.

[64] J. A. Kors et. al., "Reconstruction of the Frank vectorcardiogram from standard electrocardiographic leads: Diagnostic comparison of different methods," *Eur Heart J*, vol. 11, pp. 1083–1092, 1990.

[65] F. Castells et. al., "Principal component analysis in ECG signal processing," *EURASIP J Applied Signal Proc*, vol. 2007, no. 1, pp. 98–98, 2007.

[66] J. P. Martínez et. al., "A wavelet-based ECG delineator: evaluation on standard databases," *IEEE Transactions on Biomedical Engineering*, vol. 51, pp. 570–581, 2004.

[67] P. Laguna and R. Jané and P. Caminal, "Automatic detection of wave boundaries in multilead ECG signals: Validation with the CSE database," *Comput Biomed Res*, vol. 27, no. 1, pp. 45–60, 1994.

[68] R. Almeida et. al., "Multilead ECG delineation using spatially projected leads from wavelet transform loops," *IEEE Trans Biomed Eng*, vol. 56, pp. 1996–2005, 2009.

[69] Task Force Members, "ESC guidelines for the diagnosis and treatment of acute and chronic heart failure 2008," *Eur J Heart Fail*, pp. 933–989, 2008.

[70] W. F. Boron and E. L. Boulpaep, *Medical Physiology: a cellular amd molecular approach*. 2005.

[71] C. Yu et. al., "Correlation with fluid status and feasibility of early warning preceding hospitalization," *Am H Assoc J*, vol. 112, pp. 841–848, 2005.

[72] J. K. Oh, "Echocardiography in heart failure: beyond diagnosis," *Eur Heart J - Cardiovasc Imag*, vol. 8, pp. 4–14, Jan 2007.

[73] J. N. Kirkpatrick et. al., "Echocardiography in heart failure: applications, utility and new horizons," *J Am Coll Cardiol*, vol. 50, pp. 381–396, Jul 2007.

[74] A. Maisel, "B-type natriuretic peptide levels: diagnostic and prognostic in congestive heart failure," *Circulation*, vol. 105, pp. 2328–2331, May 2002.

[75] Q. Dao et. al., "Utility of b-type natriuretic peptide in the diagnosis of congestive heart failure in an urgent-care setting," *J Am Coll Cardiol*, vol. 37, pp. 379–385, Feb 2001.

[76] Criteria Committee, New York Heart Association, *Diseases of the heart and blood vessels. Nomenclature and criteria for diagnosis*, p. 114. 1964.

[77] S. A. Hunt et. al., "ACC/AHA guidelines for the evaluation and management of chronic heart failure in the adult: executive summary," *Circulation*, vol. 104, pp. 2996–3007, Dec 2001.

[78] F. Zannad et. al., "Clinical outcome endpoints in heart failure trials: a European Society of Cardiology Heart Failure Association consensus document," *Eur H Heart Fail*, vol. 15, pp. 1082–1094, 2013.

[79] S. D. Solomon et. al., "Effect of candesartan on cause-specific mortality in heart failure patients. The Cadersartan in heart failure assessment of reduction in mortality and morbidity (CHARM) program.," *Circulation*, vol. 110, pp. 2180–2183, 2004.

[80] MERIT-HF Study Group, "Effect of metoprolol CR/XL in chronic heart failure: Metoprolol CR/XL randomised intervention trial in congestive heart failure (MERIT-HF)," *Lancet*, vol. 353, pp. 2001–2007, 1999.

[81] M. R. Zile et. al., "Mode of death in patients with heart failure and a preserved ejection fraction. Results from the Irbesartan in heart failure with preserved ejection fraction study (O-preserve) trial," *Circulation*, vol. 121, pp. 1393–1405, 2010.

[82] R. Deo and C. M. Albert, "Epidemiology and genetics of sudden cardiac death," *Circulation*, vol. 125, pp. 620–637, Jan 2012.

[83] M. T. Keating and M. C. Sanguinetti, "Molecular and cellular mechanisms of cardiac arrhythmias.," *Cell*, vol. 104, pp. 569–580, Feb 2001.

[84] C. Antzelevitch and A. Burashnikov., "Overview of basic mechanisms of cardiac arrhythmia," *Card Electrophysiol Clin*, vol. 3, pp. 23–45, Mar 2011.

[85] P. W. Macfarlane and T. D. Veitch-Lawrie, *Theory and Practique in Health Disease*. New York, NY: Pergamon, 1989.

[86] G. R. Mines., "On circulating excitations in heart muscle and their possible relation to tachycardia and fibrillation.," *Trans Roy Soc Can*, pp. 43–52, 1914.

[87] P. Laguna et. al., "Techniques for ventricular repolarization instability assessment for the ECG," *Proceedings of the IEEE*, vol. 104, no. 2, pp. 392–415, 2016.

[88] G. F. Tomaselli et. al., "Sudden cardiac death in heart failure. The role of abnormal repolarization," *Circulation*, vol. 90, pp. 2534–2539, Nov 1994.

[89] D. J. Beuckelmann and M. Nabauer and E. Erdmann, "Alterations of K+ currents in isolated human ventricular myocytes from patients with terminal heart failure," *Circ Res*, vol. 73, pp. 379–385, 1993.

[90] R. F. Wiegerinck et. al., "Transmural dispersion of refractoriness and conduction velocity is associated with heterogeneously reduced conexin43 in a rabbit model of heart failure.," *Heart Rhythm*, 2008.

[91] B. J. D. Boukens et. al., "Developmental basis for electrophysiological heterogeneity in the ventricular and outflow tract myocardium as a substrate for life-threatening ventricular arrhythmias," *Circ Res*, vol. 104, pp. 19–31, 2009.

[92] J. T. Vermeulen et. al., "Electrophysiologic and extracellular ionic changes during acute ischemia in failing and normal rabbit myocardium.," *J Mol Cell Cardiol*, vol. 28, pp. 123–131, 1996.

[93] W. Quan and Y. Rudy., "Unidirectional block and reentry of cardiac excitation: a model study," *Circ Res*, vol. 66, pp. 367–382, 1990.

[94] D. P. Zipes and H. J. J. Wellens, "Sudden cardiac death," *Circulation*, vol. 98, pp. 2334–2351, 1998.

[95] Mosby's Medical Dictionary. Elsevier, 9th ed., 2009.

[96] G. R. Mines., "On dynamic equilibrium in the heart.," *J Physiol (Lond)*, vol. 46, pp. 349–383, 1913.

[97] M. A. Allessie and F. I. M. Bonke and F. J. G. Schopman, "Circus movement in rabbit atrial muscle as a mechanisms of tachycardia. The role of non-uniform recovery of excitability in the occurrence of unidirectional block as studied with multiple microelectrodes," *Circ Res*, vol. 39, pp. 168–177, 1976.

[98] J. Han and G. Moe., "Nonuniform recovery of excitability in ventricular muscle.," *Circ Res*, vol. 14, pp. 44–60, 1964.

[99] W. B. Gough et. al., "Reentrant ventricular arrhythmia in the late myocardial infarction period in the dog. correlation of activation and refractory maps," *Circ Res*, vol. 57, pp. 432–442, 1985.

[100] K. R. Laurita and D. S. Rosenbaum., "Interdependence of modulated dispersion and tissue structure in the mechanism of unidirectional block.," *Circ Res*, vol. 87, pp. 922–928, 2000.

[101] A. L. Wit and M. R. Rosen., *Afterdepolarizations and triggered activity: distinction from automaticity as an arrhythmogenic mechanism.*, pp. 2113–2164. Ney York: Raven Press, the heart and cardiovascular system ed., 1992.

[102] A. Lukas and C. Antzelevitch, "Differences in the electrophysiological response of canine ventricular epicardium and endocardium to ischemia. role of the transient outward current.," *Circulation*, vol. 88, pp. 2903–2915, 1993.

[103] M. Rubart and D. P. Zipes., "Mechanisms of sudden cardiac death," *J Clin Invest*, vol. 115, pp. 2305–2315, 2005.

[104] M. J. Shen and D. P. Zipes., "Role of the autonomic nervous system in modulating cardiac arrhythmias," *Circ Res*, vol. 114, pp. 1004–1021, 2014.

[105] A. M. Katz, "The cardiomyopathy of overload: an unnatural growth response in the hypertrophied heart.," *Ann Intern Med*, vol. 121, pp. 363–371, 1994.

[106] J. Narula et. al., "Apoptosis in myocytes in end-stage heart failure," *N Engl J Med*, vol. 335, pp. 1182–1189, 1996.

[107] E. Braunwald, *Pathophysiology of heart failure*, pp. 393–418. Heart disease: a text book of cardiovascular medicine, 4th ed., 1992. Philadelphia: W.B. Saunders.

[108] O. H. L. Bing, "Hypothesis: apoptosis may be a mechanism for the transition to heart failure with chronic pressure overload," *J Mol Cell Cardiol*, vol. 26, pp. 943–948, 1994.

[109] P. Santangeli et. al., "Left ventricular ejection fraction for the risk stratification of sudden cardiac death: friend or foe?," *Int Med J*, vol. 41, pp. 55–60, Jan 2011.

[110] J. L. Rouleau et. al., "Myocardial infarction patients in the 1990s–their risk factors, stratification and survival in canada: the canadian assessment of myocardial infarction (cami) study," *J Am Coll Cardiol*, vol. 27, pp. 1119–1127, Apr 1996.

[111] D. P. Zipes et. al., "Acc/aha/esc 2006 guidelines for management of patients with ventricular arrhythmias and the prevention of sudden cardiac death.," *J Am Coll Cardiol*, vol. 48, pp. e247–e346, Sep 2006.

[112] A. E. Epstein et. al., "Acc/aha/hrs 2008 guidelines for device-based therapy of cardiac rhythm abnormalities.," *J Am Coll Cardiol*, vol. 51, pp. e1–e62, May 2008.

[113] N. Dagres and G. Hindricks, "Risk stratification after myocardial infarction: is left ventricular ejection fraction enough to prevent sudden cardiac death?," *Eur Heart J*, vol. 34, pp. 1964–1971, 2013.

[114] S. S. Chugh et. al., "Epidemiology of sudden cardiac death: clinical and research implications," *Prog Cardiovasc Dis*, vol. 51, no. 3, pp. 213–228, 2008.

[115] D. B ansch et. al., "Primary prevention of sudden cardiac death in idiopathic dilated cardiomyopathy," *Circulation*, vol. 105, pp. 1453–1458, March 2002.

[116] B. Balkau et. al., "Diabetes as a risk factor for sudden death," *The Lancet*, vol. 354, pp. 1968–1969, Dec 1999.

[117] X. Jouven et. al., "Diabetes, glucose level, and risk of sudden cardiac death," *Eur Heart J*, vol. 26, no. 20, pp. 2142–2147, 2005.

[118] R. E. Lane and M. R. Cowie and A. W. C. Chow, "Prediction and prevention of sudden cardiac death in heart failure," *Heart*, vol. 91, pp. 674–680, 2005.

[119] A. J. Moss et. al., "Prophylactic implantation of a defibrillator in patients with myocardial infarction and reduced ejection fraction," *N Engl J Med*, vol. 346, pp. 877–883, 2002.

[120] B. Pitt et. al., "Eplerenone, a selective aldosterone blocker, in patients with left ventricular dysfunction after myocardial infarction," *N Engl J Med*, vol. 348, pp. 1309–1321, 2003.

[121] D. Mozaffarian et. al., "Prediction of mode of death in heart failure. The Seattle heart failure model.," *Circulation*, vol. 116, pp. 392–398, 2007.

[122] R. Vázquez et. al., "The MUSIC Risk score: a simple method for predicting mortality in ambulatory patients with chronic heart failure.," *European Heart Journal*, vol. 30, pp. 1088–1096, 2009.

[123] B. Ky et. al., "Multiple biomarkers for risk prediction in chronic heart failure," *Cir Heart Fail*, vol. 5, pp. 183–190, 2012.

[124] S. Adabag et. al., "A prediction model for sudden cardiac death in patients with heart failure and preserved ejection fraction," *Eur J Heart Fail*, vol. 16, pp. 1175–1182, Nov 2014.

[125] J. F. Viles-Gonzalez and J. J. Goldberger, "Population risk stratification for sudden cardiac death: Searching for the needle in the haystack?," *Heart Rhythm*, 2016.

[126] D. E. Ward, "Prolongation of the QT interval as an indicator of risk of a cardiac event," *Eur Heart J*, vol. 9, no. Supplement G, pp. 139–144, 1988.

[127] W. Bian and L. Tung, "Structure-related initiation of reentry by rapid pacing in monolayers of cardiac cells," *Circ Res*, vol. 98, pp. 29–38, 2006.

[128] R. J. Selvaraj et. al., "Steeper restitution slopes across right ventricular endocardium in patients with cardiomyopathy at high risk of ventricular arrhythmias," *Am J Physiol*, vol. 292, pp. 1262–1268, 2007.

[129] R. Coronel et. al., "Dispersion of repolarization and arrhythmogenesis," *Heart Rhythm*, vol. 6, no. 4, pp. 537–543, 2009.

[130] E. Pueyo et. al., "Characterization of QT interval adaptation to RR interval changes and its use as a risk-stratifier of arrhythmic mortality in amiodarone-treated survivors of acute myocardial infarction," *IEEE Transactions on Biomedical Engineering*, vol. 51, no. 9, pp. 1511–1520, 2004.

[131] A. Pathak et. al., "QT dynamicity: a prognostic factor for sudden cardiac death in chronic heart failure.," *European Journal of Heart Failure*, vol. 7, pp. 269–275, 2005.

[132] M. Iacoviello and et al., "Ventricular repolarization dynamicity provides independent prognostic information toward major arrhythmic events in patients with idiopathic dilated cardiomyopathy.," *Journal of the American College of Cardiology*, vol. 50, no. 3, pp. 225–231, 2007.

[133] K. Szydlo et. al., "QT/RR relationship in patients after remote anterior myocardial infarction with left ventricular dysfunction and different types of ventricular arrhythmias," *Annals of Noninvasive Electrocardiology*, vol. 13, pp. 61–66, 2008.

[134] A. Oehler et. al., "QRS-T angle: a review," *Annals Noninv Electrocardiol*, vol. 19, pp. 534–542, Nov 2014.

[135] J. A. Kors et. al., "Spatial QRS-T angle as a risk indicator of cardiac death in an elderly population," *J Electrocardiol*, vol. 36, pp. 113–114, 2003.

[136] M. K. de Bie et. al., "Incremental prognostic value of an abnormal baseline spatial QRS-T angle in chronic dialysis patients," *Europace*, vol. 15, no. 2, pp. 290–296, 2013.

[137] J. A. Kors and H. J. Ritsema van Eck and G. van Herpen, "The meaning of the tp-te interval and its diagnostic value," *J Electrocardiol*, vol. 41, pp. 575–580, Nov-Dec 2008.

[138] M. Yamaguchi et. al., "T wave peak-to-end interval and QT dispersion in acquired long QT syndrome: a new index for arrhythmogenicity.," *Clinical Science*, vol. 105, no. 6, pp. 671–676, 2003.

[139] T. M. Abdelrahman, "Prognostic value of T-peak-to-end interval for risk stratification after acute myocardial infarction," *The Egyptiam J Critical Care Med*, vol. 2, pp. 19–27, 2014.

[140] D. P. Morin et. al., "Relationships between the T-peak-to-end interval, ventricular tachyarrhytmia, and death in left ventricular systolic dysfunction," *Europace*, vol. 14, pp. 1172–1179, 2012.

[141] M. Shimizu et. al., "T-peak-to-end interval may be a better predictor of high-risk patients with hypertrophic cardiomyopathy associated with a cardiac troponin I mutation than QT dispersion," *Clin Cardiol*, vol. 25, pp. 335–339, 2002.

[142] R. Panikkath et. al., "Prolonged Tpeak-to-tend interval on the resting ECG is associated with increased risk of sudden cardiac death.," *Circulation Arrhythmia and Electrophysiology*, vol. 4, no. 4, pp. 441–447, 2011.

[143] K. R. Laurita and S. D. Girouard and D. S. Rosenbaum, "Modulation of ventricular repolarization by a premature stimulus: Role of epicardial dispersion of repolarization kinetics demonstrated by optical mapping of the intact guinea pig heart.," *Circ Res*, vol. 79, pp. 493–503, 1996.

[144] A. Mincholé et. al., "Quantification of restitution dispersion from the dynamic changes of the T-wave peak-to-end, measured at the surface ECG.," *IEEE Trans Biomed Eng*, vol. 58, pp. 1172–1182, 2011.

[145] W. B. Nicolson et. al., "A novel surface electrocardiogram-based marker of ventricular arrhythmia risk in patients with ischemic cardiomyopathy," *J Am Heart Assoc*, vol. 1, no. 4, p. e001552, 2012.

[146] H. E. Hering, "Experimentelle studien an s augethieren uber das elektrokardiogram," *Zschr Exper Path Therapie*, vol. 7, pp. 363–378, 1909.

[147] J. N. Weiss et. al., "Alternans and arrhythmias: from cell to heart.," *Circ Res*, vol. 108, pp. 98–112, 2011.

[148] B. D. Nearing and R. L. Verrier, "Tracking cardiac electrical instability by computing interlead heterogeneity of T-wave morphology.," *J Appl Physiol*, vol. 95, pp. 2265–2272, 2003.

[149] S. M. Narayan et. al., "Action potential dynamics explain arrhythmic vulnerability in human heart failure: a clinical and modeling study implicating abnormal calcium handling.," *J Am Coll Cardiol*, vol. 52, pp. 1782–1792, 2008.

[150] R. L. Verrier et. al., "Microvolt T-wave alternans physiological basis, methods of measurement, and clinical utility - consensus guideline by International Society for Holter and Noninvasive Electrocardiology," *J Am Coll Cardiol*, vol. 58, no. 13, pp. 1309–1324, 2011.

[151] S. M. Narayan, "T-wave alternans and the susceptibility to ventricular arrhythmias," *J Am Coll Cardiol*, vol. 47, no. 2, pp. 269–281, 2006.

[152] F. M. Merchant et. al., "T-wave alternans as an arrhuthmic risk stratifier: state of the art," *Curr Cardiol Rep*, vol. 15, pp. 1–18, Sep 2013.

[153] T. Nieminen and R. L. Verrier, "Usefulness of T-wave alternans in sudden death risk stratification and guiding medical therapy," *Rev Argent Cardiol*, pp. 17–26, 2010.

[154] Z. Qu and J. N. Weiss, "The chicken or the egg? Voltage and calcium dynamics in the heart," *Am J Physiol Heart Circ Physiol*, vol. 293, pp. H2054–H2055, 2007.

[155] B. D. Nearing and S. N. Oesterle and R. L. Verrier, "Quantification of ischaemia induced vulnearbility by precordial T-wave alternans analysis in dog and human.," *Cardiovasc Res*, vol. 28, pp. 1440–1449, 1994.

[156] V. Monasterio et. al., "Average T-wave alternans activity in ambulatory ECG records predicts sudden cardiac death in patients with chronic heart failure," *Heart Rhythm*, vol. 9, no. 3, pp. 383–389, 2012.

[157] G. E. Billman, "Heart rate variability: a historical perspective," *Frontiers Physiol*, vol. 2, no. 86, pp. 1–13, 2011.

[158] Task force of the European Society of Cardiology and the North American Society of Pacing and Electrophysiology., "Heart rate variability standards of measurement, physiological interpretation, and clinical use.," *Eur Heart J*, vol. 17, pp. 354–381, 1996.

[159] B. T. Jensen et. al., "Beat-to-beat QT dynamics in healthy subjects," *Ann Noninvasive Electrocardiol*, vol. 9, pp. 3–11, 2004.

[160] V. Starc and T. T. Schlegel, "Real-time multichannel system for beat-to-beat QT interval variability," *J Electrocardiol*, vol. 39, pp. 358–367, 2006.

[161] R. D. Berger and et. al, "Beat-to-beat QT interval variability: Novel evidence for repolarization lability in ischemic and nonischemic dilated cardiomyopathy," *Circulation*, vol. 96, no. 5, pp. 1557–1565, 1997.

[162] M. Hinterseer et. al., "Usefulness of short-term variability of QT interval as a predictor for electrical remodeling and proarrhythmia in patients with nonischemic heart failure," *Am J Cardiol*, vol. 106, pp. 216–220, 2010.

[163] P. Oosterhoff et. al., "Short-term variability of repolarization predicts ventricular tachycardia and sudden cardiac death in patients with structural heart disease: a comparison with QT variability index," *Heart Rhythm*, vol. 8, pp. 1584–1590, 2011.

[164] M. Baumert and et. al, "QT interval variability in body surface ECG: measurement, physiological basis, and clinical value: position statement and consensus guidance endorsed by the European Heart Rhythm Association jointly with the ESC Working Group on Cardiac Cellular Electrophysiology," *Europace*, vol. euv405, 2016.

[165] L. G. Tereshchenko and R. D. Berger, "Towards a better understanding of QT interval variability," *Ther Adv Drug Saf*, vol. 2, no. 6, pp. 245–251, 2011.

[166] M. Merri and M. Alberti and A. J. Moss, "Dynamic analysis of ventricular repolarization duration from 24 h Holter recordings," *IEEE Trans Biomed Eng*, vol. 40, pp. 1219–1225, 1993.

[167] F. Lombardi et. al., "Spectral analysis of short-term R-Tapex interval variability during sinus rhythm and fixed atrial rate," *Eur Heart J*, vol. 17, pp. 769–778, 1996.

[168] F. Lombardi et. al., "Assessment of the coupling between RTapex and RR interval as an index of temporal dispersion of ventricular repolarization," *Pacing Clin Electrophysiol*, vol. 21, pp. 2396–2400, 1998.

[169] R. D. Berger, "QT interval variability. Is it a measure of autonomic activity?," *J Am Coll Cardiol*, vol. 54, no. 9, p. 2009, 2009.

[170] M. C. Haigney et. al., "QT interval variability and spontaneous ventricular tachycardia or fibrillation in the Multicenter Automatic Defibrillator Implantation Trial (MADIT) ii patients.," *J Am Coll Cardiol*, vol. 44, pp. 1481–1487, 2004.

[171] G. Piccirillo, "QT variability strongly predicts sudden cardiac death in asymptomatic subjects with mild or moderate left ventricular systolic dysfunction: A prospective study.," *Eur Heart J*, vol. 28, no. 11, pp. 1344–1350, 2007.

[172] M. A. Watanabe, "Heart rate turbulence: a review," *Indian pacieng Electrophysiol J*, vol. 3, no. 1, pp. 10–22, 2003.

[173] G. Schmidt et. al., "Heart rate turbulence after ventricular premature beats as a predictor of mortality after acute myocardial infarction," *Lancet*, vol. 353, pp. 1390–1396, 1999.

[174] A. Bauer et. al., "Heart rate turbulence: standards of measurement, physiological interpretation, and clinical use. international Society for Holter and Noninvasive Electrophysiology Consensus," *J Am Coll Cardiol*, vol. 52, no. 17, pp. 1353–1365, 2008.

[175] M. Malik and D. Wichterle and G. Schmidt, "Heart rate turbulence," *G Ital Cardiol*, vol. 29, pp. 65–69, 1999.

[176] I. Cygankiewicz et. al., "Heart rate turbulence predicts all-cause mortality and sudden death in congestive heart failure patients.," *Heart Rhythm*, vol. 5, no. 8, pp. 1095–1102, 2008.

[177] J. P. Martínez et. al., "Detection performance and risk stratification using a model-based shape index characterizing heart rate turbulence," *Annals Biomed Eng*, vol. 38, pp. 3173–3184, Oct 2010.

[178] P. Arsenos and G. Manis, "Deceleration capacity of heart rate: two new methods of computation," *Biomed Sig Proc Control*, vol. 14, pp. 158–163, Nov 2014.

[179] A. Bauer et. al., "Deceleration capacity of heart rate as a predictor of mortality after myocardial infarction: cohort study," *The Lancet*, vol. 367, pp. 1674–1681, May 2006.

[180] W. Hu et. al., "Deceleration and acceleration capacities of heart rate associated with heart failure with high discriminating performance," *Sci Rep*, vol. 6, 2016.

[181] P. J. Schwartz and M. T. La Rovere and E. Vanoli, "Autonomic nervous system and sudden cardiac death: experimental basis and clinical observations for post-myocardial infarction risk stratification.," *Circulation*, vol. 85, no. suppl 1, pp. 177–191, 1992.

[182] K. D. Rizas et. al., "Sympathetic activity-associated periodic repolarization dynamics predict mortality following myocardial infarction," *J Clin Invest*, vol. 124, pp. 1770–1780, Apr 2014.

[183] D. Darbar., "Genomics, heart failure and sudden cardiac death," *Heart Fail Rev*, vol. 15, no. 3, pp. 229–238, 2010.

[184] D. B. Mark et. al., "Cost-effectiveness of defibrillator therapy or amiodarone in chronic stable heart failure results from the sudden cardiac death in heart failure trial (SCD-heft)," *Circulation*, vol. 114, no. 2, pp. 135–142, 2006.

[185] S. Neragi-Miandoab., "Non-transplant surgical therapy options of heart failure," *Minerva Cardioangiol*, vol. 62, no. 6, pp. 481–496, 2014.

[186] C. E. Garnett and et al., "Methodologies to characterize the HR/corrected QT interval in the presence of drug-induced heart rate changes or other autonomic effects.," *American Heart Journal*, vol. 163, pp. 912–930, 2012.

[187] M. Malik et. al., "QT/RR curvatures in healthy subjects: sex differences and covariates.," *American Journal of Physiology, Heart Circulation Physiology*, vol. 305, pp. H1798–H1806, 2013.

[188] K. Browne et. al., "Prolongation of the Q-T interval in man during sleep," *Am J Cardiol*, vol. 52, no. 1, pp. 55–59, 1983.

[189] F. Extramiana et. al., "Circadian modulation of QT rate dependence in healthy volunteers: gender and age differences.," *J Electrocardiol*, vol. 32, no. 1, pp. 33–43, 1999.

[190] B. Sredniawa et. al., "Circadian and sex-dependent QT dynamics," *Pacing Clin Electrophysiol*, vol. 28, no. Suppl, pp. S211–S216, 2005.

[191] E. Watanabe et. al., "Prognostic significance of circadian variability of RR and QT intervals and QT dynamicity in patients with chronic heart failure.," *Heart Rhythm*, vol. 4, no. 8, pp. 999–1005, 2007.

[192] I. Cygankiewicz and et al., "Prognostic value of QT/RR slope in predicting mortality in patients with congestive heart failure.," *Journal of Cardiovascular Electrophysiology*, vol. 19, pp. 1066–1072, 2008.

[193] S. D. Solomon et. al., "Sudden death in patients with myocardial infarction and left ventricular dysfunction, heart failure, or both.," *N Engl J Med*, vol. 352, no. 25, pp. 2581–2588, 2005.

[194] W. C Levy et. al., "The Seattle Heart Failure Model: prediction of survival in heart failure," *Circulation*, vol. 113, pp. 1424–1433, 2006.

[195] J. Ramírez et. al., "Characterization of cardiac repolarization response to heart rate changes provoked by a Tilt test," in *Computing in Cardiology*, vol. 39, pp. 673–676, 2012.

[196] C. P. Lau et. al., "Hysteresis of the ventricular paced QT interval in response to abrupt changes in pacing rate," *Cardiovasc Res*, vol. 22, pp. 67–72, Jan 1988.

[197] A. Mincholé et. al., "Modeling and quantification of repolarization feature dependency on heart rate," *Methods Inf Med*, vol. 53, pp. 324–328, 2014.

[198] W. Press et. al., *Numerical recipes in C*. 1992.

[199] E. Pueyo, and M. Malik and P. Laguna, "A dynamic model to characterize beat-to-beat adaptation of repolarization to heart rate changes," *Biomed Sig Proces Control*, vol. 3, pp. 29–43, 2008.

[200] P. C. Hansen, *Rank-deficient and discrete ill-posed problems: numerical aspects of linear inversion.*, vol. 4. Siam, 1998.

[201] J. Nocedal and S. J. Wright., *Numerical optimization*, ch. 1, p. 449. Berlin, New York, 2nd ed., 2006.

[202] E. L. Lehmann and H. J. D'abrera, *Nonparametrics: statistical methods based on ranks.* Holder-Day, 1975.

[203] R. A. Fisher., "On the interpretation of χ^2 from contingency tables, and the calculation of P.," *J Royal Stat Soc*, vol. 85, no. 1, pp. 87–94, 1922.

[204] R. Singh and K. Mukhopadhyay, "Survival analysis in clinical trials: Basics and must know areas," *Perspect Clin Res*, vol. 2, pp. 145–148, Oct-Dec 2011.

[205] E. L. Kaplan and P. Meier, "Nonparametric estimation from incomplete observations.," *J Am Stat Assoc*, vol. 53, pp. 457–481, 1958.

[206] D. R. Cox and D. Oakes, *Analysis of survival data*, vol. 21. CRC Press, 1984.

[207] N. Mantel, "Evaluation of survival data and two new rank order statistics arising in its consideration," *Cancer Chemotherapy Reports*, vol. 50, pp. 163–170, 1966.

[208] J. A. Swets., *Signal detection theory and ROC analysis in psychology and diagnostics: Collected papers.* Psychology Press, 2014.

[209] C. C. Chang and C. J. Lin, "LIBSVM: a library for support vector machines," Tech. Rep. 2(3), ACM Trans Intell Syst Technol, 1-27 2011.

[210] V. N. Vapnik, *Statistical learning theory.* 1998.

[211] F. vanderHeijden et. al., *Classification, parameter estimation and state estimation, an engineering approach using Matlab.* 2004.

[212] S. Geisser, *Predictive inference.* New York, NY, 1993.

[213] N. S. Altman, "An introduction to kernel and nearest-neighbor nonparametric regression," *Am Stat*, vol. 46, no. 3, pp. 175–185, 1992.

[214] J. Carlette, "Assessing agreement on classification tasks: the Kappa statistic," *Comput Linguist*, vol. 22, no. 2, pp. 249–254, 1996.

[215] Q. Lou et. al., "Transmural heterogeneity and remodeling of ventricular excitation-contraction coupling in human heart failure.," *Circulation*, vol. 123, no. 17, pp. 1881–1890, 2011.

[216] I. Cygankiewicz and W. Zareba and A. B. De Luna., "Prognostic value of holter monitoring in congestive heart failure.," *Cardiology Journal*, vol. 15, no. 4, pp. 313–323, 2008.

[217] I. Cygankiewicz, "Heart rate turbulence," *Prog Cardiovasc Dis*, vol. 56, no. 2, pp. 160–171, 2013.

[218] E. Valladares et. al., "Sex differences in cardiac sympathovagal balance and vagal tone during nocturnal sleep," *Sleep Med*, vol. 9, no. 3, pp. 310–316, 2008.

[219] V. M. F. Meijborg et. al., "Electrocardiographic T-wave and its relation with ventricular repolarization along major anatomical axes," *Circ: Arrhythmia Electrophysiol*, vol. 7, no. 3, pp. 524–531, 2014.

[220] M. J. Burgess, "Relation of ventricular repolarization to electrocardiographic T wave-form and arrhythmia vulnerability," *Am J Physiol*, vol. 236, no. 3, pp. H391–H402, 1979.

[221] W. Shimizu and C. Antzelevitch, "Cellular basis for long QT, transmural dispersion of repolarization, and torsade de pointes in the long QT syndrome," *J Electrocardiol*, vol. 32, no. Suppl, pp. 177–184, 1999.

[222] K. Gima and Y. Rudy, "Ionic current basis of electrocardiographic waveforms: a model study," *Circ Res*, vol. 90, no. 8, pp. 889–896, 2002.

[223] M. N. Niemeijer et. al., "Short-term QT variability markers for the prediction of ventricular arrhythmias and sudden cardiac death: a systematic review," *Heart*, vol. 100, no. 23, pp. 1831–1836, 2014.

[224] B. Acar et. al., "Spatial, temporal and wavefront direction characteristics of 12-lead t-wave morphology," *Med Biol Eng Comput*, vol. 37, no. 5, pp. 574–584, 1999.

[225] D. Cuesta-Frau et. al., "Enhanced modified moving average analysis of t-wave alternans using a curve matching method: a simulation study," *Med Biol Eng Comput*, vol. 47, no. 3, pp. 323–331, 2009.

[226] M. Kotas, "Projective filtering of time warped ECG beats," *Comput Biol Med*, vol. 38, no. 1, pp. 127–137, 2008.

[227] M. Schmidt et. al., "Two-dimensional warping for one-dimensional signals: conceptual framework and application to ECG processing," *IEEE Trans Signal Process*, vol. 62, no. 21, pp. 5577–5588, 2014.

[228] A. Srivastava et. al., "Registration of functional data using Fisher-Rao metric," in *arXiv preprint*, vol. arXiv:1103.3817, 2011.

[229] J. D. Tucker et. al., "Generative models for functional data using phase and amplitude separation," *Comput Stat Data Anal*, vol. 61, pp. 50–66, 2013.

[230] T. K. Vintsyuk, "Speech discrimination by dynamic programming," *Cybernetics*, vol. 4, pp. 52–57, 1968.

[231] J. O. Ramsay and X. Li, "Curve registration," *J R Stat Soc Series B Stat Methodol*, vol. 60, no. 2, pp. 351–363, 1998.

[232] D. P. Bertsekas, *Dynamic programming and optimal control*, ch. 1. Belmont, MA, 1995.

[233] P. W. Holland and R. E. Welsch, "Robust regression using iteratively reweighted least-squares," *Commun Stat Theory Methods*, vol. 6, no. 9, pp. 813–827, 1977.

[234] A. van Oosterom, "Genesis of the T wave as based on an quivalent surface source model," *J Electrocardiol*, vol. 34, no. Suppl, pp. 217–227, 2001.

[235] P. van Dam et. al., "Non-invasive imaging of cardiac activation and recovery," *Ann Biomed Eng*, vol. 37, no. 9, pp. 1739–1756, 2009.

[236] R. Sassi and L. Mainardi, "An estimate of the dispersion of repolarization times based on a biophysical model of the ECG," *IEEE Trans Biomed Eng*, vol. 58, pp. 3396–3405, Dec 2011.

[237] M. Orini et. al., "Detection of transient, regional cardiac repolarization alternans by time-frequency analysis of synthetic electrograms," in *Conf Proc IEEE Eng Med Biol Soc*, pp. 3773–3776, 2013.

[238] D. B. Geselowitz, "Description of cardiac sources in anisotropic cardiac muscle. Application of bidomain model.," *J Electrocardiol*, vol. 25, no. Suppl, pp. 65–67, 1992.

[239] E. Gil et. al., "Photoplethysmography pulse rate variability as a surrogate measurement of heart rate variability during non-stationary conditions," *Physiol Meas*, vol. 31, no. 9, pp. 1271–1290, 2010.

[240] D. C. Howell, *Median absolute deviation*. 2005.

[241] A. Srivastava et. al., "Shape analysis of elastic curves in euclidean spaces," *IEEE Trans Pattern Anal Mach Intell*, vol. 33, no. 7, pp. 1415–1428, 2010.

[242] R. D. Berger, "Methodology for automated QT variability measurement," Tech. Rep. 861, U.S. Patent 08/340, Oct 1st 1996.

[243] H. J. L. M. Vullings et. al., *ECG segmentation using time-warping*, pp. 275–285. International Symposium on Intelligent Data Analysis, 2006.

[244] A. Zifan et. al., "Automated segmentation of ECG signals using piecewise derivative dynamic time warping," *Int J Biol Life Sciences*, vol. 1, pp. 181–185, 2007.

[245] J. Ramírez et. al., "Variability of ventricular repolarization dispersion quantified by time-warping the morphology of the T-waves.," *IEEE Trans Biomed Eng*, vol. DOI:10.1109/TBME.2016.2614899, 2016.

[246] J. Ramírez et. al., "Automatic SVM classification of sudden cardiac death and pump failure death from autonomic and repolarization ECG markers.," *J Electrocardiol*, vol. 48, no. 4, pp. 551–557, 2015.

[247] W. B. Nicolson et. al., "Prospective evaluation of two novel ECG-based restitution biomarkers for prediction of sudden cardiac death risk in ischaemic cardiomyopathy," *Heart*, vol. 100, no. 23, pp. 1878–1885, 2014.

[248] M. S. Figueroa and J. I. Peters, "Congestive heart failure: diagnosis, pathophysiology, therapy, and implications for respiratory care.," *Respir Care*, vol. 51, no. 4, pp. 403–412, 2006.

[249] H. P. Rang, *Pharmacology*, p. 127. 2003.

[250] B. M. Curtis and J. H. O'Keefe, "Autonomic tone as a cardiovascular risk factor: The dangers of chronic fight or flight," *Mayo Clin Proc*, vol. 77, pp. 45–54, 2002.

[251] J. P. Fisher and C. N. Young and P. J. Fadel, "Central sympathetic overactivity: Maladies and mechanisms," *Auton Neurosci*, vol. 148, no. 1-2, pp. 5–15, 2009.

[252] R. J. Selvaraj et. al., "Adrenergic stimulation increases repolarization dispersion and reduces activation-repolarization coupling along the RV endocardium of patients with cardiomyopathy," *Europace*, vol. 11, pp. 1529–1535, 2009.

[253] M. Qin et. al., "Effect of isoprenaline chronic stimulation on APD restitution and ventricular arrhythmogenesis," *J Cardiol*, vol. 61, pp. 162–168, 2013.

[254] M. L. Ogletree-Hughes et. al., "Mechanical unloading restores beta-adrenergic responsiveness and reverses receptor downregulation in the failing human heart," *Circulation*, vol. 104, pp. 881–886, 2001.

[255] S. T. Dahlberg, "Gender difference in the risk factors for sudden cardiac death," *Cardiology*, vol. 77, no. Suppl 2, pp. 31–40, 1990.

[256] A. E. Buxton., "Not everyone with an ejection fraction $<30\%$ should receive an implantable cardioverter-defibrillator," *Circulation*, vol. 111, pp. 2537–2549, 2005.

[257] A. Mosterd and A. W. Hoes., "Clinical epidemiology of heart failure," *Heart*, vol. 93, no. 9, pp. 1137–1146, 2007.

[258] M. Klapholz, "Beta-blocker use for the stages of heart failure.," *Mayo Clin Proc*, vol. 84, no. 8, pp. 718–729, 2009.

[259] E. B. Friedrich and M. B ohm, "Management of end stage heart failure," *Heart*, vol. 93, pp. 626–631, 2007.

[260] R. L. Verrier et. al., "Basis for sudden cardiac death prediction by T-wave alternans from an integrative physiology perspective," *Heart Rhythm*, vol. 6, no. 3, pp. 416–422, 2009.

[261] M. T. La Rovere et. al., "Clinical and haemodynamic correlates of heart rate turbulence as a non-invasive index of baroreflex sensitivity in chronic heart failure," *Clin Sci (Lond)*, vol. 121, pp. 279–284, 2011.

[262] T. V. Kenttä et. al., "Prediction of sudden cardiac death with automated high-throughput analysis of heterogeneity in standard resting 12-lead electrocardiograms," *Heart Rhythm*, vol. 13, no. 3, pp. 713–720, 2016.

[263] C. Antzelevitch et. al., "Does Tpeak-Tend provide an index of transmural dispersion of repolarization?," *Heart Rhythm*, vol. 4, no. 8, pp. 114–116, 2007.

Awards and Publications

Awards

- *Rosanna Degani Young Investigator Award for the best written and oral presentation.* Prediction of sudden cardiac death in chronic heart failure patients by analysis of restitution dispersion. *XL International Conference on Computing in Cardiology*, Zaragoza, Spain, 2013.
- *Jos Willems Young Investigator Finalist.* Prediction of sudden cardiac death by analysis of restitution dispersion. 30^{th} *Annual conference of the international society for computerized electrocardiology.* Jacksonville, Florida (USA), 2014.
- *Michael Ringborn Young Investigator Award for the best oral presentation.* DeltaAlpha repolarization dispersion. 12^{th} *STAFF Studies Symposium.* MIT Endicott House, Dedham, MA (USA), 2014.
- *Mortara mobility fellowship.* An index for T-wave pointwise amplitude variability quantification. Computing in Cardiology. *XLIII International Conference on Computing in Cardiology*, Vancouver, Canada, 2016.
- *Michael Ringborn Young Investigator Award for the best oral presentation.* T-wave morphological restitution evaluated by time-warping metrics and its value to predict sudden cardiac death and pump failure death. 14^{th} *STAFF Studies Symposium.* Bled, Slovenia, 2016.

Publications

Journal Publications

- **J. Ramírez**, P. Laguna, A. B. De Luna, M. Malik and E. Pueyo. QT/RR and T-peak-to-end/RR curvatures and slopes in chronic heart failure: Relation to sudden cardiac death. *J Electrocardiol*, 2014;47:842-848.
- **J. Ramírez**, V. Monasterio, A. Mincholé, M. Llamedo, G. Lenis, I. Cygankiewicz, A. B. De Luna, M. Malik, J. P. Martínez, P. Laguna and E. Pueyo. Automatic

SVM classification of sudden cardiac death and pump failure death from autonomic and repolarization ECG markers. *J Electrocardiol*, 2015;48:551-557.

- **J. Ramírez**, M. Orini, J. D. Tucker, E. Pueyo and P. Laguna. Variability of ventricular repolarization dispersion quantified by time-warping the morphology of the T-waves. *IEEE Transactions on Biomedical Engineering*, 2016; DOI: 10.1109/TBME.2016.2614899.

Submitted Publications

- **J. Ramírez**, M. Orini, A. Mincholé, V. Monasterio, I. Cygankiewicz, A. B. De Luna, J. P. Martínez, E. Pueyo and P. Laguna. T-wave Morphology Restitution Predicts Sudden Cardiac Death in Patients with Chronic Heart Failure. Submitted to *Journal of the American Heart Association*.

- **J. Ramírez**, M. Orini, A. Mincholé, V. Monasterio, I. Cygankiewicz, A. B. De Luna, J. P. Martínez, E. Pueyo and P. Laguna. Improvement of Sudden Cardiac Death and Pump Failure Death Prediction by Including ECG-derived Markers to a Clinical Model. Submitted to *Heart Rhythm*.

Conference Publications

- **J. Ramírez**, A. Mincholé, P. Laguna and E. Pueyo. Characterization of cardiac repolarization response to heart rate changes provoked by a Tilt test. *XXXIX International Conference on Computing in Cardiology*, Krakow, Poland, 673-676, 2012.

- **J. Ramírez**, A. Mincholé, J. Bolea, P. Laguna and E. Pueyo. Prediction of sudden cardiac death in chronic heart failure patients by analysis of restitution dispersion. *XL International Conference on Computing in Cardiology*, Zaragoza, Spain, 1-4, 2013.

- **J. Ramírez**, I. Cygankiewicz, P. Laguna, M. Malik and E. Pueyo. Circadian pattern and sex differences of QT/RR and T-peak-to-end/RR curvatures and slopes in chronic heart failure patients. *XLI International Conference on Computing in Cardiology*, Boston (MA), U.S.A., 173-176, 2014.

- **J. Ramírez**, M. Orini, J. D. Tucker, E. Pueyo and P. Laguna. An index for T-wave pointwise amplitude variability quantification. *XLIII International Conference on Computing in Cardiology*, Vancouver, Canada, 49-52, 2016.

- G. Lenis, R. Menges, **J. Ramírez**, I. Cygankiewicz, A. Bayés de Luna, P. Laguna and O. D ossel. Post extrasystolic T wave change to stratify risk of pump failure death in patients with chronic heart failure. *XLIII International Conference on Computing in Cardiology*, Vancouver, Canada, 37-40, 2016.